UNIVERSITY of CALIFORNIA
Santa Barbara

Radioassay of Gadolinium-Loaded Liquid Scintillator and Other Studies for the LZ Outer Detector

A dissertation submitted in partial satisfaction of the
requirements for the degree of

Doctor of Philosophy

in

Physics

by

Scott John Haselschwardt

Committee in charge:

Professor Harry Nelson, Chair
Professor David Stuart
Professor Mark Srednicki

December 2018

The dissertation of Scott John Haselschwardt is approved:

Professor David Stuart

Professor Mark Srednicki

Professor Harry Nelson, Chair

October 2018

I dedicate this dissertation to my late father, Howard John Haselschwardt, who was responsible for instilling in me the "work hard, play hard" mentality and teaching me everything I know about how to build things. Both of these have proved invaluable throughout this work and my life. Thanks, Dad.

Acknowledgements

I am extremely grateful for the guidance of my advisor, Harry Nelson, who has consistently demonstrated and shared his joy and aptitude for scientific research. I learned early on in my PhD that a good approach would be to spend as much time as possible listening to Harry. Whether it was focused problem solving, stories of various Manhattan Project endeavors, or historical accounts of particle physics discoveries, I was listening and attempting to absorb as many crucial lessons as I could. I am extremely fortunate to have had such a fantastic mentor.

At the outset of my studies I also benefited from focused insights and guidance of Mike Witherell. I am very grateful for the many interactions that Mike and I shared, especially in discussions of the Outer Detector design and performance.

Of course, the crazy gadgets we physicists dream up only come to fruition with the help of talented engineers. The primary work in this dissertation could not have happened without the assistance and expertise of Dean White and Susanne Kyre. Both of them deserve many praise for tolerating my almost-daily intrusions into their office during the construction and commissioning of the Screener. Dean, of course, deserves special mention as he accompanied me on multiple occasions during the frozen winter months in South Dakota for the Screener project.

I'd like to acknowledge my cohorts within our group at UCSB. Melih Solmaz deserves praise for injecting some culture and broader world views into our discussions while also providing sound physics insight. Sally Shaw deserves special mention as she has consistently been a great source of insight and helped immensely with parts of the Screener analysis. Finally, Curt Nehrkorn was a pleasure to work with, both at UCSB and during our trips to South Dakota

Working in the LUX and LZ collaborations has been a fantastic experience. Indeed, the research in this dissertation would not have been possible without the help and support of many collaborators. Among others (you know who you are!), I would like to thank: Scott Hertel, Brian Lenardo, James Morad, Dev Khaitan, Lucie Tvrznikova, Kevin Lesko, Andy Cole, Simon Fiorucci, David Woodward, Markus Horn, Dave Taylor, John Keefner, Doug Tiedt, Will Taylor, and Minfang Yeh.

I felt particularly lucky to be surrounded by an amazing group of friends over the course of graduate school. In particular, the residents of Za City both old and new have always provided a profoundly goofy environment in which to relax. The original cast comprised of Andrew, Jason, Kenny, Nick, and Kurt deserve special recognition. Attempts to find the best surf in the area all year round would not have been nearly as enjoyable without the presence of Andrew, Jason, and Eric.

My family has always provided me with love and support in anything I do. Thanks to my mother, father, and my sister for a life of opportunity and fun. My wife, Sarah, is always supportive and loving. Throughout the ups and downs of grad school and all the long stints in South Dakota she has been there for me. Not only that, but she has also learned the 5 minute overview of searching for dark matter with LZ so well that I usually let her do all the talking at parties. Thank you and I love you.

Curriculum Vitæ

Scott John Haselschwardt

Education

(2018) Ph.D., Physics, University of California, Santa Barbara, CA

(2012) B.S.E., Engineering Physics, University of Michigan, Ann Arbor, MI

Professional Experience

(2013-2018) Graduate Student Researcher, LUX & LZ Collaborations
Supervisor: Dr. Harry Nelson
University of California, Santa Barbara, CA

(2012-2013) Teaching Assistant, Senior Laboratory & Analog Electronics
University of California, Santa Barbara, CA

(2011-2012) Undergraduate Researcher, CDF Collaboration
Supervisor: Dr. Dante Amidei
University of Michigan, Ann Arbor, MI

(2010-2011) Laboratory Technician
University of Michigan, Ann Arbor, MI

Selected Publications

A Liquid Scintillation Detector for Radioassay of Gadolinium-Loaded Liquid Scintillator for the LZ Outer Detector, S.J. Haselschwardt et al., arXiv:1808.05595

Results from a Search for Dark Matter in the Complete LUX Exposure, D.S. Akerib et al. (LUX Collaboration), *Phys. Rev. Lett.* 118, 021303 (2017)

LUX-ZEPLIN (LZ) Technical Design Report, B.J. Mount et al. (LZ Collaboration), arXiv:1703.09144

Improved Limits on Scattering of Weakly Interacting Massive Particles from Reanalysis of 2013 LUX Data, D.S. Akerib et al. (LUX Collaboration), *Phys. Rev. Lett.* 116, 161301 (2016)

Abstract

Radioassay of Gadolinium-Loaded Liquid Scintillator and Other Studies for the LZ Outer Detector

by

Scott John Haselschwardt

It is now well established that over 80% of the matter in our Universe is comprised of a non-luminous substance known as dark matter. By far the most popular dark matter candidate is the weakly interacting massive particle (WIMP). Attempting to discover the nature of WIMP dark matter through direct detection has been a central activity of experimental physics for at least the last 20 years. To date, no conclusive signal consistent with WIMP interactions has been observed.

The LZ (LUX-ZEPLIN) experiment is a second generation direct dark matter detector under construction one mile underground in the Davis Laboratory of the Sanford Underground Research Facility (SURF) in Lead, South Dakota, USA. LZ will use a 7 tonne central liquid xenon target, arranged in a dual-phase time projection chamber (TPC), to seek evidence for nuclear recoils from a hypothesized galactic flux of WIMPs. Two active detector elements will surround the TPC: a layer of liquid xenon, the xenon skin, optimized to detect γ's, and the outer detector (OD), optimized to detect neutrons. Together, these detectors will tag backgrounds to the sought-after WIMP signal and

characterize the background environment around LZ.

The OD is comprised of acrylic tanks filled with 17.3 tonnes of LAB-based gadolinium-loaded liquid scintillator (GdLS) that will surround the central cryostat of LZ in a near-hermetic fashion. Its primary function will be to tag neutron single-scatter events in the liquid xenon which could mimic a WIMP dark matter signal. I summarize simulation studies of the OD expected performance as a neutron veto and expected light collection.

The rate of single background pulses in the OD is also discussed. The three primary sources of rate in the OD are identified as: LZ detector components, γ-rays from the Davis Laboratory walls, and the radioimpurities in the GdLS. The radioimpurities in the GdLS are particularly troublesome because the OD is sensitive to both the α and β/γ decays of these isotopes. To meet the requirements for the OD, the radioimpurity levels in the GdLS must be kept below $\lesssim 0.07$ mBq/kg. This background level corresponds to a rate of ≈ 50 Hz above an energy threshold of 100 keV.

I report on the design and performance of the "Screener", a small liquid scintillator detector consisting of $\approx$ 23 kg of the GdLS to be used in the OD. The Screener was operated in the ultra-low-background environment of the former LUX water shield in the Davis Laboratory at SURF for radioassay of the GdLS. Careful selection of detector materials and use of ultra-low-background PMTs allows the measurement of a variety of radioimpurities. The $^{14}C/^{12}C$ ratio in the scintillator is measured to be $(2.83 \pm 0.06(\text{stat.}) \pm 0.01(\text{sys.})) \times 10^{-17}$. Use of pulse shape discrimination allows the concentration of isotopes throughout the ^{238}U, ^{235}U, and ^{232}Th chains to be measured by

fitting the collected spectra from α and β events. It is found that equilibrium is broken in the ^{238}U and ^{232}Th chains and that a significant portion of the contamination in the GdLS results from decays in the ^{227}Ac subchain of the ^{235}U series.

Predictions for the singles rate in the OD are presented. The rate from radioimpurities above 100 keV in the GdLS is estimated to be 97.5 ± 6.3 Hz, with 65.0 ± 1.4 Hz resulting from α-decays.

Contents

Chapter 1

Dark Matter in the Universe

Since the 1930's the body of scientific evidence which suggests the existence of dark matter (DM) in our Universe has been growing ever stronger. In that time the fundamental nature of this substance has grown to become one of the biggest puzzles in all of physics. Our information about DM's basic properties can only be obtained through inference and observations made in astronomy and cosmology.

1.1 Evidence for Dark Matter

Partly what makes the DM hypothesis so intriguing is the large range of scales over which the theory is experimentally supported. Here I briefly discuss two of the important findings that have lead to the formation and support of a DM hypothesis: the measured rotational dynamics of galaxies and signatures in the cosmic background radiation.

1.1.1 Rotation Curves of Galaxies

In the 1970's, Vera Rubin and her team made spectroscopic measurements of the fainter emission regions of the Andromeda galaxy [1]. Using Doppler shifted lines to measure the circular velocity of matter around the central nucleus of the galaxy, Rubin set out to survey the dynamics of Andromeda and determine its mass.

From a force balance in Newtonian physics, the expected velocity at a specified radius r, will be given by

$$v(r) = \sqrt{\frac{GM(r)}{r}} \quad , \tag{1.1}$$

where $M(r)$ is the mass contained within a shell of radius r. At larger radii, far from the luminous galactic center, we would expect that nearly all the mass of Andromeda is accounted for in $M(r)$ so that the velocity profile of objects behaves as $v(r) \sim \sqrt{1/r}$.

Instead, what was measured was a relatively flat distribution of velocities at steadily increasing radii. Another survey conducted by Rubin and her team [2], this time including multiple spiral galaxies, had the same conclusions, and the rotation curves from this study are shown in Fig. 1.1. The flat distribution of velocities at such large radii implies the existence of non-luminous matter with $M(r) \sim r$ and is nowadays one of the most cited pieces of evidence for halos of DM thought to surround all galaxies. A classic example of accounting for the observed rotation curves is shown in Fig. 1.2 where the contributions from visible matter, gas and DM halo components are summed to provide good agreement with the collected data. It is now believed that the structure of galaxies and clusters of galaxies we observe today could not have formed with the deep gravitational potential

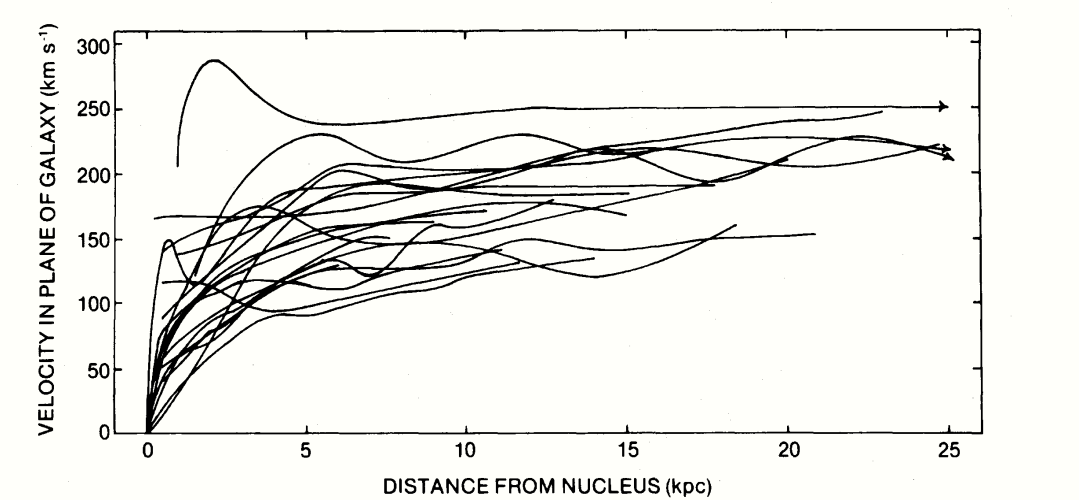

Figure 1.1: Rotation curves for 21 galaxies plotting velocity of luminous matter as a function of radial distance to the galactic center. All curves show a characteristic flatness in the velocity at large radii. From [2].

wells provided by DM halos.

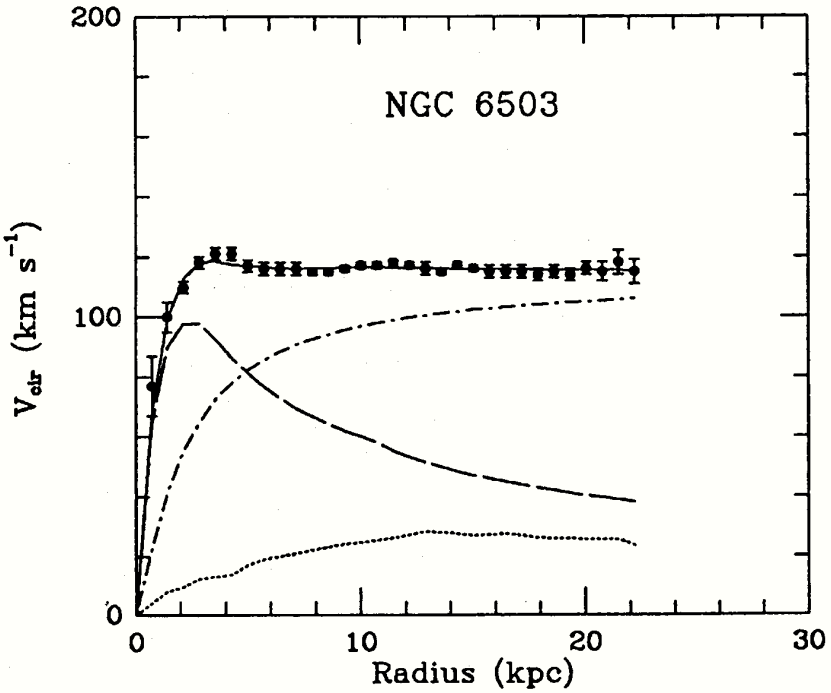

Figure 1.2: A rotation curve from [3] with a fit (solid line) that attempts to quantify the relative contributions to the observed velocities from various components. The components considered are: visible matter (dashed), gas (dotted), and the DM halo (dotted-dashed).

1.1.2 Cosmic Microwave Background

Observations of the cosmic microwave background (CMB) provide the most stringent tests of cosmological models which seek to understand the structure and evolution of our Universe. The CMB is comprised of a very nearly isotropic sea of photons with energies following very closely that expected from a black body with temperature $T = 2.7$ K. These photons are the remnant of the recombination epoch when the expansion rate of the Universe became larger than their typical scattering length on free electrons. Unable to stay in thermal equilibrium with each other, the electrons cooled and combined with protons to form neutral hydrogen, allowing the photons to propagate uninhibited and the Universe to become "transparent". Since that time the photons have been redshifted due to the expansion of the Universe.

Precise measurements of anisotropies in the CMB temperature provide rich information about the cosmology of our Universe and provide a testbed for theories seeking to explain its evolution. Fig. 1.3 shows the distribution of the CMB temperature fluctuations. The statistical information contained in this data is usually extracted by decomposing the temperature fluctuations into a basis of spherical harmonics Y_{lm}:

$$\frac{\Delta T}{T}(\theta,\phi) = \sum_{l=2}^{\infty} \sum_{m=-l}^{+l} a_{lm} Y_{lm}(\theta,\phi) \quad . \tag{1.2}$$

The correlation function between two points in the sky, C_l, is then formed from the coefficients, a_{lm}, averaged over values of m: $C_l \equiv \langle |a_{lm}|^2 \rangle$. The resulting power spectrum, which plots $l(l+1)C_l/2\pi$ is shown in Fig. 1.4.

The most successful model of our Universe to date is one which includes a "cold

Table 1.1: A sample of Planck 2015 ΛCDM fit results from Ref. [4].

Parameter	Symbol	Fit value
Baryonic matter density	$\Omega_{\rm b}$	0.0488 ± 0.0003
Cold dark matter density	$\Omega_{\rm c}$	0.2601 ± 0.0022
Total matter density	$\Omega_{\rm m} = \Omega_{\rm c} + \Omega_{\rm b}$	0.3089 ± 0.0062
Dark energy density	Ω_Λ	0.6911 ± 0.0062
Critical density	ρ_c	$(8.62 \pm 0.12) \times 10^{-27}$ kg/m^3

dark matter" (CDM) component as well as a cosmological constant, Λ, in the underlying curvature/energy density relation provided by Einstein's general relativity. The result of a multi-parameter fit under the ΛCDM model framework is shown as the red line in Fig. 1.4: agreement with the data is very good. Important parameters extracted from these fits include the energy density of baryons, $\Omega_{\rm b}$, cold dark matter, $\Omega_{\rm c}$, and dark energy, Ω_Λ, where the densities are reported relative to the "critical density" needed to produce a spacetime which is flat:

$$\rho_c = \frac{3H^2}{8\pi G} \quad . \tag{1.3}$$

Here, H is the Hubble constant and G is the universal gravitational constant. Tab. 1.1 provides a sample of fit values found in Ref. [4]. These parameters paint the modern picture of our Universe: over 80% of matter is comprised of cold dark matter, while nearly 70% of the entire energy density budget is formed by "dark energy", a form a energy which appears to be directly stitched into spacetime itself.

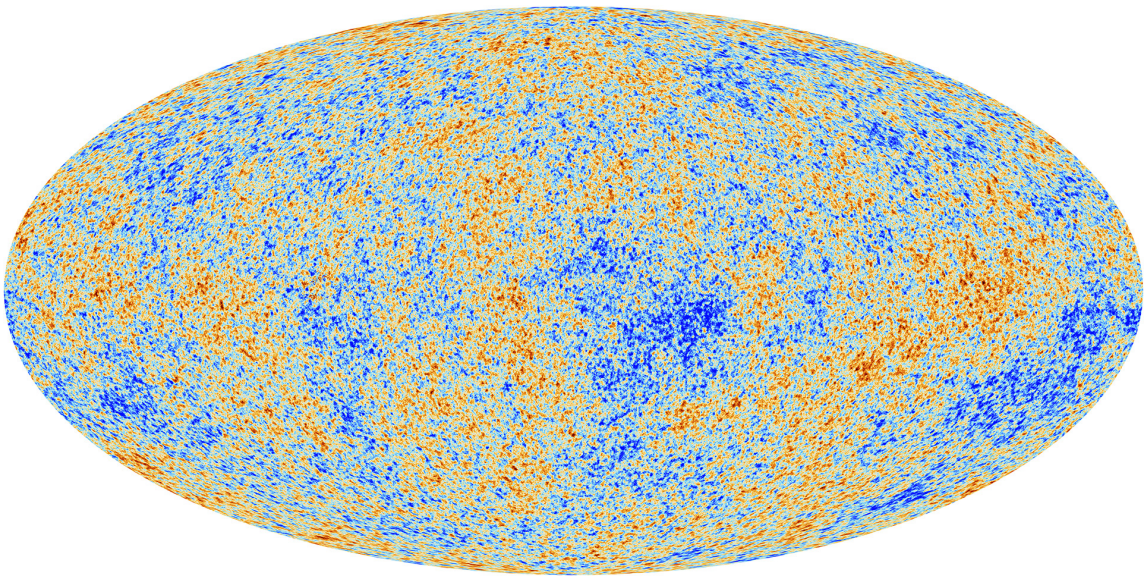

Figure 1.3: Skymap of CMB temperature fluctuations as measured by Planck.

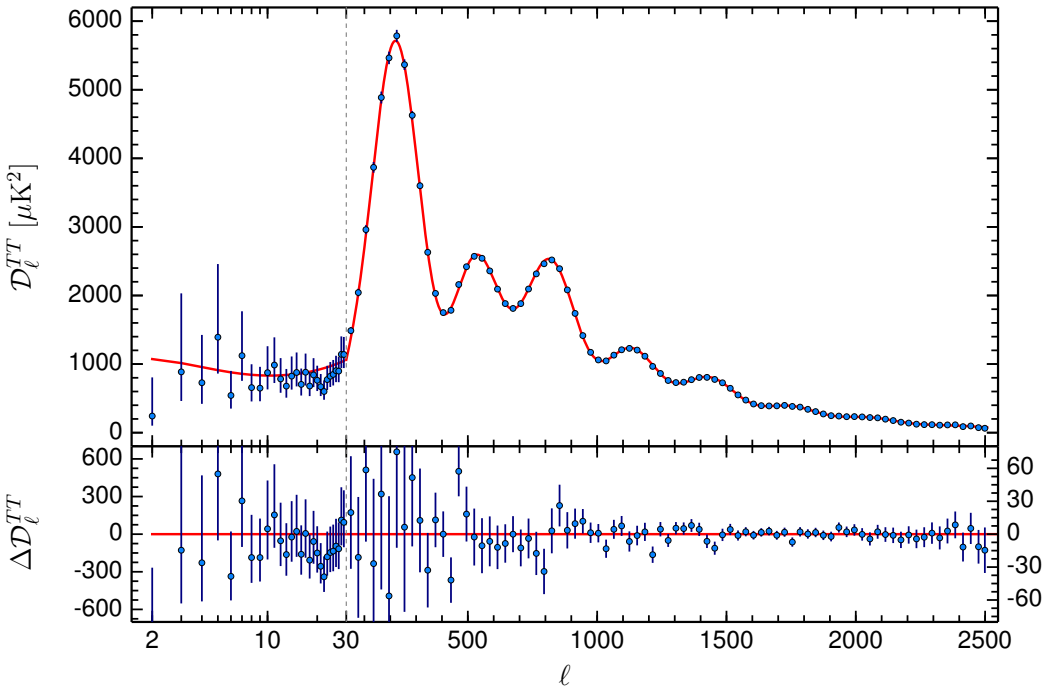

Figure 1.4: Observed (blue points) angular power spectrum in Planck 2015 CMB data and best-fit ΛCDM model (red line) From Ref. [4].

1.2 The WIMP Dark Matter Candidate

While there are a plethora of candidates for what may be comprising the DM, I will focus specifically on the most popular: the weakly interacting massive particle or WIMP. Such is the focus of many reviews on the subject; Refs. [5; 6] in particular can provide many more details and references than the brief overview given here.

WIMPs are a hypothesized, stable (or have mean life much greater than the age of the Universe) particle species conjectured to have existed in thermal equilibrium in the hot, early Universe. In this environment, the temperature T is assumed to be much larger than the WIMP mass m_χ. As their name implies, WIMPs are assumed to have some mechanism of interaction with particles of the Standard Model (SM). In the high T early Universe, the annihilation processes of WIMPs (χ) to SM particles (l), $\chi\bar{\chi} \to l\bar{l}$, and the creation processes, $l\bar{l} \to \chi\bar{\chi}$, are in equilibrium so that the number density n of WIMPs is a constant: $n = n_{\rm eq}$. As the Universe expands and cools, the rate of WIMP annihilation falls below the rate of spacetime expansion: $\langle\sigma_{\rm A} v\rangle n \lesssim H$, where $\langle\sigma_{\rm A} v\rangle$ is the thermally averaged annihilation cross section and H is the Hubble parameter. The rate change of WIMP particle density is expressed by the famous Boltzmann equation:

$$\frac{dn}{dt} = -3Hn - \langle\sigma_{\rm A} v\rangle \left(n^2 - n_{\rm eq}^2\right) \quad , \tag{1.4}$$

where the first term carries a negative sign as the Universe expands and depletes the number density of WIMPs. In the second term, WIMPs are removed through the annihilation process (proportional to n^2), but created through the $l\bar{l} \to \chi\bar{\chi}$ process (proportional to $n_{\rm eq}^2$).

Numerical solutions to Eq. 1.4 lead to the well-known "WIMP miracle", whereby cross sections characteristic of weak interactions lead to a "freeze out" of the WIMP density consistent with the DM density observed today (by measurements of the CMB as above). Furthermore, as pointed on in Ref. [6], the WIMP mass often enters in the calculation of an annihilation cross section. Typical mass scales are of order GeV up to TeV, which is characteristic of electroweak-scale particles.

Supersymmetry (SUSY), by far most ubiquitous extension for the SM, also supports the WIMP hypothesis through the prediction of WIMP-like particles. In SUSY, a host of new particle species are predicted as the super partners of the SM particles having the same quantum numbers, but differing in their intrinsic spin by 1/2 (i.e. fermions have bosonic super partners and vice versa). The least massive of these states, the lightest supersymmetric particle (LSP), is a natural WIMP candidate as it is stable and electrically neutral.

Chapter 2

Direct Detection of WIMP Dark Matter

To date we have only "observed" DM through its influence on luminous objects in the sky. Supposing that the DM is comprised of WIMPs, we expect that it can interact with particles of the SM and, therefore, might be "detected". Three principle detection schemes are identified as: production, indirect detection, and direct detection. In the production approach, high-energy collisions of SM particles such as those at the LHC may be used to produce DM directly. A key signature of a DM signal would be an excess of events with missing transverse energy above the SM background. In "indirect" detection, experiments attempt to detect the SM particle products of DM annihilation or interactions taking place in various astrophysical regions such as the galactic center, in the merging of galaxy cluster, and in our own Sun.

The final method of "direct" detection is what concerns us here. In direct detection, we suppose that the relative motion of the Earth to the DM halo in our galaxy creates a flux of DM particles. We therefore wish to observe the scattering of an incident DM particle off a target in a laboratory. The recoil energy E_R imparted to a target nuclei or electron during the scattering event results in some kind of detector response leading to a detectable signal. In this chapter we derive the expected rate of WIMP DM scatters in such a detector and provide an overview of the liquid-xenon time-projection chamber, the leading detector technology in the hunt for WIMP direct detection.

2.1 WIMP Interaction Rate

In any counting experiment we need to know the expected rate of signal events in our detector. This rate will ultimately constrain the amount of background allowed in the experiment and often drives the principle design choices of the experiment (e.g. DM experiments need to operate underground).

The specific process we which to observe in a direct detection experiment is the elastic scattering of a WIMP off a target nucleus with masses m_χ and m_T, respectively. The nucleus recoils with energy E_R from the transfer of momentum q given by

$$E_R = \frac{q^2}{2m_T} = \frac{\mu^2 v^2}{m_T}(1 - \cos\theta) \quad , \tag{2.1}$$

where $\mu = m_\chi m_T/(m_\chi + m_T)$ is the reduced mass of the WIMP-nucleus system, v is the incoming WIMP velocity and θ is the scattering angle measured in the center-of-mass

frame.

Generically, the differential rate per unit recoil energy in our detector subject to an incident flux of WIMPs with well-defined velocity will be

$$\frac{dR}{dE_R} = (\text{Diff. Cross Section}) \times (\#\text{ Target Nuclei}) \times (\text{Incident Particle Flux}) \tag{2.2}$$

$$\frac{dR}{dE_R} = \frac{d\sigma}{dE_R}(v, E_R) n_T \left(\frac{\rho_\chi}{m_\chi} v\right) \tag{2.3}$$

where the incident particle flux has been written in terms of the local WIMP density ρ_χ. In reality, WIMPs are not incident on our detector with a single velocity. Instead, the velocity is assumed to have some (suitably normalized) distribution $f(v)$, so that the differential rate requires an integral over velocities:

$$\frac{dR}{dE_R} = \left(\frac{\rho_\chi n_T}{m_\chi}\right) \int_{v_{\min}(E_R)}^{\infty} dv\, f(v)\, v\, \frac{d\sigma}{dE_R}(v, E_R) \tag{2.4}$$

In the above equation, the lower bound of integration is the minimum WIMP velocity required to produce a recoil energy E_R. From Eq. 2.1, we take the case of a head-on collision ($\cos\theta = -1$) to find:

$$v_{\min}(E_R) = \sqrt{\frac{E_R m_T}{2\mu^2}} \tag{2.5}$$

The differential WIMP-nucleus cross section, $d\sigma/dE_R(v, E_R)$ contains all the particle and nuclear physics assumptions about the interaction we wish to detect. We will decompose this quantity further by using the expression given in the review of Ref. [5]:

$$\frac{d\sigma}{dq^2} = \frac{G_F^2 C}{v^2} F^2(q) \tag{2.6}$$

so that

$$\frac{d\sigma}{dE_R}(v, E_R) = \frac{d\sigma}{dq^2}\frac{dq^2}{dE_R} = \frac{2m_T G_F^2 C}{v^2} F^2(E_R) \tag{2.7}$$

In this expression, G_F is the Fermi coupling constant, C is a dimensionless quantity that will encode particle physics information, and $F(E_R)$ is a nuclear form factor that encodes information about nucleons are distributed in the target nucleus. Substitution into Eq. 2.4 yields:

$$\frac{dR}{dE_R} = 2m_T G_F^2 C \left(\frac{\rho_\chi n_T}{m_\chi}\right) F^2(E_R) \int_{v_{\min}(E_R)}^{\infty} dv \, \frac{f(v)}{v} \tag{2.8}$$

Eq. 2.8 is our fundamental expression for the differential event rate in our detector. More specific details about the WIMP interaction, the nuclear physics, and the velocity distribution of WIMPs are incorporated through C, $F(E_R)$, and $f(v)$, respectively. Virtually every experiment seeking to detect WIMPs has adopted a standard set of assumptions for these three ingredients so that results can be compared without worrying about differences in the physics inputs. I will stick to these assumptions here.

2.1.1 Standard Halo Model

The Standard Halo Model (SHM) used in nearly all direct detection experiments assumes an isotropic and isothermal halo of WIMPs around our galaxy. In the rest frame of the halo, WIMPs are assumed to have a Maxwell-Boltzmann velocity distribution:

$$f(\vec{v}) = \frac{1}{N} e^{\vec{v}^2/v_0^2} \quad , \tag{2.9}$$

where N is a normalization constant. If one integrates $f(\vec{v})$ over all velocities (and directions in velocity space) $N = \pi^{3/2} v_0^3$. More realistically, the normalization is adjusted by only considering WIMPs which have $v = |\vec{v}| < v_{\rm esc}$, the galactic escape velocity. WIMPs with velocity above the escape velocity are not gravitationally bound in the galaxy and should therefore not be included in the isothermal ensemble.

To calculate the rate in our detector we must obtain the velocity distribution in the frame of the Earth where our experiment is located while also including the constraint $v < v_{\rm esc}$. The distribution we want is then [7]

$$f_\oplus(\vec{v}, \vec{v}_{\rm obs}) = f(\vec{v} + \vec{v}_{\rm obs}) = \begin{cases} \frac{1}{N}\, e^{-(\vec{v}+\vec{v}_{\rm obs})^2/v_0^2} & |\vec{v} + \vec{v}_{\rm obs}| < v_{\rm esc} \\ 0 & |\vec{v} + \vec{v}_{\rm obs}| > v_{\rm esc} \end{cases} \quad , \tag{2.10}$$

where the velocity of the Earth-bound observer is the vector sum of the Sun's velocity relative to the galactic plane and the velocity of the Earth around the Sun: $\vec{v}_{\rm obs} = \vec{v}_\odot + \vec{v}_\oplus$. This this the distribution that should be used for calculating WIMP interaction rates. The appropriate modification of Eq. 2.8 is

$$\frac{dR}{dE_R} = 2 m_T G_F^2 C \left(\frac{\rho_\chi n_T}{m_\chi}\right) F^2(E_R) \int_{v_{\rm min}(E_R)}^{\infty} d^3v\, \frac{f_\oplus(\vec{v}, \vec{v}_{\rm obs})}{v} \quad , \tag{2.11}$$

where we now integrate over all of three-dimensional velocity space in the frame of the detector on Earth. The definition Eq. 2.10 automatically truncates the integral to account for the galactic escape velocity.

What remains is to compute the velocity integral

$$\zeta(E_R) = \int_{v_{\rm min}(E_R)}^{\infty} d^3v\, \frac{f_\oplus(\vec{v}, \vec{v}_{\rm obs})}{v} \quad , \tag{2.12}$$

using the notation of Ref. [7]. This has been done in the classic review of Lewin and

Smith [8], but due to an error in that text pointed out in Ref. [9], the standard reference has become Refs. [10; 7]. For the complete evaluation of $\zeta(E_R)$ refer to Ref. [7].

For direct detection experiments with run durations on the order of a year or more, the time dependence of Eq. 2.11 is neglected by using the time-averaged value of $v_{\rm obs}$. Detecting an annual modulation in the WIMP scattering rate due to the increased and decreased relative velocity of the Earth to the WIMP halo is the principle goal of ongoing [11] and newer [12; 13] direct detection experiments.

2.1.2 Nuclear Form Factor

The form factor $F(E_R)$ encodes the presence of nuclear structure in our target nuclei. When the de Broglie wavelength $\lambda = h/q$ associated with the WIMP momentum transfer is comparable or smaller than the typical radius of the nucleus ($\sim$10 fm), the scattering process begins to resolve the individual nucleons. In fact, it can be shown (see, for example, Appendices B and C in Ref. [14]) in the Born approximation that

$$\frac{d\sigma}{d\Omega} = \left(\frac{d\sigma}{d\Omega}\right)_{\rm point} |F(E_R)|^2 \quad , \tag{2.13}$$

where the form factor (now in terms of the momentum transfer q) is the Fourier transform of the nuclear charge/matter density:

$$F(q) = \int d^3r\, \rho(\vec{r}) e^{i\vec{q}\cdot\vec{r}} \quad . \tag{2.14}$$

Experiments which measure the angular dependence of the elastic scattering cross section of electrons off nuclei are able to probe the distribution of charge (protons) within the nucleus. For the case of WIMP-nucleus scattering we expect that both neutrons and

protons participate. The standard assumption is to assume, then, that the matter in the nucleus is distributed similarly to the charge. In the case of spin-dependent (SD) WIMP scattering, a more detailed calculation is required to obtain the form factor for protons and neutrons separately (see, for example, Ref. [15] and the references therein). For spin-independent (SI) WIMP scattering, the Helm form factor [16] is commonly used among direct detection experiments, which results from using a spherically symmetric distribution of nuclear matter:

$$\rho_0(r) = \begin{cases} 3/(4\pi r_n^3) & r < r_n \\ \\ 0 & r > r_n \end{cases} \tag{2.15}$$

$$\rho_1(r) = \frac{1}{(2\pi s^2)^{3/2}} e^{-r^2/2s^2} \tag{2.16}$$

$$\rho(\vec{r}) = \int \rho_0(\vec{r}\,')\rho_1(\vec{r} - \vec{r}\,')d^3\vec{r}\,' \quad . \tag{2.17}$$

This description of the density agrees with elastic scattering data over a wide range of nuclear sizes. The data is well described by a flat distribution out to the nuclear radius r_n that then slowly decays over the "skin thickness", s. The resulting form factor is

$$F(q) = 3\,\frac{j_1(qr_n)}{qr_n}\,e^{-(qs)^2/2} \quad , \tag{2.18}$$

with spherical Bessel function:

$$j_1(x) = \frac{\sin x}{x^2} - \frac{\cos x}{x} \quad . \tag{2.19}$$

Fig. 2.1 shows the squared form factor as a function of nuclear recoil energy using the

parameterization for the nuclear radius from Ref. [8]:

$$r_n = \sqrt{c^2 + \frac{7}{3}\pi^2 a^2 - 5s^2} \quad , \tag{2.20}$$

where

$$c/[1\text{ fm}] = 1.23A^{1/3} - 0.60 \quad , \tag{2.21}$$

and $a = 0.52$ fm and $s = 0.9$ fm. The diffraction-like structure is obvious, with xenon being the first target to suffer from form factor suppression at higher recoil energies (corresponding to scattering of WIMPs in the high-tail of the velocity distribution or very massive WIMPs).

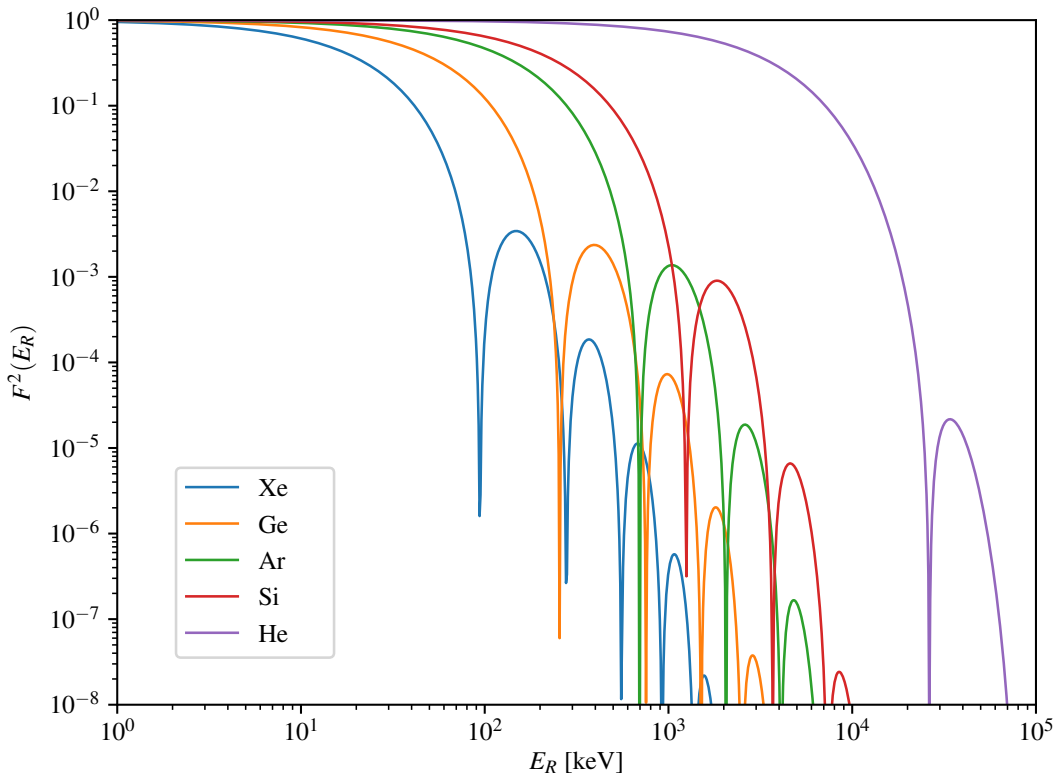

Figure 2.1: Helm form factor for various target nuclei commonly used in direct detection experiments. From Ref. [17].

2.1.3 Cross Section

Conceptually, the form factor converts our expressions for WIMP scattering from that on the entire nucleus to that on the individual nucleons. In direct detection experiments this is where experimental results are presented. In other words, the fundamental interactions between WIMPs and the quarks and gluons inside the nucleons are not specified in order to keep the results agnostic from specific particle physics models. The operators which appear in the Lagrangian density must, however, be specified in order to compare the results of direct detection experiments and those from colliders. See, for example, Ref. [18]. In general, all Lorentz-invariant operators (scalar, vector, axial-vector, and tensor) between WIMPs and quarks/gluons are possible, making the number of particle physics models to probe vast. In Ref. [19] the specific particle model is left behind and the full set of effective field theory operators between WIMPs and nucleons is given in the non-relativistic limit.

Here we will outline the usual procedure used by direct detection experiments by identifying, as in Ref. [5], the standard WIMP-nucleus cross section at zero momentum transfer:

$$\sigma_N = \int_0^{4\mu^2 v^2} \frac{d\sigma(q=0)}{dq^2} dq^2 = 4\mu^2 G_F^2 C \quad . \tag{2.22}$$

For SI interactions, the cross section is usually written as

$$\sigma_N^{\mathrm{SI}} = \frac{4\mu^2}{\pi} \left[Z f_p + (A-Z) f_n \right]^2 \quad . \tag{2.23}$$

The couplings to protons and neutrons are usually assumed equal, $f_p = f_n \equiv f_N$, which

gives

$$\sigma_N^{\rm SI} = \frac{4\mu^2 f_N^2 A^2}{\pi} = \left(\frac{\mu}{\mu_n}\right)^2 A^2 \sigma_n^{\rm SI} \quad , \tag{2.24}$$

and we have defined the WIMP-*nucleon* cross section, containing the WIMP-nucleon reduced mass, μ_n:

$$\sigma_n^{\rm SI} = \frac{4\mu_n^2 f_N^2}{\pi} \quad . \tag{2.25}$$

Eq. 2.24 contains the famous A^2 enhancement factor which favors heavy targets for low recoil energies (low momentum transfer). Furthermore, when the WIMP mass becomes large: $\mu \to m_T$ and $\mu_n \to m_n$ so that $\mu/\mu_n \to A$, giving in an overall A^4 dependence.

Using Eq. 2.22 we can find that

$$C = \frac{A^2 \sigma_n^{\rm SI}}{4\mu_n^2 G_F^2} \tag{2.26}$$

which allows us to write the differential WIMP rate as

$$\frac{dR}{dE_R} = \sigma_n^{\rm SI} \left(\frac{m_T A^2}{\mu_n^2}\right) \left(\frac{\rho_\chi n_T}{m_\chi}\right) F^2(E_R) \int_{v_{\rm min}(E_R)}^{\infty} d^3v \, \frac{f_\oplus(\vec{v}, \vec{v}_{\rm obs})}{v} \quad . \tag{2.27}$$

This is our final expression for the differential rate of SI WIMP scattering. The quantity $\sigma_n^{\rm SI}$ is the normalization factor which is used for the interpretation of direct detection results. In the absence of a WIMP signal, limits on the size of this quantity are placed. Within the direct detection community this has become standard practice, with all experiments using the same assumptions about the form factor and halo model so that limits on $\sigma_n^{\rm SI}$ are directly comparable.

Eq. 2.27 is plotted in Fig. 2.2 for commonly used WIMP detector targets assuming $\sigma_n^{\rm SI} = 1$ zb (1 zb $= 10^{-21}$ b $= 10^{-45}$ cm^2). At high recoil energies, the coherence loss

effects from the form factor can be seen, while at the lowest energies, the heaviest target nucleus wins. In Fig. 2.3 the integrated event rate above a given recoil energy is plotted for each target also assuming $\sigma_n^{\mathrm{SI}} = 1$ zb. In a year-long run with a 1 tonne xenon detector with a $\approx$5 keV threshold, we expect of order hundreds of events from a 50 GeV WIMP. The current best limit, however, is $\sigma_n^{\mathrm{SI}} \lesssim 0.05$ zb [20] which implies that we should plan for of order ten events for a competitive experiment. This sets the scale for the allowed background rates in our experiment.

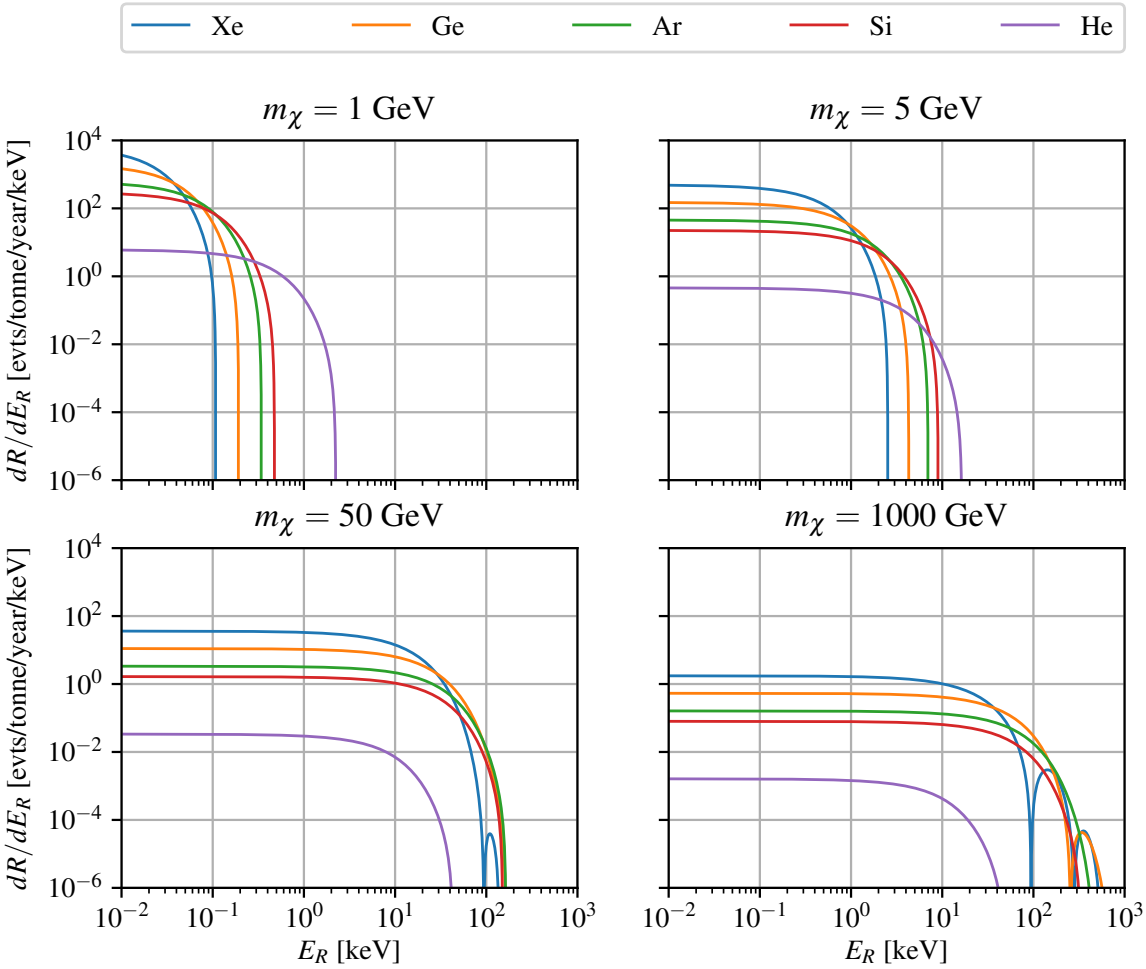

Figure 2.2: Differential WIMP scattering rate for SI cross section of 1 zb for commonly used WIMP target materials. From Ref. [17].

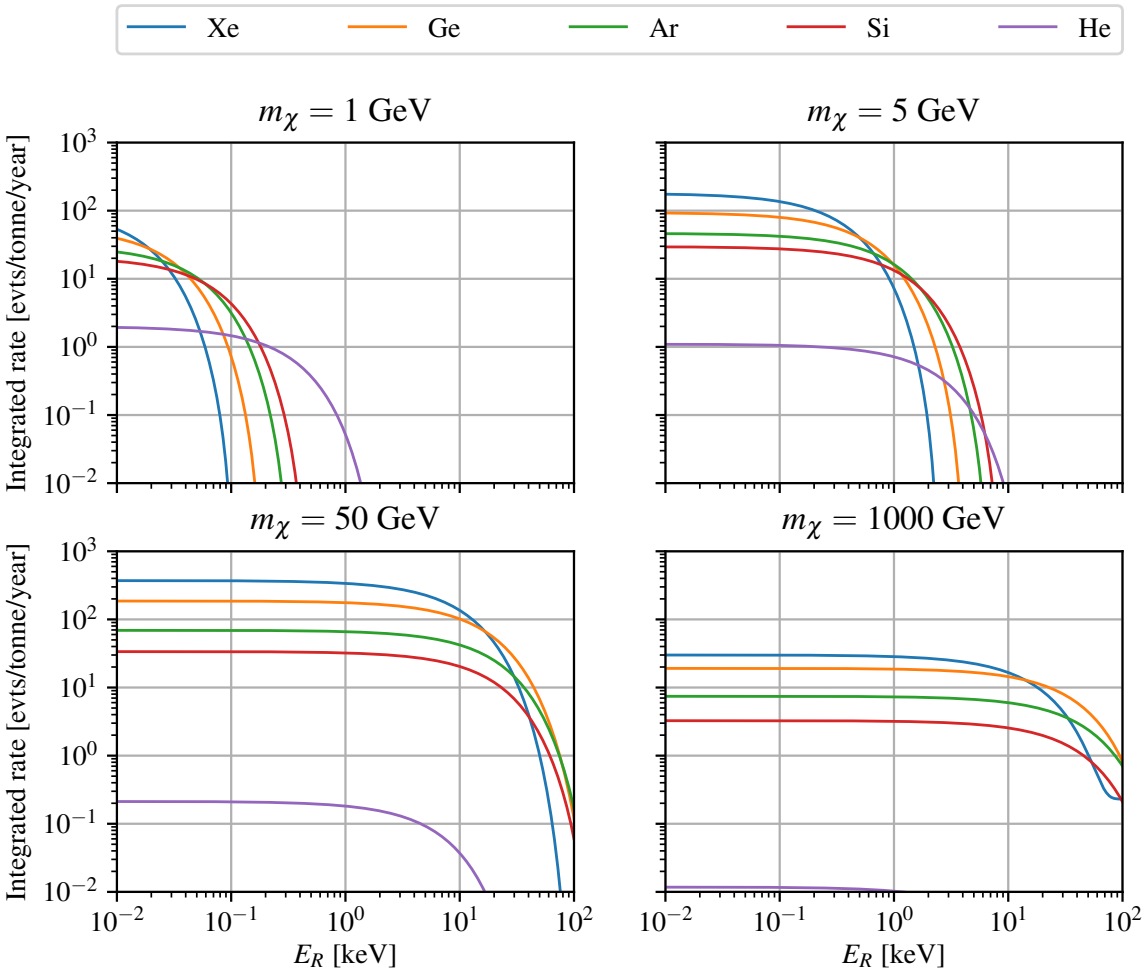

Figure 2.3: Integrated number of WIMP scattering events above a given E_R for SI cross section of 1 zb for commonly used WIMP target materials. . From Ref. [17].

2.2 Dual-Phase Time Projection Chambers

In the last decade, the dual-phase time projection chamber, or TPC, has become the leading technology in the search for dark matter and rare-events in general. In principle a TPC can be filled with any suitable scintillating material, however, noble gases have been identified as having many properties that make them ideal for use in this detector arrangement [21]. In particular, TPCs using liquid xenon (LXe) as their detection medium have dominated advancements in this sector.

The general setup of a dual-phase TPC is illustrated in Fig. 2.4. Two arrays of photosensors, often photomultiplier tubes (PMTs), define the top and bottom of a volume in which the chosen medium is maintained as a liquid over most of the space. At the top of the chamber the medium is in gaseous form (hence the "dual-phase" TPC). When an incident particle deposits energy in the liquid, prompt scintillation light is detected in both sensor arrays (however, the change in index of refraction at the liquid-gas interface typically leads to more light being collected in the bottom array). This prompt signal is known as the S1 signal. Charge, in the form of individual electrons, freed during the interaction are made to drift upwards by way of an applied electric field. Electrostatic grids are held at constant high voltage values create these fields. A stronger electric field is maintained across the liquid-gas interface allowing the electrons to overcome the potential barrier and be extracted into the gas phase. When the electrons are extracted, a second burst of scintillation light is emitted via electroluminescence and detected primarily in the top photosensor array. This is known as the S2 signal.

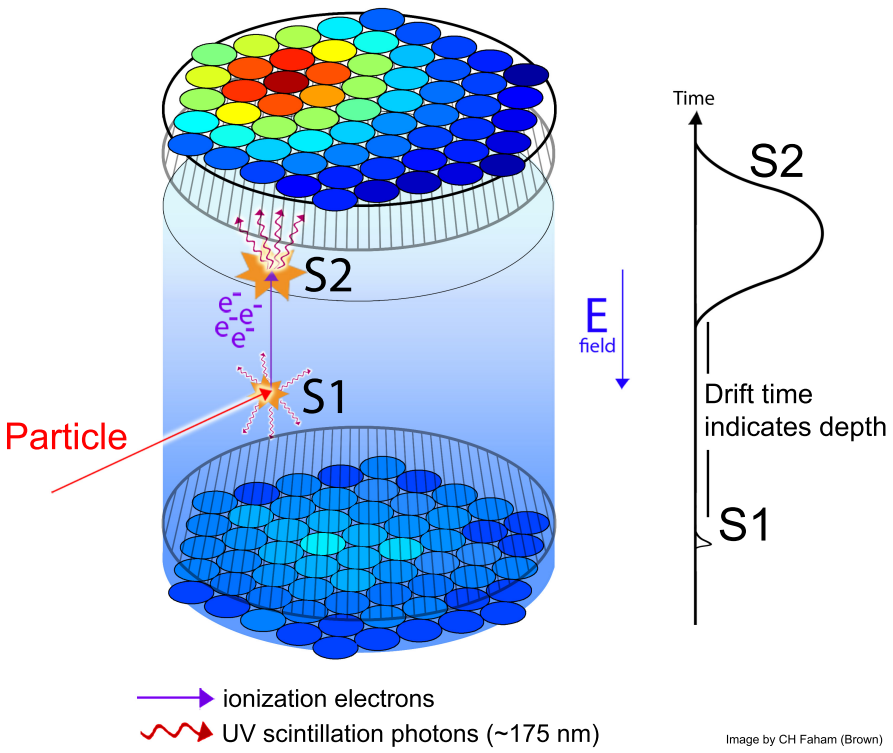

Figure 2.4: Schematic of the dual-phase TPC detection method. Here the detection medium is assumed to be liquid xenon, as the wavelength of the scintillation photons are specifically called out.

This detection scheme allows for measurements of both the 3D position of the event inside the liquid volume and the energy deposited in the event. First, the temporal separation between the S1 and S2 signals–dependent on the drift velocity of electrons in the medium–gives the depth of the event below the liquid surface. Then, the hit pattern of collected S2 light in the top array is used to reconstruct the (x, y) position of the event. The collected number of S1 photons, often given as a pulse area in number of photoelectrons (phe) in a PMT, is a good proxy for the deposited energy. Better energy resolution and linearity is obtained, however, when both S1 and S2 are used to form an energy scale [22].

The measurement of both prompt photons and the released charge in a particle interaction additionally allows for particle discrimination with the dual-phase TPC. Quite simply, the ratio of the charge signal to that of the prompt scintillation signal, S2/S1, serves as a discrimination parameter between particles primarily interacting with the target atom's electron cloud (electronic recoils or "ER") and particles interacting with the atomic nucleus (nuclear recoils or "NR"). Taken together, the position reconstruction and particle discrimination capabilities of the LXe TPC make it a powerful tool for low-background physics searches.

2.3 Liquid Xenon as a Detection Medium

As mentioned, LXe has become the material of choice for sensitive searches for dark matter. Here I quickly identify a few key features of why this is the case.

Firstly, Xe has only a single, "super long-lived" radioactive isotope, ^{136}Xe. Present with a natural abundance of 8.9 %, this isotope decays by two-neutrino double-beta ($2\nu\beta\beta$) decay with a half-life of 2.2×10^{21} y and is a candidate isotope for neutrinoless double-beta ($0\nu\beta\beta$) decay. Only recently in the so-called "second generation" of LXe dark matter experiments soon to come online is this isotope becoming a significant source of background. This is primarily a result of the much larger mass of Xe being deployed, but also results from the reduction of other background sources. The next longest-lived isotope of Xe is ^{127}Xe which is created through cosmogenic activation of Xe and has a half-life of 36.3 d and begins to decay away after being brought underground.

Xe is heavy, with 54 protons and an average atomic weight of 131.3 u. The large number of total nucleons gives Xe an advantage over other detection media in the spin-independent hypothesis of dark matter-nucleus scatter because the infamous A^2 enhancement previously mentioned. Similarly, the significant abundance of ^{129}Xe and ^{131}Xe in natural Xe allows Xe-based experiments to interpret their results under the SD and more complete effective field theory (EFT) assumptions [19].

The large atomic number of Xe, together with its high density ($3\,\mathrm{g/cm^3}$) when condensed as a liquid make it a favorable medium for the construction of large, non-segmented detectors. Self shielding of external backgrounds allows the use of a fiducial volume at the detector center, where the background rate is minimal. The boiling point of LXe is 165 K so such a large mass can be kept cool with the use of liquid nitrogen.

Xenon can be purified so that free electrons (the source of the S2 signal) may drift long distances before being captured by electronegative impurities. The 178 nm VUV scintillation photons produced by interactions also travel long distances in LXe due to their fundamental production through the formation of dimer state de-excitation, detuned from single Xe atom absorption bands. In fact, the key driver in the absorption length is the presence of impurities that absorb in this wavelength regime. For very high purity, one can expect absorption lengths of order 100 m or greater.

2.3.1 Signal Generation in Liquid Xenon

Ultimately, the S1 and S2 signals detected in a LXe TPC result from response of the LXe medium to particle energy depositions. Here I only provide a brief overview of the concepts in this rich area of study. For a more detailed description of the microphysics involved in signal generation in Xe, Ref. [23] can serve as a useful starting point.

When a particle loses energy in the LXe medium it leaves a track of ionized and excited atoms: ions and "excitons". In the absence of recombination (the process in which electrons neutralize ionized atoms) these two populations result in the S2 and S1 signals, respectively. Some fraction of the deposited energy is also imparted to Xe atoms which do not become excited or ionize. In a LXe TPC, this energy goes undetected and is generally very small for electronic recoils. The energy deposited can therefore be expressed as

$$E = Wf(n_{ex} + n_i) = Wf\left(1 + \frac{n_{ex}}{n_i}\right) n_i \tag{2.28}$$

where n_{ex} and n_i are the number of excitons and ions and $W = 13.7 \pm 0.2$ eV [23] is the average energy to create an exciton or an ion. The quenching factor f is the fraction of the deposited energy that creates excitons and ions and is of order unity for electronic recoils.

In reality, some fraction, r, of the ionization electrons recombine with ions, effectively increasing the number of excitons that emit the detectable 178 nm photons. The expected

number of detectable scintillation photons is expressed as

$$n_\gamma = \left(\frac{n_{ex}}{n_i} + r\right) n_i, \tag{2.29}$$

while the number of electrons available to form the S2 signal is

$$n_e = (1 - r) n_i. \tag{2.30}$$

The fraction r varies with both the particle energy and the applied electric field.

The deposited energy can be expressed in terms of the resulting number of electrons and photons and, furthermore, to the observed S1 and S2 signals:

$$E = W(n_e + n_\gamma) = W\left(\frac{S1}{g_1} + \frac{S2}{g_2}\right) \tag{2.31}$$

The factors g_1 and g_2 convert the initially created quanta to the observed signals. Intuitively then, g_1 is the product of the average light collection in the detector and the average quantum efficiency of the photosensors. Similarly, g_2 is the product of the measured signal size corresponding to a single extracted electron from the liquid surface (the "single electron size"), SE, and the efficiency with which electrons are extracted from the liquid (the "electron extraction efficiency"), ϵ: $g_2 = \epsilon \times \mathrm{SE}$. Both ϵ and SE depend on the strength of the extraction electric field.

In the case of nuclear recoils, Eq. 2.28 is often re-expressed as

$$E_{\mathrm{NR}} = \frac{W(n_{ex} + n_i)}{L}, \tag{2.32}$$

where L is now an energy-dependent factor that quantifies the quenching effects. Standard practice is to use Lindhard theory to parametrize L as a function of energy [24]:

$$L = \frac{kg(\epsilon)}{1 + kg(\epsilon)}, \tag{2.33}$$

with $\epsilon = 11.5(E_{\mathrm{NR}}/\mathrm{keV}_{\mathrm{NR}})Z^{-7/3}$ a dimensionless energy and $g(\epsilon) = 3\epsilon^{0.15} + 0.7\epsilon^{0.6} + \epsilon$.

When quoting the energy of an event reconstructed using Eq. 2.31, the interaction is presumed to be of the electron recoil type. It is therefore common practice to denote these energies with the subscript "*ee*" standing for "electron equivalent" (e.g. keV_{ee}). Alternatively, one can include the quenching factor f and report energies using a subscript "*nr*" (e.g keV_{nr}).

For the interpretation of collected data from a LXe TPC, a faithful model that can convert between specified particle energy deposit and observable signals is needed. The Noble Element Simulation Technique (NEST) represents the current standard for such a framework [25]. NEST is regularly tuned using the world's data on LXe response to particle energy depositions and is used extensively for modeling signal and background topologies.

2.4 LXe TPC Calibrations

As with any particle detector, the response to signals representative of the sought after signal and background events must be calibrated and understood. In a LXe TPC this means characterizing the detector's response to ER and NR events. In addition, the ability to spatially reconstruct events in the detector means that detector-specific effects (e.g. variations in light collection) can be corrected for. This also allows for the measurement of more fundamental properties of the LXe target such as the light and charge yields.

During its science runs, the LUX experiment [26] developed several novel methods for

LXe TPC calibrations of both the ER and NR type. The discussion of calibrations here is focussed on those performed in LUX, as all of these techniques will be used in future detectors such as LZ and represent the state of the art.

2.4.1 Electronic Recoils

While the self-shielding properties of LXe make it desirable for WIMP searches, high statistics calibrations of the detector response to ER events in the fiducial volume prove to be difficult when standard sources external to the LXe are used. For this reason, it has become standard practice to inject radioactive calibration sources directly into the Xe as it is being recirculated. The desired result is a spatially uniform distribution of calibration events inside the TPC.

^{83m}Kr Injections

The LUX experiment frequently employed this technique first by flowing a stream of the recirculating Xe gas past a ^{83}Rb source. ^{83}Rb decays to ^{83m}Kr, a metastable state with a half-life of 1.8 h. This is a convenient half-life as it is long enough to allow thorough mixing of the ^{83m}Kr in the detector volume while simultaneously being short enough that no residual activity remains after a few hours. ^{83m}Kr decays primarily by the emission of 32.1 keV and 9.4 keV internal conversion (IC) electrons with a 154 ns intervening half-life between them. The result is a total 41.5 keV of energy being completely absorbed in the LXe, well outside the energy range used for WIMP signals.

The spatially uniform, mono-energetic signals from ^{83m}Kr proved essential for the

correction of S1 and S2 signals in the LUX detector. This is shown on the left of Fig. 2.5 where the relative sizes of the collected signals are shown as a function of spatial position in the detector. By correcting for non-uniformities in signal size, the overall detector resolution is increased as shown on the right of Fig. 2.5. Full details on the use of ^{83m}Kr in LUX are given in Ref. [27]. In addition to correcting all LUX S1 and S2 signals, the frequent injections of ^{83m}Kr allowed for monitoring and characterization of the temporarily and spatially changing electric fields in the LUX Run 4 WIMP search exposure.

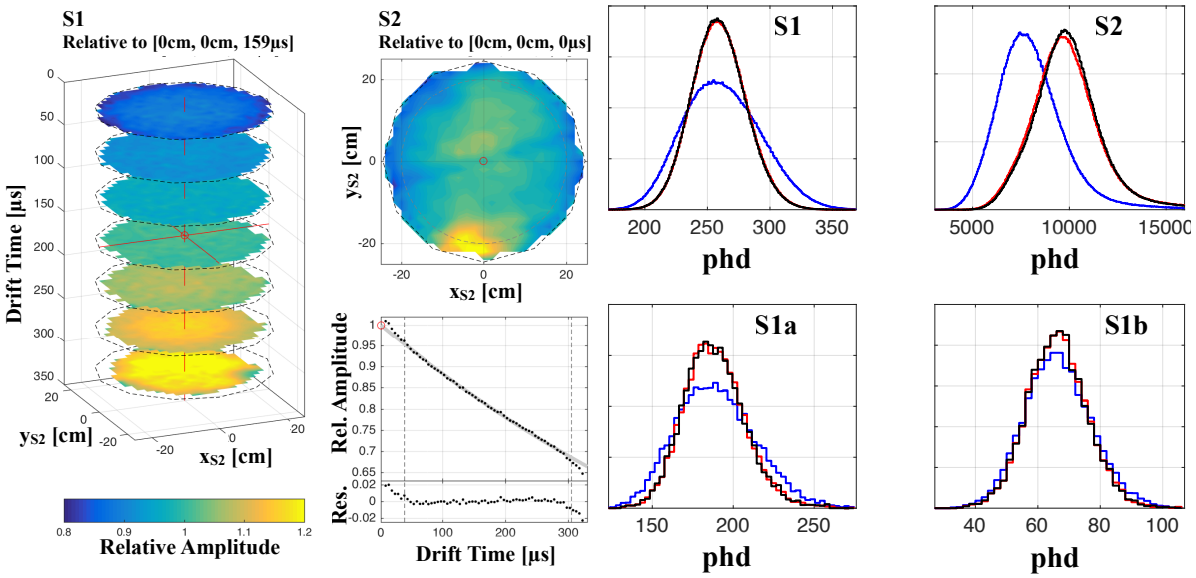

Figure 2.5: *Left:* An example map of relative S1 and S2 signal amplitudes throughout the LUX detector. *Right:* Effects of applying corrections to the S1 and S2 signals. In blue are the uncorrected distributions, while those after receiving corrections in the z direction are shown in red. The final black distributions have been corrected for all three spatial directions. Taken from Ref. [27].

Tritiated Methane Injections

While ^{83m}Kr is invaluable for signal corrections, its two-step decay sequence and the associated decay energies make it less useful for calibrating the separation of ER and NR events in the energy range of interest for WIMP searches. Accurate knowledge of the extent to which these event types can be separated is central for achieving good sensitivity to a supposed WIMP signal.

For this task, LUX made use of tritium (^{3}H), which β decays with an endpoint energy of 18.6 keV. The resulting continuum of deposited energy completely covers the energy range of interest. However, naive injection of pure tritium would prove disastrous for a dark matter search because of its long, 12.2 y half-life. The solution is to package the tritium atom in a larger molecule, one that can be efficiently removed by the Xe purification system. In LUX, tritiated methane (CH_3T) was injected to perform high statistics calibrations of the low-energy, ER detector response and was subsequently removed by the getter used in its purification system. The details of the methods and data analysis are given in Ref. [28].

Fig. 2.6 shows data collected during a CH_3T injection. Good agreement between the theoretical β spectrum and the collected data is observed and used to determine the 50 % acceptance energy threshold of LUX to be (1.240 ± 0.026) keV. The resulting ER band plotted in the often used $\log_{10}(S2/S1)$ vs $S1$ space is shown along with the NR band obtained using calibrations described in the following section. A leakage fraction, f, defined as the fraction of ER events observed below the NR band mean can then be calculated,

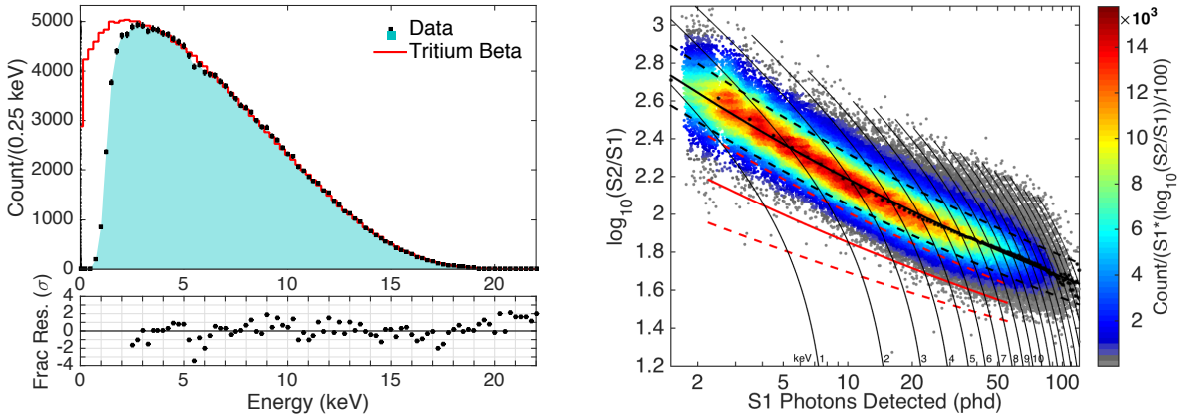

Figure 2.6: *Left:* Collected energy spectrum of tritium events compared to the theoretical spectrum. The finite detector threshold results reduced detection efficiency at very low energy. *Right:* The ER band in $\log_{10}(S2/S1)$ vs $S1$ space created using tritium events. Included are black solid and dashed lines defining the band mean and 10 % and 90 % contours of the ER population. Similar quantities for the LUX NR band are shown in red. Lines of constant electron equivalent energy are also shown. Taken from Ref. [28].

however, what is often quoted is the discrimination power, $1 - f$. The discrimination found in Ref. [28] is $(98.81 \pm 0.02)\,\%$. In a cut-and-count analysis, this number would be needed in order to accurately predict the expected number of background events to the WIMP search.

Energy Scale

A fit to the collected full-energy peaks from various sources in the $S1/E$ vs $S2/E$ plane allows for the direct determination of the g_1 and g_2 factors introduced in Eq. 2.31. This is shown in Fig. 2.7 for the calibration of LUX in its first WIMP search period. Here, peaks from injected ^{83m}Kr and those from external γ sources (^{137}Cs and ^{214}Bi) are used. Additionally, peaks resulting from decays of short-lived isotopes caused by cosmogenic activation of the Xe are used.

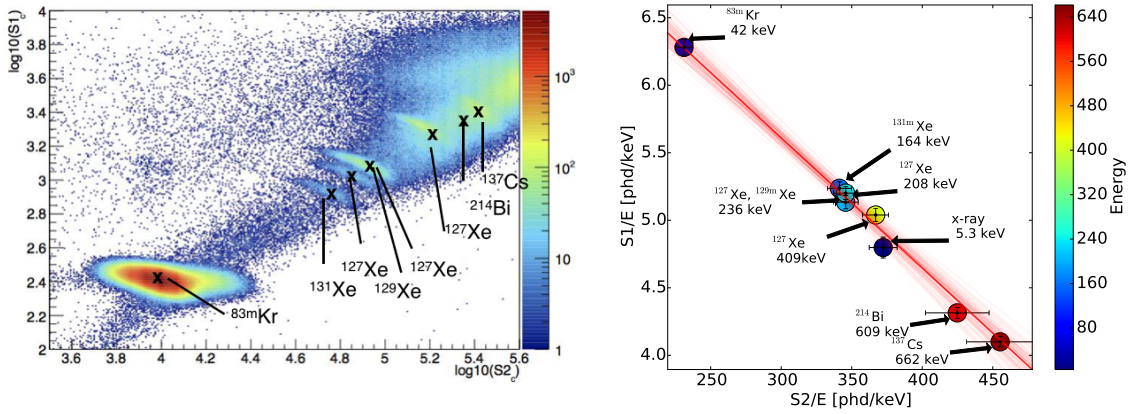

Figure 2.7: *Left:* Mono-energetic peaks shown in the $S1$-$S2$ plane. *Right:* Fit to determine g_1 and g_2. The values found in LUX here were $g_1 = 0.117 \pm 0.003$ and $g_2 = 12.1 \pm 0.8$. Taken from Ref. [29].

2.4.2 Nuclear Recoils

To date, there has been no method developed which allows the injection of a neutron source into the LXe flow path as is done for ER calibrations. However, the $\mathcal{O}(10$ cm) path length of MeV neutrons in LXe does allow for the use of sources external to the TPC.

Deuterium-Deuterium Neutrons

Between its two WIMP search runs, LUX employed a deuterium-deuterium (DD) neutron generator as a source of mono-energetic, 2.45 MeV neutrons. The generator was placed externally to the water tank while a sealed, air-filled PVC pipe was used to displace a column of water leading directly to the outer cryostat of the LUX detector. Neutrons born in the generator were therefore allowed to penetrate into the active TPC and deposit energy through multiple and single scattering interactions. The left side of Fig. 2.8

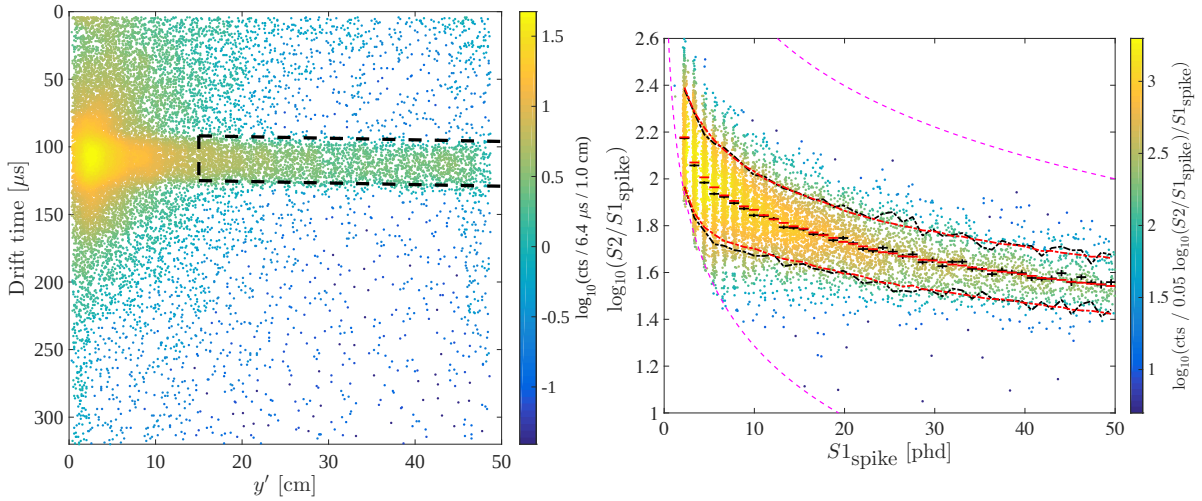

Figure 2.8: *Left:* Reconstructed positions of single scatter DD neutron events. The black box region defines a cut used to select a pure sample of unscattered, 2.45 MeV neutrons. Neutrons which have scattered in the surrounding detector materials before reaching the TPC are clearly visible where the beam enters the detector. *Right:* Single scatter events defining the NR band from DD data. Black points are the Gaussian mean, 10 %, and 90 % limits derived from the data, while the red points are the same quantities calculated using the NEST model tuned to the DD data. Taken from Ref. [30].

shows the spatial distribution of reconstructed single scatter events in the TPC where the collimating effects of the water shield/tube configuration are obvious.

The full analysis of this calibration data is given in Ref. [30]. The mono-energetic neutrons may scatter in a range of angles producing Xe recoils up to the endpoint energy of 74 keV, corresponding to completely backscattered neutrons. However, by selecting double scatter events, the reconstructed positions of each interaction constrains the scattering angle and therefore the Xe recoil energy at the first interaction site. Provided the two vertices are far enough separated in z, the S2 signals are distinct, allowing a measurement of the charge yield from the known energy deposited in the first scatter. With the charge yield measured, the single scatter sample is used to measure the scintillation light yield with the S2 size serving as a calibrated measure of the recoil energy. Use of the

Lindhard description of Eq. 2.33 to model these results provided a direct measurement of $k = 0.1735 \pm 0.0060$

The population of single scatter events calibrates the NR band as shown on the right of Fig. 2.8. However, the band resulting from a DD neutron energy spectrum is different than that expected from a WIMP energy spectrum. The central task is to properly the tune the Xe response Monte Carlo until agreement with the DD data is obtained. The measurement of the NR light and charge yields in the same data sample makes this process even more robust.

Chapter 3

The LZ Experiment

At the time of writing, construction for the LUX-ZEPLIN (LZ) experiment has begun. LZ is a second-generation ("G2") dark matter experiment based on the LXe TPC technology formed from the merging of the LUX and ZEPLIN collaborations. This chapter briefly describes the overall design and expected performance of LZ. Many details on both of these can be found in the LZ Technical Design Report [31] and the recent paper on expected WIMP sensitivity [32].

3.1 The LZ Detector

LZ will replace LUX inside the underground water tank located in Davis Cavern on the 4,850 ft level (4,300 m w e) at the Sanford Underground Research Facility (SURF) [33] in Lead, South Dakota, USA. The active detectors of LZ are designed to fit within the existing water tank which shields from radioactivity in the cavern environment. Fig. 3.1

shows a CAD model of the experiment inside the water tank. Three active detectors form the experiment as a whole: the central LXe TPC, the Xe Skin (XS), and the Outer Detector (OD).

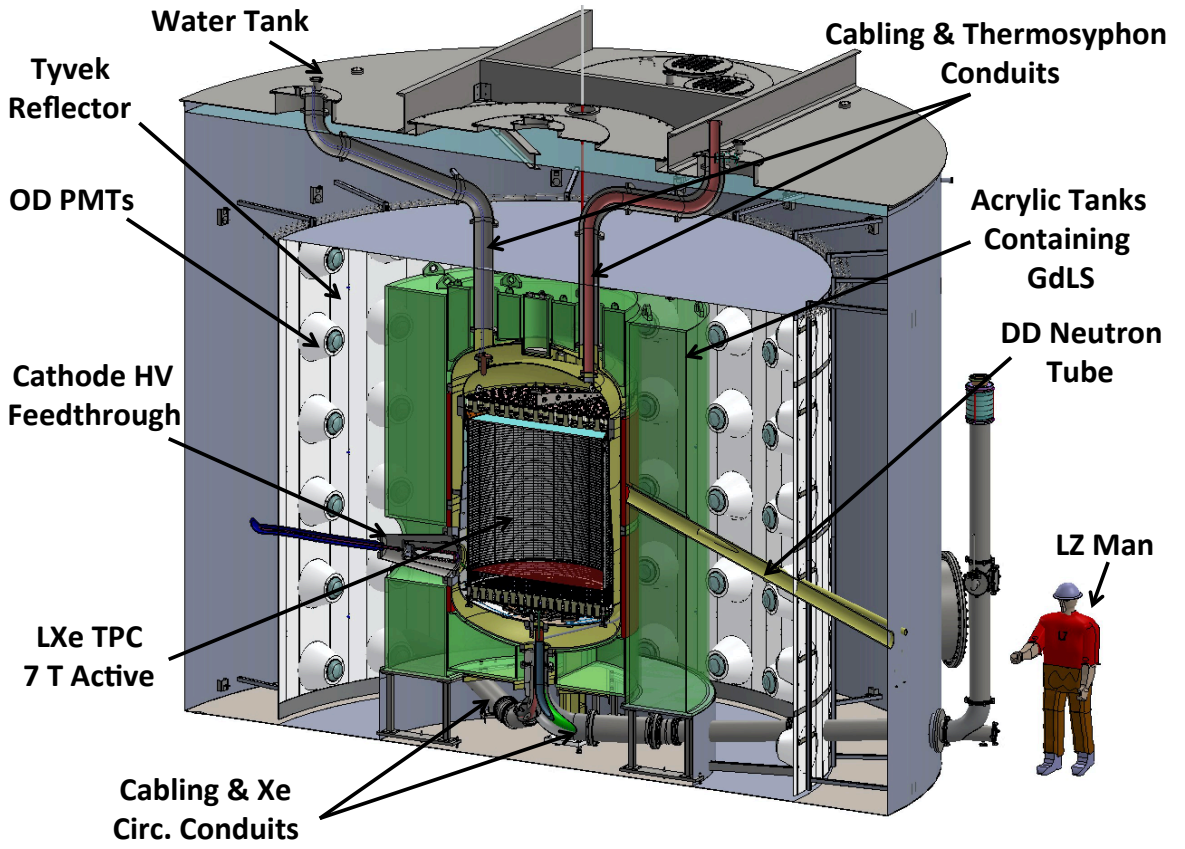

Figure 3.1: CAD model of the LZ detector inside the water tank in the Davis Cavern at SURF. Important components are labeled.

3.1.1 Liquid Xenon TPC

The primary detector of LZ is the LXe TPC and is shown in Fig. 3.2. The assembly sits inside two nested cryostats: the outer cryostat vessel (OCV) isolates the inner cryostat vessel (ICV), creating a vacuum layer in between them which allows the ICV to be held

at 175 K. The height (cathode to gate grid) and diameter of the active TPC are both 1.46 m. The total mass of liquid xenon in the ICV will be approximately 10 tonnes, while 7 tonnes will lie within the active TPC itself.

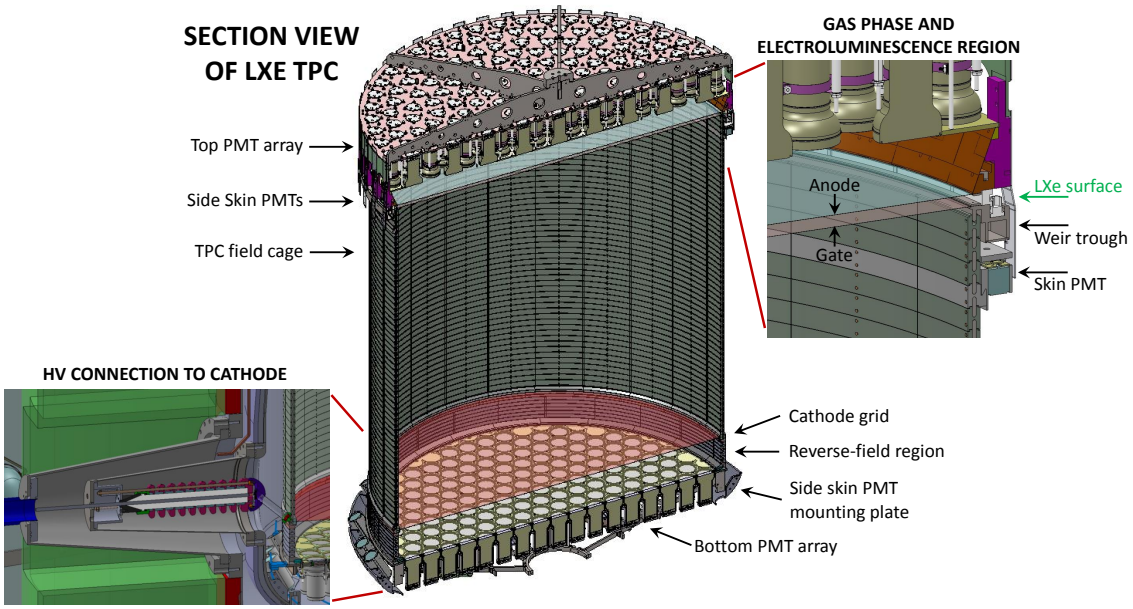

Figure 3.2: Schematic of LZ central Xe detector components showing at the center the TPC. Insets show the detailed geometry for cathode grid HV delivery and the extraction field region. Taken from Ref. [31].

Grids and PTFE Walls

Four stainless steel wire grids will be used to establish the necessary drift and extraction fields in LZ. The anode and gate grids straddle liquid surface (anode in the gas phase, gate in the liquid) providing the electric field for extraction of drifted electrons. Defining the bottom of the active region of the TPC is the cathode grid. The voltage difference between cathode and gate grids provide the primary drift field of 310 V/cm (nominal). A significant amount of R&D within LZ has been devoted to ensuring a sufficiently large

voltage can be maintained on the cathode. Its nominal operating voltage is $-50\,\mathrm{kV}$. Finally, 1 cm above the bottom PMT array is the bottom grid, the purpose of which is to shield the PMTs from the high voltage of the cathode grid. All the grids are 90° woven mesh type.

The bottom grid is held at a much lower voltage than the cathode which creates a 13.8 cm tall "reverse field" region (RFR) between them. Energy deposits in this region produce S1 light only, as the freed electrons drift downward and are not detected. A special class of events known as "gamma-X" events result when a γ-ray scatters once in the RFR and once again in the active region. The result can be an event reconstructed as a single scatter with S2/S1 ratio similar to that of a NR, as the S1 signals are merged. Luckily these events can be efficiently rejected using metrics such as the top-bottom PMT array asymmetry of the S1 signal.

The TPC walls are made of PTFE in order to maximize collection of S1 photons in both PMT arrays. PTFE is chosen for its high reflectivity, but also because of its availability as a very radiopure substance. Achieving low levels of ^{238}U and ^{232}Th in PTFE is not only important because of direct γ production, but also because of the potential for high neutron production rates owing to the high (α, n) cross section of fluorine. Embedded inside the PTFE walls are 57 field shaping rings which act to straighten the field lines that begin and end on the grids, creating a uniform set of electric field lines.

PMTs

In total, 494 Hamamatsu R11410-22 3"-diameter PMTs (pictured in Fig. 3.3) will collect light in the TPC: 241 in the bottom PMT array and 253 in the top PMT array. The PMTs of the bottom array will be arranged in a close-packed hexagonal pattern, which maximizes collection of S1 light by maximizing photocathode area in the available space. The top PMTs are arranged in a hybrid pattern that begins as hexagonal in the center and becomes nearly circular at the TPC perimeter. This configuration was chosen to optimize the spatial reconstruction of events near the TPC walls. The outermost circle of PMTs are located at the maximum possible radius which aligns the PMT centers with the TPC wall. This is to reduce the inward bias in the position reconstruction of events near the wall.

Due to their complex construction, total mass, and closeness with the active LXe of LZ, the radioactivity of the 3" PMTs (and their bases) contributes significantly to the background from detector materials. Various versions of the R11410 model have demonstrated fantastic radiopurity with respect to older models used in dark matter searches [34; 35]. These PMTs are subject to a strict screening campaign within LZ. Activities are of order 1 mBq/PMT for U/Th/Co and ≈10 mBq/PMT for K.

The R11410-22 is also characterized by having quantum efficiency >30 % at 175 nm, gain of at least 2×10^6 at bias voltage of 1,500 V, and a high peak-to-valley ratio (>2) for single photoelectrons [34].

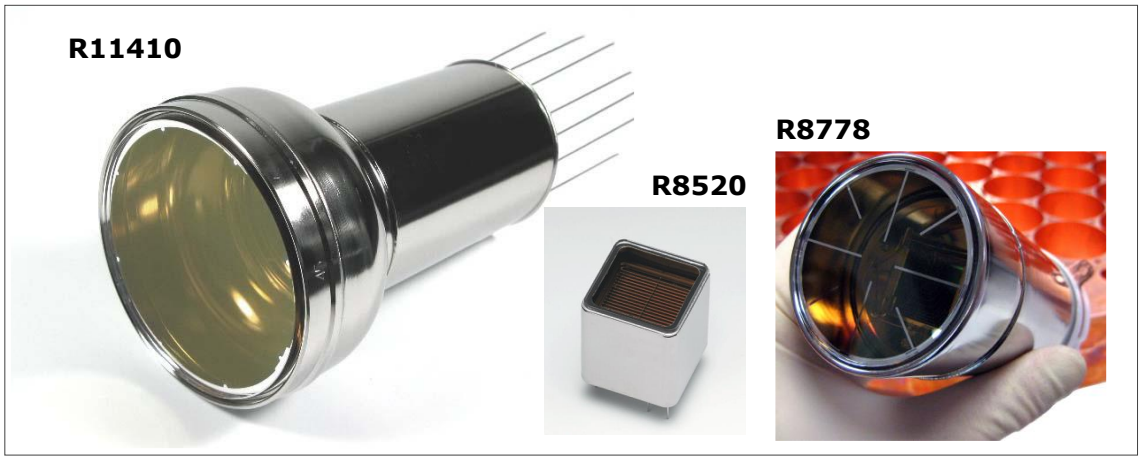

Figure 3.3: Photos of all three PMT types being used in the central Xe detector of LZ. Taken from Ref. [31].

3.1.2 Xenon Skin (XS)

The XS consists of the ≈2 tonnes of LXe between the outer edge of the TPC wall and the ICV wall. This region is meant to be optically separated from the central TPC, however, interactions in this region can result in a visible S1 signal in the TPC. The thickness of LXe in the XS varies from 4 cm to 8 cm along the outside of the TPC walls ("side skin" region). The LXe underneath the bottom PMT array is even thicker and known as the "dome skin". The XS is required by mechanical space constraints for the TPC but is also required to provide a dielectric buffer between electrically biased components in the TPC and the grounded ICV. This relatively thick (the interaction length of a 1 MeV γ in LXe is ≈5 cm) layer of LXe poses a problem by effectively blocking radiation that has interacted in the TPC from reaching the OD and being vetoed.

The solution adopted in LZ is to instrument the LXe in this region and readout the S1 light produced by interactions here. The benefits of doing so are threefold: (1) another

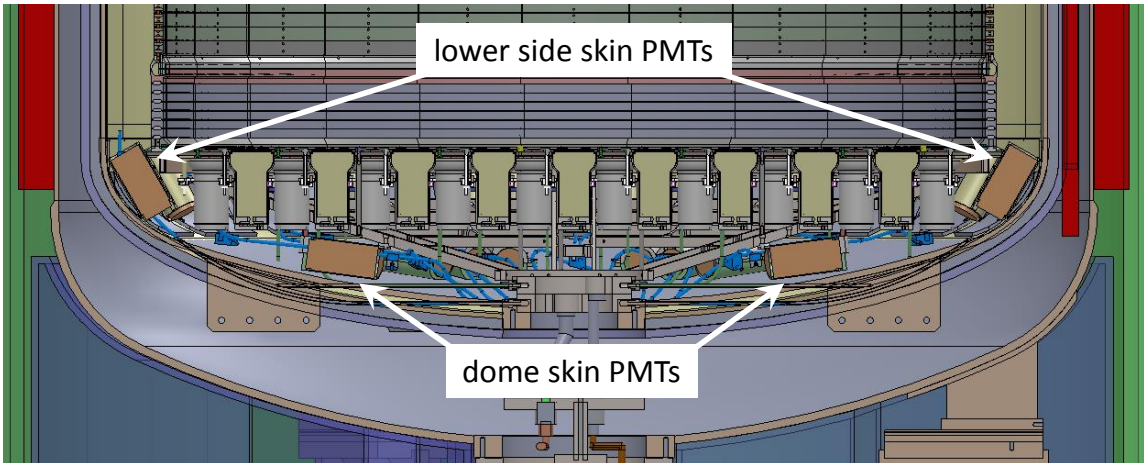

Figure 3.4: CAD model showing the layout of the R8778 dome skin and lower side skin PMTs. Taken from Ref. [31].

veto detector allows for increased veto efficiency, (2) another detector allows for further characterization of the radiation environment around the central TPC target, and (3) events where S1 light in the skin has leaked into the TPC, reducing the S2/S1 ratio there, can be vetoed. The instrumentation of the skin is as follows: At the top of the side skin region, 93 Hamamatsu R8520 1" PMTs are mounted near the Xe liquid surface, facing downward. In the dome skin region, 38 of the Hamamatsu R8778 2" PMTs used in LUX are configured as shown in Fig 3.4. Photos of both PMT types are shown in Fig. 3.3. The outside of the TPC wall provides a reflective PTFE surface. To further increase light collection in the skin the inner wall of the ICV is tiled with PTFE panels.

The XS has the principle power to reject γ-related backgrounds in LZ, owing to its proximity to the central TPC and the high density of its detection medium. In addition to tagging γ-rays scattering in the TPC, the XS also acts to detect the burst of γ's following a neutron capture in the OD, effectively increasing the neutron tagging

efficiency. The LZ goal is to achieve an energy threshold for observing ER scatters of $100\,\mathrm{keV_{ee}}$ in over 95 % of the volume of the XS. Specification of the volume fraction results from the somewhat high variability of light collection in the XS as depicted in Fig. 3.5. To create this figure, the XS is divided into $1 \times 1 \times 1$ cm pixels and the number of photons expected from a $100\,\mathrm{keV_{ee}}$ energy deposit is predicted using the NEST model. The number of photoelectrons detected divided the number of initial photons (the photon detection efficiency) is then plotted. The result is that over 97 % of the volume detects >3 phe in 50 % of the simulated interactions, meeting the goal.

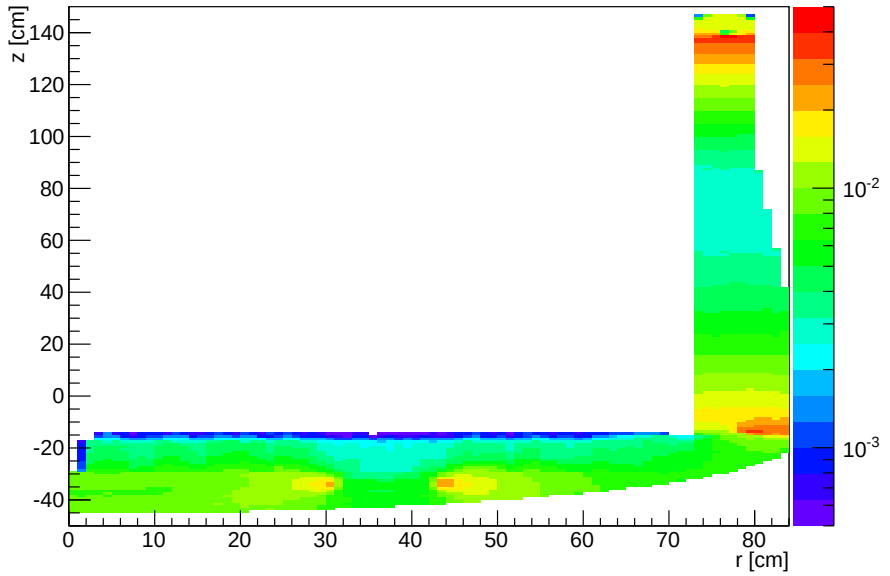

Figure 3.5: Light collection efficiency in the XS as a function of position (averaged over azimuth). Over 97 % of the XS region achieves an energy threshold of $100\,\mathrm{keV_{ee}}$. Taken from Ref. [31].

3.1.3 Outer Detector (OD)

The third detector element of LZ is the OD. As details of the OD design and expected performance are given in the following chapter, I give here a short summary of its layout and key contributions to the LZ WIMP search analysis.

The OD is comprised of ten segmented acrylic tanks designed to fit around the LZ OCV in a hermetic fashion. The tanks are shown in Fig. 3.6 both in an exploded view and as assembled. Contained within the tanks is a liquid scintillator (LS) loaded to 0.1 % by mass with gadolinium (Gd). The combined mixture is referred to as "GdLS". The characteristic thickness of the GdLS around LZ is ≈60 cm and the total GdLS mass is 17.3 tonnes.

Scintillation photons generated by interactions in the GdLS are detected via 120 Hamamatsu R5912 8"-diameter PMTs which surround the tank assembly submerged in ultra-pure water. The PMT faces are located 84 cm from the outside of the acrylic tank walls. A curtain of Tyvek reflector surrounds the PMTs and envelopes the LZ OCV in order to increase the overall light collection efficiency of the system. These components are shown in Fig. 3.1.

The OD (together with the XS) will serve to operate both as an anti-coincidence detector for the TPC and as a standalone, low-background detector capable of measuring and characterizing the radiation field of LZ. Of principle importance to the LZ WIMP search is the function of the OD to tag neutrons. Natural Gd has an extremely high cross section to capture thermal neutrons due to the natural abundance of the isotopes ^{155}Gd

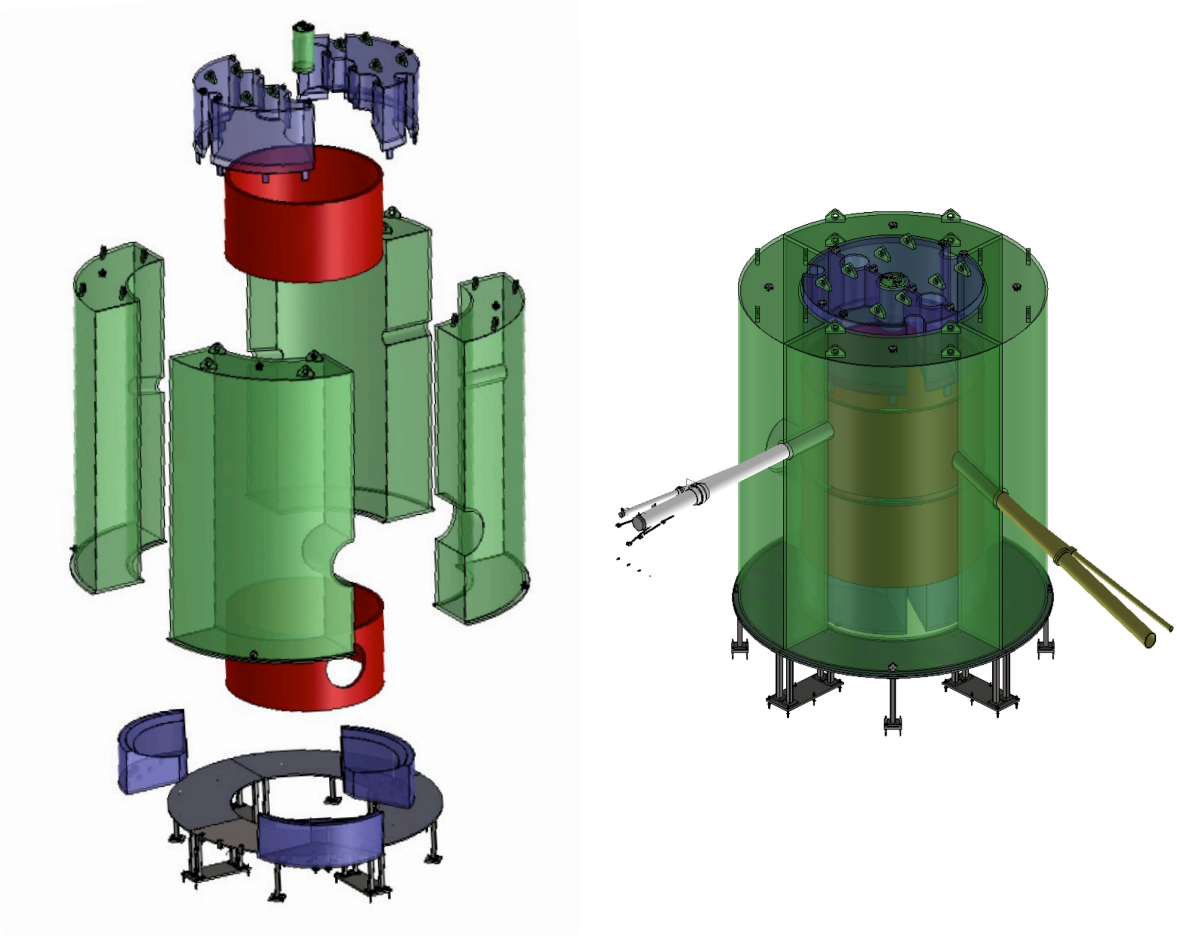

Figure 3.6: The OD acrylic tanks in exploded view (left) and fully assembled (right). Also shown in red is displacer foam used between the tanks and the OCV and the two DD neutron conduits.

(14.8 %) and ^{157}Gd (15.7 %). The addition of Gd to the LS therefore allows the detection of neutrons which thermalize and capture on nuclei in the LS. The result of a neutron capture is a nucleus left in an excited nuclear state which de-excites by the emission of γ-rays. These γ's then lose energy to Compton scattering and photo-absorption in the LS resulting in the emission of detectable scintillation photons.

The LZ requirement is that the combined veto system of the OD and XS have an efficiency of >95 % for tagging neutron events in the WIMP search event sample (the

precise definition of this sample to be defined in Sec. 3.3). Studies detailed in the next chapter demonstrate that this can be achieved using a 200 keV analysis threshold in the OD (and a 100 keV_{ee} XS threshold), however, the goal is to maximize veto efficiency by using an OD threshold of 100 keV.

3.2 LZ Calibration Systems

LZ will build off the pioneering calibrations campaign achieved in LUX and will make use of several new sources as well. Here I provide a brief overview of some of the newer sources planned for LZ.

3.2.1 Internal Sources

It may be the case that the liquid mixing timescale in LZ is too long compared to the 1.8 h half-life of ^{83m}Kr which would prevent this source from being evenly distributed in the LXe volume. This makes calibrations of the position reconstruction difficult as the underlying spatial distribution of the source is less well known. As a longer-lived alternative to ^{83m}Kr, a source of ^{131m}Xe is being developed. This metastable state has half-live of 11.9 d which will guarantee a homogeneous distribution in the TPC. This state decays by emission of a 164 keV γ. Injection of this source is achieved in nearly the same way as that for ^{83m}Kr. The parent isotope, ^{131}I, is available from the medical isotope industry as a solid pill over which Xe gas can be flown.

^{220}Rn is likely to be injected as a high-energy source for calibration of the XS response.

Injection of ^{220}Rn would be achieved via gas flow over an electroplated ^{228}Th source. The details of resulting decay structure is described in more detail in Chap. 5 of this thesis. The XENON collaboration has used a similar source as a calibration of their ER band [36].

3.2.2 External Sources

Most external sources will be deployed by lowering them into one of three 23.6 mm stainless-steel tubes which vertically penetrate into the vacuum space between the ICV and OCV. Photoneutron sources and the DD neutron calibrations will each have their own specific deployment geometries. Sources to be deployed in the source tubes include AmLi and ^{252}Cf for neutrons and ^{57}Co, ^{228}Th, and ^{22}Na for γ's of varying energy.

Of particular interest is the planned use of photoneutron sources in LZ. These are sources which place a strong (of order MBq [37]) gamma source next to a target nucleus which undergoes the (γ, n) reaction with some nominal cross section. Typical cross sections are low which explains the use of such a high activity γ source. The resulting neutron is approximately mono-energetic. In LZ, two sources of this type are planned: ^{88}Y Be and ^{205}Bi Be. ^{205}Bi Be creates neutrons of three different energies, the dominant one having an energy of 88.5 keV, with a nuclear recoil end point of 2.7 $\mathrm{keV_{nr}}$ in Xe. The nuclear recoil end point from a 152 keV neutron from ^{88}Y Be is 4.6 $\mathrm{keV_{nr}}$. These calibrations primarily serve to characterize the LZ response from low-energy NR events like those expected from ^{8}B neutrinos. With a thorough calibration of this region, the ^{8}B background can be properly modeled for the WIMP search analysis.

Practically, the photoneutron sources are deployed inside a 20 cm square cylinder tungsten "pig" which acts to shield LZ from the strong γ source. During a calibration, the small "YBe plug" acrylic tank of the OD will be removed and the pig will be lowered to sit on top of the OCV center. Many more details on this deployment and other LZ calibrations can be found in Ref. [31].

3.3 LZ WIMP Search

As its primary physics goal, LZ will search for NR scattering events from a hypothesized galactic flux of WIMPs. The signal sought in LZ are NR events identified as having only scattered once (single-scatter events) in a 5.6 tonne fiducial volume of LXe with no accompanying signals in the XS and OD systems.

In this section I give an overview of the LZ WIMP analysis leading to its expected WIMP sensitivity. Primarily, this involves the construction of a background model through the use of Monte Carlo (MC) simulations.

3.3.1 Sources of Background

Ultimately, the backgrounds in LZ fall into two categories: ER and NR. Overall, the number of ER events in LZ is roughly a thousand times greater than the number of NR events. The powerful discrimination between ER and NR events afforded by the TPC technology then provides the final reduction factor, bringing the total count down to a handful of candidate signal events. Both types of background must be kept to a

minimum, however, extra attention must be given to the sources of NR background as their signature is identical to that of a WIMP. Sources of ER and NR events in LZ come from trace radioactivity in the detector construction materials, radioactivity dissolved in the Xe itself, and from the scattering of astrophysical and solar neutrinos.

Detector Materials

The trace radioactivity in the detector construction materials is an ever-present background in nearly all direct searches for dark matter. In LZ, detector materials contain the isotopes ^{40}K, ^{137}Cs, and ^{60}Co, as well as the ^{238}U ($4n+2$), ^{235}U ($4n+3$), and ^{232}Th ($4n$) decay chains which contain on the order of ten radioisotopes each. A more thorough discussion of the decay chains is given in the following chapter.

The β decays of these radioisotopes sometimes leads to the formation of excited nuclear states in the daughter nucleus, ultimately resulting in the emission of γ-rays. These γ's, with energies $\lesssim$2.6 MeV, may then undergo a single Compton scatter in the LXe fiducial volume and exit or be fully absorbed via photoelectric absorption. The result is a single ER energy deposit. Those γ's which do not deposit sufficient energy in the XS or the OD (or both) are a background.

In addition to their emission of γ-rays, the ^{238}U, ^{235}U, and ^{232}Th progeny present in detector materials also contribute to the NR background through the production of neutrons which may single scatter in the fiducial volume. The very heavy nuclei at the head of each chain may undergo spontaneous fission (SF) in order to reach a more stable position on the curve of binding energy per nucleon. The SF process results in the

emission of several neutrons and γ's in coincidence, the average being roughly 2 neutrons and 6 γ's in the SFs of ^{238}U, ^{234}U, ^{235}U, and ^{232}Th. This source of background was studied extensively in Ref. [38] and found to be negligible for LZ due to the high neutron + γ multiplicity of these events. Specifically, these events are very efficiently tagged by the XS and OD vetoes.

A more dangerous neutron background results from the (α, n) process caused by the α decays of ^{238}U, ^{235}U, and ^{232}Th chain progeny. These α's react with the surrounding material to produce single neutrons, often, without coincident γ's. The (α, n) cross section depends on both the incident α energy and the size of the Coulomb barrier presented by the target nucleus, making the radiopurity of low-Z materials especially important. The PTFE which defines the TPC volume in LZ is one such material, as fluorine ($Z = 9$) has an exceptionally high (α, n) cross section. Contamination of the raw powder used to make the PTFE with the radon daughter ^{210}Po is of primary concern in LZ. This is the largest source of NR background from the detector materials. The PMTs and their associated parts (bases, mountings, etc) contain a number of low-Z materials, making them a large contributor as well.

Backgrounds from the construction of the detector are minimized through a comprehensive materials screening program. LZ uses a variety of methods for determining the trace levels of radioimpurities in materials and determining if they are suitable for use in the experiment. Examples include counting with high purity germanium detectors (HPGe), Neutron Activation Analysis (NAA), and Inductively-Coupled Plasma Mass

Spectrometry (ICP-MS). The interested reader should consult Ref. [31] for more details.

Internal Backgrounds

Uniform sources of ER background arise from trace amounts of radioactivity dissolved in the LXe. The largest of these is caused by the emanation of noble ^{222}Rn (radon) and ^{220}Rn (thoron) gas produced in the ^{238}U and ^{232}Th chains in nearby detector materials. Both ^{222}Rn and ^{220}Rn decay to isotopes of Pb which undergo "naked" β-decay, corresponding to a β-decay with no associated γ emission. ^{222}Rn and ^{220}Rn from dust contamination are also a concern here. The ER events that result from these decays are the largest background in LZ.

Contamination of the Xe with atmospheric Kr and Ar is also expected. This results in events from the β-decays of ^{85}Kr (Q = 687 keV, $T_{1/2}$ = 10.7 yr) and ^{39}Ar (Q = 565 keV, $T_{1/2}$ = 269 yr), respectively. The Xe gas is therefore extensively purified using chromatography [39] to reduce the concentrations of these isotopes to an acceptable level. In the final purification for LZ, the expected concentrations, $^{\text{nat}}$Kr/Xe and $^{\text{nat}}$Ar/Xe, are 0.015 ppt g/g and < 0.45 ppb g/g, respectively [32].

Physics Backgrounds

These backgrounds result from physics processes that are interesting in their own right. None of these backgrounds were significant in LUX, demonstrating the large increase in sensitivity of LZ. For the primary WIMP search analysis, three sources of physics backgrounds have been identified: neutrino-electron scattering, $2\nu\beta\beta$ decay of ^{136}Xe,

and neutrino-nucleus scattering.

Neutrinos that enter as a background in sensitive, Earth-based experiments such as LZ come from three primary sources. This is shown in Fig. 3.7, where the energy spectra of neutrinos from our Sun as well as those produced in the Earth's atmosphere and those from the diffuse supernovae background are shown. The neutrinos produced through the primary proton-proton fusion process in our Sun, so called *pp* neutrinos, have by far largest incident flux but their energies are rather low, extending up to only ≈400 keV. At the very highest energies, neutrinos produced in the upper atmosphere dominate.

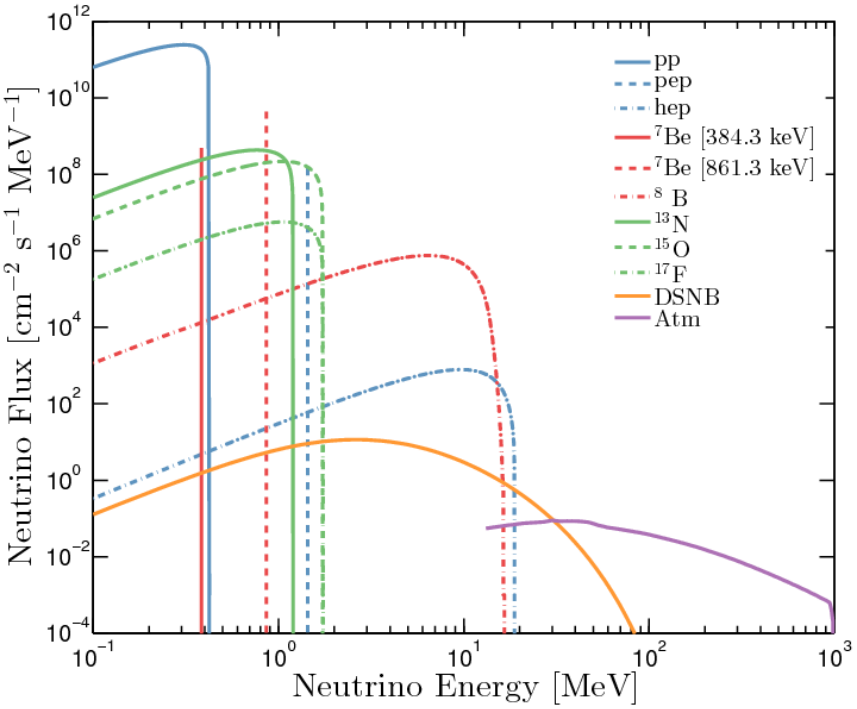

Figure 3.7: Energy spectra of principle neutrino species that are/could be backgrounds to direct dark matter experiments like LZ. Taken from Ref. [40].

The rate of elastic neutrino-electron scatters in the LXe target that enter as a background for the WIMP search analysis is dominated by the *pp* neutrino flux, but those

from ^{7}Be and ^{13}N also contribute. As these scatters occur on electrons, this background is of the ER type.

The higher energy neutrinos from the atmosphere will contribute the single largest NR background in LZ through the coherent scattering of neutrinos off Xe nuclei. This Standard Model process has only recently been observed [41] due to its very small cross section [42]. Compared to scattering off electrons, the energy transferred to the nucleus will usually be suppressed by $\approx m_e/m_N$ which leads to the requirement of a higher incident neutrino energy to achieve a NR above threshold. The relatively high flux of solar neutrinos from ^{8}B is a particular case in which the resulting signal in LZ is very similar to that of a 6 GeV WIMP. The low energy NR calibrations planned in LZ aim to characterize the expected response to this background.

Finally, the Standard Model $2\nu\beta\beta$ decay of ^{136}Xe will contribute to the ER background of LZ. ^{136}Xe has a $2\nu\beta\beta$ half-life of 2.2×10^{21} y and results in a continuum of ER energy deposits up to the Q-value of 2.456 MeV [43].

3.3.2 Simulations and Analysis Cuts

The LZ simulation framework makes use of the generalized BACCARAT (Basically a Component-Centric Analog Response to AnyThing) software package. BACCARAT provides a user-friendly interface for building a detector simulation in the GEANT4 toolkit [44]. An accurate geometry of LZ is coded into BACCARAT (see Fig. 4.12), allowing for simulations of the various backgrounds outlined above. A series of event

generators are implemented as well. Those of primary importance simulate: decays of any requested radioisotope, specifically, all decays in the ^{238}U, ^{235}U, and ^{232}Th chains; SF of ^{238}U, ^{234}U, ^{235}U, and ^{232}Th; and neutrons from the (α, n) process. The geometry also includes relevant material optical properties which allows for simulations involving the propagation of scintillation photons to PMT photocathodes. In the XS and TPC, simulations of uniformly distributed scintillation photon sources are performed and used to map out the light collection as a function of position.

To simulate events from a given detector component (e.g. the OCV), the desired generator is run (e.g. 1 mBq/kg of ^{238}U) a specified number of times (number of events) and the steps in which energy is deposited in the TPC and XS LXe and the OD GdLS are recorded and saved. In processing the simulation output, energy deposits in the LXe volumes within 400 µm are clustered. The resulting energy clusters are fed into the NEST package along with other key parameters such as the electric field at the energy deposit location and the position-dependent light collection. The outputs of NEST are the position/drift time corrected signals, $S1_c$ and $S2_c$. The number of surviving events after all cuts is then scaled by the corresponding detector component activity measured or inferred from materials screening.

In parallel, the energy deposits in the TPC are used to create energy-weighted position variables. In particular, the weighted radius and z-coordinate of the event in the TPC

and their dispersions are defined as follows:

$$\begin{aligned} \langle r \rangle &= \frac{\sum_i E_i r_i}{\sum_i E_i} \\ \langle z \rangle &= \frac{\sum_i E_i z_i}{\sum_i E_i} \end{aligned} \tag{3.1}$$

$$\begin{aligned} \sigma_r^2 &= \frac{\sum_i E_i (r_i - \langle r \rangle)^2 \times \sum_i E_i}{\left(\sum_i E_i\right)^2 - \sum_i (E_i)^2} \\ \sigma_z^2 &= \frac{\sum_i E_i (z_i - \langle z \rangle)^2 \times \sum_i E_i}{\left(\sum_i E_i\right)^2 - \sum_i (E_i)^2} \end{aligned} \tag{3.2}$$

using the individual energy deposits, E_i, located at r_i and z_i.

With fundamental event quantities in hand, WIMP-like events are selected using the following set of analysis cuts:

1. Region of interest (ROI) cut: the S1 signal in the TPC must have at least 3-fold coincidence in the TPC PMTs and the corrected $S1_c$ signal must be less than 80 phd. In addition, the uncorrected S2 signal must be at least 415 phd, corresponding to about 5 emitted electrons to ensure accurate position reconstruction of the event. The corresponding energy window is approximately 1.5–6.5 keV for ERs and 6–30 keV for NRs.

2. Single scatter (SS) cut: the dispersion of the energy weighted radius and z of the event must satisfy $\sigma_r < 3.0$ cm and σ_z <0.2 cm. These cut values represent the typical resolution of the position reconstruction at low, near-threshold S2 values (the resolution rapidly improving at higher S2 values).

3. XS cut: a valid WIMP-like event must have no signal greater than 3 phd (corresponding to $\approx$100 $\mathrm{keV_{ee}}$) in a 800 µs coincidence window before or after the event

time registered in the TPC.

4. OD cut: a valid WIMP-like event must also have no signal greater than 200 keV in a 500 µs coincidence window before or after the event time registered in the TPC.

5. Fiducial volume (FV) cut: an event's energy weighted position must be within the 5.6 tonne fiducial volume. The FV is cylindrical with boundaries defined to be 4 cm from the TPC walls, 2 cm above the cathode grid (with 14.8 cm of LXe below the cathode providing further shielding) and 13 cm below the gate grid.

Events which pass all of these cuts are backgrounds in the WIMP search analysis.

The expected backgrounds passing all cuts in the nominal 1000 live day run of LZ are summarized in Tab. 3.1. Also included in the table is an estimate of the NR background from surface contamination of the TPC walls with ^{210}Pb daughters. Known as "wall events", they result from mis-reconstruction of the S2 signal from decays on the wall that allows them to enter the edges of the FV.

Fig. 3.8 shows the energy spectra of ER background sources in the LZ FV. In the WIMP search ROI, the ER rate is dominated by the decays resulting from emanation of radon. The γ background from trace radioactivity in the detector materials is subdominant as is also the case for NR backgrounds, the energy spectra of which are shown in Fig. 3.9. The dominant source of NR background results from the coherent scattering of atmospheric neutrinos. At the lowest NR energies, coherent scattering of ^{8}B neutrinos dominates.

Table 3.1: Estimated backgrounds from all significant sources in the LZ 1000 day WIMP search exposure. Counts are for a region of interest relevant to a 40 GeV/c^2 WIMP: approximately 1.5–6.5 keV for ERs and 6–30 keV for NRs; and after application of the single scatter, XS and OD veto, and 5.6 tonne fiducial volume cuts. Mass-weighted average activities are shown for composite materials and the ^{238}U and ^{232}Th chains are split into contributions from early- and late-chain, with the latter defined as those coming from isotopes below and including ^{226}Ra and ^{224}Ra, respectively. Taken from Ref. [32]

Background Source	**Mass (kg)**	**^{238}U$_e$**	**^{238}U$_l$**	**^{232}Th$_e$**	**^{232}Th$_l$**	**^{60}Co**	**^{40}K**	**n/yr**	**ER (cts)**	**NR (cts)**
		mBq/kg								
Detector Components										
PMT systems	308	31.2	5.20	2.32	2.29	1.46	18.6	248	2.82	0.027
TPC systems	373	3.28	1.01	0.84	0.76	2.58	7.80	79.9	4.33	0.022
Cryostat	2778	2.88	0.63	0.48	0.51	0.31	2.62	323	1.27	0.018
Outer detector (OD)	22950	6.13	4.74	3.78	3.71	0.33	13.8	8061	0.62	0.001
All else	358	3.61	1.25	0.55	0.65	1.31	2.64	39.1	0.11	0.003
								subtotal	**9**	**0.07**
Surface Contamination										
Dust (intrinsic activity, 500 ng/cm^2)									0.2	0.05
Plate-out (PTFE panels, 50 nBq/cm^2)									-	0.05
^{210}Bi mobility (0.1 µBq/kg LXe)									40.0	-
Ion misreconstruction (50 nBq/cm^2)									-	0.16
^{210}Pb (in bulk PTFE, 10 mBq/kg PTFE)									-	0.12
								subtotal	**40**	**0.39**
Xenon contaminants										
^{222}Rn (1.81 µBq/kg)									681	-
^{220}Rn (0.09 µBq/kg)									111	-
^{nat}Kr (0.015 ppt g/g)									24.5	-
^{nat}Ar (0.45 ppb g/g)									2.5	-
								subtotal	**819**	**0**
Laboratory and Cosmogenics										
Laboratory rock walls									4.6	0.00
Muon induced neutrons									-	0.06
Cosmogenic activation									0.2	-
								subtotal	**5**	**0.06**
Physics										
^{136}Xe $2\nu\beta\beta$									67	-
Solar neutrinos: pp+^{7}Be+^{13}N									255	-
Diffuse supernova neutrinos (DSN)									-	0.05
Atmospheric neutrinos (Atm)									-	0.46
								subtotal	**322**	**0.51**
Total									1195	1.03
Total (with 99.5% ER discrimination, 50% NR efficiency)									5.97	0.52
Sum of ER and NR in LZ for 1000 days, 5.6 tonne FV, with all analysis cuts									**6.49**	

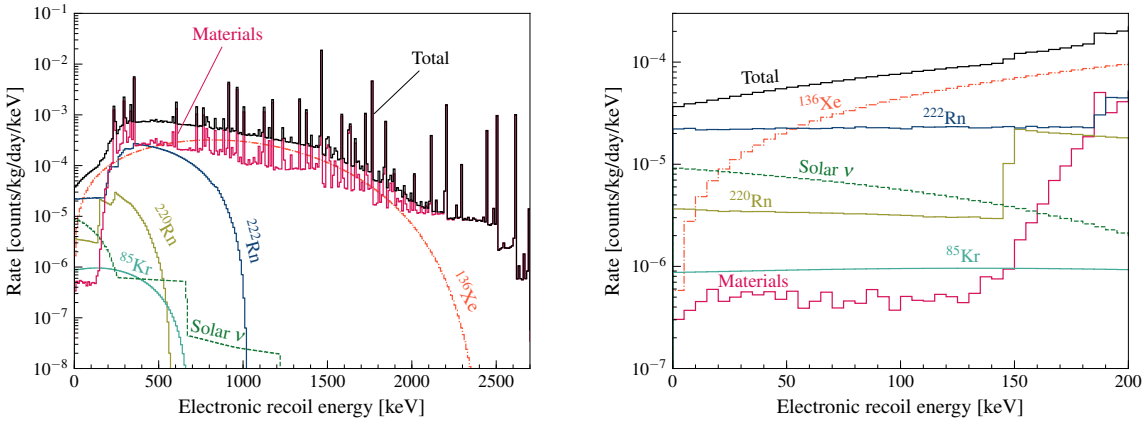

Figure 3.8: ER background spectra in the 5.6-tonne fiducial volume for single scatter events with neither a xenon skin nor an OD veto signal. No detector efficiency or WIMP-search region of interest cuts on $S1_c$ have been applied. The right-hand panel shows a close-up of the 0–200 keV region of the left-hand panel. Taken from Ref. [32].

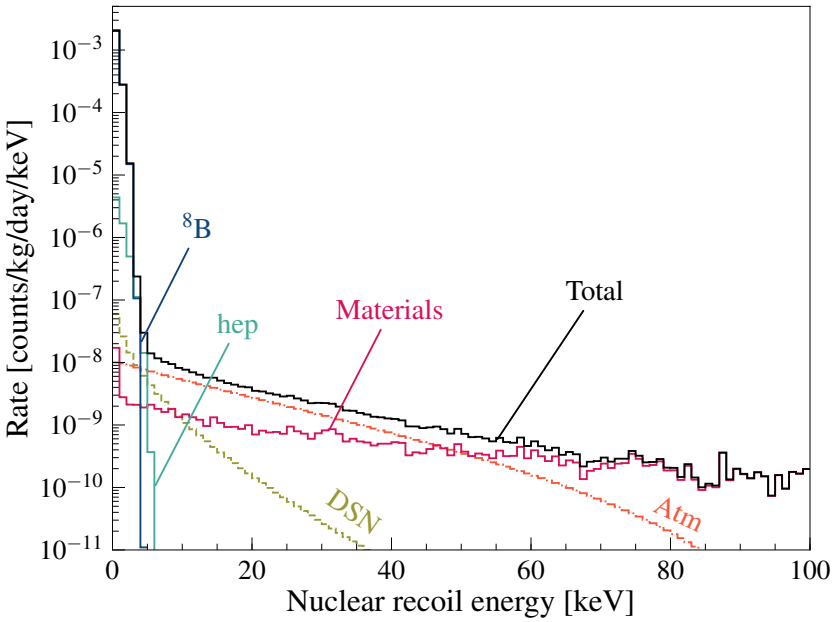

Figure 3.9: NR background spectra in the 5.6-tonne fiducial volume for single scatter events with neither a xenon skin nor an OD veto signal. No detector efficiency or WIMP-search region of interest cuts on S1c have been applied. Taken from Ref. [32].

3.3.3 Expected Sensitivity

LZ's sensitivity to the scattering (SI or SD) of a WIMP of given mass is stated as the 90% coinfidence level (CL) upper limit on the WIMP-nucleon cross section obtained in repeated experiments under the background-only hypothesis. The Profile Likelihood Ratio (PLR) test statistic is used. It is defined as [45]:

$$q \equiv -2\ln(\lambda(\sigma)), \tag{3.3}$$

where the PLR itself is

$$\lambda(\sigma) = \frac{\mathcal{L}(H_0)}{\mathcal{L}(H_1)} = \frac{\mathcal{L}(\sigma, \hat{\hat{\boldsymbol{\theta}}})}{\mathcal{L}(\hat{\sigma}, \hat{\boldsymbol{\theta}})}. \tag{3.4}$$

For obtaining upper limit sensitivity, the null hypothesis here includes the presence of a WIMP signal constrained to have cross section σ. The vector of quantities $\boldsymbol{\theta}$ is a set of nuisance parameters (NP) that are allowed to float in the likelihood fit. Specifically for the LZ projections reviewed here, they are the normalizations of each of the background components used in the likelihood model. Hatted quantities represent their maximum likelihood estimate (MLE), while double hatted quantities are the "conditional MLE values" (CMLE) which maximize the likelihood function when the signal strength is constrained to be σ (the cross section being tested).

The test statistic distribution is then used to obtain a p-value under the test cross section σ according to

$$p(\sigma) = \int_{q_{\text{Median Bkg}}}^{\infty} f(q|\sigma)\, dq \quad , \tag{3.5}$$

where $q_{\text{Median Bkg}}$ is the median value of the test statistic obtained from repeated fits

using the background-only hypothesis. In the presence of only background, this is a "expected value" for q. When LZ obtains actual physics data, it will use the value of q calculated with that data as the lower bound for this integral to set an upper limit (assuming there is no evidence for a WIMP signal). The upper limit cross section at 90% CL then corresponds to $p(\sigma_{\mathrm{UL}}) = 0.1$.

The likelihood functions above are evaluated using probability distribution functions (PDFs) in the S2 and S1 variables for both signal and background events. PDFs for the background sources are generated by using the energy spectra shown Fig. 3.8 and Fig. 3.9 as input to the NEST framework which produces the resulting distribution in the S2 vs S1 plane. Similarly, the WIMP signal PDF for each WIMP mass is evaluated using NEST with the energy spectrum given in Chap. 2. A sample comparison between signal and background is given in Fig. 3.10 which shows a simulated dataset of the expected backgrounds from the 1000 day run along with the PDFs for the ^{8}B background and the signal PDF for a 40 GeV/c^2 WIMP.

LZ's SI WIMP sensitivity is shown in Fig. 3.11 where the best sensitivity reaches a minimum cross section of 1.6×10^{-48} cm^2 at a WIMP mass of 40 GeV/c^2. This is an order of magnitude lower than the expected sensitivity of any currently running LXe experiment. The sensitivity to SD WIMP scattering is shown in Fig. 3.12. Here, the unpaired neutrons in Xe isotopes give rise to better sensitivity to WIMP-neutron scattering than to WIMP-proton scattering.

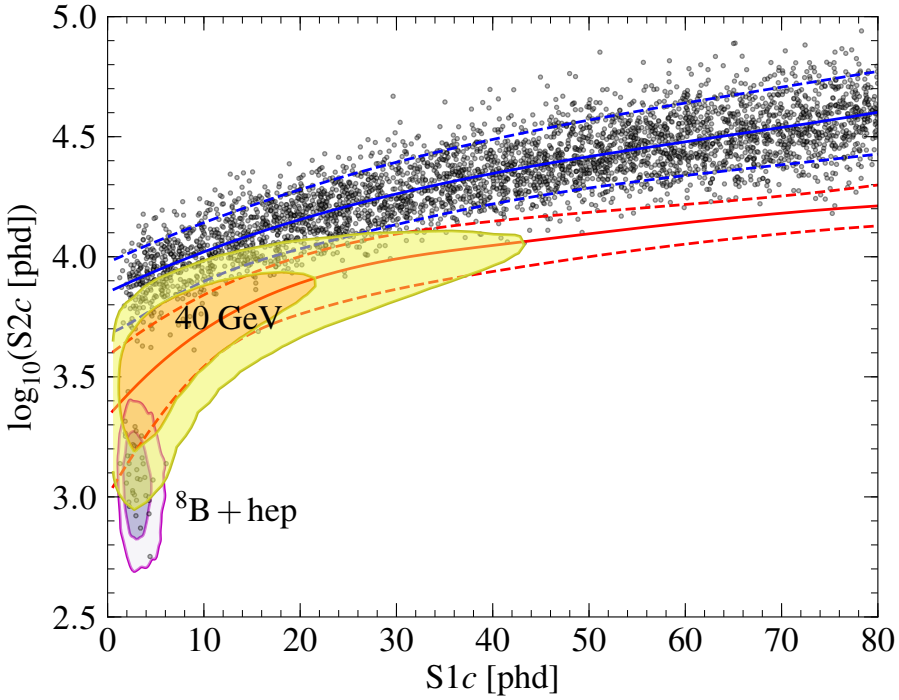

Figure 3.10: LZ simulated data set for a background-only 1000 live day run and a 5.6 tonne fiducial mass. ER and NR bands are indicated in blue and red, respectively (solid: mean; dashed: 10% and 90%). The 1σ and 2σ contours for the low-energy ^{8}B and *hep* NR backgrounds, and a 40 GeV/c^2 WIMP are shown as shaded regions. Taken from Ref. [32].

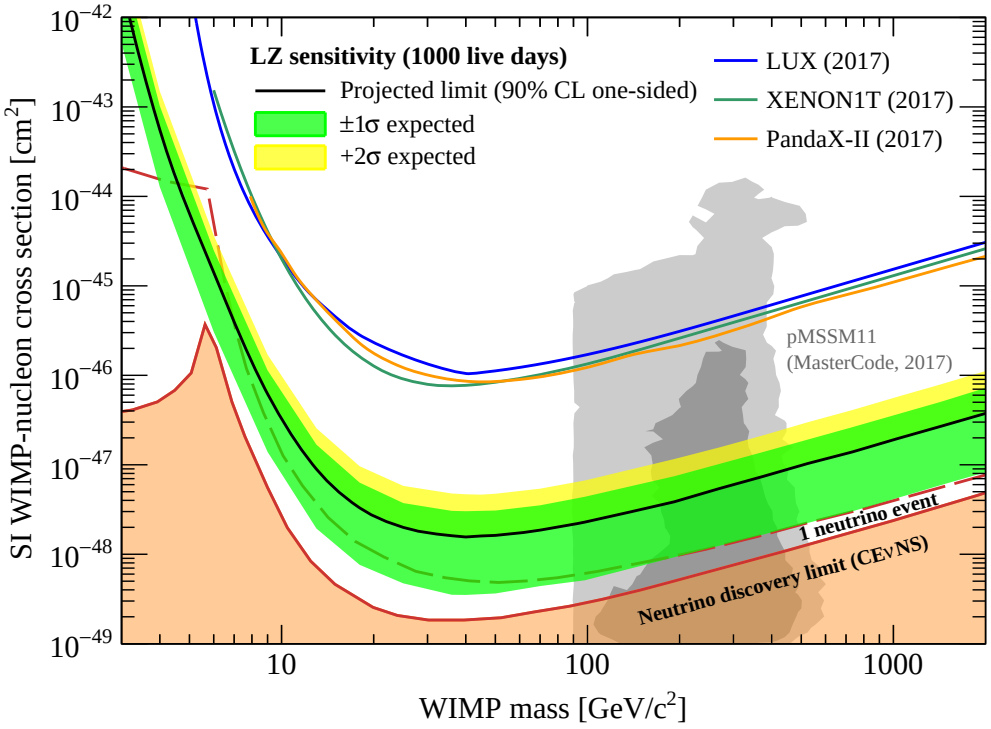

Figure 3.11: LZ projected sensitivity to SI WIMP-nucleon elastic scattering for 1000 live days and a 5.6 tonne fiducial mass. The best sensitivity of 1.6×10^{-48} cm^2 is achieved at a WIMP mass of 40 GeV/c^2. The -2σ expected region is omitted based on the expectation that the limit will be power constrained [46]. Results from other LXe experiments are also shown [47; 48; 49]. The lower shaded region and dashed line indicate the emergence of backgrounds from coherent scattering of neutrinos [50; 51] and the gray contoured regions show the favored regions from recent pMSSM11 model scans [52]. Taken from Ref. [32].

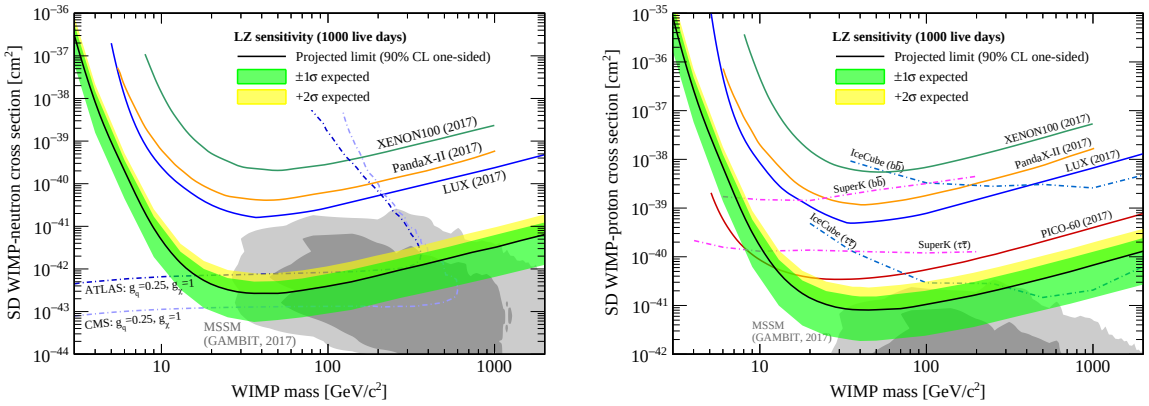

Figure 3.12: LZ projected sensitivity to SD WIMP-neutron (left) and WIMP-proton (right) scattering for a 1000 live day run with a 5.6 tonne fiducial mass. For SD WIMP-neutron(-proton) scattering a minimum sensitivity of 2.7×10^{-43} cm^2 (8.1×10^{-42} cm^2) is expected at 40 GeV/c^2. Recent limits from direct detection experiments are shown as solid lines [53; 54; 55; 15]. Dashed lines indicate the model dependent collider constraints from the LHC (for WIMP-neutron) [56; 57] and the leading indirect limits from neutrino telescopes (for WIMP-proton) [58; 59]. The gray contoured regions show the favored regions from recent MSSM7 model predictions [60]. Taken from Ref. [32].

Chapter 4

The LZ Outer Detector

In this chapter I describe in greater detail the LZ Outer Detector (OD), providing an overview of its various subsystems. The use of GdLS in the OD to detect neutrons and expected performance of the OD assessed through MC simulations are also discussed.

4.1 Function and Goals

The scattering of a WIMP in the central TPC of LZ will never be accompanied by a second WIMP interaction in the surrounding medium. However, the γ's and neutrons which are backgrounds to the WIMP search endeavor often scatter multiple times before or after leaving a signal in the TPC. This is the principle insight for the use of auxiliary or "veto" detectors to reduce backgrounds. LZ will make use of three such detectors:

1. The 4–8 cm thick layer of LXe outside of the TPC walls known as the "xenon skin" (XS)

2. The ≈60 cm, near-hermetic layer of GdLS around the OCV

3. The ≈80 cm of ultra-pure water which lies outside the GdLS layer, made active with PMTs suspended in water

The OD is comprised of the last two.

The XS and OD detectors serve two primary functions in LZ. The first is to act as anti-coincidence detectors for the central TPC and efficiently tag background events for removal in the final WIMP search analysis. The second is to provide an in-situ characterization of the backgrounds near LZ. This last point is important as LZ has significant potential to make a WIMP discovery. If such a discovery is to be claimed, extraordinary supporting evidence will be required, primarily in the form of detailed knowledge of the expected background rates. The XS and OD detectors will provide this information in the form of independent surveys of the radiation field around LZ.

As discussed in the previous chapter, backgrounds to a WIMP signal can arise from radioactive impurities in and near to the LXe TPC. An important class of backgrounds arise when a γ or a neutron is emitted due to a radioactive impurity in material on the perimeter of the LXe TPC, scatters once in the LXe TPC causing an energy deposit, and then exits. The XS has the principal power to veto γ's, because of the small amount of material separating it from the LXe TPC and its dense LXe detection medium. The OD, on the other hand, is designed to veto neutrons. Their combined action to remove backgrounds is seen in Fig. 4.1 which shows the spatial distribution of single scatter NR event vertices with energy deposits within the WIMP search ROI without (left) and with

(right) the use of the XS and OD veto cuts. The main effect of the vetoes is to increase the amount of LXe in which the background rate is low enough for WIMP search. In the left panel of Fig. 4.1, a FV of only ≈3.2 tonne would be required, compared to the 5.6 tonne FV (black line) available when the vetoes are used in the right panel.

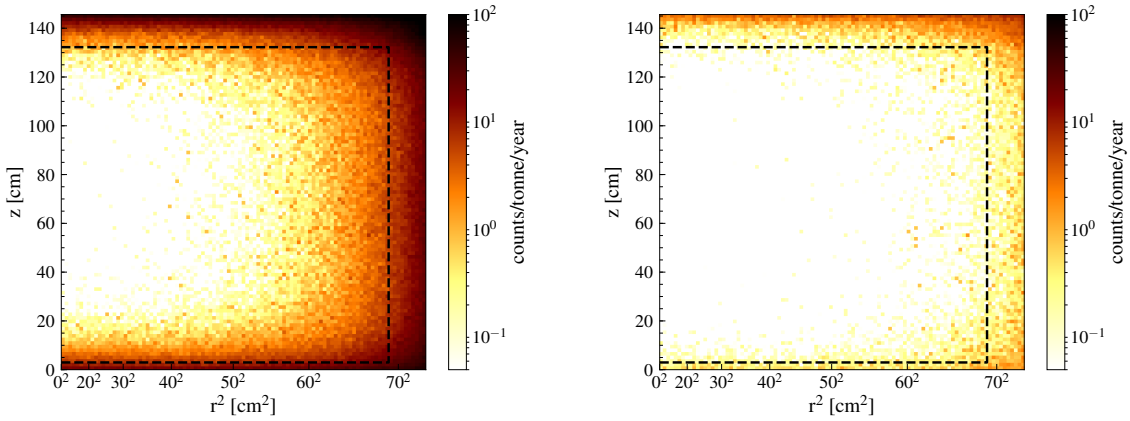

Figure 4.1: Single scatter event distributions for all NR backgrounds in the region of interest with no vetoing (left) and after application of both XS and OD vetoes (right). Not included here are the uniform NR events from neutrino backgrounds or the distribution from wall events. The integrated counts for the 5.6 tonne fiducial volume (dashed line) are reduced from 12.31 cts/1000 days with no vetoing to 1.03 cts/1000 days after application of the vetoes. Taken from Ref. [32].

4.2 Detector Overview

A brief description of the OD layout was given back in Sec. 3.1.3. Here I provide more detailed descriptions of the various OD components.

4.2.1 Acrylic Tanks

A total of ten UV-transparent (UVT) acrylic tanks will hold the GdLS: four side tanks surround the outer perimeter of the OCV, while three bottom tanks and two top tanks sit below and on top of the OCV, respectively. Lastly, a small, ≈30 cm diameter tank fills the gap created for deployment of the YBe neutron calibration source (known as the "YBe plug"). The four side tanks sit atop a stainless steel stand. The bottom tanks sit on the legs which also support the OCV and the top tanks and YBe plug sit on top of the OCV's top flange. To minimize the amount of water (which is a good neutron moderator) between the TPC and the GdLS, polyethylene displacer foam is wrapped around the straight wall sections of the cryostat, filling the 2 inch gap created between the side tank walls and the OCV flange. These components are labelled in Fig. 4.2.

The wall thickness of the acrylic tanks is 1 inch or 2.54 cm. Maintaining the structural integrity of the acrylic during the lifetime of the experiment prevents a thinner wall thickness, which would otherwise be preferred, as neutrons that thermalize in the acrylic tend to lengthen the average time to neutron capture (more on this later). The characteristic thickness of GdLS surrounding the OCV, largely determined by that of the side tanks, is ≈60 cm. A thinner layer is present directly above and below the OCV top and bottom. Fig. 4.3 shows the assembled OD in LZ, with important dimensions called out.

The acrylic tanks are being manufactured by Reynolds Polymer Technology, Inc. (RPT) [61] in Grand Junction, Co, USA. The four side tanks are formed by bonding

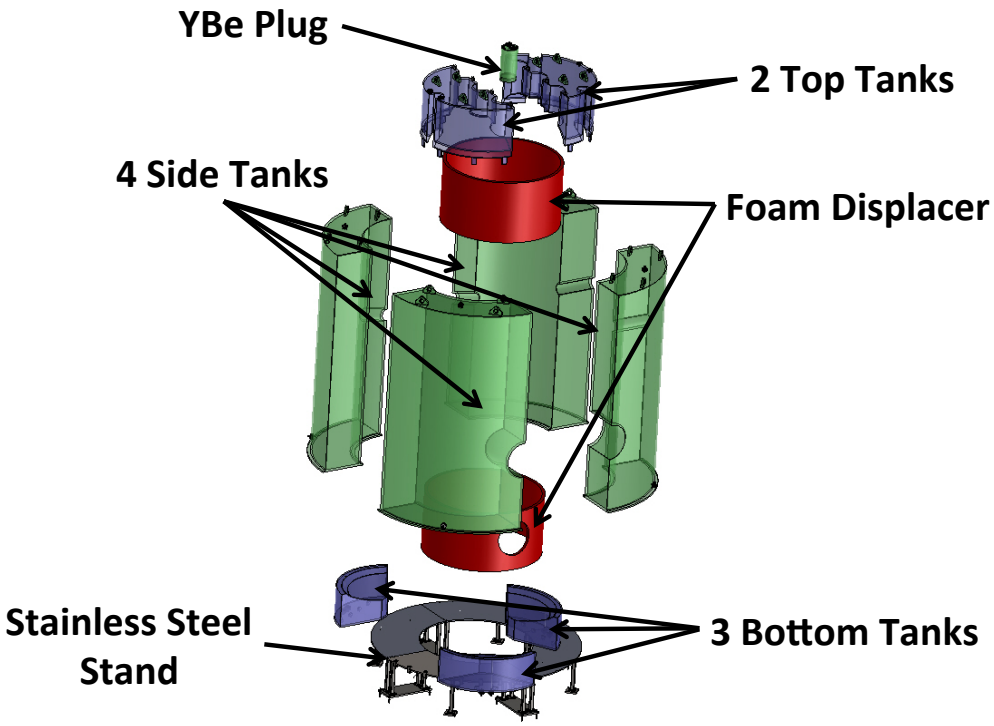

Figure 4.2: Exploded view of the OD acrylic tanks.

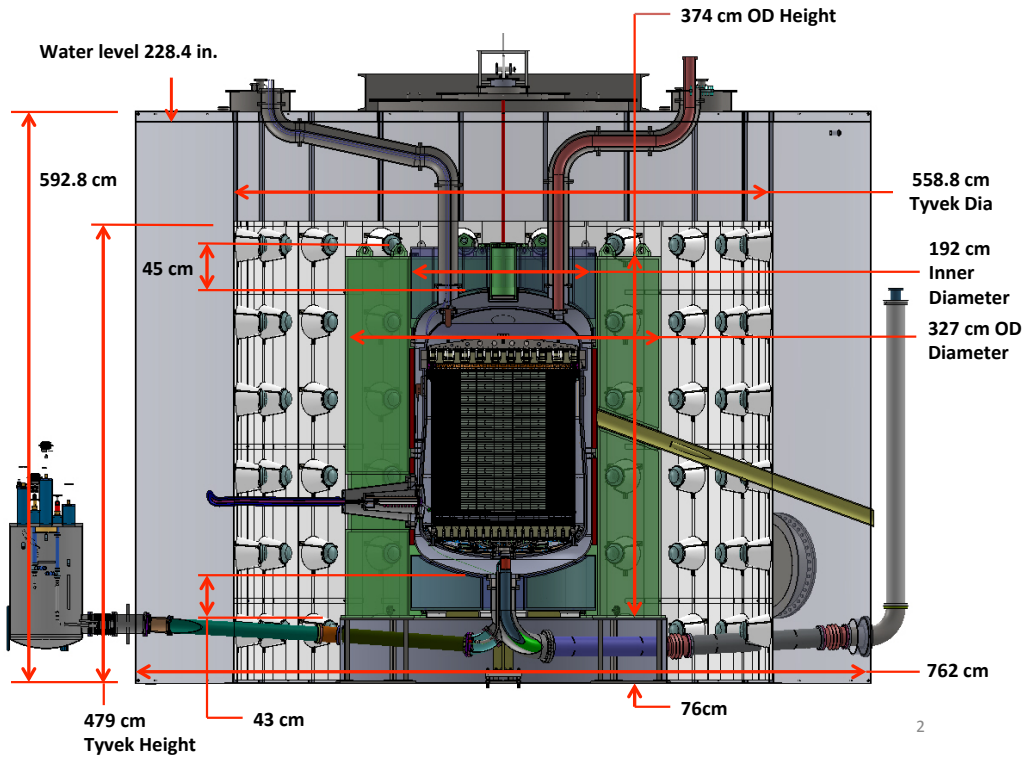

Figure 4.3: Dimensioned drawing of the assembled OD around the central Xe detector of LZ.

cast acrylic sheets. Curved surfaces are achieved by heating flat sheets in an oven over a large form with the correct curvature. The side walls of the side tanks also include bonded-in conduits for various LZ services that need to penetrate the OD to reach the OCV (cathode HV feedthrough, DD neutron tubes, etc). The top and bottom tanks are more complex and are therefore created from a pre-formed mold into which the raw acrylic monomer is injected and allowed to cure.

Use of UVT acrylic is necessary to allow for transmission of the optical photons generated in the GdLS. In the absence of the additives used in non-UVT acrylic, the acrylic will begin to discolor after exposures to large amounts of UV light. The tanks are therefore kept in a dark environment whenever work is not being performed. Additionally, radon daughter plate-out on the acrylic surface is minimized by keeping an adhesive film on acrylic surfaces while they are not being worked on. The typical radon concentration at RPT is $\sim$10 Bq/m^3.

After the inner surface of each tank is polished clear, it is thoroughly cleaned before the final acrylic bond is made to seal off the inside of the tank. After polishing, the acrylic is rinsed with deionized water (DI) with resistivity >1 MΩ. The surface is then wiped with a rag soaked with purified LAB allowing any contaminants that would otherwise dissolve in the (non-polar) GdLS to be removed. Next, the acrylic is cleaned with an Alconox solution made with DI water and thoroughly rinsed. The acrylic is considered clean when the rinse water resistivity is measured as $\geq$1 MΩ. Finally, the acrylic is thoroughly dried with lint-free wipes. Fig. 4.4 shows a nearly completed side tank (the

outside has yet to be cleaned) with penetrations for the straight DD neutron tube (left) and the cathode HV feedthrough (right).

Figure 4.4: Photograph of an acrylic side tank for the LZ OD taken at RPT in Colorado. After the outside is cleaned, the tank will be wrapped with several protective layers for shipping and transport underground.

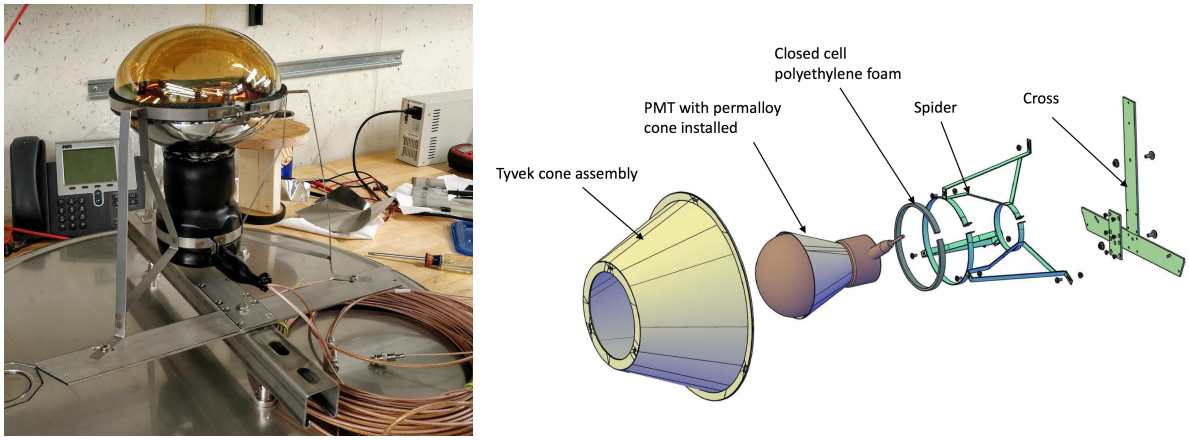

Figure 4.5: *Left:* Photo of a water-proof Hamamatsu R5912 8"-diameter PMT for the OD in a prototype spider mount. *Right:* Model of the PMT assembly for mounting to a ladder.

4.2.2 PMTs and Reflector System

8-inch PMTs

To detect scintillation and Cherenkov light in the OD, 120 Hamamatsu R5912 8"-diameter PMTs surround the assembled acrylic vessels inside the water tank. The PMTs are arranged in 20 vertical ladders, with 6 PMTs per ladder. The radial distance from the outer acrylic wall to the PMT faces is 84 cm.

The PMTs are purchased as a water-proof PMT+base assembly from Hamamatsu as shown in Fig. 4.5. Each PMT is secured using the "spider" mount shown on the right of Fig. 4.5 to a ladder, comprised of a piece of stainless steel Unistrut. The spider mount also includes a cone of μ-metal to shield the PMT dynode chain from stray magnetic fields. Each ladder then attaches to the side of the water tank.

The OD PMTs will operate with positive bias voltage which results in the photocathode being grounded. In the ultra-pure DI water, a large voltage across the PMT glass

when using negative HV can lead to ion depletion in the glass, making it brittle over time. A decoupling capacitor in the PMT base filters the transient signal into a separate signal cable. Therefore each PMT has two cables, one for HV and the other for signal. These cables will be secured up each ladder, around a set of cable trays and through a port in the water tank to the DAQ system.

The R5912 PMTs have quantum efficiency of $\geq$25 % for an incident photon of wavelength 420 nm, well matched to the peak emission wavelength of the GdLS. A typical gain of 10^7 is achieved at a bias voltage of 1,500 V. The large diameter provides $\approx$520 cm^2 of sensitive photocathode area.

At room temperature, a dark rate of $\approx$4 kHz is assumed for these PMTs; initial measurements, however, suggest an average value closer to $\approx$1.5 kHz. Assuming the higher of these two, the probability for a dark pulse from any of the 120 OD PMTs to fall in a typical pulse width window of 200 ns is simply: 200 ns $\times$ 4 kHz $\times$ 120 $\approx$ 0.1. Therefore, the probability of a dark pulse contributing to a pulse formed with n-fold PMT coincidence is 0.1^n.

Tyvek Reflector

To aid in the collection of scintillation and Cherenkov photons, the OD system is surrounded by a curtain of 262 µm-thick 1085D Tyvek [62; 63]. The Tyvek will also cover the water tank floor, side tank stand, and the OCV vessel (including the displacer foam) to maximize light collection. Each PMT mount will additionally include a cone of Tyvek which covers the μ-metal shield. This is can be seen in Fig. 4.3.

The Tyvek has a reflectivity $\gtrsim$95 % over the range of GdLS light emission of 350 nm to 550 nm [64; 65; 66]. Tyvek was chosen over other reflector materials (e.g. Lumirror) because of its easy availablity, comparable reflectivity, and better radiopurity for LZ. A comparison of the measured radioimpurities in Tyvek using an LZ HPGe counter to those measured in Lumirror by the Darkside collaboration is given in Tab. 4.1. The high γ multiplity per decay of late series ^{238}U makes Lumirror unattractive for LZ. Additionally, the 2.45 MeV γ from ^{214}Bi decay (branching ratio 1.55%) contributes to the background in the search for $0\nu\beta\beta$ in ^{136}Xe.

Table 4.1: Comparison of LZ and Darkside HPGe screening results for Tyvek and Lumirror, respectively.

Isotope or Subchain	**Measured mBq/kg**	
	Tyvek (LZ)	**Lumirror (Darkside)**
$^{238}U_e$	70	150
$^{238}U_l$	8	657
$^{232}Th_e$	15	72
$^{232}Th_l$	22	31
^{40}K	1330	430

4.2.3 LS Filling System

Brookhaven National Laboratory (BNL) will produce the GdLS and package the liquid double-bagged inside 55 gallon drums. Roughly 112 drums will hold the 17.3 tonnes needed to fill the OD vessels. These drums will then be shipped to SURF in a temperature controlled truck and brought underground. The LS filling system comprises the interface with the drum, an LS sampling detector, a staging reservoir for the LS on top of the water tank, and the final interface with the acrylic vessels. A prototype of this system at

UCSB is being used to finalize the filling procedures. Of primary concern is minimizing the exposure of the LS to underground mine air, which contains both ^{222}Rn and ^{85}Kr that can produce large rates in the OD if dissolved in the liquid.

Drums will be brought into a temporary cleanroom and opened. The outer bag of the LS packaging will then be opened and nitrogen gas will be used to create a nitrogen-rich environment above the cap to the inner LS bag. A custom PTFE cap which supplies the LS pump line and a nitrogen purge line will be quickly fitted to the bag.

At the start of filling operations we wish to check that the LS has not been contaminated in a way that compromises its light output. A sample of LS will be pumped into the "LS Sampler", the small LS detector shown in Fig. 4.6. A radioactive source will be used to collect a pulse height spectrum ensuring that the LS light yield is as expected. The Sampler has the ability to bubble nitrogen through its LS volume allowing a quick test for the presence of oxygen quenching in the LS.

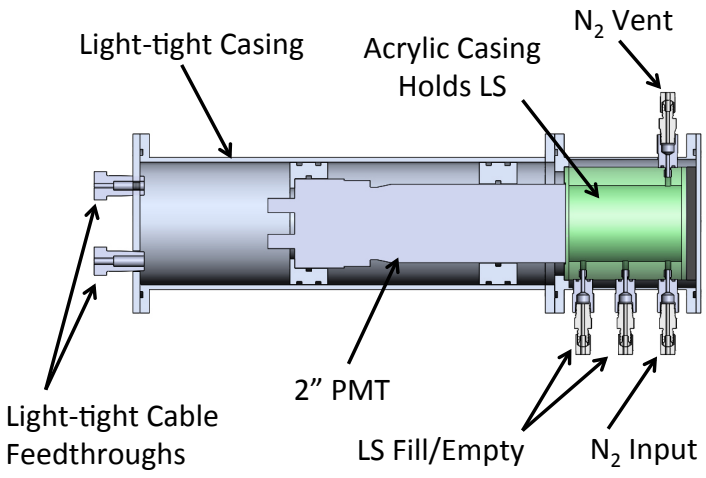

Figure 4.6: CAD model of the LS Sampler to be used in the GdLS filling system. LS will be pumped into the light-tight chamber and tested for its light yield with a radioactive source.

Each drum's volume of LS will be pumped using PTFE lines to a reservoir that sits atop the water tank. Nitrogen gas will then be bubbled through the LS to strip any oxygen that may have been dissolved in the liquid. This process should also remove some amount of dissolved ^{222}Rn and ^{85}Kr as well. A manifold of valves will then be used to direct liquid via gravity into the desired acrylic tank. The thin walls of the acrylic tanks demand that the LS and water filling happen simultaneously to minimize the stress on the acrylic. As the LS is less dense than water, the water level outside the acrylic should lag behind the LS level inside the tanks by no more than 20 inches.

4.3 Gd-Loaded Liquid Scintillator

As previously mentioned, the OD acrylic vessels will hold a total of 17.3 tonnes of GdLS to be produced at BNL. In this section I describe the key characteristics of GdLS as a detection medium for the OD.

4.3.1 Composition

The solvent for the OD LS is linear-alkylbenzene (LAB), which consists of a benzene ring with a long hydrocarbon chain attached, as shown Fig. 4.7. The aromatic benzene ring helps transfer deposited energy between LAB molecules until a transfer is made to the fluor, which emits scintillation light. LAB has a high flash point of 130 °C, making it combustible, not flammable [67]. This simplifies safety mitigations required in underground laboratories. The LAB is purchased from CEPSA [68] and is derived from

underground sources, to minimize ^{14}C content [69].

The fluor is PPO (2,5-diphenyloxazole), with a structure shown in Fig. 4.8a, and chemical formula $C_{15}H_{11}NO$. A waveshifter, bis-MSB (1,4-bis(2-methylstyryl)benzene), with the structure shown in Fig. 4.8b, absorbs the PPO scintillation and re-emits it a wavelength that is both less absorbed by the LS and is better matched to PMT response (see Sec. 4.3.2). The masses of the components used to make 1 liter of GdLS, as well as other data, are given in Tab. 4.2.

For neutron detection, Gd is dissolved into the LS through the chelating ligand TMHA (3,5,5-trimethylhexanoic acid) with the structure shown in Fig. 4.9 and chemical formula $C_9H_{18}O_2$. The usual oxidation state of Gd is 3, so three $TMHA^-$ ions bind with Gd, permitting $Gd(C_9H_{17}O_2)_3$ to dissolve in non-polar LAB.

Table 4.2: Chemical components in 1 L of GdLS.

Acronym	**Molecular Formula**	**Molecular Weight (g/mol)**	**Mass (g)**
LAB	$C_{17.14}H_{28.28}$	234.4	853.55
PPO	$C_{15}H_{11}NO$	221.3	3.00
bis-MSB	$C_{24}H_{22}$	310.4	0.015
TMHA	$C_9H_{17}O_2^-$	157.2	2.58
Gd	Gd	157.3	0.86
GdLS	$C_{17.072}H_{28.128}O_{0.0126}N_{0.0037}Gd_{0.0015}$	233.9	860.0

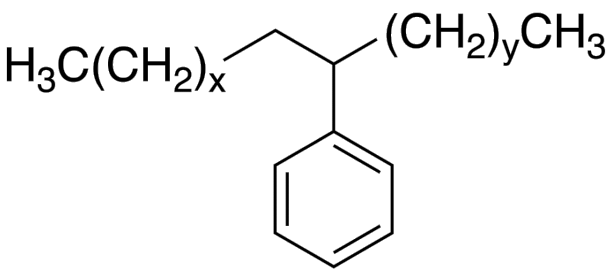

Figure 4.7: Linear-alkylbenzene (LAB) structure

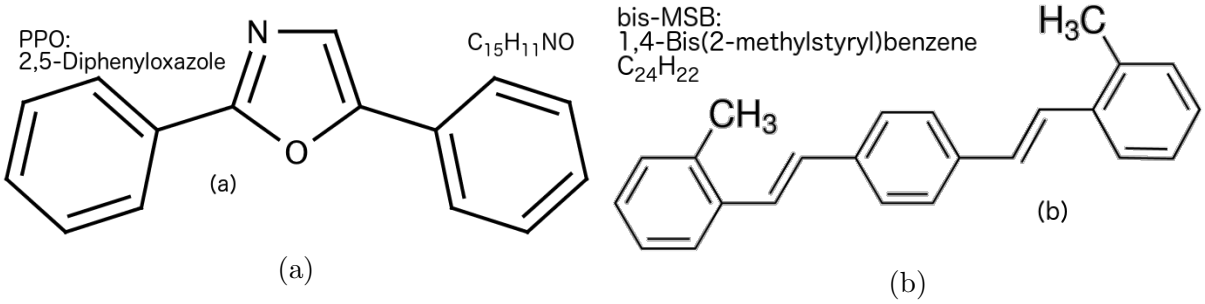

(a) (b)

Figure 4.8: Formulas for PPO and bis-MSB.

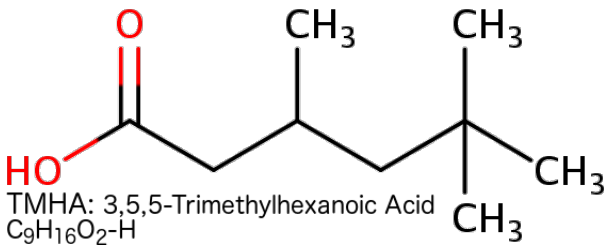

Figure 4.9: TMHA structure

All components of the GdLS are purified [70; 71] with the exception of the bis-MSB because of the extremely small quantity used in GdLS. The LAB solvent is purified by distillation, while the PPO is cleaned using recrystallization and water extraction. The Gd compound is purified by pH-controlled partial hydrolysis, during which Gd remains in solution while certain radioactive actinides such as uranium and thorium are precipitated out. Actinium itself, however, tends to remain in solution with Gd [71], resulting in an out-of-equilibrium level of ^{227}Ac.

4.3.2 Optical Properties

Energy deposited in the GdLS causes excitations of LAB molecules. These excitations are transferred to PPO [72] resulting in the emission of fluorescent light, primarily below $\lesssim$380 nm [73]. The PPO fluorescent light is absorbed and re-emitted at longer wavelength [74] by the bis-MSB according to the spectrum shown at the top of Fig. 4.11. The emission spectrum peaks in the 410 nm to 425 nm range [75], well matched to the photocathode response of typical PMTs.

The GdLS light yield in response to a 662 keV γ is 53 % of anthracene [70]. A similar electromagnetic energy deposited in anthracene needs (55 ± 5) eV per transmitted 452 nm photon [76; 77], resulting in $(10{,}000 \pm 1{,}000)$ photons/MeV in GdLS. The description of light yield for different specific energy depositions $\mathrm{d}E/\mathrm{d}x$ is often described by a generalized [78] Birk's Law [79]:

$$\frac{\mathrm{d}L}{\mathrm{d}x} = Y \frac{{}^{\mathrm{d}E}/_{\mathrm{d}x}}{1 + kB\left({}^{\mathrm{d}E}/_{\mathrm{d}x}\right) + C\left({}^{\mathrm{d}E}/_{\mathrm{d}x}\right)^2} \tag{4.1}$$

where Y is the light yield. kB and C are parameters that are determined separately for electron recoils in response to γ's (Compton scattered or photoabsorbed electrons), protons, and α's [80]. The light signals (total number of photons produced) resulting from energy loss of protons and α's is heavily quenched relative to that from electrons. This is shown in Fig. 4.10 which plots the reconstructed electron equivalent energy measured for energy deposits from α's (left) and protons (right) in LAB-based LS (no Gd). Fits to that data using a model as in Eq. 4.1 are also shown.

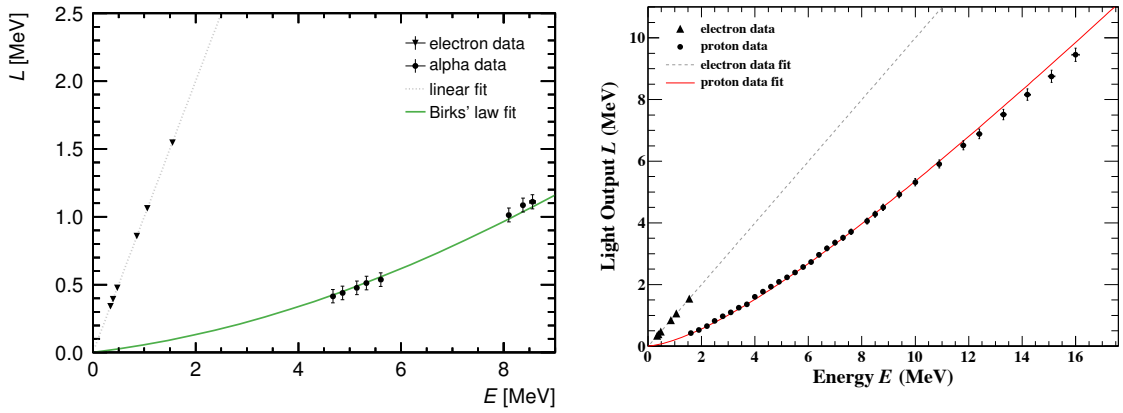

Figure 4.10: Electron equivalent energy deposits from incident α's (left) and protons (right) of various energies in LAB-based LS with the same PPO and bis-MSB concentrations as the LZ LS. Electron energy deposits are shown for comparison. From [81] and [82], respectively.

Optical photons traversing the GdLS may be absorbed by the liquid. The e-folding absorption length is shown at the bottom of Fig. 4.11. A long absorption length is desired for increased detection efficiency. The GdLS absorption length rises from $\approx$1 m at 410 nm to >10 m at 425 nm, resulting in little self-absorption of the emitted scintillation light.

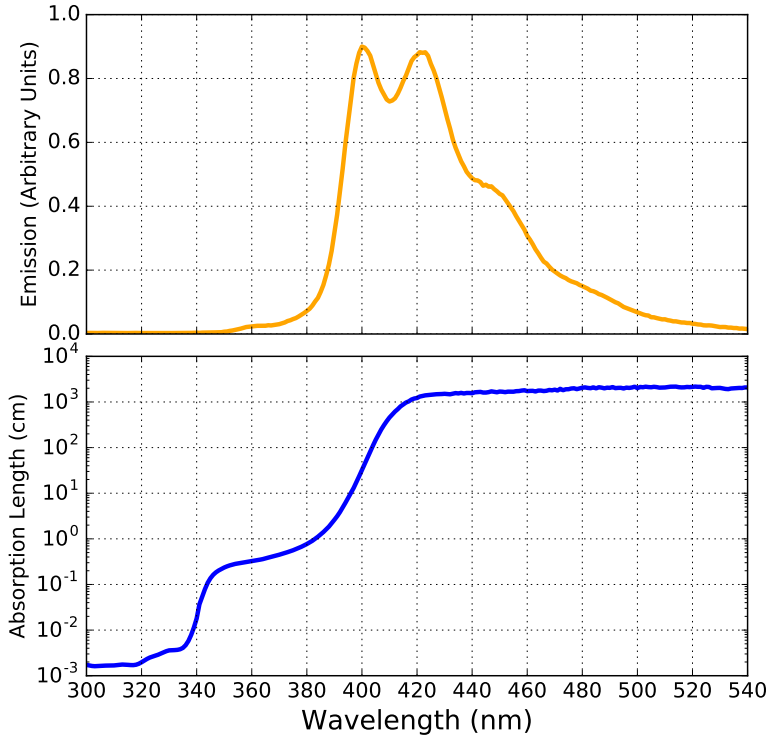

Figure 4.11: Wavelength dependence of key optical properties of the GdLS. *Top:* The emission spectrum of the GdLS scintillation light (in arbitrary units). *Bottom:* The absorption length of GdLS.

4.3.3 Neutron Detection with GdLS in the OD

The primary goal of the GdLS in the OD is the detection of ∼1 MeV neutrons born largely via (α,n) reactions and fission in the material surrounding the LXe TPC. Neutrons of this kinetic energy or higher can cause Xe recoils in the same energy window as those expected from a WIMP interaction. The interaction length of 1 MeV neutrons in LXe is about 11 cm, allowing a neutron from the perimeter to enter the LXe TPC, scatter once, exit, and then penetrate to the OD. The LZ requirement is to achieve an efficiency for the detection of neutrons which single-scatter in the LXe TPC of >95 % (or an inefficiency of <5 %).

In the LS, neutrons are rapidly moderated to near-thermal energies via elastic collisions with hydrogen. In general, for a target nucleus of mass A at rest, the ratio between the final neutron energy, E', and the initial neutron energy, E, (both measured in the lab frame) is given by

$$\frac{E'}{E} = \frac{A^2 + 1 + 2A\cos\theta}{(A+1)^2} \ , \tag{4.2}$$

where θ is the scattering angle in the center-of-mass frame. Thus a single, hard-sphere (independent of θ) elastic scatter results in a flat distribution of outgoing neutron energies from $E'_{max} = E$ down to

$$E'_{min} = E\left(\frac{A-1}{A+1}\right)^2 . \tag{4.3}$$

In elastic collisions with hydrogen (protons) we have $A = 1$, so neutrons lose on average half their energy in each scatter. The scattered protons have energy $E_R = E - E'$. The result will be a quenched scintillation signal representing the sum of signals from each scattered proton during the neutron moderation process. The proton recoil signal in the OD will be prompt, that is, close in time to a coincident signal from the neutron scattering in the TPC volume. For example, taking the neutron energy to be 1 MeV, the time to travel the 150 cm from the center of the TPC to the GdLS is ≈110 ns.

Once they reach approximately thermal energies (nominally, 0.0253 eV corresponding to an ambient temperature of 293.6 K), neutrons diffuse until captured by a nucleus. In pure LS, 99.4 % of neutrons will capture on ^{1}H, resulting in the emission of a 2.2 MeV γ-ray and a deuteron; Compton scattering and photoelectric absorption of the γ give rise to detectable scintillation signals. In GdLS, two neutron capture properties of Gd

are exploited: first, the thermal capture cross section of natural Gd is large due to the large cross sections of the two isotopes ^{155}Gd and ^{157}Gd. The addition of only 0.1 % Gd by mass therefore reduces the mean time to capture to ≈28 µs. By comparison, the mean time to capture in pure LS is ≈218 µs. Reduction of the time to capture ultimately reduces the rate of false neutron vetoes caused by accidental activity in the GdLS. Second, neutron capture on Gd is followed by a cascade of several γ's which release a total energy of ≈8 MeV. The probability of missing all of the several γ's in this cascade is substantially lower than missing the single 2.2 MeV γ from capture on hydrogen. This energy is distinctly larger than that from background radioactivity in or near the GdLS (namely, the 2.6 MeV γ from ^{208}Tl), making neutron induced signals somewhat background-free in this region. The unique pulse pair combination from proton recoils during neutron moderation and the γ cascade following neutron capture also allows for nearly background-free neutron identification. The neutron capture properties for the relevant nuclei in GdLS are given in Tab. 4.3.

4.4 The Outer Detector in LZ Simulations

Over the course of this PhD work, simulations of the OD have matured significantly. Furthermore, the results of these simulations have had a direct impact on the final design and dimensions of the acrylic vessels. Here I hope to provide a description of the implementation of the OD design as it currently exists in the GEANT4-based LZ simulation framework. A few results from older designs are also described, as they contributed

Table 4.3: Principal components of GdLS which capture neutrons. The neutron separation energy, $^{A+1}S_n$, listed is for the isotope with nucleon number A + 1. The isotope fractions f_I are normalized to that element's natural abundance. The number densities of each isotope, n_I, are computed from the information in Tab. 4.2. The capture cross section σ_c is given at the standard neutron thermal velocity of 2.2×10^3 m/s. The Westcott factor g_w allows correction for non-$1/v$ behavior in the capture cross section, convoluted with a Maxwellian velocity distribution, and is significant for the two Gd isotopes, resulting in an estimated overall mean distance to capture of 6.2 cm and a mean time to capture of 28.1 µs. The fractions captured, f_c, are normalized to those neutrons which capture in GdLS, and the sum of all captures on other isotopes are smaller than 0.01 %. The final column shows the fractions measured by the Daya Bay (DB) collaboration [83].

^{A}Z	$^{A+1}S_n$ [84]	f_I(%)	n_I(cm^{-3})	σ_c(b) [85; 86]	g_w [87; 86]	f_c(%)	f_c^{DB}(%)
^{157}Gd	7.94 MeV	15.7	5.15×10^{17}	2.52×10^5	0.89	71.5	68.5
^{155}Gd	8.54 MeV	14.8	4.87×10^{17}	6.02×10^4	0.86	15.6	15.5
^{1}H	2.22 MeV	100	6.23×10^{22}	0.333	1.00	12.9	16
^{12}C	4.95 MeV	98.9	3.74×10^{22}	3.5×10^{-3}	1.00	0.084	-

to our understanding of the OD performance.

4.4.1 Geometry

The geometry of the OD acrylic vessels is one of the most complex in all of the LZ simulation framework. This is mostly due to the various penetrations in the tank design for services to the TPC and for calibrations. When this work was started, none of these penetrations were present in the simulation geometry. The current model, on the other hand, is extremely accurate and fully reflects the final design sent off to the manufacturer. Fig. 4.12 shows this progression of the OD geometry from left to right.

A visualization of the current simulation geometry is shown on the right side of Fig. 4.12. The low-density displacement foam fills the 2" gap between the acrylic and OCV straight wall. The OCV is also wrapped in a diffuse reflector (more on its properties later). The active part of the water tank is defined by the diffuse reflector curtain shown

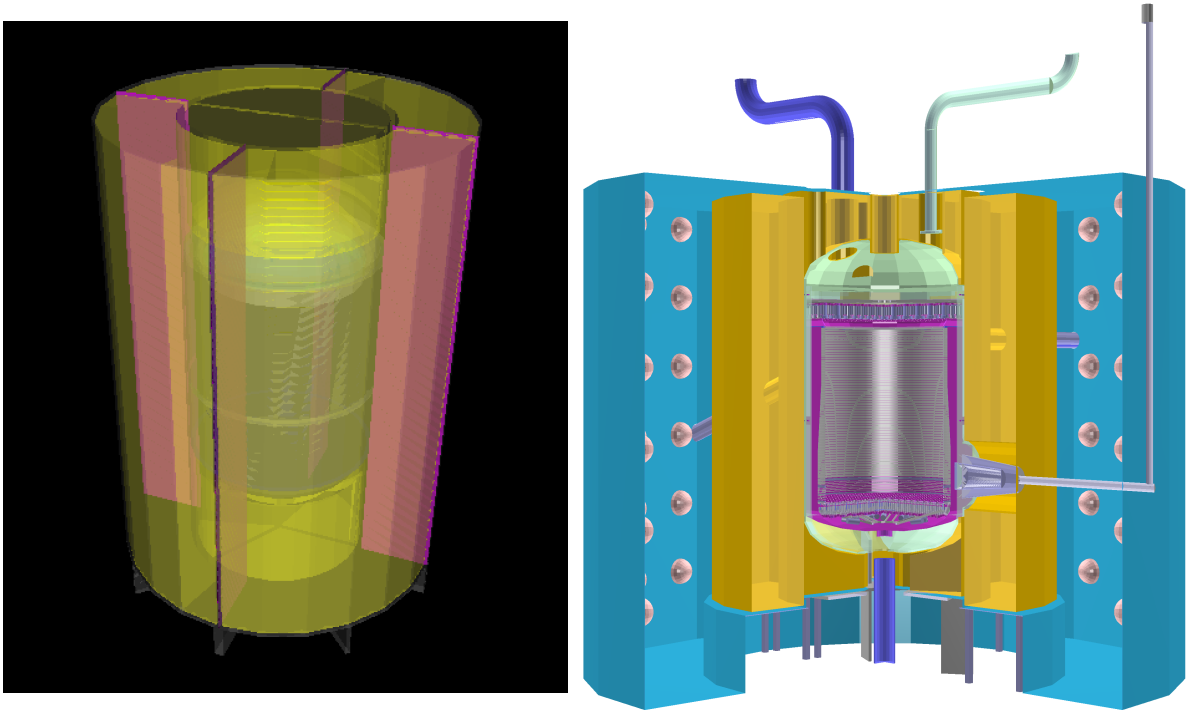

Figure 4.12: A comparison of the OD geometry implemented in the simulation at the beginning of this PhD (left) and the current model (right) which reflects the final design.

in blue. Inside the curtain are the 120 8" PMTs modeled simply as hemispheres with a quartz window containing an active photocathode with the correct area.

4.4.2 Optical Simulations

The principle optical properties of the OD components are implemented in the simulation. Ultimately, these properties determine the number of detected photoelectrons in the PMTs for a given energy deposit (phe/MeV). This number will generally depend on the location of the energy deposit within the GdLS volume.

Starting in the GdLS, the number of scintillation photons born with the spectrum shown at the top of Fig. 4.11 is determined through an implementation of Eq. 4.1 with

$Y = 9000$ photons/MeV and with kB and C values equal to those found in Sec. 6.3.2. The photons are subject to absorption in the GdLS, as previously discussed, with an absorption length that depends on photon energy according to the bottom plot of Fig. 4.11. Photons absorbed by the GdLS have a nonzero probability that they will be reemitted (again, according to the GdLS emission spectrum) and that probability depends on the absorbed photon energy. This property of the GdLS has also been implemented in the OD optical model after simulations for the studies in Chap. 6 validated its importance. See Sec. 6.3.1 for more details.

Photons may also be absorbed in the acrylic. The absorption length in acrylic assumed in our simulations is that reported in Ref. [88], where acrylic from RPT was also used. In order for photons to reach the PMT photocathodes they must cross several boundaries: GdLS-acrylic, acrylic-water, and water-quartz. The wavelength-dependent indices of refraction for these materials is also used in the simulation to calculate the required transmission and reflection probabilities at each interface.

The Tyvek covering the OCV and surrounding the PMT ladders is assumed to have the diffuse reflectivity of the blue curve shown in Fig. 4.13. In general, the reflectivity of the Tyvek is a function of its thickness, as shown in the figure. The 262 µm-thick 1085D Tyvek planned for use in the OD has been verified as having a higher reflectivity than that of the blue curve by studies done in Chaps. 5 and 6. Our OD light collection is likely somewhat conservative in this regard.

Early studies of the reflector configuration in the OD considered the use of a spec-

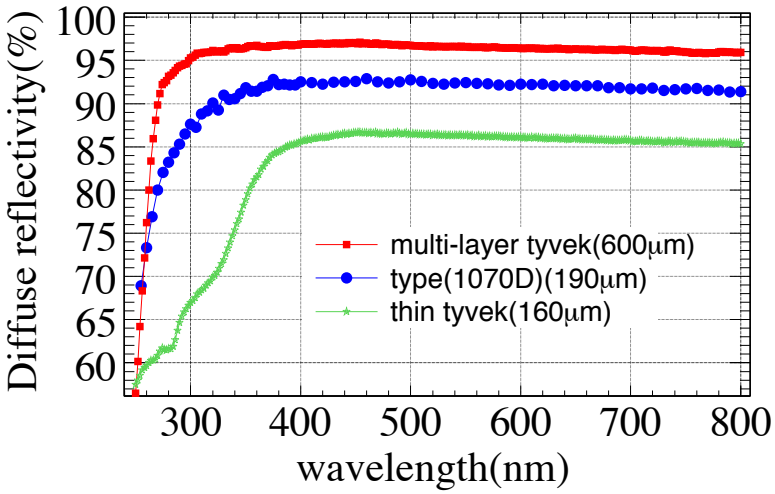

Figure 4.13: Diffuse reflectivity for various forms of Tyvek reflector. The LZ Tyvek is 262 µm-thick 1085D type. The blue curve is currently used for OD simulations.

ular (mirror-like) reflector. No significant improvement in overall light collection was found and so the diffuse Tyvek reflector was chosen (Tyvek is also easy to work with mechanically compared to the specular reflector that we considered). The possibility of deploying Tyvek sheets in between the four joints of the side tanks was also considered. Some improvement was observed in the localization of the collected light pattern in the PMTs, but the overall light collection was actually lower (due to the presence of more imperfect reflecting surfaces), so this configuration was not adopted in the OD.

Photoelectrons are generated in the PMT photocathodes according to the wavelength-dependent quantum efficiency shown in Fig. 4.14. This dependence is a 3rd-order polynomial fit to the quantum efficiency data provided by Hamamatsu.

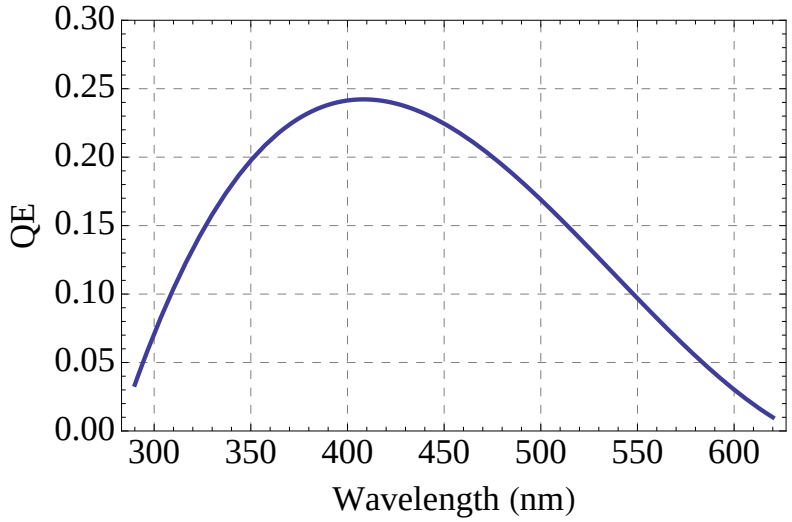

Figure 4.14: Assumed quantum efficiency of the OD PMTs in simulation.

Light Collection and Uniformity

Simulations are performed to calculate the light collection efficiency (LCE), defined as the fraction of initial photons simulated that end up in a PMT photocathode. The LCE in the current OD simulation is ≈7 % averaged over the entire GdLS volume. Crudely, this implies a photoelectron yield of: (9000 photons/MeV) × (7% LCE) × (0.25 QE) ≈ 158 phe/MeV. The LZ requirement is for > 80 phe/MeV.

A good cross-check of the optical response in the OD is to simulate a low-energy physics signal. In the GdLS we expect ≈28 Hz of rate to be uniformly distributed from ^{152}Gd, which is naturally present due to the Gd-loading of the LS and decays by emission of a 2.2 MeV α. The high stopping power of α's in the liquid results in a very localized energy deposit that produces a quenched light signal similar to that of a ≈100 keV electron. The resulting peak at low pulse areas provides a good measure of the light collection near the planned analysis threshold.

An optical simulation of 100k ^{152}Gd α decays uniformly distributed in the GdLS volume was performed. In Fig. 4.15 the average number of collected photoelectrons from these decays is plotted spatially (averaged over azimuth) so that the variations in light collection are visible. As expected, more light is collected for events in the large side tanks while the bottom and top tanks have poorer light collection due to their distance from the PMTs and the penetrations through these tanks. On the right of Fig. 4.16 the z dependence of the collected pulse area is shown. Along the height of the side tanks, the reconstructed ^{152}Gd peak mean is very stable. The poorer light collection of the top an bottom tanks causes a downward shift of the mean of about $\approx$12 % at the highest and lowest z positions. The left side of Fig. 4.16 shows the pulse area distribution collected for all events across the entire GdLS volume. Over 99 % of these events result in pulse areas larger than the expected coincidence requirement in the DAQ to generate a trigger (we might expect something of order 5-fold coincidence). These events therefore provide a reliable calibration source for the OD during the lifetime of the experiment.

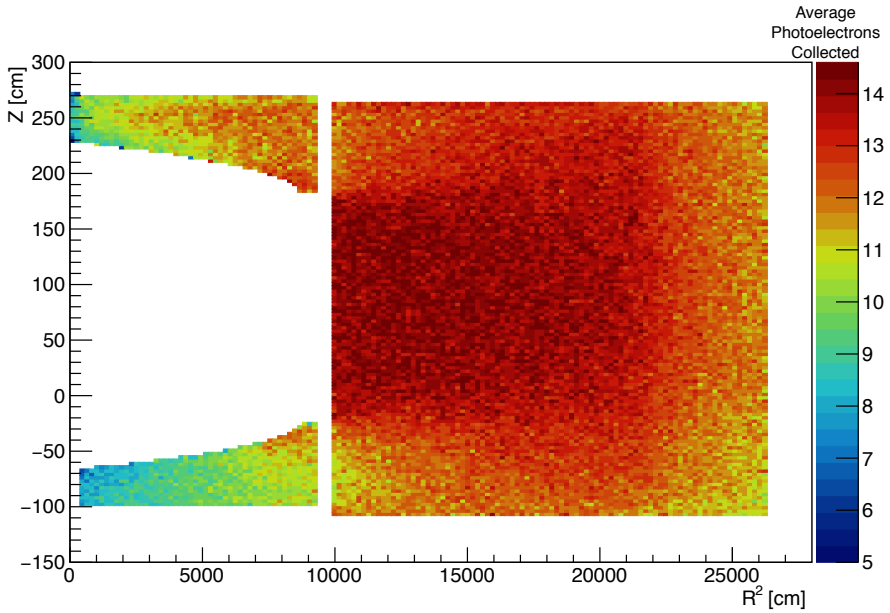

Figure 4.15: Spatial variation in the average number of collected photoelectrons for α decays of ^{152}Gd uniformly distributed in the GdLS volume. Plot by S. Shaw.

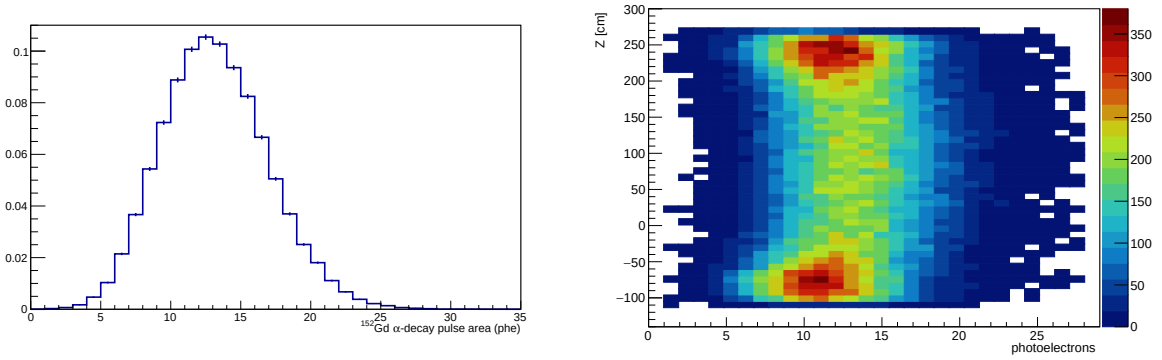

Figure 4.16: *Left:* Distribution of collected photoelectrons from uniform ^{152}Gd decays. *Right:* z-dependence of the collected pulse area. Plots by S. Shaw.

4.4.3 Neutron Inefficiency

Perhaps the most important goal of simulations with the OD is to assess its performance in regard to its primary role within LZ: tagging WIMP-like neutron events. In LZ, the convention has been adopted to express this performance using the "veto inefficiency" or

just "inefficiency", for short. The inefficiency is defined as the number of events which survive all analysis cuts to become a background in LZ, divided by the number of events which undergo a SS in the LXe falling into the WIMP ROI:

$$\text{Inefficiency} = \frac{\text{\# events SS in WIMP ROI passing XS and OD cuts}}{\text{\# events SS in WIMP ROI}} \tag{4.4}$$

Intuitively, this definition makes sense: it is the ratio of "unvetoed" events to those that we wish could be vetoed. The inefficiency will sometimes also include the FV cut in the numerator and denominator. The inefficiency is a function of the XS and OD energy thresholds and coincidence window lengths. It is also a function of the SS position in the LXe TPC as certain positions require more or less path length through active LXe from the background source or are close to a region of the OD/XS containing inactive material.

Influence of Acrylic Thickness

We are particularly interested in the neutron inefficiency and how this quantity is influenced by the OD design. Ultimately, the final inefficiency is calculated using "full" neutron simulations of the type described in the previous chapter: neutrons begin in an LZ component (PMTs, PTFE, etc) and are followed until they are captured. However, the survival probability to pass all the cuts required in the both the numerator and denominator of the inefficiency is small, requiring many primary events to be run.

In order to quickly study how design choices for the OD impact the veto inefficiency, an event generator for simulating "background neutrons" was created. Neutrons from

this generator begin with their positions biased according to the distribution of SS events in the LXe from the TPC PMT, PTFE walls, and cryostat vessel sources. Neutrons are emitted isotropically with an energy spectrum characteristic of those from (α, n) in these components. Fig. 4.17 shows the initial positions and energy spectra of the neutrons.

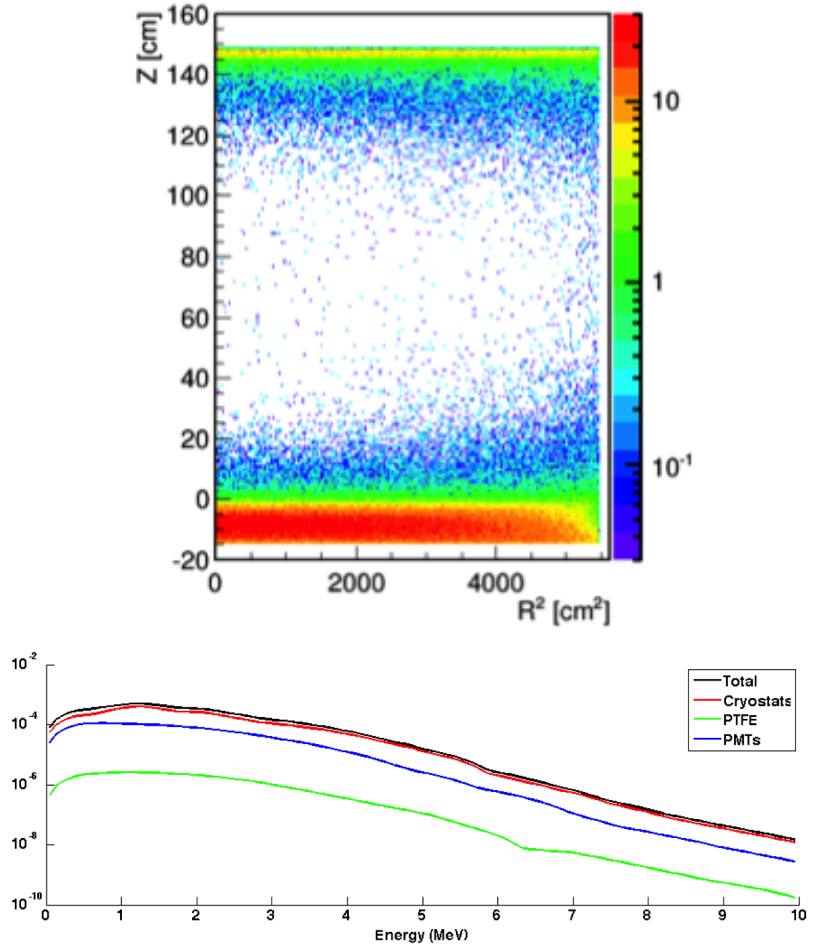

Figure 4.17: *Left:* Example of primary position distribution of neutrons used in the generator for inefficiency studies. *Right:* Energy spectra of the generated neutrons. Plots by S. Shaw.

In analysis of these simulations, we are pretending as though these neutrons have already undergone their low-energy SS in the LXe and are on their path outward. The sample of these primary neutrons used in the denominator of the inefficiency are those

that give no energy deposit in the LXe volume. The numerator is then computed from this sample by applying the cuts in the XS and OD.

Changes in the computed inefficiency were used to track the OD performance in a number of studies. I wish to highlight one study in particular, the results from which illustrate the importance of minimizing the amount of acrylic in the OD system. This is summarized in Tab. 4.4 where the fraction of unvetoed event neutron captures occurring in each LZ volume is shown. On the left side of Fig. 4.18, the spatial locations of nonzero energy deposits from those unvetoed events are shown. From both the table and the figure, it is obvious that the inner curved walls of the top and bottom acrylic tanks capture and absorb neutrons and energy in unvetoed events. The solution was to thin these walls, minimizing the amount of dead material between the LXe and the GdLS volume. The curved walls are permitted to be thinned from 1" to 1/2" as they are less prone to stress due to curvature. The rightmost column of Tab. 4.4 and right side of Fig. 4.18 show the improvement in the number of neutrons captured in acrylic and the amount of unvetoed energy deposited there. The fraction of unvetoed neutrons that capture in OD-related components is reduced to less than that in non-OD components. Overall, the inefficiency is halved by this modification, as shown in Fig. 4.19.

Impact of Coincidence Window Length

The aforementioned study demonstrates the impact of the acrylic tanks on the OD neutron veto performance. This is especially true in regard to the dependence of the neutron veto inefficiency on the choice of coincidence window, shown in Fig. 4.20. Here, the co-

Table 4.4: Fraction of unvetoed neutrons captured in the given LZ components with 1" and 1/2" thick top and bottom tank curved walls.

Component	**Fraction of Unvetoed n-Captures (%)**	
	1" Walls	**1/2" Walls**
Acrylic Tanks	52.4	26.8
Outer Cryostat	20.2	26.8
Inner Cryostat	8.6	12.1
GdLS	8.3	15.8
LZ Conduits	2.3	6.3
Displacer & Tyvek	0.8	2.2
Water	4.4	5.8
Other	3	4.2
Total OD	61.5	44.8
Total non-OD	38.5	55.2

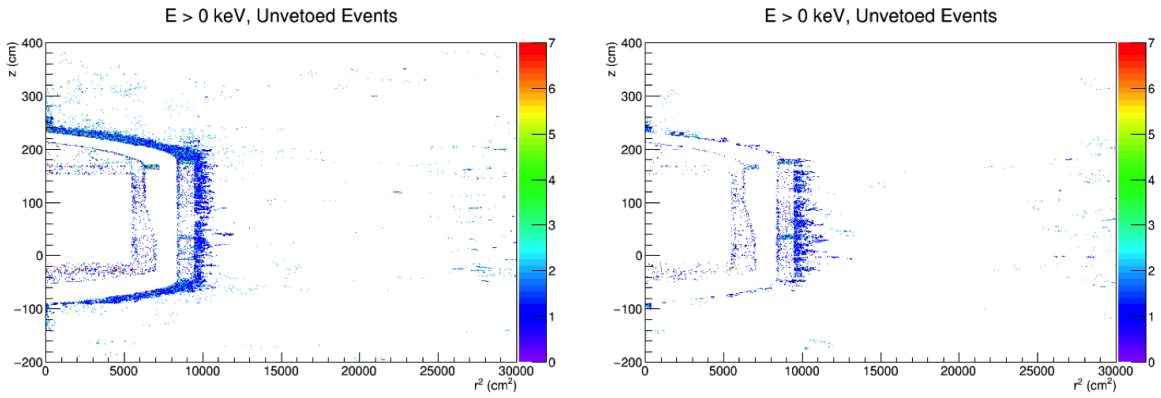

Figure 4.18: Position of nonzero energy deposited in unvetoed neutron events with 1"-thick (left) and 1/2"-thick (right) top and bottom tank curved acrylic walls. By thinning the walls, the inefficiency was roughly halved. The cryostats and other TPC components are also visible.

incidence window is defined as the time between the S1 pulse in the TPC and the first electron energy deposit in the OD.

Studies in Ref. [38] show that neutrons may thermalize and find their way into the acrylic walls of the OD resulting in a mean time to capture characteristic of that on hydrogen (≈220 µs) rather than that in GdLS (≈30 µs). The result is an exponential-like dependence on veto window that decays slower than expected of a purely GdLS-based system. To accomodate this class of neutron events, a coincidence window of 500 µs is

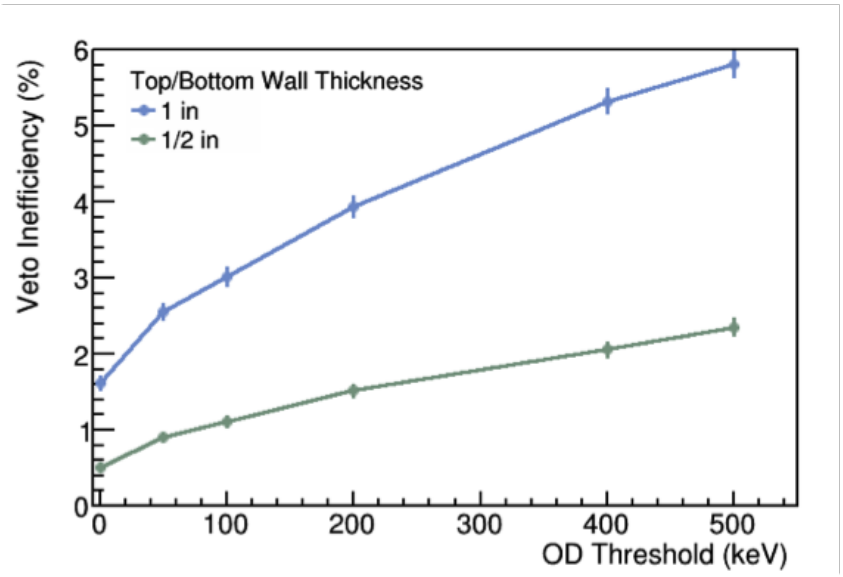

Figure 4.19: Veto inefficiency as a function of OD energy threshold before and after thinning the top and bottom tank curved walls calculated using the neutron generator described in the text.

used in LZ analysis. This number directly impacts the requirement on the background rate in the OD. A high rate of external backgrounds in the OD will result in a large number of falsely vetoed events. As shown in Fig. 4.20, the neutron inefficiency assuming a 500 µs coincidence window and a 200 keV energy threshold in the OD is 3.5%. Use of a lower energy threshold enables the use of a shorter coincidence window.

4.4.4 Gd Neutron Capture with DICEBOX

In pure LS, neutrons capture on the nuclei of hydrogen atoms, i.e. protons, with subsequent emission of a single 2.22 MeV γ associated with the formation of ^{2}H. When a neutron captures on Gd, the deexcitation process is more complex; there are $\sim 10^6$ levels between the excited and the ground state for the final Gd isotopes. Energy is released

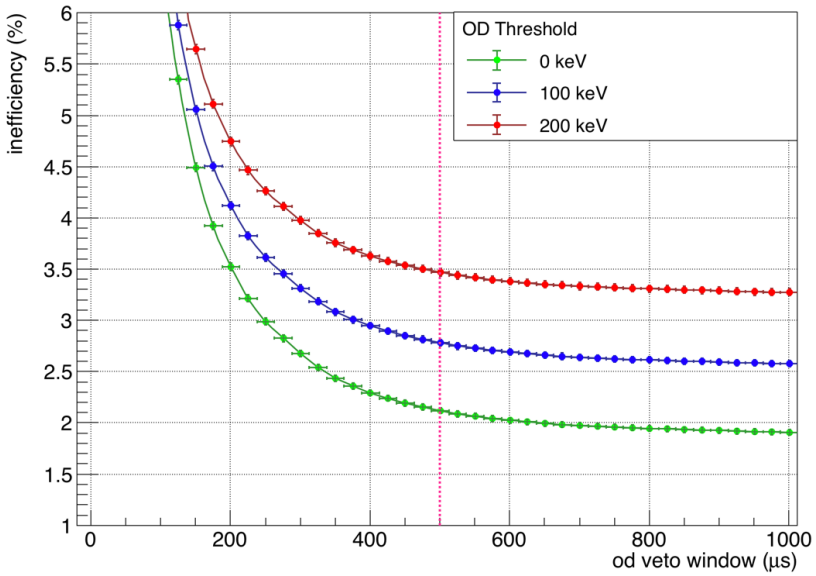

Figure 4.20: Neutron veto inefficiency as a function of the coincidence window length using full LZ neutron simulations with the final OD design. Plot by S. Shaw.

in a deexcitation cascade of γ-rays, internal conversion electrons (ICE), and x-rays. The modeling of Gd deexcitation cascades is complicated, and outside the standard particle physics toolkit.

For total absorption GdLS calorimeters, such as Daya Bay [89] or RENO [90], the details of the cascade are unimportant, because the entire de-excitation energy is usually deposited in the calorimeter. The LZ OD is much thinner than the Daya Bay or RENO calorimeters. Many of the γ-rays in the Gd deexcitation cascade thus escape the LZ OD. Correctly modeling this effect is crucial for a thorough understanding of the OD response to neutrons. This can be seen directly in Fig. 4.21 which shows the simulated pulse area distribution in the OD PMTs with an AmLi neutron source deployed in an LZ calibration tube. The peak from the 2.22 MeV γ from capture on hydrogen is clearly

visible while the multiple γ cascade released from capture on Gd forms a continuum out to the maximum possible energy deposit of 8.54 MeV when all Gd capture γ's are collected. By contrast, in the larger GdLS detectors like Daya Bay and RENO, capture on Gd results in a clear peak with a minimal amount of continuum from escaping γ's.

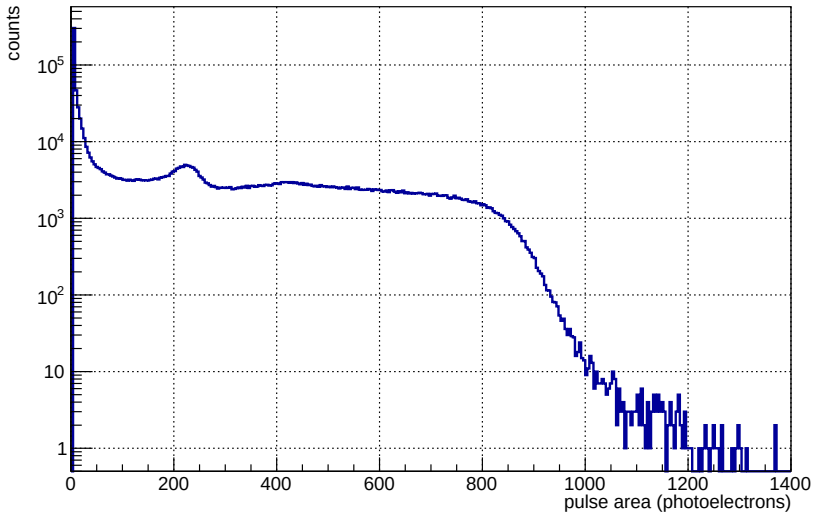

Figure 4.21: Simulated pulse area distribution for AmLi neutron events in the OD. Plot by S. Shaw.

DICEBOX

The DICEBOX [91] description of the γ-cascade after neutron capture on ^{155}Gd and ^{157}Gd has been implemented in the LZ simulation framework to address the shortcomings of the default GEANT4 "Final State" (FS) model. This work was performed by M. Solmaz and so I only highlight the important results here.

The most noticeable improvement of DICEBOX is that energy is conserved: the sum of γ and internal conversion electron (ICE) energies equals the neutron separation

energy, ${}^{A+1}S_n$, for the isotope formed after capture. The comparisons between GEANT4 and DICEBOX are shown for ^{157}Gd and ^{155}Gd in Fig. 4.22. It is ^{157}Gd which dominates the neutron-capture response of $^{\text{nat}}$Gd, as indicated in Tab. 4.3. For both Gd isotopes, the default GEANT4 simulation conserves energy in about 20 % of neutron captures.

The adaptation of the DICEBOX simulation in GEANT4 leads to more γ-rays, ICE, and x-rays emitted per neutron capture event than GEANT4 alone. This can be seen, for example, in Fig. 4.23 where the multiplity of γ's emitted after neutron capture on ^{155}Gd and ^{157}Gd for the FS model and the DICEBOX model are shown. This results in the prediction of a lower inefficiency for neutron detection than does GEANT4, by approximately 1.1 % (absolute). The inefficiency evaluated with DICEBOX (for the final OD tank design) is 3.8 %, while the inefficiency evaluated with GEANT4 for the same configuration is 4.9 %. These numbers are slightly different than those of the previous section because they use a slightly different set of LZ background components. The results of the previous section *do* make use of DICEBOX. The inefficiency as a function of OD threshold is shown for both capture models in Fig. 4.24.

4.5 Outer Detector Backgrounds

In the OD, a "background" is a source of event rate which is not the neutrons or γ's that have single scattered in the TPC which we wish to tag for removal in the WIMP search. The requirement for a false veto rate of <5 % with a 500 µs coincidence window immediately implies that the rate of single background events in the OD above a given

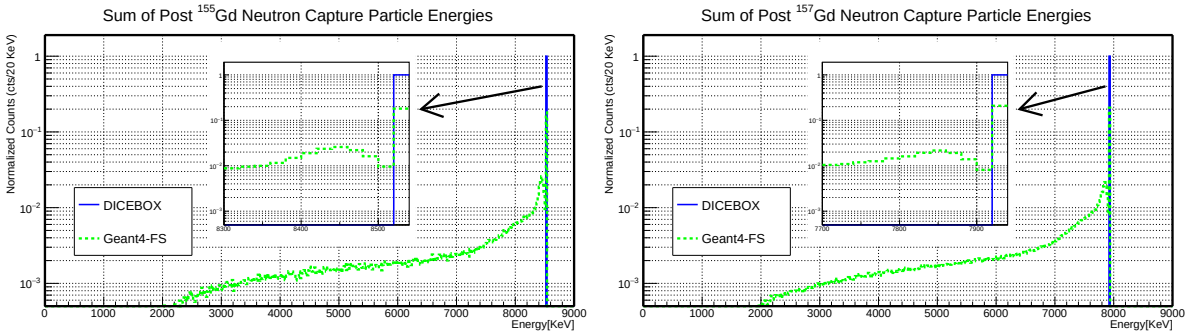

Figure 4.22: *Left:* Energy sum for all particles following ^{155}Gd neutron captures. The solid blue box at the neutron separation energy for ^{156}Gd of $^{156}S_n$=8.54 MeV is from DICEBOX and the dashed green line is the distribution from the default GEANT4 FS model. *Right:* Energy sum for all particles following ^{157}Gd neutron captures. The solid blue box at the neutron separation energy for ^{158}Gd of $^{158}S_n$=7.94 MeV is from DICEBOX and dashed green line is the distribution from the default GEANT4 FS model. Plots by M. Solmaz.

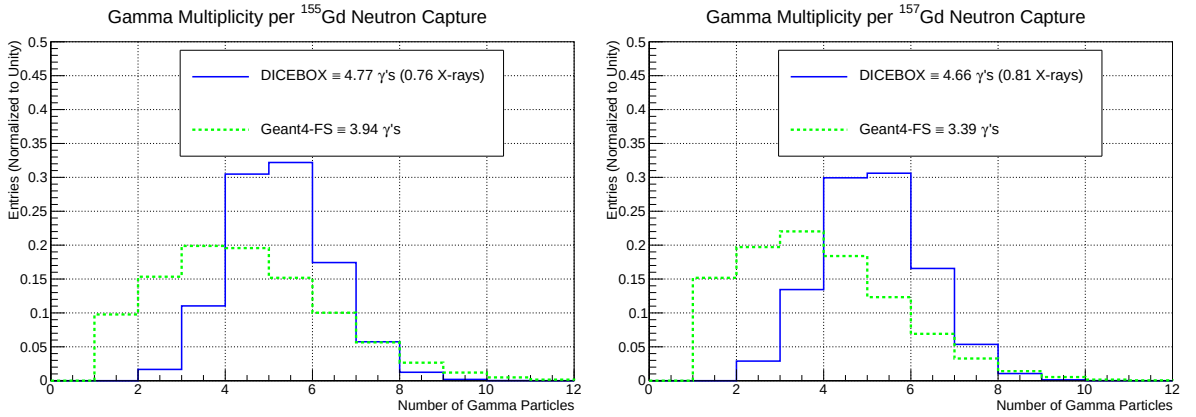

Figure 4.23: Gamma multiplicity for ^{155}Gd (left) and ^{157}Gd (right) neutron captures. The solid blue is the distribution from DICEBOX and the dashed green line is that from the default GEANT4 FS model. Plots by M. Solmaz.

threshold should be <100 Hz. As previously mentioned, the requirement for a <5 % false veto probability carries with it an assumed analysis threshold of 200 keV. However, the goal for the OD is to be able to use a 100 keV threshold for this purpose. Which threshold actually gets used is ultimately determined by the measured rate of backgrounds in the final experiment.

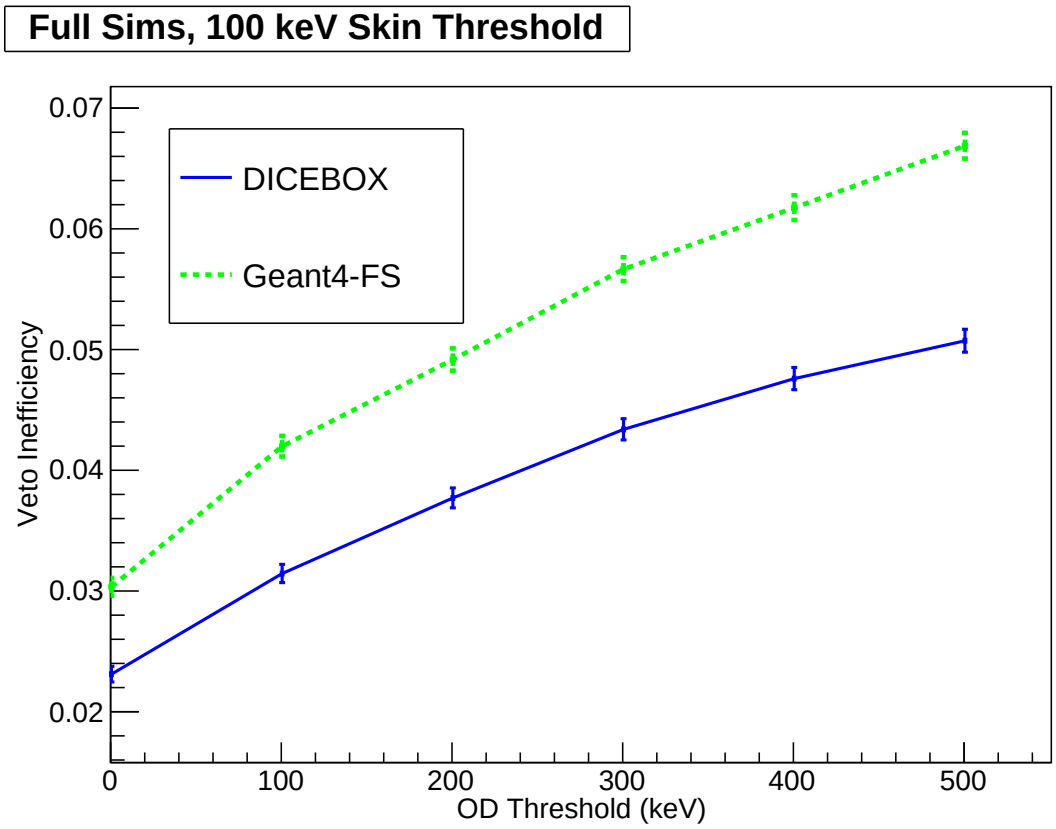

Figure 4.24: The LZ neutron inefficiency versus OD energy threshold. The solid blue line shows the result from DICEBOX simulations for Gd neutron capture, and the dashed green line shows the result using the default GEANT4 FS neutron capture model. The baseline threshold for the OD is 200 keV and the goal is 100 keV. Plot by M. Solmaz.

The primary sources of rate in the OD are identified as: radioactivity from the detector components of the LZ experiment, γ-rays from radioactivity in the Davis Cavern rock walls, and radioimpurities in the GdLS detection medium. Other sources of background must be considered as well, such as contamination of the GdLS and acrylic surfaces with dust and radon daughters. In addition to keeping the overall background rate in the OD to a minimum, we wish to simultaneously keep the ratio of rates from non-OD related components to OD-related components high. This amounts to using the OD as

an auxiliary detector for characterizing the radiation environment of the LZ experiment as a whole.

4.5.1 LZ Detector Components

The trace radioimpurities in LZ detector components result in a count rate in the OD. The same simulations used to calculate the expected WIMP search backgrounds in the TPC are also used to calculate the expected rate in the OD. The major component rates are given in Tab. 4.5, which predicts a total rate of 11.9 Hz above a threshold of 200 keV.

Table 4.5: Predicted rate in the OD from various LZ components.

System	Component	OD Rate > 200 keV (Hz)
TPC PMTs	3" PMTs & Bases	0.42
	Skin PMTs & Bases	0.12
	PMT Supports	0.16
	PMT Cabling	0.14
	Total	0.85
TPC Parts	PTFE Walls	0.0
	Grid Holders & Wires	0.23
	Field Rings	0.03
	Sensors	0.03
	Conduits, Cabling & Tubing	0.22
	Total	0.52
Cryostat	Vessels	1.43
	Seals	0.63
	Insulation	0.45
	Total	2.51
Outer Detector	Acrylic & Supports	5.42
	OD PMTs	2.48
	PMT Supports	0.09
	Total	7.99
Grand Total		**11.9**

4.5.2 Davis Cavern γ's

Simulations of the ^{238}U, ^{232}Th, and ^{40}K in the rock walls of the Davis Cavern were performed to provide an estimate of the background rate from this source in the central TPC. High energy γ's from this source can penetrate the water and LS to make a background in searches for $0\nu\beta\beta$ decay.

The simulations rely on a GEANT4 model of the cavern which surrounds the water tank and the inverted steel pyramid beneath it with a shell of rock of thickness 30 cm. The geometry of the model and a schematic of the simulation technique are shown in Fig. 4.25. The simulations are performed in stages in order to obtain a statistically useful number of events which survive through the thick shielding of the water and LS. First, the decays of ^{238}U, ^{232}Th, and ^{40}K and their progeny are simulated in the rock volume. The resulting γ's which reach the first "saving surface" are terminated on the surface while their location, direction, and energy are written to the output. In the next stage, each saved γ is generated 100$\times$ using the recorded information. The simulation stages then repeat, with the generated γ's being saved on a further inward surface and receiving a statistical boost at each stage. In the final iteration, the surviving number of events is normalized to a livetime which accounts for the boost factor at each stage and uses an assumed specific activity for the ^{238}U, ^{232}Th, and ^{40}K content of the rock.

The second stage output of these sims are used to assess the rate in the OD from γ's which penetrate the water. Initial simulations predicted the OD rate above 200 keV from this source to be $\approx$92 Hz, with most of this rate happening in the top and bottom of the

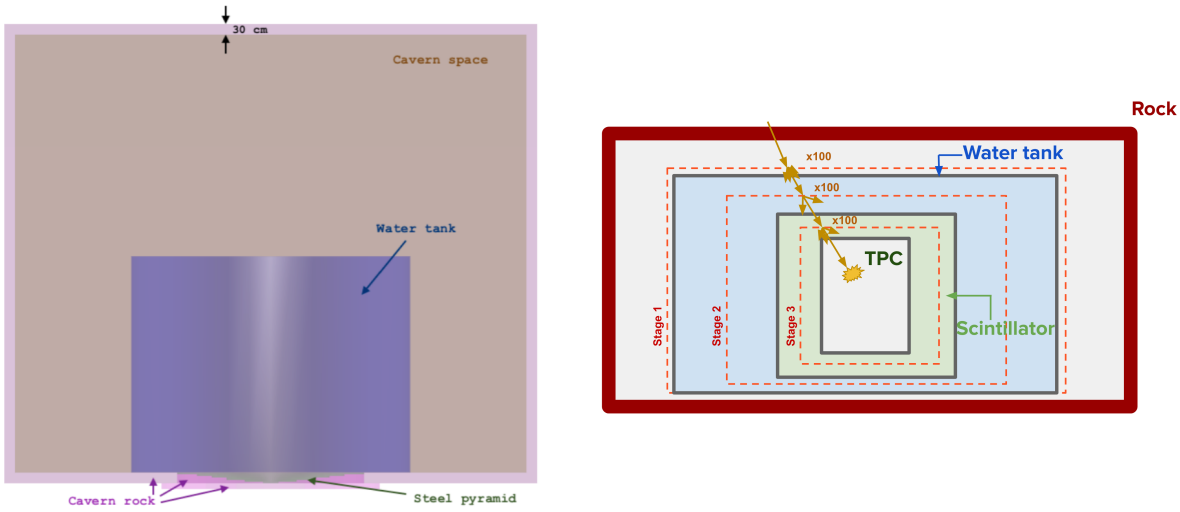

Figure 4.25: *Left:* Model of cavern rock implemented in GEANT4 for rock radioactivity simulations. *Right:* Schematic of the event biasing technique used to perform rock radioactivity simulations described in text. From [92] and [93], respectively.

OD tanks where the amount of water shielding is smallest. This unacceptably high rate had two outcomes:

1. The height of the OD was reduced in order to increase the amount of water shielding. This was also motivated by simulations that demonstrated a weak dependence of veto inefficiency with GdLS thickness, especially at the top and bottom of the OCV.

2. The assumed activity of the rock was called into question. The values used for the initial simulations were based on a rough estimate from HPGe data and known to overestimate the rock activity by a factor of 2–5.

Data was taken as a part of this thesis which demonstrated the rock activity assumed in these simulations was indeed too high (see Sec. 6.4). Motivated by that result, a dedicated campaign was undertaken to more thoroughly characterize the cavern γ envi-

ronment. A 5"×5" sodium iodide (NaI) detector was used to take energy spectra in a variety of locations and lead-shielding configurations in and near the underground water tank. The energy spectra measured were then compared to simulations of the detector in the cavern, resulting in a new measurement of the ^{238}U, ^{232}Th, and ^{40}K content of the rock. That work is thoroughly described in Ref. [94], while Tab. 4.6 compares the old activities to the newly measured activities.

Table 4.6: Old and newly measured specific activities of the Davis Cavern rock.

Isotope	**Old (Bq/kg)**	**Measured (Bq/kg) [94]**
^{238}U	73.4	50 ± 6
^{232}Th	26.1	13 ± 1
^{40}K	716	240 ± 70

Finally, a 2.7 m square plate of steel with thickness 7.6 cm was incorporated into the LZ design to sit directly above the center port of the water tank. This plate is also used as a work platform for OCV assembly on top of the water tank. Its benefit as a radiation shield for the top of the OD was identified and so it will sit in place during the lifetime of the experiment.

Fig. 4.26 shows the spatial distribution (summed along azimuth) of energy deposits from the cavern rock γ's in the OD. With the newly measured rock activities, the shortened OD height, and the steel plate shield the predicted rate in the OD from these γ's above 200 keV is 35 ± 3 Hz.

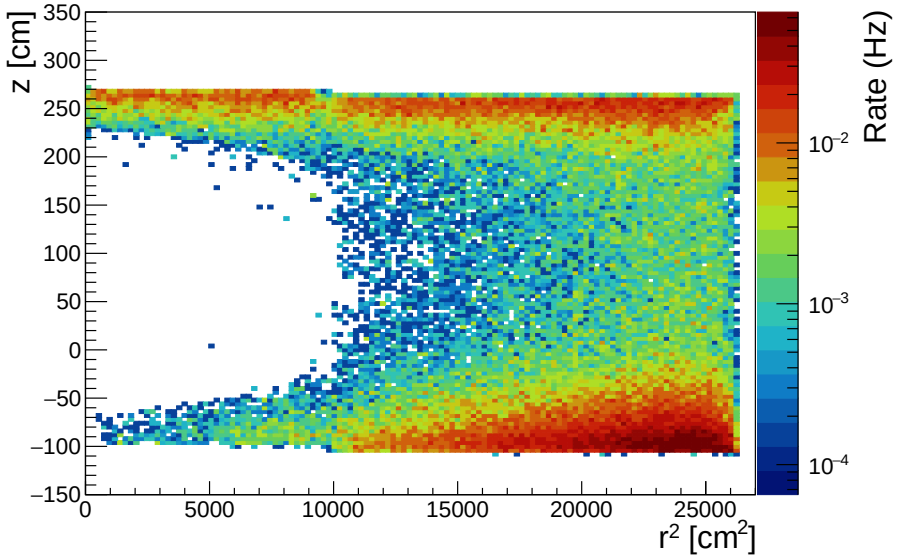

Figure 4.26: Spatial distribution of energy deposits in the OD from γ-rays that are born in the Davis Cavern rock walls. Plot by S. Shaw.

4.5.3 Radioimpurities in the GdLS

The radioimpurities dissolved directly in the GdLS represent the most dangerous background to the OD rate. This is because decays from internal contaminants are not subject to branching ratios that would otherwise reduce the ratio of detectable decays to the number of true decays (i.e. the ratio of the rate [Hz] in a detector to the true number of decays per second [Bq] of an isotope). In the case of contamination from the ^{238}U, ^{235}U, and ^{232}Th decay chains, this ratio is roughly a factor of ten, as the stated number of decays per second refers only to a single isotope's activity at the head of the chain. Quantifying the radioimpurities in the GdLS for LZ is the central study of this thesis. The primary results are given in the final chapter, but are stated here as well for the sake of completeness. Here I primarily wish to provide an introduction which motivates and

provides context for this study.

Overview

The LS used in large-mass experiments devoted to the detection of ν's is one of the most radiopure materials known [95; 96] and would easily satisfy the radiopurity requirements for LZ. The purpose of the LS detector in LZ is, however, to detect neutrons, so the requirements are similar to those for the detectors in $\overline{\nu}_{\mathrm{e}}$ experiments, which are sensitive to the process $\overline{\nu}_{\mathrm{e}} + \mathrm{p} \rightarrow \mathrm{e}^{+} + \mathrm{n}$. The addition of Gd to LS enhances the efficiency for neutron detection [97] and has been used successfully in several $\overline{\nu}_{\mathrm{e}}$ experiments [98; 83; 99; 100]. However, since these experiments benefit from the high flux of $\overline{\nu}_{\mathrm{e}}$ from nuclear reactors and have higher energy thresholds, the radiopurity of the GdLS was not a great concern. Other studies [101; 102] have found that isotopes from the ^{235}U chain can be present at a level far out of proportion to the usual relative abundance of ^{235}U to ^{238}U. That result had not been predicted, although in retrospect the enhanced level of ^{231}Pa and/or ^{227}Ac in Gd is understandable [103] because of their chemical similarities.

Radioactive impurities in the GdLS consist of generally common isotopes and more unusual isotopes which enter with Gd. Common isotopes include ^{14}C, ^{85}Kr, ^{40}K, and the isotopes in the ^{238}U and ^{232}Th chains. Unusual isotopes that enter with Gd include ^{138}La, ^{147}Sm, ^{152}Gd, ^{176}Lu, and isotopes in the ^{235}U chain. Approximately 40 isotopes produce energy deposits above a threshold of 100 keV. Considering the OD rates of the previous two sections, we allow for roughly 50 Hz of rate to come from internal radioimpurities, resulting in a specific activity for an average isotope that should not exceed 0.07 mBq/kg

(an impurity at this level would contribute 1.2 Hz of rate in the OD). Natural Gd contains 0.2 % ^{152}Gd by weight, which contributes 1.6 mBq/kg in GdLS with 0.1 % Gd by mass. The signal from the 2.2 MeV α from ^{152}Gd is heavily quenched and emits light similar to that of a ≈100 keV β signal.

The abundance of radioactive impurities can be influenced by chemical processing and purification of the components of GdLS. The specific activity levels reported by a variety of experiments which have used LS, as well as by experiments that use gadolinium, converted to the expectation in the GdLS for LZ, are given in Tab. 4.7. Many of the specific activities exceed 0.07 mBq/kg.

Table 4.7: Summary of specific activities in units of mBq/kg, converted to a kilogram of LZ GdLS. To meet the LZ OD specifications, an average specific activity ≤0.07 mBq/kg is needed.

Isotope	**Large Detectors**	**GADZOOKS! Gd [102]**		**Boiko Gd [104]**	
	Highest	**Lowest**	**Highest**	**Purified**	**Raw**
^{14}C	5000 [105]				
^{40}K	6.3 [106]	$<1.9 \times 10^{-3}$	0.25 ± 0.01	< 0.04	< 0.09
^{85}Kr	0.88 ± 0.02 [107]				
^{238}U$_l$/^{210}Po	0.20 ± 0.05 [83]				
^{238}U$_l$/^{210}Bi	0.07 ± 0.01 [107]				
^{238}U$_l$/^{210}Pb	0.06 ± 0.01 [107]				
^{232}Th$_e$		$<3.9 \times 10^{-4}$	2.12 ± 0.02	< 0.005	0.09 ± 0.01
^{232}Th$_l$	$\approx 8 \times 10^{-3}$ [83]	$(5.8 \pm 4.0) \times 10^{-4}$	0.97 ± 0.01		
^{238}U$_e$		< 0.013	1.9 ± 0.1	< 0.8	< 1.3
^{238}U$_m$	$\approx 4.5 \times 10^{-4}$ [83]	$<3.8 \times 10^{-4}$	0.143 ± 0.004	< 0.01	< 0.009
^{235}U$_e$		$<7.7 \times 10^{-4}$	< 0.22	< 0.01	0.11 ± 0.01
^{235}U$_l$	≈0.01 [83]	$<1.0 \times 10^{-3}$	4.7 ± 0.1	2.2 ± 0.1	1.6 ± 0.1
^{138}La		$<2.9 \times 10^{-4}$	1.32 ± 0.03	0.030 ± 0.003	0.014 ± 0.002
^{176}Lu		$(4.4 \pm 1.7) \times 10^{-4}$	1.09 ± 0.01	0.035 ± 0.003	0.038 ± 0.004

The isotope with the highest specific activity in Tab. 4.7 is ^{14}C. Use of underground hydrocarbon sources for the LS chemicals results in ^{14}C specific activities near 1 mBq/kg, while use of biogenic hydrocarbon sources caused the higher value in the table. The ^{14}C

β-decay spectrum endpoint is 156.5 keV, with 8 % of single pulses exceeding 100 keV. An increase of energy threshold can suppress single pulses from ^{14}C, but multiple pulses from pileup of ^{14}C decays during the planned LZ time window of 500 µs can still be troublesome. The surveying technique of accelerator mass spectrometry (AMS) has a sensitivity to $^{14}C/^{12}C$ of 10^{-15}, corresponding to a specific activity of 100 mBq/kg, which is not sufficient for the LZ OD.

Isotopes in the ^{235}U chain have been detected in Gd for GADZOOKS! [101] and also in GdLS at the level of 0.01 mBq/kg in Daya Bay [83]. In Tab. 4.7, the specific activity per kg LZ GdLS is extrapolated from various samples studied in Ref. [102]. The lowest and highest values in Ref. [102] arise from variation among the samples obtained from different suppliers. Tab. 4.7 also shows the specific activities in LZ GdLS from the gadolinium evaluated in Ref. [104], both before and after purification. The highest ^{235}U levels from both Gd studies exceed the specification for LZ GdLS.

Exposure to mine air must be avoided during OD filling operations. ^{85}Kr, a β emitter with half-life of 10.7 y, is present at a level of $\approx$1.5 Bq/m^3 in the air [108]. The Ostwald coefficienct (ratio of gas volume absorbed to volume of absorbing solvent) for Kr absorbed in organic scintillator is conservatively equal to unity [109], implying that the 20.1 m^3 of OD GdLS should not be exposed to more than 3.3 m^3 of air in order to keep the ^{85}Kr rate below 1 Hz. This results in a maximum exposure of 30 L of air for each of the 112 GdLS drums. This should be relatively easy to achieve.

Two radioactive isotopes are not included in Tab. 4.7. The first is ^{152}Gd, which is

unavoidable when using natural gadolinium and has ≈60 % probability of exceeding a light output equivalent to a 100 keV β pulse. A rate in the OD of ≈17 Hz is expected from ^{152}Gd above 100 keV. ^{147}Sm emits an α of energy 2.3 MeV, which will have a ≈70 % chance of exceeding the light output of a 100 keV β pulse.

The principle topic of this thesis is a characterization of the radioimpurities in the GdLS by way of direct counting in a small, LS detector that we call the "LS Screener" or "Screener" for short. The primary motivation for building the Screener was to measure ^{14}C with the required sensitivity, noting that AMS is insensitive by roughly two orders of magnitude. Additionally, the Screener has demonstrated the ability to measure the other radioimpurities discussed above, primarily those in the ^{238}U, ^{235}U, and ^{232}Th decay chains by detecting α decays with nearly no background. The final two chapters of this thesis detail the construction, commissioning, data collection, and data analysis of the Screener with the end result of a prediction for the OD rate from internal radioimpurities.

The ^{238}U, ^{235}U, and ^{232}Th Decay Chains

The two uranium decay chains and the thorium decay chain each contribute ≈ 10 unstable isotopes. It is common to assume that the isotopes in these chains are in secular equilibrium, with all isotopes within one chain, from the head (^{238}U, ^{235}U, and ^{232}Th, respectively) to a step prior to the stable final isotope (^{206}Pb, ^{207}Pb, and ^{208}Pb respectively) contributing a rate equal to all other isotopes within the respective chain. Violations of secular equilibrium make the definition of subchains useful [110].

The subchains defined for ^{238}U are shown in Fig. 4.27. Of the five isotopes in the

early $^{238}U_e$ subchain, three are long-lived, and are chemically similar, while the other two re-equilibrate rapidly after chemical processing. The six isotopes in the middle $^{238}U_m$ subchain equilibrate rapidly with the chemically distinct ^{226}Ra after processing. Emanation of ^{222}Rn from surfaces contributes to $^{238}U_m$. The level of $^{238}U_m$ is often measured in LS by the distinct β-α pulse pair from ^{214}Bi and ^{214}Po. Of the three radioactive isotopes in the late $^{238}U_l$ subchain, the β from ^{210}Pb has an energy below the OD threshold of 100 keV. Surfaces contain ^{210}Pb deposited by environmental ^{222}Rn and frequently contribute ^{210}Bi and ^{210}Po at rates higher than the other ^{238}U subchains.

The subchains defined for ^{235}U are shown in Fig. 4.28. The early $^{235}U_e$ subchain contains two isotopes: the long-lived head of the chain, ^{235}U, and the short-lived ^{231}Th, which rapidly comes to equilibrium with ^{235}U after chemical processing. The nine isotopes in the late $^{235}U_l$ subchain start with the long-lived ^{231}Pa, which is chemically distinct from uranium and not necessarily suppressed by chemical processes that suppress uranium. While ^{227}Ac is long-lived enough to re-establish equilibrium quickly after chemical processing, its chemistry may be similar enough to that of protactinium to stay in equilibrium following chemical processing. Both protactinium and actinium are chemically similar to gadolinium. The β from ^{227}Ac has an energy below the OD threshold of 100 keV. The other seven isotopes in $^{235}U_l$ rapidly re-equilibrate after chemical processing. The level of $^{235}U_l$ can be measured in LS by the distinct α-α pulse pair from ^{219}Rn and ^{215}Po.

The subchains defined for ^{232}Th are shown in Fig. 4.29. Of the three isotopes in the early $^{232}Th_e$ subchain, only the head isotope is long-lived, while the other two re-

equilibrate rapidly after chemical processing. The β from ^{228}Ra has an energy below the OD threshold of 100 keV. There are eight distinct radioactive isotopes in the late ^{232}Th$_l$ subchain, but weighting by the branching ratios of ^{212}Bi reduces the count to seven. The isotopes in ^{232}Th$_l$ may rapidly re-equilibrate with ^{228}Th after chemical processing, and are influenced by emanation of ^{220}Rn from surfaces. The level of ^{232}Th$_l$ is often measured in LS by the distinct β-α pulse pair from ^{212}Bi and ^{212}Po.

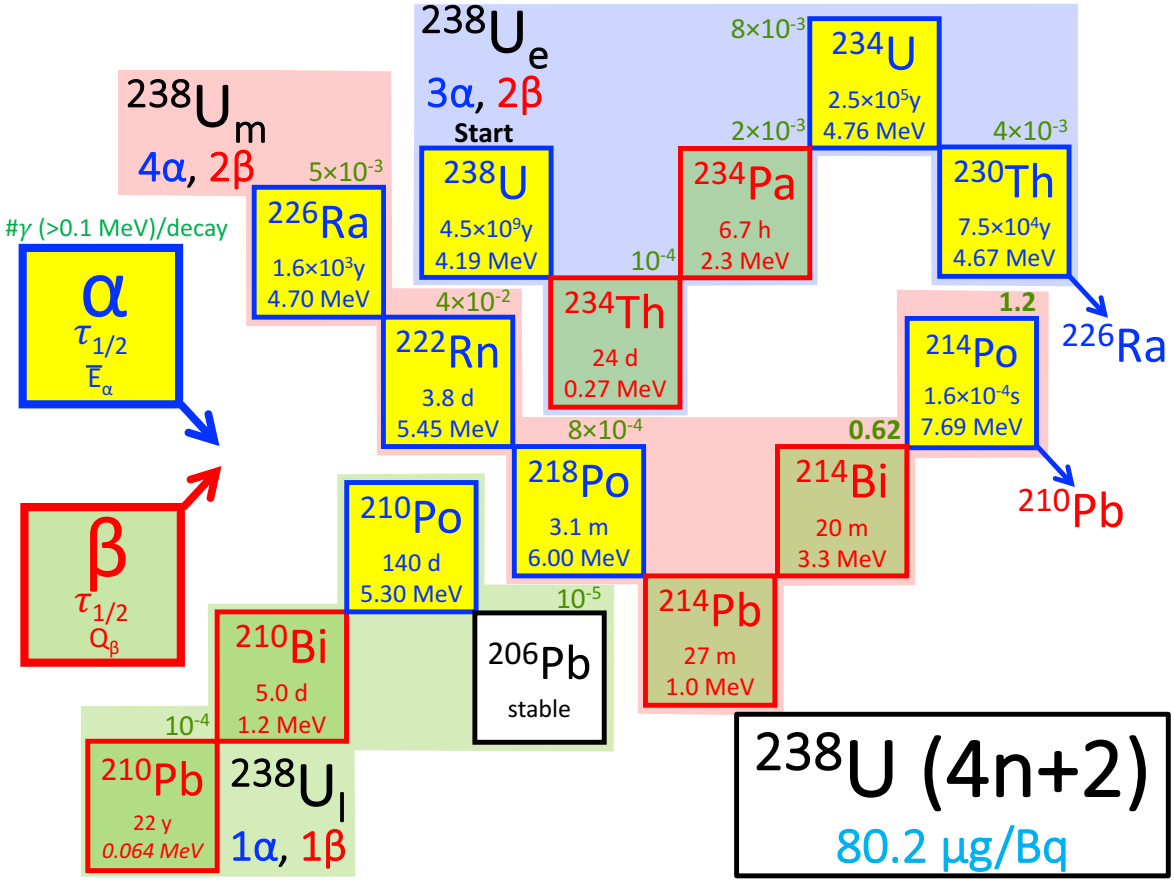

Figure 4.27: Definition of subchains for ^{238}U. The 14 principal radioactive isotopes in the ^{238}U decay chain are each shown in a box, with the half-life and energy released into α's and into β's. The branching ratio into clear (>100 keV) γ's is shown in bold above the daughter, while for weak γ emitters, the largest branching ratio is shown. The one isotope with an energy release below the OD threshold, ^{210}Pb, is not included in OD rate analyses or in the count of β decays shown.

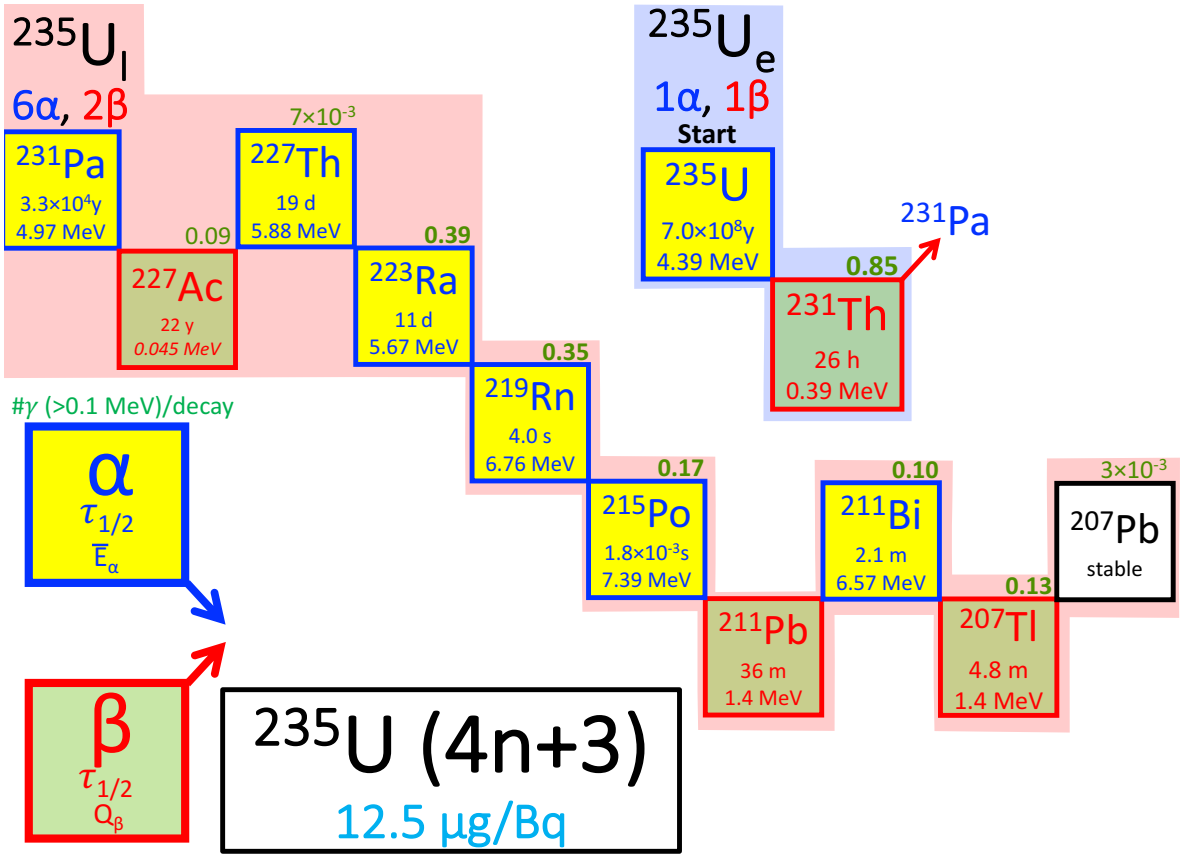

Figure 4.28: Definition of subchains for ^{235}U. The 11 principal radioactive isotopes in the ^{235}U decay chain are each shown in a box, with the half-life and energy released into α's and into β's. The branching ratio into clear (>100 keV) γ's is shown in bold above the daughter, while for weak γ emitters, the largest branching ratio is shown. The one isotope with an energy release below the OD threshold, ^{227}Ac, is not included in OD rate analyses or in the count of β decays shown.

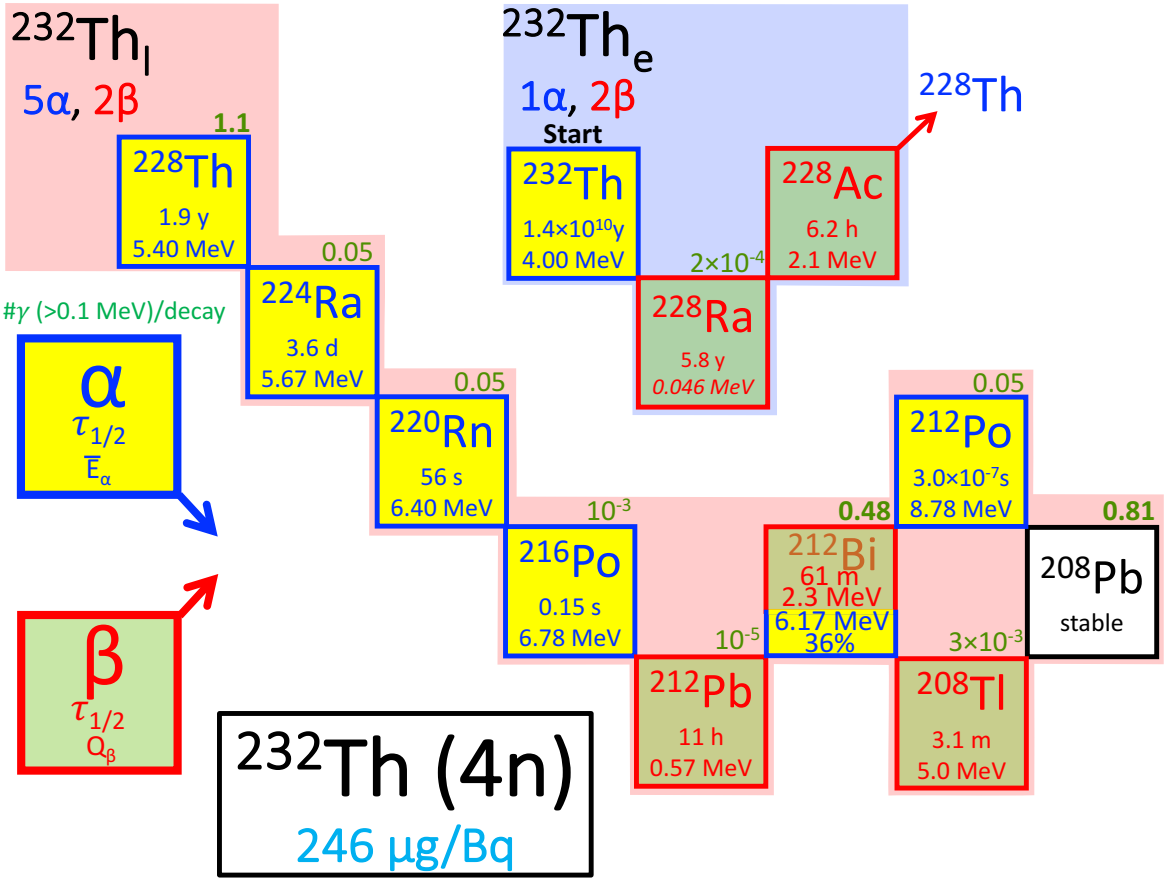

Figure 4.29: Definition of subchains for ^{232}Th. The 11 principal radioactive isotopes in the ^{232}Th decay chain are each shown in a box, with the half-life and energy released into α's and into β's. The branching ratio into clear (>100 keV) γ's is shown in bold above the daughter, while for weak γ emitters, the largest branching ratio is shown. The one isotope with an energy release below the OD threshold, ^{228}Ra, is not included in OD rate analyses or in the count of β decays shown.

HPGe Screening of Gd Additives

In the course of data collection with the Screener it was realized that a significant portion of the total impurity level results from the Gd-loading process. Therefore, a 0.307 kg sample of the same chelated compound $Gd(TMHA)_3$ dissolved in the Screener GdLS was counted for 18 d in a HPGe detector [111]. Concentration causes the specific activity in mBq/kg as measured for the chelated compound to be 250 times higher than the specific activity for GdLS. Results from the HPGe exposure are reported in Tab. 4.9. The measured level of $^{238}U_m$ in this sample may have been caused by radon contamination in the sample. Reasonable sensitivities are achieved for γ-emitting isotopes with high branching ratios such as ^{176}Lu, but this is not the case for the decay chain progeny. Detection of these isotopes through their α decays in the GdLS itself provides a more sensitive measurement of their concentrations.

A principle outcome of the Screener results was recognizing that the Gd compound should be further purified. Results from a 44.5 d screening of a 1.44 kg sample of compound are also given in Tab. 4.9. This sample was produced using a higher pH during the partial hydrolysis purification of the Gd compound. The result is a more aggressive purification of radioimpurities at the expense of losing more raw Gd product to precipitation. The improvement in radiopurity is obvious and quantified in the last column. The improvement in the reported upper limits is expected to scale as $(m_2/m_1)\sqrt{t_2/t_1}$, where m_1, m_2 are the masses of the first and second samples and t_1, t_2 are their corresponding livetimes. Thus we expect upper limits that are smaller by a factor of ≈ 7.5,

consistent with what is reported in the table. Perhaps the most remarkable result is the large reduction of ^{176}Lu. This result is robust given that the isotope is detected above background in both samples. This will be the purification used to produce the GdLS for the LZ OD. The energy spectrum collected for this sample is shown in Fig. 4.30, while the principle γ lines used for these measurements are given in Tab. 4.8.

Table 4.8: Principle γ-ray lines used to determine the concentrations of various isotopes and decay chains.

Chain	Isotope	Gamma Energy (keV)	BR (%)
$^{235}\mathbf{U_e}$	^{235}U	143.8	11.0
	^{235}U	185.7	57.0
$^{235}\mathbf{U_l}$	^{227}Th	236.0	12.9
	^{223}Ra	269.5	13.9
	^{219}Rn	271.2	10.8
	^{211}Bi	351.1	13.02
$^{238}\mathbf{U_m}$	^{214}Pb	242.0	7.3
	^{214}Pb	295.2	18.4
	^{214}Pb	351.9	35.6
	^{214}Bi	609.3	45.5
	^{214}Bi	1120.3	14.9
	^{214}Bi	1764.5	15.3
$^{232}\mathbf{Th_e}$	^{228}Ac	338.3	11.7
	^{228}Ac	911.2	26.5
	^{228}Ac	969.0	16.1
$^{232}\mathbf{Th_l}$	^{212}Pb	238.6	81.6
	^{208}Tl	583.2	85.0
	^{208}Tl	2614.5	99.8
$^{40}\mathbf{K}$	^{40}K	1460.8	10.7
$^{176}\mathbf{Lu}$	^{176}Lu	201.83	78
	^{176}Lu	306.78	93.6
$^{138}\mathbf{La}$	^{138}La	788.7	34.5
	^{138}La	1435.8	65.5

Table 4.9: Results from HPGe counting of two purified $Gd(TMHA)_3$ powder samples given in mBq/kg of $Gd(TMHA)_3$ and in mBq/kg of GdLS, loaded to 0.1% Gd by mass. The reduction factors of the limits/central values for the improved purification results are also given. Limits are given at 68% CL.

Isotope or Subchain	**0.307 kg, Initial Purification**		**1.44 kg, Improved Purification**		**Reduction**
	mBq/(kg $Gd(TMHA)_3$)	**mBq/(kg GdLS)**	**mBq/(kg $Gd(TMHA)_3$)**	**mBq/(kg GdLS)**	
$^{238}U_e$	< 259	< 1.04	< 4.36	< 0.017	59.4
$^{238}U_m$	23 ± 5	0.092 ± 0.02	2.6 ± 0.9	0.010 ± 0.004	8.8
$^{235}U_e$	< 2.8	< 0.011	< 4.5	< 0.018	0.6
$^{235}U_l$	26 ± 10	0.10 ± 0.04	< 3.0	< 0.012	8.7
$^{232}Th_e$	< 6.7	< 0.027	< 0.89	< 0.0036	7.5
$^{232}Th_l$	< 5.1	< 0.020	< 0.76	< 0.0030	6.7
^{40}K	< 56	< 0.22	< 2.29	< 0.0092	24.5
^{138}La	< 1.4	< 0.0055	< 0.42	< 0.0017	3.3
^{176}Lu	75 ± 18	0.30 ± 0.07	2.03 ± 0.46	0.0081 ± 0.0018	36.9

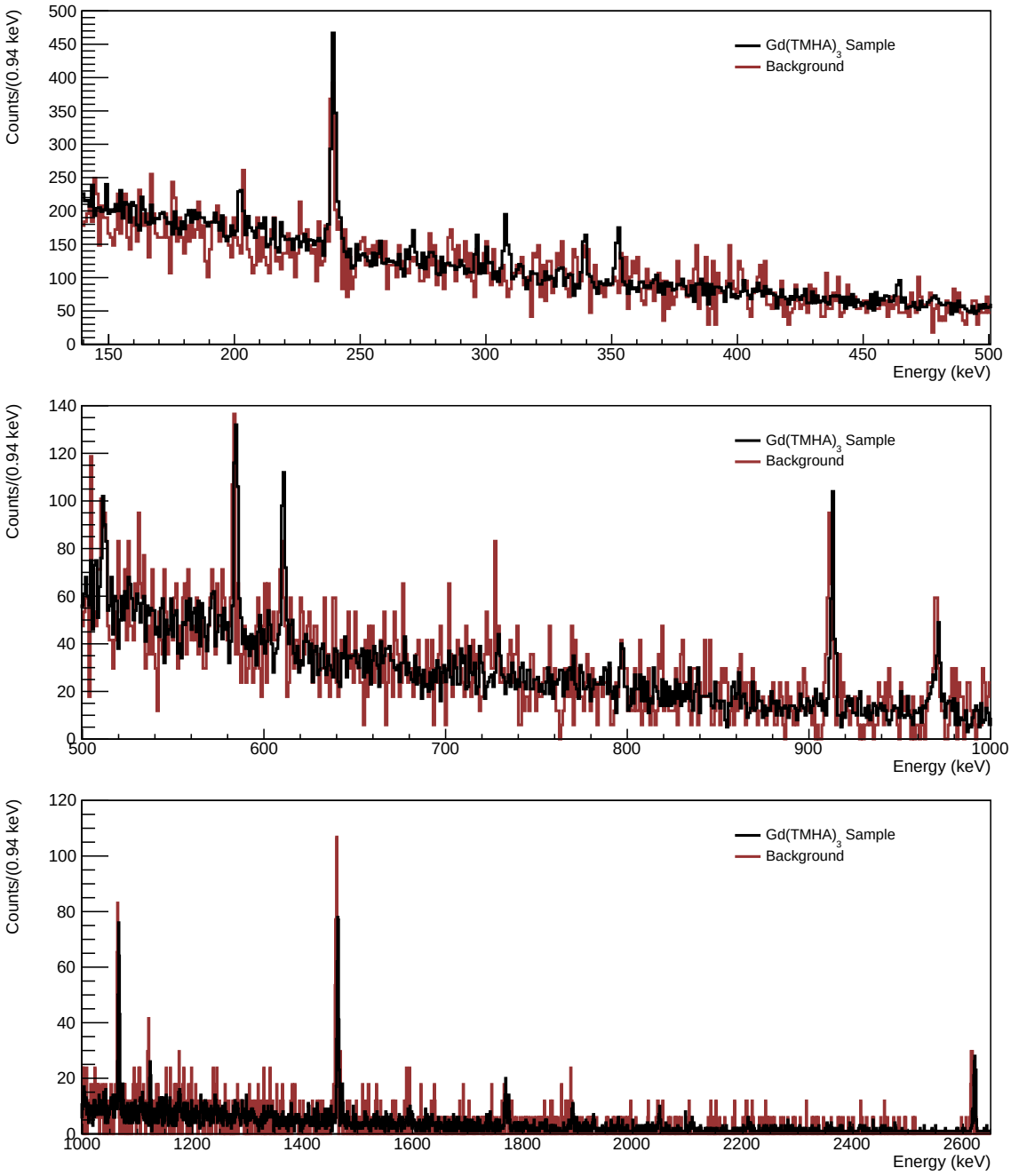

Figure 4.30: Energy spectrum of events collected from HPGe screening of 1.44 kg of purified $Gd(TMHA)_3$ powder arranged in an S6 Marinelli beaker.

4.5.4 Summary

Tab. 4.10 summarizes the results of the previous sections by providing an estimate for the OD singles rate above an energy threshold of 200 keV. The rates from various internal radioimpurities are predicted using the results from Chap. 6. A lower predicted rate from internal sources is also given by using the factors from Tab. 4.9 to downscale the respective isotopes anticipating that the final GdLS will have better radiopurity than that measured in Chap. 6. An additional 37.0 ± 1.1 Hz from ^{14}C β's and ^{152}Gd and ^{147}Sm α's can be added to the rate from internals to obtain the predicted rate above 100 keV. The increased rate from other β's at this lower threshold is negligible compared to the quoted errors.

Table 4.10: Summary of predicted OD rate from dominant sources.

Source		**Rate in OD > 200 keV (Hz)** **First Purification**	**Improved Purification**
LZ Components		11.9	11.9
Davis Cavern γ's		35 ± 3	35 ± 3
Internals	^{238}U	22.1 ± 3.3	1.3 ± 0.4
	^{235}U	24.3 ± 0.3	2.80 ± 0.03
	^{232}Th	3.6 ± 2.8	0.5 ± 0.4
	^{40}K	1.5 ± 2.7	0.06 ± 0.11
	^{176}Lu	4.3 ± 1.2	0.12 ± 0.03
	^{85}Kr	1.1 ± 1.6	1.1 ± 1.6
Total		103.8 ± 6.3	52.8 ± 3.4

Chapter 5

The LZ LS Screener Detector

In this chapter I discuss the design and fabrication of the Screener and initial tests performed at UCSB in the summer and fall of 2016. The detector's primary goal was to assay the GdLS to be used in the LZ OD. In particular, the Screener was motivated as a means of measuring of the ^{14}C content of the GdLS at the required sensitivity for the OD.

5.1 Detector Design Overview

The Screener is designed to operate in the ultra-low background environment of the LUX/LZ water tank. The characteristic size of the Screener was set by considering that a device about 1/1000 the size of the LZ OD is manageable, i.e. movable by a person. This sets the approximate goal for the background rates in the Screener: LS impurities which give $\mathcal{O}$(Hz) rates in the OD will give $\mathcal{O}$(mHz) rates in the Screener. In practice

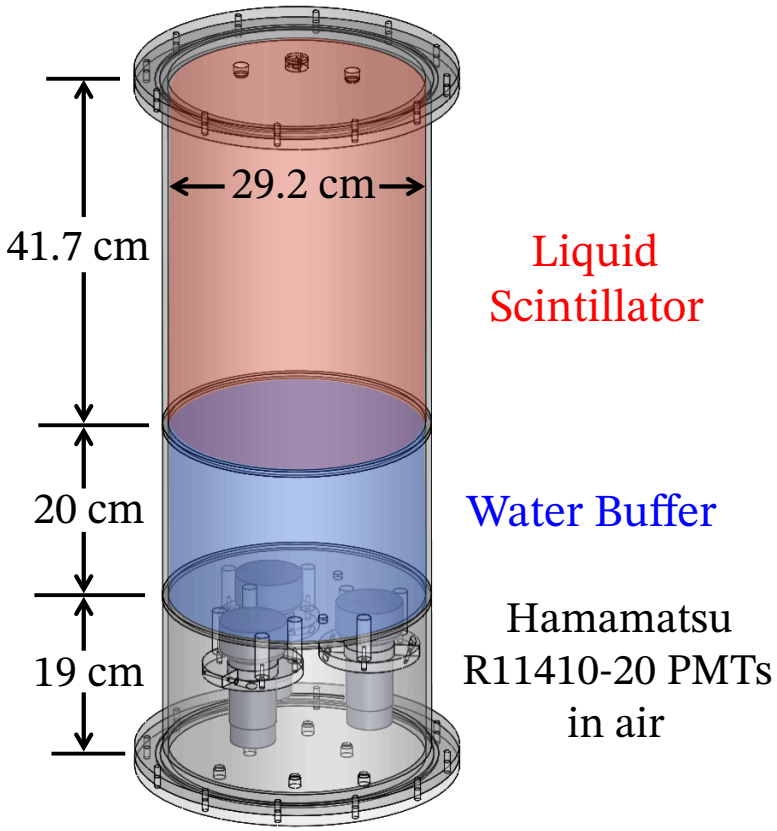

Figure 5.1: Annotated CAD drawing of the LS Screener showing the three PMTs facing the water and GdLS volumes.

the LS mass in the Screener is about 1/750 the mass in the OD, as changes to the final OD design resulted in less LS mass.

The detector is comprised of a clear UV-transparent acrylic tube of inner diameter 29.2 cm and wall thickness 0.64 cm segmented along its length into three chambers, fabricated by Reynolds Polymer Technology, Inc. [61]. The partitions between chambers are 0.64 cm thick, and the chamber lids are 1.3 cm thick. The top chamber is 41.7 cm long and has a capacity of 28 L, so it can hold up to 24 kg of LS. The middle chamber is 20 cm

long and is filled with 14.3 kg of distilled, deionized water that shields the LS from γ-rays generated in the PMTs. The bottom chamber is 19 cm long, filled with air, and holds the three low-background PMTs. The PMTs face the LS and are coupled to the acrylic wall between their chamber and the water volume using optical grease. The chambers on each end of the vessel are sealed by tightening 12 brass bolts and compressing an O-ring between the vessel flange and the chamber lid. The assembly is wrapped in the same 262 µm-thick 1085D Tyvek that will be used in the OD. A diagram of the detector is shown in Fig. 5.1.

The three PMTs are 7.6 cm Hamamatsu R11410-20, which have radiompurity levels $\approx$1 mBq/PMT for the U/Th chain and (12 ± 2) mBq/PMT for ^{40}K [35]. The R11410-20 has a quantum efficiency of $\approx$35 % at a wavelength of 420 nm, the peak of GdLS emission, and resolves single photoelectrons [34]. The use of these low-background PMTs was a key insight in the Screener's development. Typical PMT activities are $\sim$1 Bq/PMT or higher, making them unsuitable for the goals of the Screener.

5.2 Assembly at UCSB

The acrylic vessel and LS chamber lid were shipped to UCSB in May 2016. Fig. 5.2 right shows the vessel as received, wrapped in a plastic coating. The vessel and lid were immediately placed in a dark container under nitrogen purge in a cleanroom.

In June 2016, a dark box and detector stand were designed and built to hold the detector. The dark box with detector stand is show in Fig. 5.2. A feedthrough panel was

Figure 5.2: *Left and Middle:* The custom dark box built to house the Screener and detector stand. *Right:* The acrylic vessel as received being secured to the detector stand.

designed to deliver each of the three PMTs' signal and HV, a connection to a fiber optic cable, and nitrogen purge in and out lines.

5.2.1 Water Buffer Filling

Access to the water buffer is through two National Pipe Thread (NPT) ports in the acrylic separating the water buffer and PMT chamber volumes. Tygon tubing is connected to barbed fittings that screw into the acrylic. The volume is purged with nitrogen gas and then filled with water. The vessel is tilted to minimize the amount of trapped nitrogen bubbles left in the volume. Each barbed fitting is then replaced by a PTFE plug.

The water was sourced from the Lipman biophysics group on campus at UCSB. The deionized water provided by the building is further distilled in-house to remove any additional impurities.

(a) (b)

Figure 5.3: (a) A PMT with pins cut to length. (b) The PTFE pieces and a base.

5.2.2 PMT Mounting and Cabling

On the back of the PMTs are 20 pins that connect to the various dynode stages, anode, and photocathode. These pins were carefully cut to a long length of 18 mm and short length of 10 mm so that the PMT base would properly connect to the PMT and the base-PMT assembly would fit in the PMT chamber. Custom PTFE parts shown in Fig. 5.3b were made to slide onto the PMT pins and sandwich the base, preventing electrical breakdown between PMT pins and the base itself. Each PMT and base have a serial number. The PMTs are numbered and mated with a base according to the following:

PMT1, serial #KB0060, mated with base serial #PT64

PMT2, serial #KB0064, mated with base serial #PT38

PMT3, serial #KB0089, mated with base serial #PT74

Inside the PMT chamber, each PMT is mounted using a custom acrylic clamp which

fastens to three acrylic rods glued to the main vessel. The acrylic rods were glued to the main vessel using a small amount of Weld-On 40 acrylic cement. The positions of the PMT centers are half the radius of the PMT chamber inner wall. A printed-to-scale CAD drawing was used to ensure accurate positioning of the PMTs. Fig. 5.4 shows the mounted PMTs in the chamber. Nylon screws are used to both clamp around the PMT body and fasten the clamp to the rods in the chamber. Once they are mounted, each PMT's signal and HV cables are connected to the PMT base. For tests at UCSB, the PMT chamber was left open.

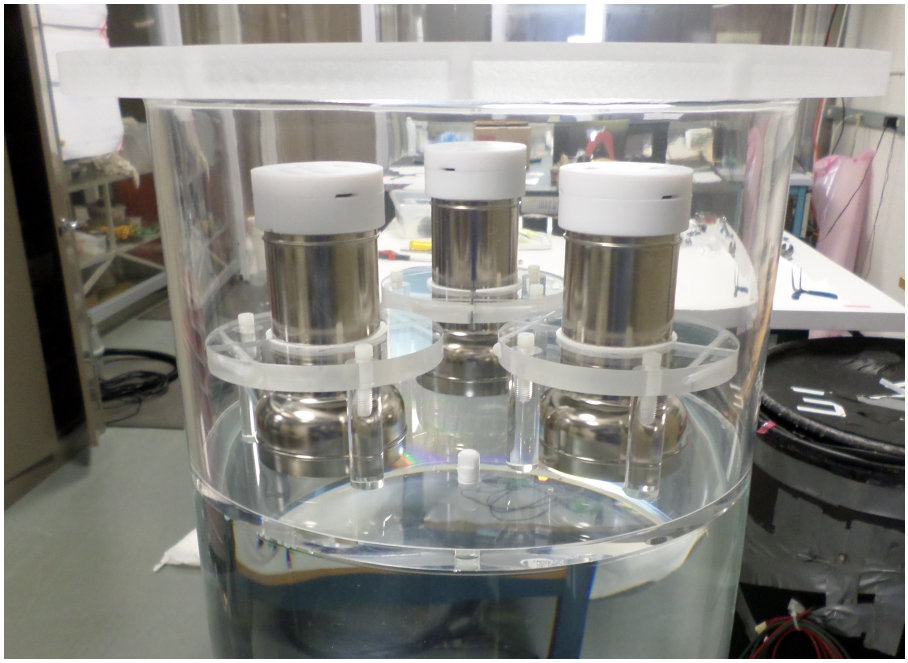

Figure 5.4: All three PMTs mounted in the Screener using the custom acrylic mounting scheme. The acrylic rods are glued directly to the main vessel.

5.2.3 Filling with LS

The LS chamber must be filled in a way that minimizes the exposure of both the LS and the chamber volume to ambient air. This is especially important when filling in the radon-rich environment underground. Exposure to air not only introduces sources of background from radon and ^{85}Kr, but it also acts to degrade the light yield of the LS through oxygen quenching.

The Screener provided a nice testbed for experimenting with different filling procedures. These tests have helped improve the plan for filling the OD. At UCSB, the Screener was filled twice: first, with pure LAB and, second, with LS not loaded with Gd. After the first fill with pure LAB, the detector was left to "soak" for about two weeks, allowing any mobile impurities to leach out of the acrylic chamber walls. The pure LAB was then pumped out and replaced with the LS for further tests. The LS remained in the detector for approximately one and a half months. The LS chamber lid was kept closed from the time of the first fill to underground deployment. When no liquid was in the chamber, the volume purged with nitrogen gas.

A schematic of the final system used for underground deployment is shown in Fig. 5.5. Any plumbing coming in direct contact with the LS was made of PTFE or glass to ensure chemical compatibility. This includes the KNF pump, the active parts of which are made from PTFE. The liquid itself was double-bagged in PTFE bags and shipped in small, steel drums. Fig. 5.6a shows the interface between the fill and purge lines and the LS bags. The purge line is used to inflate the inner bag which allows easy pumping on the

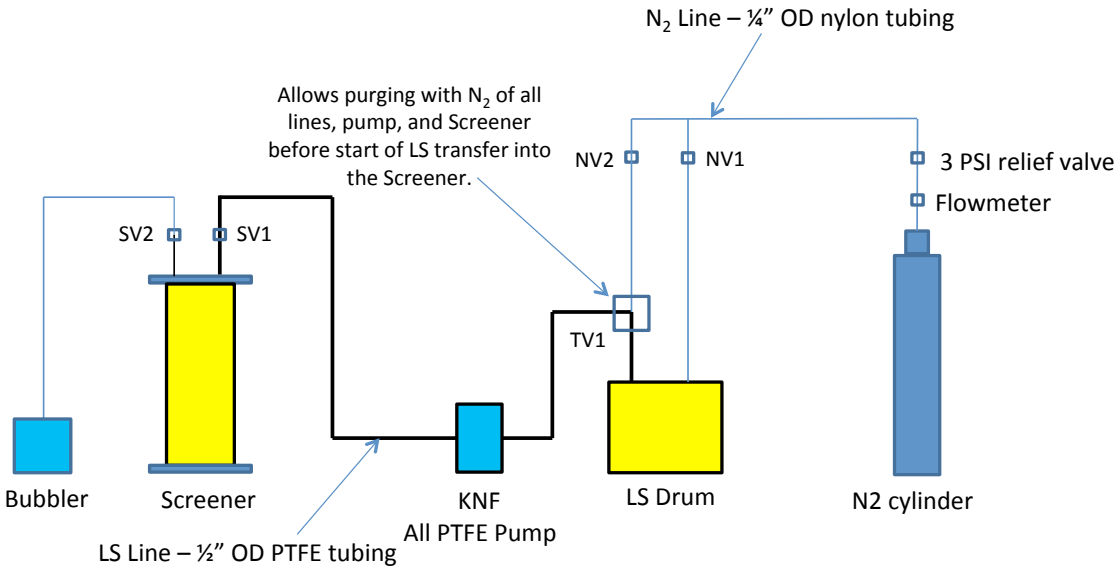

Figure 5.5: Diagram of final filling system used for underground deployment. Bold lines represent PTFE lines for moving LS and thinner lines represent nylon lines used for nitrogen gas transport.

liquid in a nitrogen gas environment.

Two NPT ports in the LS chamber lid provide the interface between the plumbing and the chamber volume. PTFE fittings made by International Polymer Solutions (IPS) [112] are used to adapt the NPT connection in the acrylic to a flare connection with the PTFE fill lines. Just above these connections are PTFE valves. This interface is shown in Fig. 5.6b.

Nitrogen gas is used to purge all volumes before filling begins. The gas is regulated by a 3 psi relief valve that prevents damage to the acrylic vessel from overpressure, while the flow can be controlled via a flow meter. With all valves in the system open, gas is allowed to flow for several minutes, purging all lines and volumes. Next, the three-way

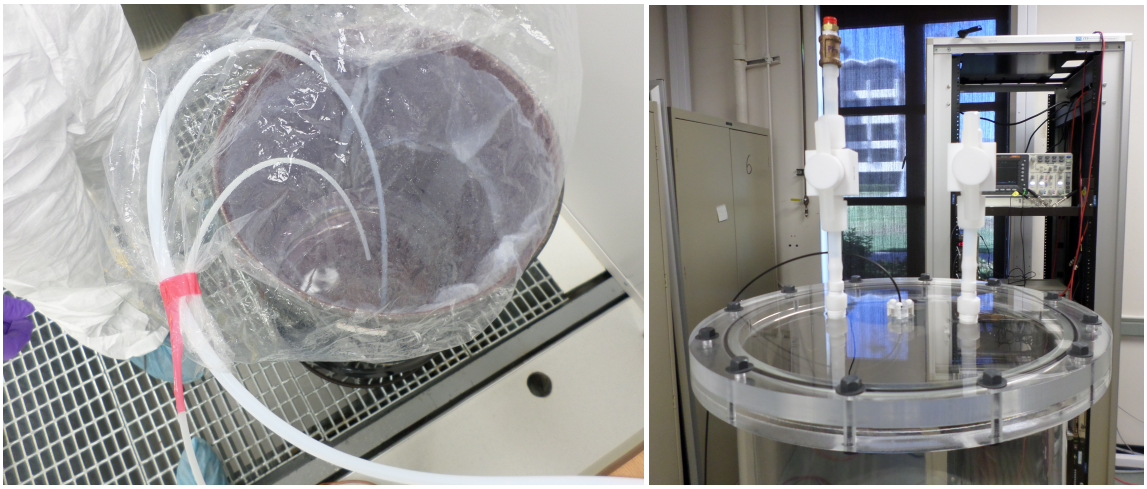

(a) (b)

Figure 5.6: (a) Purge and LS fill lines in the PTFE bag. Nitrogen gas from the purge line inflates the bag allowing efficient pumping of LS and keeps ambient air out. (b) The two ports on the LS chamber lid with flare fittings and PTFE valves in place.

valve TV1 is opened so that flow is only permitted between the LS drum and the pump. The pump is then turned on and LS is moved into the detector until the desired level in the Screener is achieved. A $\sim$1 cm head of nitrogen gas is left at the top of the LS chamber.

5.3 Commissioning and Testing at UCSB

In parallel with detector assembly, many tests were performed with the Screener to better understand its performance and characteristics in different configurations. In this section I discuss some of these studies undertaken in preparation for its primary physics run at SURF.

5.3.1 Signal Chain and Data Acquisition System

It is the job of the data acquisition system (DAQ) to record the raw waveform output of each PMT to a computer so that it may be further processed and analyzed. The signal chain and DAQ used with the Screener is largely based on components or prototype components planned for use in LZ.

A coaxial cable carries the signals from a PMT base directly to a custom, 4-channel amplifier designed and built at UC Davis for LZ. DC voltages of 4.5 V and −10 V (plus a common ground connection) power the amplifier. For each amplifier input channel there are two output channels: "low-energy" (LE) and "high-energy" (HE). In the LE (HE) output, the input signal from the PMT has been amplified by a factor of 40 (4) and shaped using a characteristic time of 30 ns (60 ns).

Both LE and HE outputs are then fed into a bench-top waveform digitizer known as the "DDC10", which was designed and built at the University of Rochester. The DDC10 consists of a series of analog-to-digital converters (ADCs) which digitize the signal at each input channel at 100 MHz (1 sample = 10 ns). An FPGA monitors the ADC outputs so that pre-programed fast logic decisions can be made (e.g. a trigger is generated). An onboard 100 MHz clock logs each event's livetime and deadtime. Configuration of the DDC10 is achieved via an on-board Linux operating system which issues commands directly to the FPGA and enables easy control by the user. Communication with the DDC10 is through a gigabit ethernet connection to a PC. Data is off-loaded directly from the DDC10 to a specified location on the connected PC via this same connection after a

trigger. The user issues commands using the combination of a terminal program and a GUI program hosted on the DDC10's operating system.

The DDC10 has ten input channels (numbered 0-9), each with 2 V dynamic range. These channels are used in the following way: channel 0 is used for input from an external trigger (such as when taking single photoelectron datasets); channels 2, 3, and 4 are used for the LE amplifier outputs of PMTs 1, 2, and 3, respectively; channels 7, 8, and 9 are used for the HE amplifier outputs of PMTs 1, 2, and 3, respectively. The two channel gap between LE and HE groups is to prevent cross-talk between the LE and HE signal channels.

DAQ Settings and Output

A screenshot of the DDC10 GUI panel is shown in Fig. 5.7. The settings used for data taking with the Screener are called out explicitly. The maximum event window length for the DDC10 is 8192 samples or 81.92 µs. The "post-trigger delay" specifies where in this event window the pulse which triggered the event should be placed. The triggering pulse sample will then be placed at sample equal to 8191 minus the post-trigger delay. In nearly all datasets, this value was set to 7992 so that the triggering pulse would appear at about sample 200. This provides a good amount of waveform before the trigger pulse to use for baseline determination and subtraction. Next, the option to flip the recorded signal in each channel's ADC is provided by the "ADC Invert" option. The raw pulses from a PMT are always negative, so we enable this option for the Screener.

Any channel selected with "Trigger Enable" option will participate in the trigger logic.

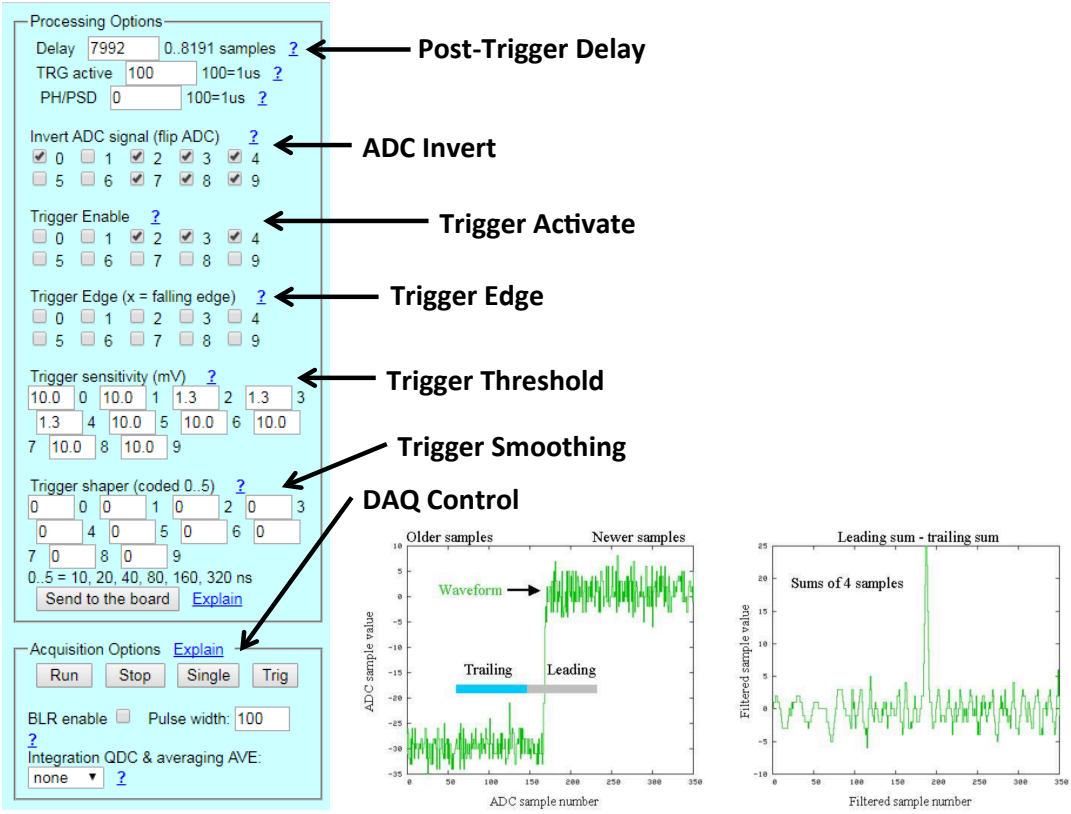

Figure 5.7: Screenshot showing portion of the DDC10 GUI used for establishing DAQ settings.

With no additional input from the user, the default setting for the DDC10 is to look for the OR condition among all channels that are enabled. Each channel's trigger threshold is set by a value in mV. In order for a channel to trigger, the difference between the waveform's "leading sample sum" and its "trailing sample sum" must exceed the given threshold. These sums are computed over a number of samples given by in the "Trigger Smoothing" field. An example of this type of triggering is shown on the right side Fig. 5.7. With the Screener, a single sample leading and trailing was used.

The PMTs used with the Screener have dark rates of order 1 kHz to 10 kHz, the dominate source of this dark rate being single photoelectron in nature. To keep the overall

trigger rate low, thresholds that correspond to pulse areas of ≈1.5 phe are chosen for each channel. That way, only upward fluctuations of true single photoelectron pulses will break threshold. In order to determine this threshold for each channel, single photoelectron datasets were taken using an LED light source (see the next section for a the method of generating largely single photoelectron datasets) at varying channel threshold values. At each threshold, the fraction of pulses of a given area that are detected can then be calculated (i.e. a CDF is created) from the distribution of pulse areas. Fig. 5.8 shows these distributions for varying values of the DAQ channel thresholds in each PMT. The 1.5 phe threshold is defined such that 50% of pulses with this area are detected. Based on Fig. 5.8 then, a DAQ threshold of 5 mV is adequate for PMT 1, while PMTs 2 and 3 require a slightly smaller value.

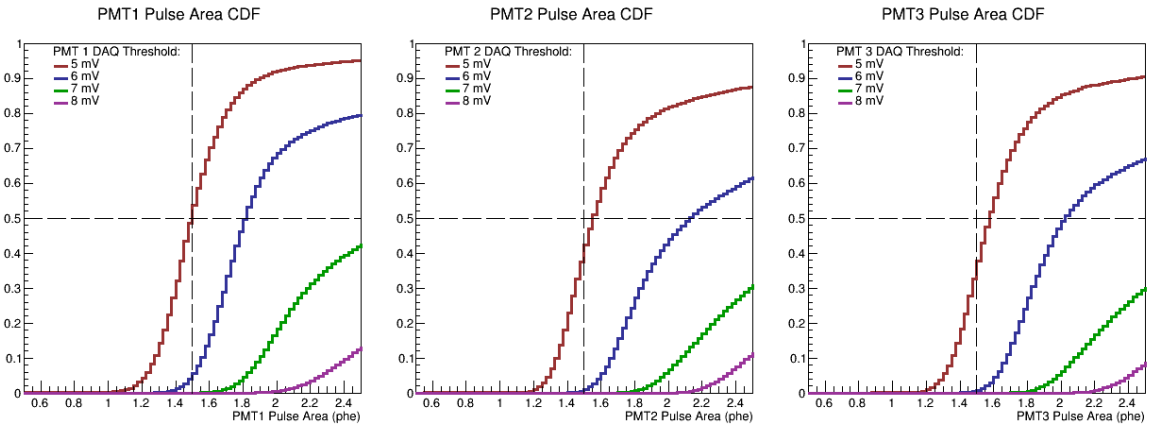

Figure 5.8: CDFs in pulse area for various DAQ channel threshold levels. Dashed lines are drawn to indicate the desired 50% efficiency at 1.5 phe pulse area.

A large trigger rate caused by PMT dark rates is additionally avoided by requiring coincidence among all three PMTs within a 50 ns time window. This is achieved by running a program on the DDC10 called `DDC10_SetCW` which switches the default OR

logic to an AND condition for all trigger enabled channels and takes a coincidence time window length as input.

When a trigger is generated in the DDC10, the digitized event window in each active channel along with the event's livetime and deadtime are written to disk via the ethernet connection. Subsequent triggering is only re-enabled after this write is completed. This introduces a fair amount of deadtime depending on the chosen length of the event window. For nearly all data taken at SURF the full event window of 81.9 µs was used. The corresponding deadtime was on average 30 ms. The reconstruction of pulse pair rates in the next chapter must account for deadtime when the second decaying nucleus has lifetime comparable to the digitization window or the re-enable time interval.

5.3.2 PMT Calibration

The gain of a PMT (in the physicist definition) is the number of electrons appearing at the anode when a single electron is emitted from the photocathode. Typical values for PMT gain range from 10^5 to 10^8 A PMT's gain depends on the applied bias voltage via a power law. However, every PMT is slightly different, so the same bias voltage will generally not produce the same gain. In a multi-PMT detector such a the Screener, we wish to sum all the PMT signals to know the total number of collected photoelectrons, as this is proportional to the energy deposition in the event. We therefore must know each PMT's gain. Additionally, it is convenient for the PMTs to be "gain matched", which means that the response to a single photoelectron is approximately the same in

each tube.

Obtaining Samples of Single Photoelectrons

I now discuss a standard way to obtain a sample of single photoelectron pulses in a PMT. The setup used for the Screener is a 420 nm LED attached to a pulse generator. A trigger pulse is then fed from the generator into the DDC10 so that a trigger is generated each time the pulser sends voltage to the LED.

The arrival of photons at the photocathode and subsequent emission of a photoelectron is a Poisson process. So we may write the probability to observe n photoelectrons given an expected (mean) number, μ, as

$$P(n) = \frac{\mu^n e^{-\mu}}{n!}. \tag{5.1}$$

The mean can be determined by inverting the above equation and substituting the fraction of triggers that give no output pulse from the PMT:

$$\mu = -\log P(0) = -\log\left(\frac{\#\text{ triggers with no signal}}{\#\text{ triggers}}\right). \tag{5.2}$$

Of the triggers that do give an output pulse in the PMT, the fraction that result from single photoelectrons, f_{sphe}, is

$$f_{\text{sphe}} = \frac{P(1)}{\sum_{n=2}^{\infty} P(n)} \tag{5.3}$$

which, when μ is made small (i.e. a very large number of triggers do not yield an output from the PMT), reduces to

$$f_{\text{sphe}} \approx \frac{P(1)}{P(1) + P(2)}. \tag{5.4}$$

A typical configuration will set the pulser voltage to the LED such that 90% of triggers do not yield a PMT response. One can then calculate $\mu = 0.0458$ and $f_{\text{sphe}} \approx 0.978$. That is, about 98% of the triggers that do show a response in the PMT will be from single photoelectrons.

Fig. 5.9 shows the result of performing the above procedure with the three Screener PMTs. The distribution of pulse areas obtained by triggering on the LED pulser is plotted for each PMT. The pulses at low area results from triggers that do not produce an output pulse in the PMT and are largely just integrated baseline noise. The single photoelectron pulses produce a Gaussian-like distribution, the mean of which is the all-important "single photoelectron size".

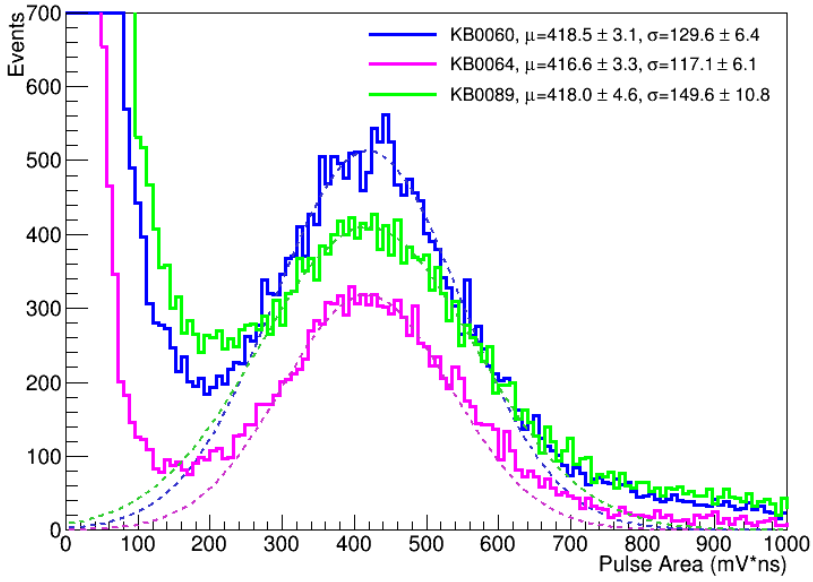

Figure 5.9: Typical pulse area distributions for each of the three Screener PMTs. Empty triggers populate the low pulse area region, while single photoelectron pulses form a peak that determines the single photoelectron size.

Another important parameter obtained from Fig. 5.9 is the fraction of single pho-

toelectron pulses that are distinguishable from noise pulses. This corresponds to the integral of the pulse area distributions above the "valley" where the falling tail from noise pulses intersects the rising peak from single photoelectron pulses. In LZ, for example, this fraction is required to be at >90 %. Because the Screener triggers on 1.5 phe in each PMT, this number does not need to be as high. For all data in this thesis, this fraction was at >80 %.

PMT Gain Curves

The large gain typical of PMTs is achieved through electron amplification at each dynode stage. Specifically, the multiplication factor at each stage is known as the secondary electron yield, δ, and is defined as the number of electrons emitted from the dynode for every electron incident on the dynode. As long as this number is larger than one, amplification can take place. The R11410-20 PMTs used in the Screener have 12 dynode stages. In general, a PMT with N dynodes will have a gain, G, given by

$$G = c\delta^N, \tag{5.5}$$

where c is a constant. The secondary electron yield is a function of the incident electron energy, which is determined by the inter-dynode electric field. If we assume that all dynode stages are approximately the same, then this electric field is proportional to the overall bias voltage on the PMT, V, and we may write:

$$G = \beta V^\alpha. \tag{5.6}$$

Taking the logarithm of both sides we obtain the equation of a line in $\log G$ vs $\log V$

space.

By taking single photoelectron data at various bias voltages we can create "gain curves" that characterize the PMT and are useful for predicting the gain of the PMT at different voltages. The gain of the PMT is calculated using the measured mean single photoelectron size, x_0, as:

$$G = \frac{x_0[\mathrm{mV\,ns}]}{AR_{\mathrm{eff}}[\Omega]\, q_e[\mathrm{C}]} 10^{-12}. \tag{5.7}$$

Here, R_{eff} is the effective resistance seen by the current pulse caused by a single photoelectron. In the case of the Screener PMTs, a 50 Ω resistor is used on the PMT base, which is connected to coaxial cable with a characteristic impedance of 50 Ω. The effective resistance to use is therefore the parallel combination of two 50 Ω resistors, or, 25 Ω. q_e is the charge of the electron in Coulombs. The factor A included here is the gain of the amplifier used. Gain curves for the three Screener PMTs are shown in Fig. 5.10.

While performing tests at UCSB, the following bias voltages where used:

PMT1: 1,520 V

PMT2: 1,468 V

PMT3: 1,517 V

resulting in a gain of 2.6×10^6 assuming a single photoelectron size of 418 mV ns and amplifier gain of 40.

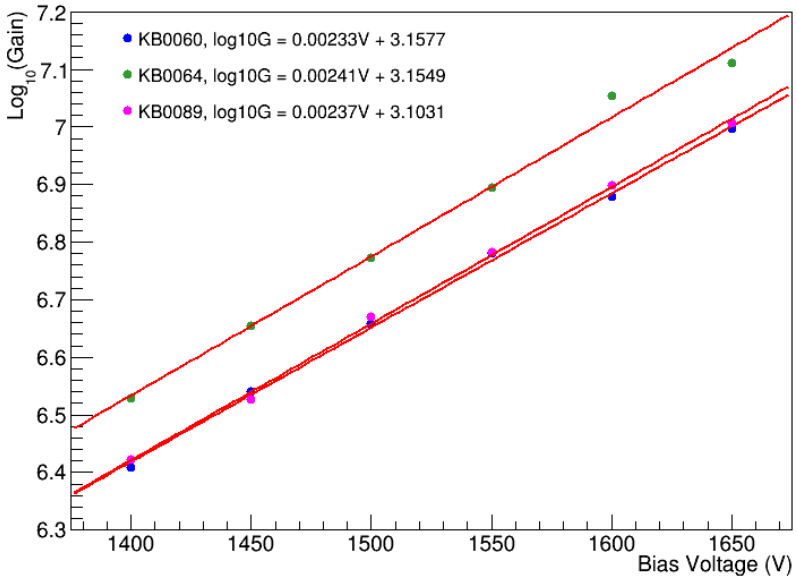

Figure 5.10: caption.

5.3.3 Tagging Muons Through the Screener

The flux of cosmic-ray muons that forces low-background experiments such as LUX and LZ to operate underground can serve as a useful calibration source. After the Screener's water buffer was filled, it was realized that tagging vertical through-going muons may provide useful insights into the detector performance and help calibrate parameters used in the simulation of the detector. Before describing the experimental setup, I first review some basic properties of cosmic-ray muons at sea level and Cherenkov light, both discussed in greater detail in [113].

At sea level, muons are the most abundant charged particles. Created primarily through charged meson decay in the upper atmosphere, the muons at sea level have a mean energy of ~ 4 GeV. The integrated flux of vertical muons with momentum greater

than 1 GeV/c is ≈ 70 m^{-2}s^{-1}sr^{-1}, which gives rise to the commonly known number of ≈ 1 cm^{-2}min^{-1} for a horizontal detector (an experimentalist would say "about one muon through the palm of your hand per second"). The angular distribution for muons with energies ~ 3 GeV goes like $\propto \cos^2\theta$.

In a material, muons of these velocities will deposit energy via ionization and excitation of the atoms and molecules of the medium. These muons are "minimum ionizing particles", and a typical energy loss given is $\sim$2 MeV/cm. Additionally, however, muons at these energies will create Cherenkov photons as they pass through a material with index of refraction, n, sufficiently different from 1. The threshold velocity to create Cherenkov light is $\beta_t = 1/n$, corresponding to muon threshold energies of 53 MeV in water ($n = 1.338$ for $\lambda = 425$ nm) and 37 MeV in acrylic ($n = 1.485$ for $\lambda \approx 425$ nm).

The number of Cherenkov photons produced along a charged particle's (with charge ze) track per unit length and per unit of photon wavelength is

$$\frac{d^2N}{dxd\lambda} = \frac{2\pi\alpha z^2}{\lambda^2}\left(1 - \frac{1}{\beta^2 n^2(\lambda)}\right). \tag{5.8}$$

In particular, two important conclusions can be made from this equation:

1. The total number of photons produced, N, is simply proportional to the total path length of the particle track in the material.

2. Ignoring the wavelength dependence of n for a moment, the distribution of photons produced goes as $\propto \lambda^{-2}$, which favors shorter wavelengths over longer wavelengths.

The first of these justifies the use of muon-generated Cherenkov light as an "absolute

calibration source", meaning, we do not need to worry about any additional parameters that govern the number of photons created, such as scintillator light yield and quenching effects. The second is important for modeling the expected signal from through-going muons. The absorption spectrum of the surrounding materials, the reflectivity of surrounding materials, and the spectral response of the PMT (or, in general, any light detection device) must all be properly accounted for in the detector model.

Experimental Setup

To tag muons through the Screener, two solid scintillator paddles, each with a mounted PMT, were used. The dark box holding the Screener was placed on top of the larger paddle with approximate (the true paddle shape was that of a rectangle plus a trapezoid) dimensions of 30" wide × 62" long × 2" thick, while a much smaller paddle, with approximate dimensions of 4" wide × 7" long × 1" thick, was placed on top of the dark box positioned over the center. This setup is shown in Fig. 5.11.

The PMT signals from each paddle were fed into a LeCroy 623B discriminator unit. From the known muon flux at sea level, an estimate of the muon rate in each paddle was made: about 2.4 Hz in the small paddle and about 180 Hz in the large paddle. The discriminator threshold was then set so that the observed trigger rate above threshold from each paddle is slightly less than the expected rate. The discriminator logic outputs were then fed into a LeCroy 465 coincidence unit, set to generate a logic output pulse if both paddles break threshold within a 100 ns time window. The coincidence unit output pulse was then connected to channel 0 of the DAQ where it could serve as an external

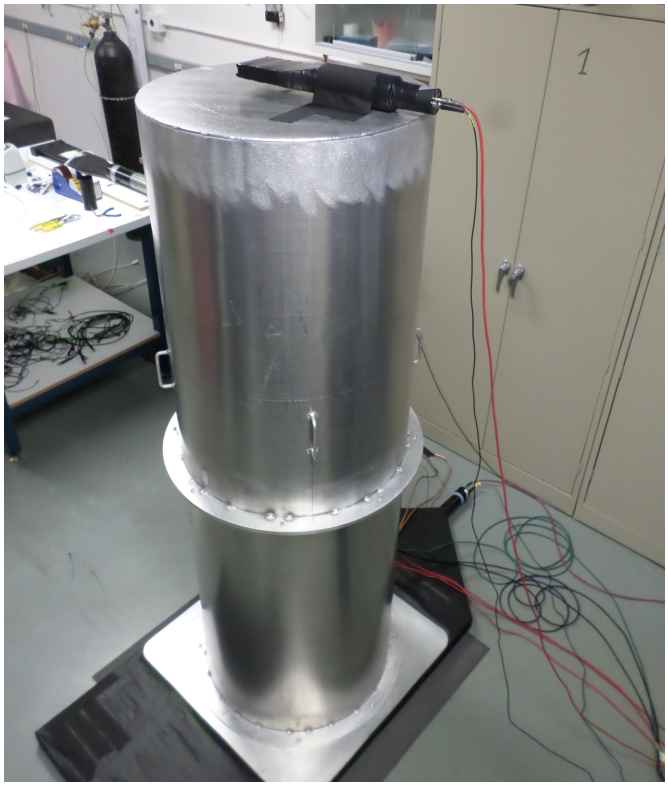

Figure 5.11: The arrangement of two scintillator paddles above and below the Screener dark box. In some datasets, the top paddle was arranged vertically to better constrain angular variance of tagged muons.

trigger.

The primary datasets of interest were collected with the detector in three configurations. First, with the water buffer filled and the PMTs mounted, data was taken without the Tyvek reflector. Next, the detector was covered with 1085D Tyvek reflector. The final dataset was taken with the Tyvek around the main cylindical side replaced with the thicker, multi-layer Tyvek mentioned in the previous chapter.

Results

The primary result is summarized in Fig. 5.12 which shows the summed spectrum of collected photoelectrons in each of the three detector configurations for events with a muon tag. In each configuration the tagged muons form a clear peak consistent with a reasonably well-constrained path length through the acrylic and water. A sharper peak could be obtained by using a smaller scintillator paddle under the detector. Events at low pulse area are believed to result from muons which clip the acrylic vessel, but are still tagged by the bottom paddle. Those at higher pulse area are thought to have close proximity to or gone straight through the PMT faces.

The improvement in light collection by adding Tyvek is roughly a factor of two as indicated by the clear shift in the peak position. Using the thicker Tyvek around the detector body improves the light collection further, but only by 4.5 % compared to the 1085D Tyvek.

A model of the muon tagging setup was created in LUXSim. A visualization of the geometry is shown in Fig. 5.13b. To simulate tagged events, muons of energy 3 GeV are started in the top scintillator paddle volume and shot downward with polar angles biased to have a $\cos^2\theta$ dependence. In analysis events with nonzero energy in the bottom paddle are then selected. Fig. 5.13a shows a comparison of the simulation to data with no Tyvek reflector around the detector. Also shown is the effect of turning off δ-ray radiation in the simulation.

Simulations of tagged muon events were compared to data with Tyvek reflector around

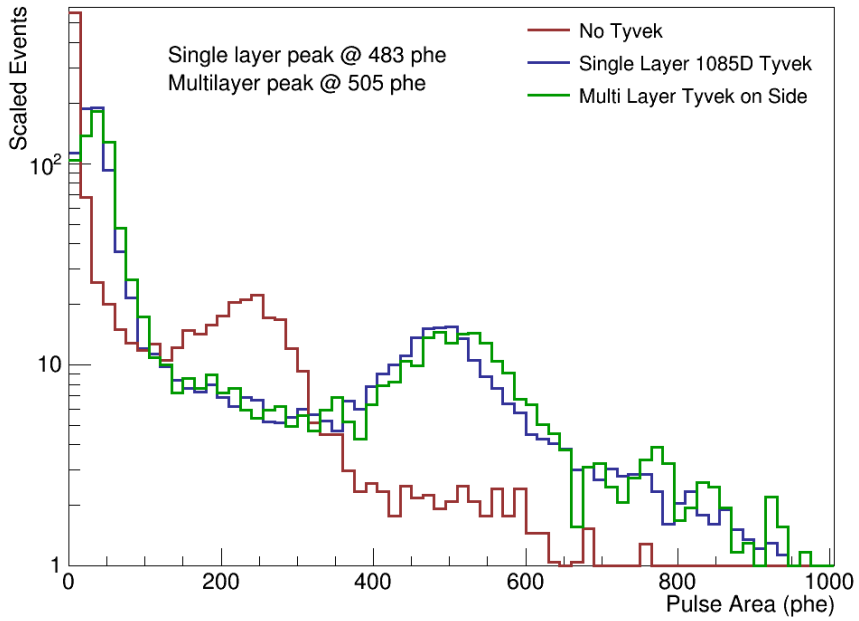

Figure 5.12: Spectrum of collected photoelectrons for events tagged by the muon paddles in the three reflector configurations discussed in the text.

the detector. An overall scale factor on the wavelength-dependent Tyvek reflectivity was adjusted until the peak position in the simulated spectrum was in good agreement that in data as shown in Fig. 5.14. The scale factor was found to be 1.01, i.e. the reflectivity at all wavelengths was increased by 1 %.

5.3.4 Testing a Thoron Calibration Source

During the post-Run 4 LUX calibration campaign, a flow-through source was built and used to inject thoron (^{220}Rn) into the Xe circulation path to internally calibrate LUX. It was realized that this same source could be used to calibrate the Screener by using nitrogen as the carrier gas to bubble thoron into the LS.

The source is constructed as shown in Fig. 5.15. A disk electroplated with ^{228}Th

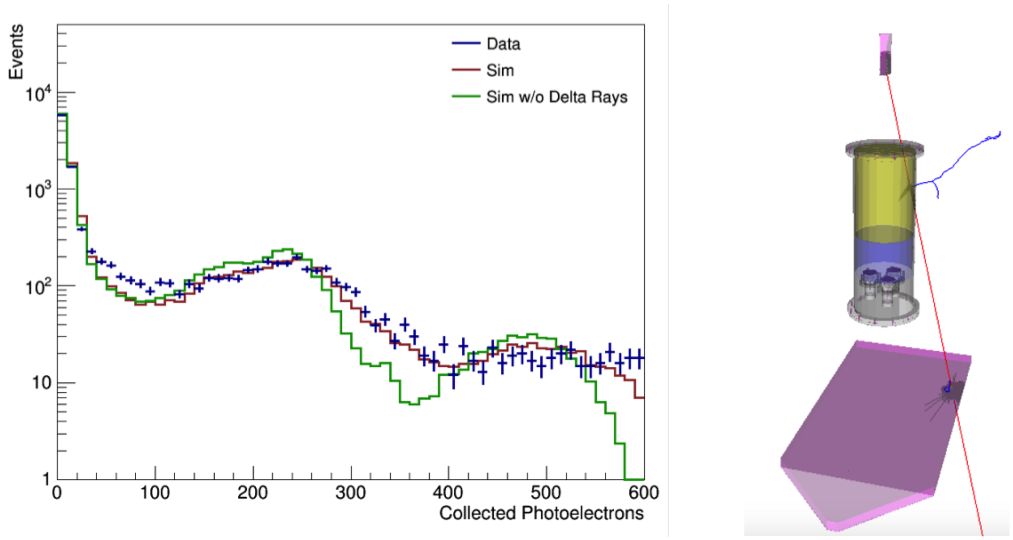

(a) (b)

Figure 5.13: (a) Comparison of collected pulse area spectra in data and simulation with and without δ-ray effects turned on. (b) Visualization of muon tagging geometry implemented in the simulation. The primary muon track is shown in red with optical photons shown in grey. δ-rays created in the acrylic and bottom paddle are shown as blue tracks.

manufactured by Eckert & Ziegler [114] is secured into a chamber of conflat plumbing. In order to ensure there is no contaimination of ^{222}Rn via the $4n+2$ chain, the ^{228}Th is created by allowing artifically made ^{232}U to decay.

Thoron gas is created two decays after ^{228}Th in the $4n$ chain. As a noble gas, it is then free to diffuse throughout the volume surrounding the source. A flow of nitrogen gas through the plumbing and into the Screener LS volume allows calibration of the detector response to energy deposits from α's, β's, and γ's resulting from the decays of thoron and its decay products. The signals from the thoron source have a distinct time dependence: while nitrogen gas is flowing, a merged peak from the α-decays of ^{220}Rn and ^{216}Po appear due to their relatively short half-lives (55 s and 0.14 s, respectively). These peaks promptly disappear once nitrogen flow is stopped. The population of daughter

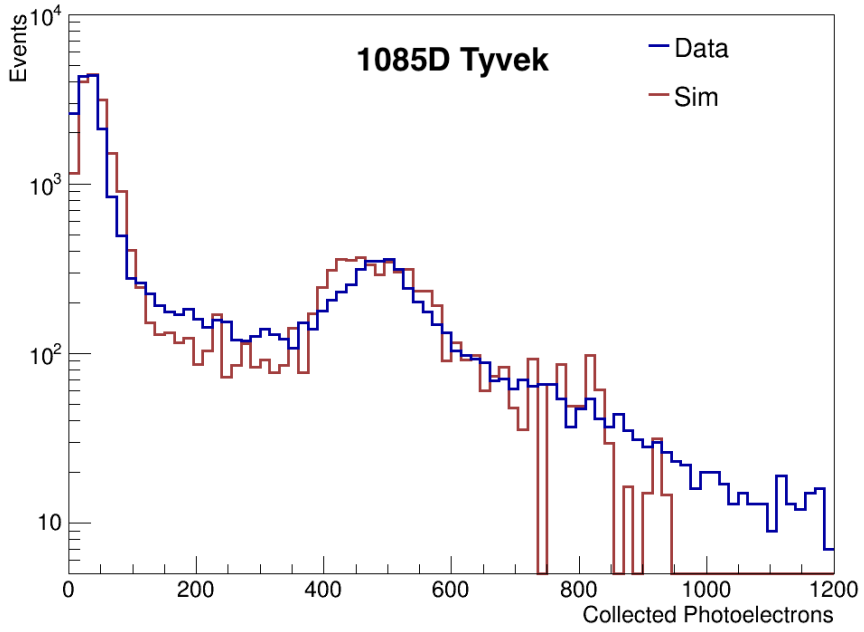

Figure 5.14: Comparison of muon tagged data and simulation with the Tyvek reflectivity scaled up by 1 %.

^{212}Pb atoms then feeds the rest of the chain according to its 10.6 h half-life. After a suitable amount of time (depending on the amount of thoron bubbled in), no signals from the source remain.

Implementation in the Screener

The ability to bubble thoron-spiked nitrogen gas into the Screener was achieved by constructing a line of concentric plastic tubing that could mait to the existing PTFE fittings used for LS filling. A line of 1/4" diameter polyethylene (PE) tubing was used to carry incoming nitrogen gas inside the larger PTFE tubing used for LS filling. At the top of the LS chamber, a barbed fitting was used to mait the PE tubing with a rigid tube of PTFE approximately 43 cm in length and with inner diameter ≈3 mm. The PTFE tube

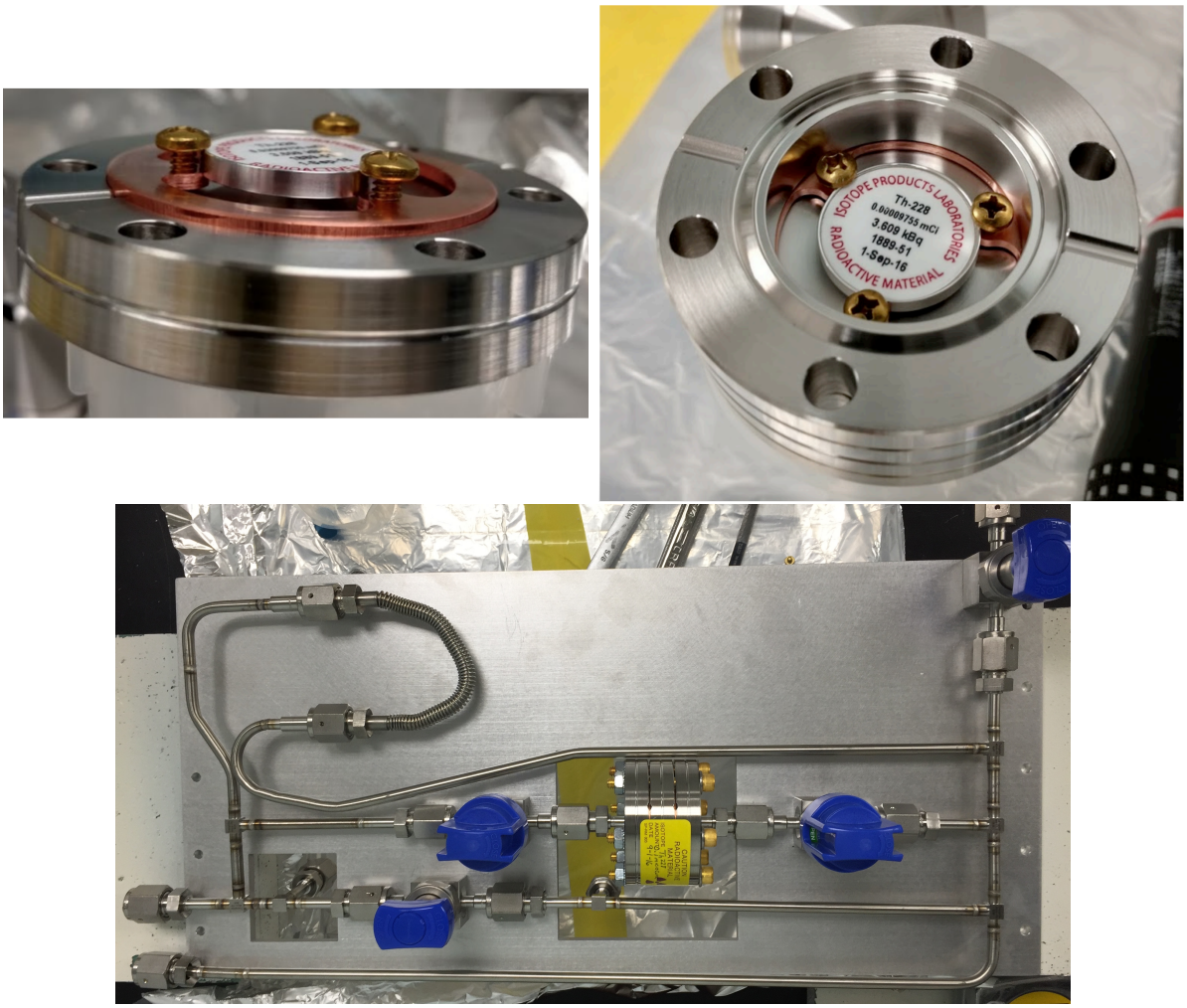

Figure 5.15: Internals and panel mount of the flow-through thoron source. Photos by S.A. Hertel.

extended to nearly the bottom of the LS chamber. Nitrogen bubbled out the end of the tube was then vented between the inner PE tubing and the outer PTFE tubing. At the other end, the concentric tubing was converted to separate input and vent lines via a PVC T-connector. This design would allow for a single gas line to be attached to the Screener during deployment in the water tank and avoid having to drill and tap another hole in the LS chamber lid.

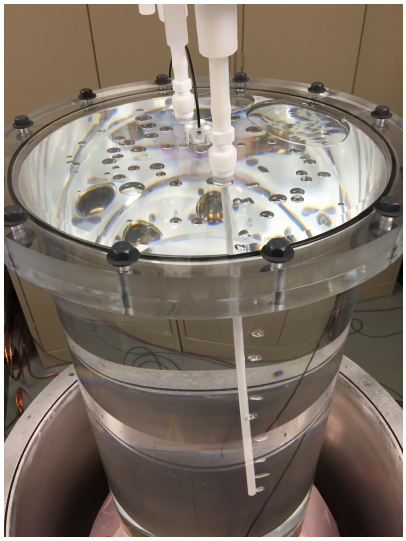

(a)

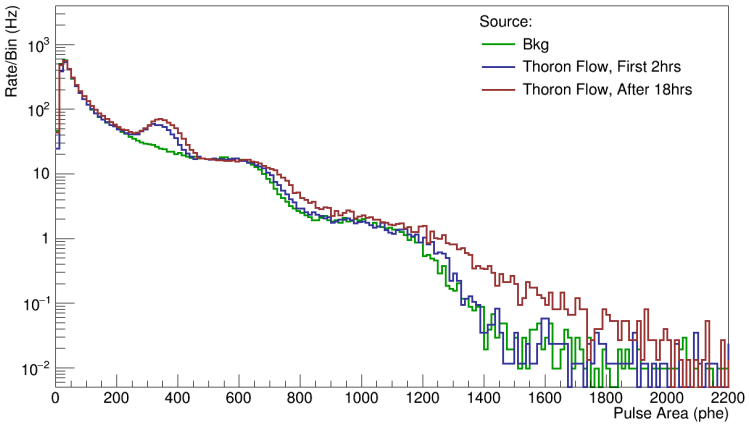

(b)

Figure 5.16: (a) Demonstrating the concentric tubing design for bubbling nitrogen gas. (b) Data collected while bubbling with the thoron source.

A sucessful demonstration of this design is shown in Fig. 5.16a. Once nitrogen gas was successfully bubbled in, the thoron source was plumbed into the input and data was taken during active bubbling of the LS for approximately 20 h with the detector wrapped in 1085D Tyvek. Those data are shown in Fig. 5.16b where a clear peak above backgound from the merged ^{220}Rn and ^{216}Po α's is seen during bubbling. After 18 h, the influence of more energetic β's below ^{212}Pb is observed at large pulse areas.

Chapter 6

Measurement of GdLS Radioimpurities using the LS Screener

From early November 2016 to the end of February 2017, data was taken with the Screener deployed the LUX water tank. Two batches of LS were counted: the first was the GdLS planned for use in the OD, while the second was LS without Gd loading. The goal of these runs was to measure the levels of radioimpurities in each LS batch. Additionally, at the end of each run the detector was moved to different positions in the water tank to measure the change in count rate with vertical position. This data provided a useful cross-check of the assumed activities of the Davis cavern rock. In this chapter I discuss the collection and analyses of these data, the results, and their implications.

6.1 Underground Commissioning and Deployment

The Screener was shipped empty to the Davis Laboratory, where it was filled and commissioned in the Davis Laboratory cleanroom. When work was not being performed, the detector was kept in its dark box, continuously purged with nitrogen gas in order to limit exposure to the $\approx$300 Bq/m^3 [115] radon level in the Davis Laboratory air. The detector stand was mounted on a rail cart allowing safe transport out of the cleanroom once commissioning was completed.

6.1.1 Cleanroom Commissioning

The water buffer volume was filled using the same distilled-deionized water used at UCSB. The PMTs were then mounted (Fig. 6.1) and the PMT cable feedthroughs were prepared. Each PMT cable was fed through a custom Delrin feedthrough and potted against the cable using marine epoxy. Additionally, a marine sealant was used on each end of the feedthrough to allow a more flexible seal to be maintained. Each feedthrough screws into the acrylic PMT chamber lid. These connections are shown in Fig. 6.2 along with the zip-tie connections to each cable for strain relief. The acrylic lid is then held over the PMT chamber while connections to the PMT bases are made. An additional zip-tie connection for each cable inside the chamber prevents movement of the cable at the PMT base.

Before filling with the LS to be counted, the LS chamber was rinsed with purified LAB. This was also done between runs to prevent cross-contamination of the LS batches.

The Screener was then filled according to the procedure outline in the previous chapter. Nitrogen gas displaced from the chamber during LS filling was allowed to vent through the concentric tubing installed for thoron calibrations. The Screener was then wrapped in 1085D Tyvek.

Figure 6.1: SJH mounting PMTs inside the underground cleanroom.

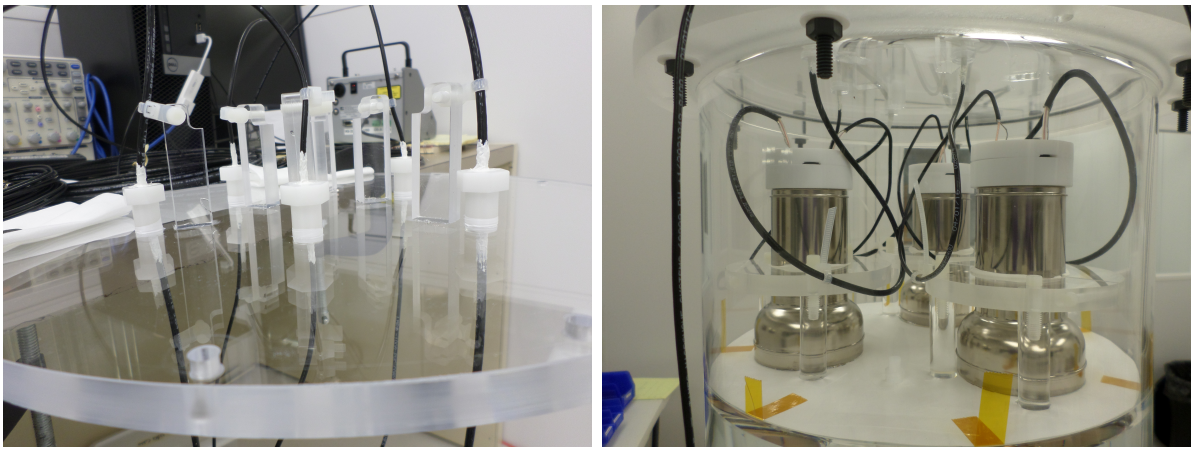

Figure 6.2: Left: The Delrin feedthroughs screwed into the acrylic PMT chamber lid. Right: The PMTs mounted with cable connections to the PMT bases made.

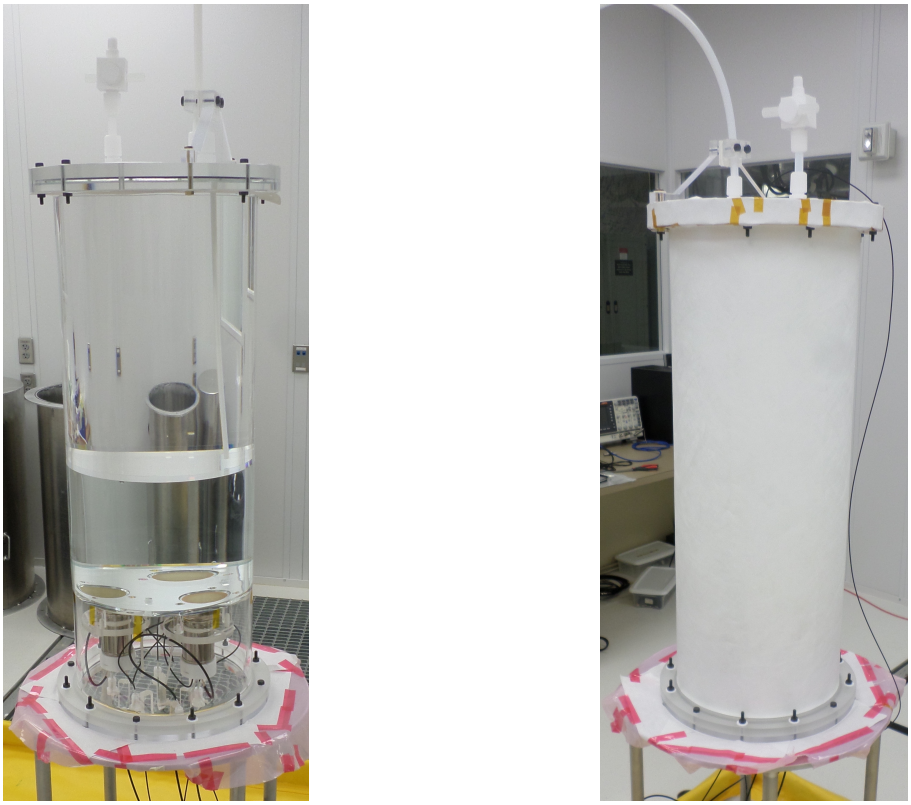

Figure 6.3: *Left:* The detector in the Davis Laboratory cleanroom with PMTs mounted, water and LS chambers filled. *Right:* The detector wrapped with Tyvek reflector before deployment.

6.1.2 Water Tank Deployment

To deploy the Screener in the water tank, the detector was rolled out of the cleanroom and lifted off its stand using an overhead hoist. Polyethylene ropes were used to suspend the detector assembly inside the water tank. A 20 kg ballast of the ultra-pure titanium [116] making up the LZ cryostat vessels was suspended ≈80 cm from the bottom of the vessel to counteract the vessel buoyant force and to provide stability. Custom Delrin brackets were used to connect the ropes to the Screener's top and bottom flanges.

The 13.7 m long RG174 and RG58 coaxial cables providing PMT signal and HV were zip-tied to the vessel's top and bottom flanges and routed out of the water tank through light-tight cable grips installed in the water tank port. The cables were then connected to the HV power supply and data acquisition system (DAQ) in a nearby electronics rack. Fig. 6.4 shows photographs of the Screener during its first deployment.

Fig. 6.5 shows a diagram of the Screener assembly depolyed in the water tank. The tank height is 591 cm, and its radius is 381 cm. An inverted steel pyramid underneath the tank of maximum thickness 30.5 cm and diameter 500 cm provides additional shielding from the rock in the floor. As LUX had just been removed, its stainless steel detector stand was present in the water tank during the Screener deployment.

The vertical position in the water tank was chosen to minimize the rate from external γ's originating from the LUX detector stand and from the Davis Laboratory walls. The γ's from ^{238}U, ^{232}Th, ^{40}K, and ^{60}Co decays were described with a GEANT4-based [44] simulation package. At this location, there was 160 cm (366 cm) between the bottom

(top) of the detector scintillator volume and the bottom (top) of the water volume. The estimated stand and wall contribution to the Screener rate is (0.57 ± 0.03) mHz above an energy deposit threshold of 100 keV [94].

The resistivity and dissolved oxygen in the water was monitored during runs. An earlier measurement of radon in the nitrogen used to purge the water tank found a concentration of $(0.054 \pm 0.026)\,\mathrm{Bq/m^3}$ while the dissolved oxygen was below the 1 ppb sensitivity of the oxygen monitor. Simulations predict a rate of (3.6 ± 1.7) mHz above 100 keV from ^{222}Rn decays in the water at this concentration.

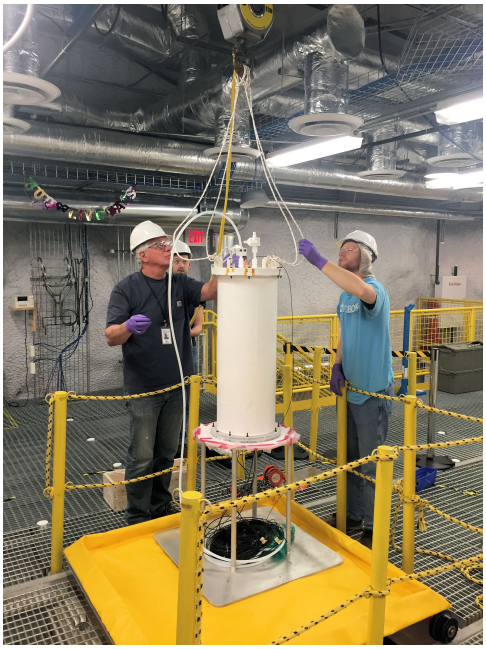

(a)

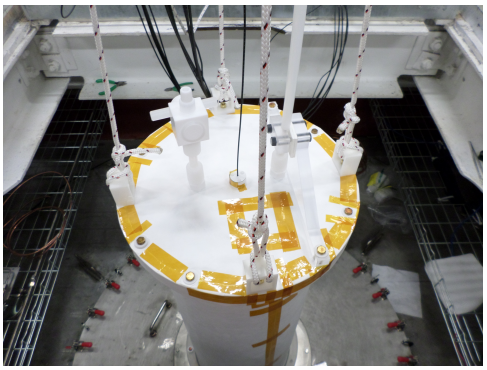

(b)

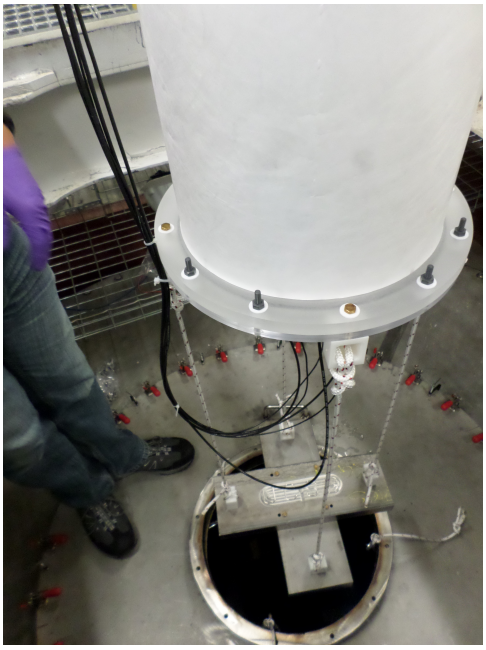

(c)

(d)

Figure 6.4: Photos during Screener deployment: (a) The attaching the detector to the overhead hoist. (b) Top view of the detector showing the attachment of the ropes and the acrylic support bracket for the thoron calibration line. (c) Bottom view showing the Ti ballast attachment and the arrangement of the PMT cables. (d) Guiding the detector into the water tank.

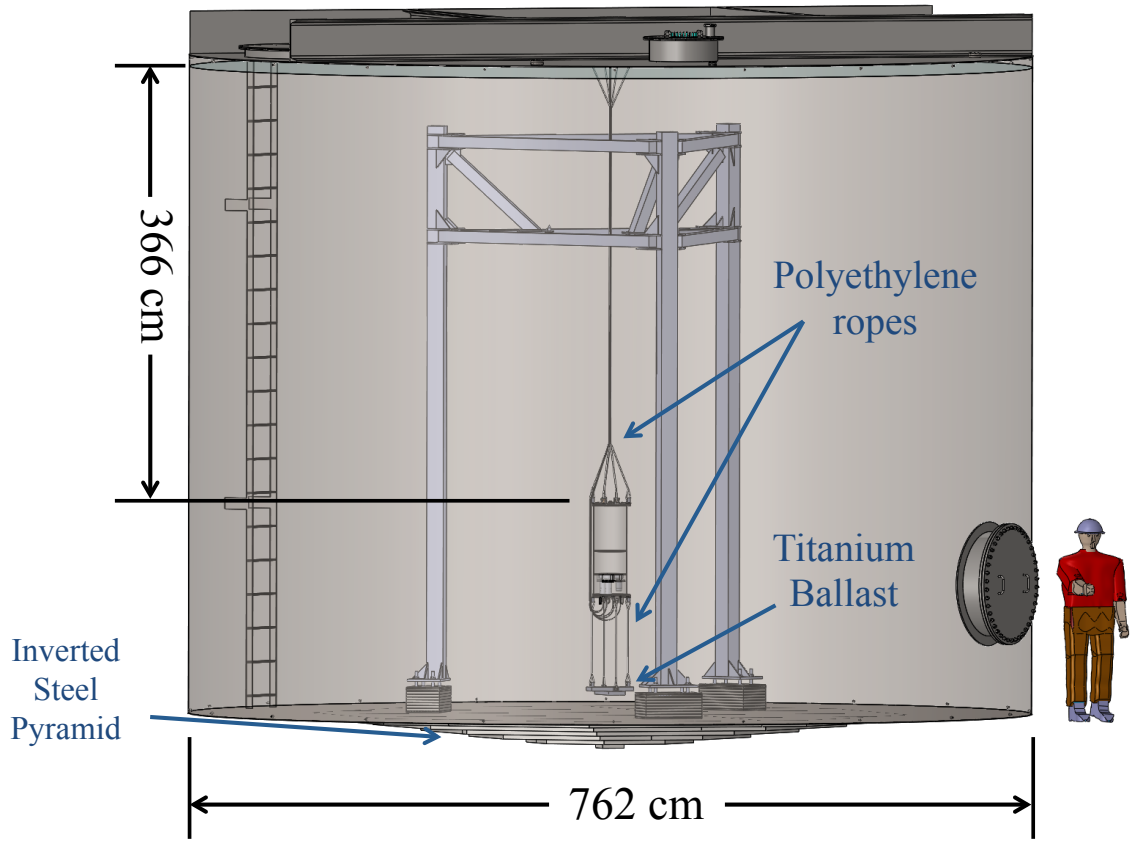

Figure 6.5: Deployment of the Screener in the water tank. The stand for the LUX detector is visible along with the inverted steel pyramid underneath the water tank floor.

6.2 Data Collection and Calibrations

Data was taken in two runs. "Run 1" data were taken between November 2016 and early January 2017, using 23.7 ± 0.1 kg of GdLS. Data in "Run 2" were taken between mid-January 2017 and February 2017, using the same scintillator mixture, but without Gd loading. In Run 2 the LS mass was 23.2 ± 0.1 kg. In this section I provide an overview of each run's timeline and relevant calibrations, primarily calling attention to major changes in the detector state or settings used.

The first data collected in both runs show a peak from dissolved ^{222}Rn. This is believed to result from exposure of the LS to a small amount of underground air during filling. As a result, each run is comprised of two broad data collection periods: one in which the rate is decreasing in time from residual ^{222}Rn decays and one in which the rate has plateaued to a nearly constant level. In this thesis, data collected during the latter periods are referred to as "low-background data". Ultimately, the goal of Screener data analysis is to understand the various sources contributing to the low-background data rate. Plots of the collected pulse area spectra at various times throughout each run are shown in Fig. 6.6.

Because ^{222}Rn decays with a 3.8 d half-life, its rate and the rate from its short-lived daughters do not directly impact the ultimate performance of the experiment as we can just wait for it to decay away. In contrast, the background from radon in LZ results from its steady state emanation from materials, so radon and its short-lived daughters *do* directly influence the experiment's ultimate background rate. The primary concern

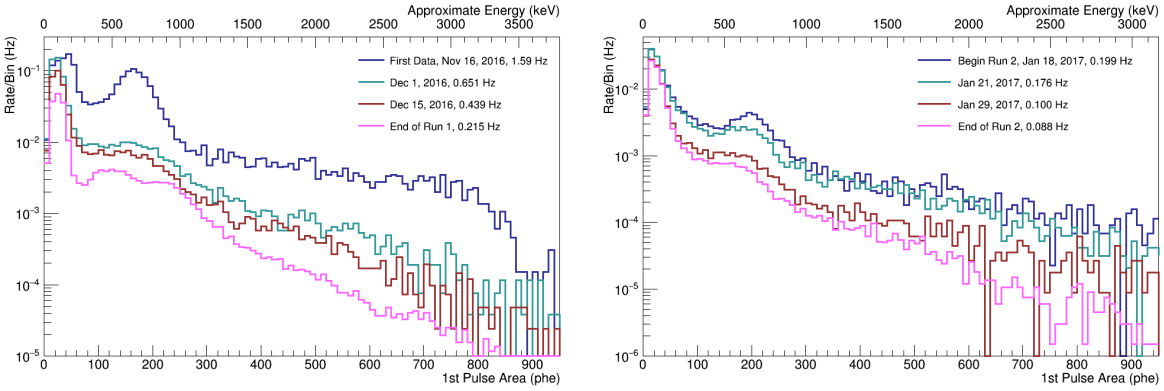

Figure 6.6: Collected pulse area spectra at various times during Run 1 (left) and Run 2 (right). The α peak from ^{222}Rn decays is visible at the beginning of each run.

with dissolved radon in the LS is the build-up of long-lived ^{210}Pb with half-life of 22.2 y. This isotope feeds the rest of the $^{238}\mathrm{U_l}$ subchain, containing an energetic β and α from ^{210}Bi and ^{210}Po, respectively. A fixed number of radon atoms, N_{Rn}, in the LS results in a rate, R_{Rn}, of radon decays, which lead to the creation of the same number of ^{210}Pb atoms. The resulting ^{210}Pb rate will be

$$R_{\mathrm{Pb}} = \frac{N_{\mathrm{Pb}}}{\tau_{\mathrm{Pb}}} = R_{\mathrm{Rn}} \frac{\tau_{\mathrm{Rn}}}{\tau_{\mathrm{Pb}}}. \tag{6.1}$$

The ^{210}Pb rate is therefore suppressed by a factor of $(\tau_{\mathrm{Rn}}/\tau_{\mathrm{Pb}})^{-1} \approx 2132$ compared to the initial ^{222}Rn rate.

At the beginning of Run 1, the raw trigger rate was 2.3 Hz. After approximately 21 days the trigger rate had plateaued to 0.3 Hz. The trigger rate at the beginning of Run 2 was 0.32 Hz. After 14 days the plateaued trigger rate was 0.16 Hz. The smaller contamination from radon in Run 2 was a result of an improved LS filling procedure.

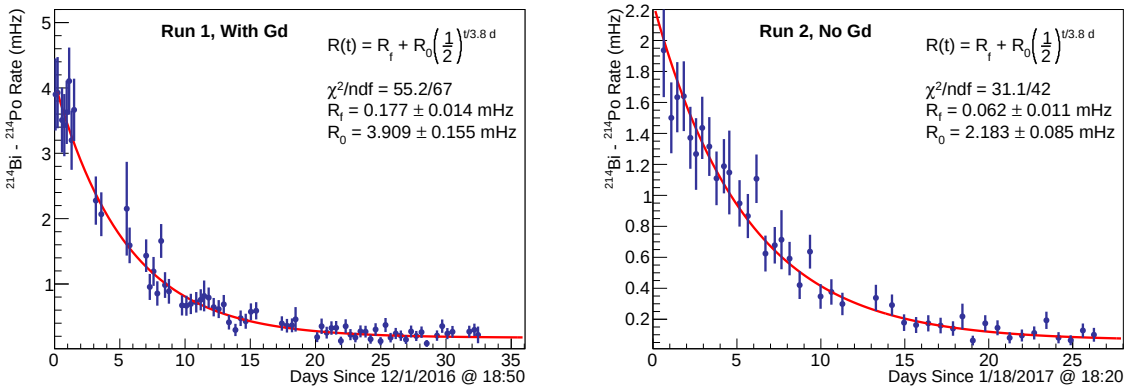

Figure 6.7: Rate of ^{214}Bi-^{214}Po coincidences as a function of time since start of each run fit with the expected dependence from ^{222}Rn decays.

6.2.1 Run 1: Gd-Loaded LS

A timeline for Run 1 is shown in Fig. 6.8. Data taking began on November 16, 2016 with the Screener in the optimal vertical position in the water tank. As described above, a prominant peak from ^{222}Rn was present. While opening the water tank port to perform a γ calibration the following day, it was noticed that some of the plumbing for the thoron calibration tube had been compromised due to improper strain relief. This was repaired immediately. Before the end of the day, a first thoron calibration was performed. Nitrogen infused with thoron was bubbled into the Screener for ≈ 25 minutes while data was being acquired.

Two days later, it was noticed that peaks in the collected pulse area spectra had shifted indicating a sudden change in PMT gain. The next set of PMT calibrations showed that this was in fact the case, and the detector was pulled out of the water tank. Upon inspection of the PMT chamber, leaks in the NPT cable feedthroughs were discovered. A small ($\sim$100 cm^3) amount of water had leaked into the chamber, resulting in

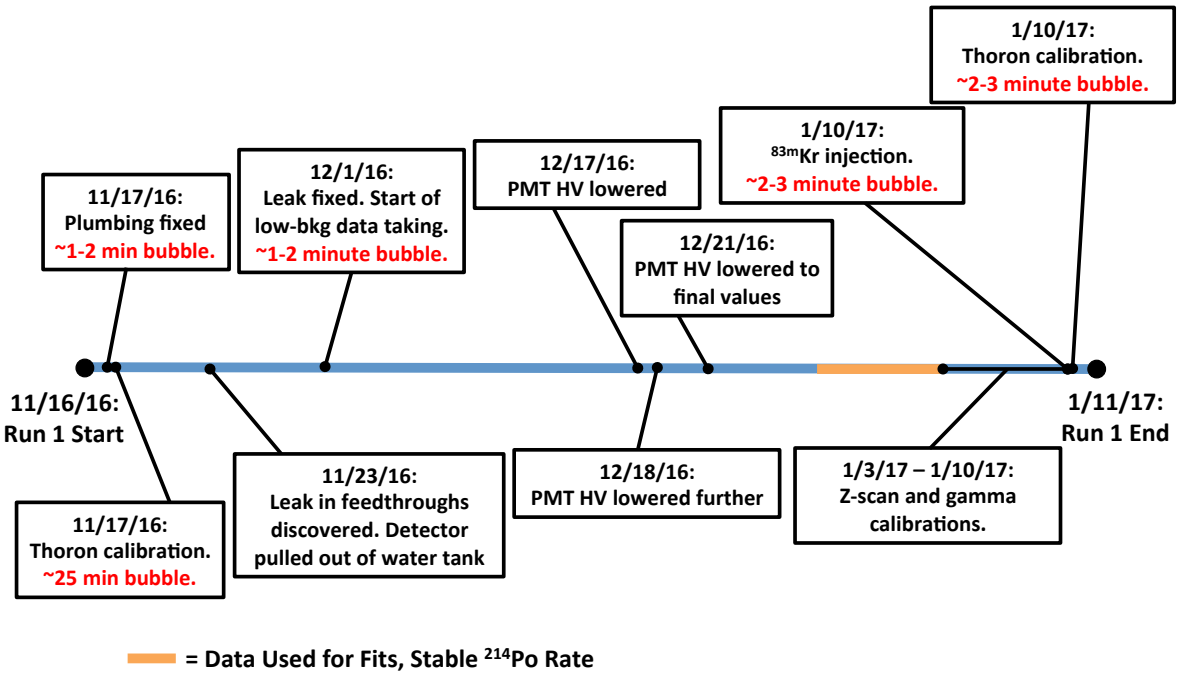

Figure 6.8: Timeline of Run 1 showing significant changes in detector conditions. Instances of nitrogen bubbling are shown in red text with their estimated bubbling duration.

an increase in humidity which likely changed the PMT gain. The detector was suspended over the closed water tank lid while the water was dried and sealant was added around the feedthroughs. Seven days later, it was determined that the leak was fixed after having the detector submerged back in the water tank for three days with no leaking observed. Data taking after this repair was relatively smooth.

At the end of the run, a series of calibrations were done. First, γ source calibrations were performed (see Sec. 6.2.4). Then, the same ^{83m}Kr used in LUX was bubbled in as its source was plumbed into the thoron source panel. This was mostly for fun to see if the low energy decays could be detected. Roughly 6 hours later, the second thoron calibration was done.

PMT Light Emission

Diagnostic datasets were taken early in the run in which only two PMTs were used to form the coincidence trigger. That data revealed a higher trigger rate when PMT2 was included in the coincidence. A hypothesis was formed that PMT2 might be emitting photons during the dynode amplification of photoelectrons from the photocathode, an effect known as "flashing". Evidence for light emission in the R11410-20 PMT had, in fact, been noted elsewhere [117]. In particular, the effect was found to be dependent on the PMT HV, low voltages resulting in less flashing.

To confirm this hypothesis, the background data were investigated on a type of "Dalitz plot", which shows, for each event, the fraction of total collected pulse area in each PMT. In the Screener we expect that on average the light will be shared equally among all three PMTs. If a PMT is detecting its own light from flashing, an asymmetry in the Dalitz plot should be present. This can be seen in Fig. 6.9a which shows background data collected at the bias voltages used at UCSB. Once this was discovered, the PMT HV was lowered sequentially. The improvement with decreased bias voltage can be seen in Figs. 6.9b and 6.9c. The bias voltages used in each step are given in Tab. tab:HV. The "Low HV" values were used for the rest of Run 1 and for all of Run 2.

Table 6.1: PMT bias voltages used early in Run 1. Low-background data was collected using the "Low HV" values in both runs.

PMT Number	High HV (V)	Intermediate HV (V)	Low HV (V)
1	1520	1475	1385
2	1397	1353	1282
3	1517	1473	1377

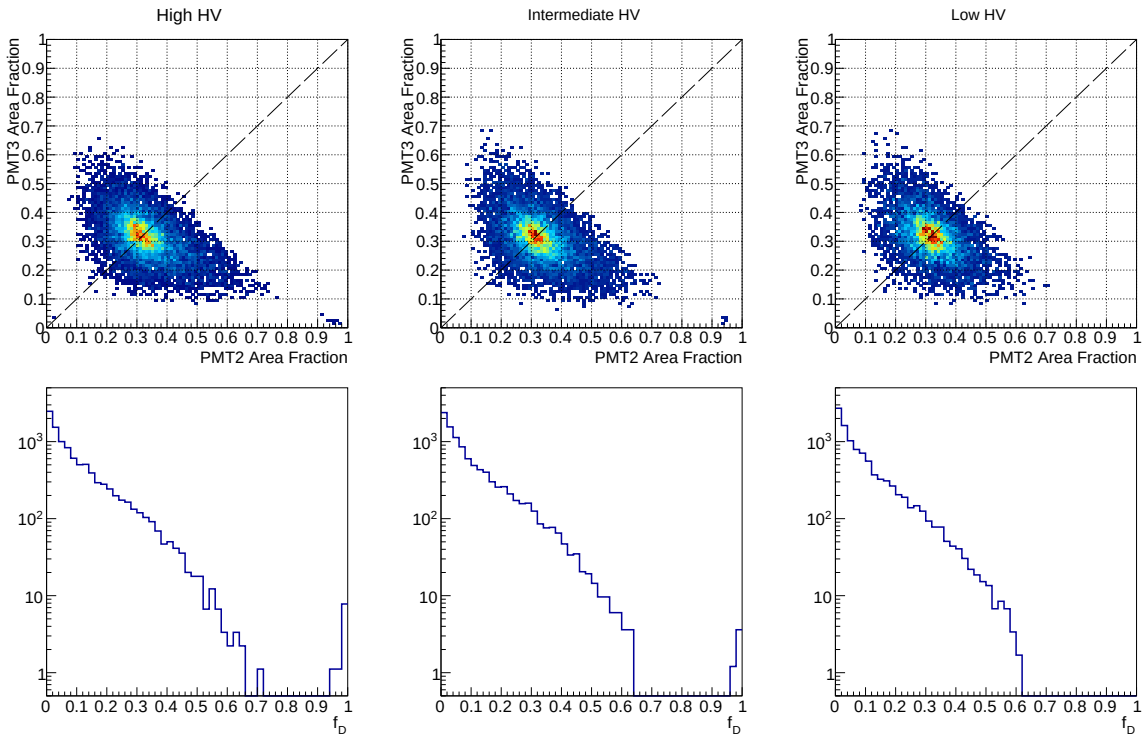

Figure 6.9: Dalitz plots of pulse area fraction in each PMT and associated f_D distributions for (a) high, (b) intermediate, and (c) low values of PMT bias voltages. The improvement in symmetry with decreasing HV is noticable.

Ideal event distributions in this space can be described using the following function:

$$f_D = 1 - 27\left[f_{A2}f_{A3}(1 - f_{A2} - f_{A3})\right], \tag{6.2}$$

where f_{Ai} is the fraction of total event area in PMT i. This function is normalized so that a completely symmetrical event, with one-third the total event area appearing in each PMT has $f_D = 0$, while an event with all its light in a single PMT has $f_D = 1$.

Lowering the PMT HV was the most effective method for reducing the flashing effect. To further prevent very asymmetrical events from being used in analysis, a data quality cut demanding $f_D < 0.8$ was used. Simulations of uniform energy deposits in the LS

verify that asymmetry in the Dalitz plots becomes more common below ≈200 keV, as flucuations in PMT area fraction increase due to an overall smaller number of photons being produced in the event. This is primarily a concern for measuring the ^{14}C content of the LS. However, the cut $f_D < 0.8$ is found to have >99.9 % efficiency for events with pulse area >20 phe which is the lower bound for the ^{14}C analysis.

6.2.2 Run 2: Unloaded LS

In mid-January 2017 the Screener was pulled out of the water tank back into the clean-room. The GdLS was removed and the LS chamber was rinsed with purified LAB before (23.2 ± 0.1) kg of unloaded LS was pumped in. The detector was then redeployed in the water tank at the same vertical position as in Run 1. Fig. 6.10 shows the timeline for Run 2 calling out changes in detector state and calibration activity. In general, the detector was left undisturbed so that the decay of dissolved radon could be monitored. The LS in Run 2 was exposed to less air during the filling process. This was largely due to better integrity of the LS bags inside the steel shipping drum. The result is a lower initial rate of ^{222}Rn decays and a higher LS light yield.

Besides the amount of LS in the detector, the other difference in detector setup was the arrangement of ropes and the cable bundle above the detector. The point where the four ropes join together was made closer to the detector top, allowing a higher vertical position in the water tank to be probed during z-scan data collection. This results in slightly higher predicted rates from radioactivity in the ropes and cables.

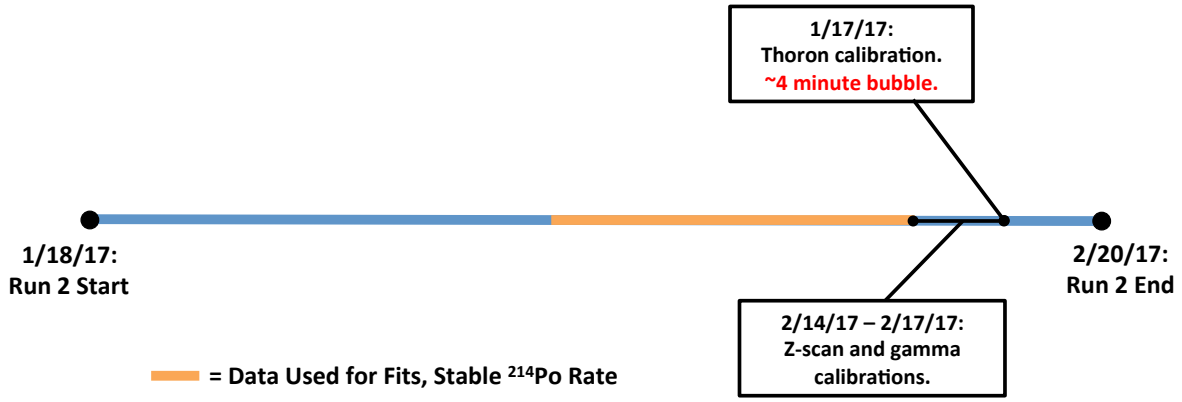

Figure 6.10: Timeline of Run 2 showing significant changes in detector conditions. Instances of nitrogen bubbling are shown in red text with their estimated bubbling duration.

Except for a single ^{22}Na calibration at the very beginning, all calibrations in Run 2 were performed at the end of the run.

6.2.3 PMT Calibrations

The response of the PMTs was monitored ∼weekly with single photoelectron calibrations performed using the method described in the previous chapter. Light from the 420 nm LED was fed through an optical fiber through the water tank port to the Screener to provide dedicated single photoelectron datasets. Sometimes these calibrations indicated drift in the PMT or amplifier response, so single photoelectron pulses in the midst of data taking were identified offline and used to correct drift in each dataset. The algorithm to find single photoelectron pulses in the event waveforms was implemented by S. Shaw. The single photoelectron size for each PMT, obtained during an LED calibration and obtained from the offline processing are shown as a function of date for both runs in

Fig. 6.11.

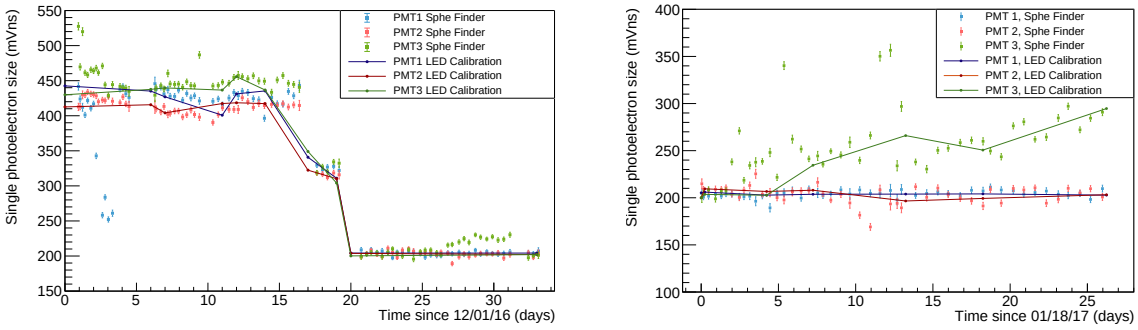

Figure 6.11: Single photoelectron size in each PMT in Run 1 (left) and Run 2 (right) obtained using LED calibration data (circles with lines) and offline processing (squares). Offline processing sizes are used to corrected all datasets. The large, decreasing steps of single photoelectron sizes in Run 1 are due to the reduction of the PMT bias voltages. Plots by S. Shaw.

6.2.4 Radioactive Source Calibrations

Sources used to calibrate the detector fall into two categories: external γ sources and the flow-through thoron source.

External γ Sources

^{137}Cs and ^{228}Th disk sources provide the principal electron recoil calibrations for tuning the detector response model. The ^{137}Cs source provides a γ-ray at 662 keV while ^{228}Th provides multiple γ's through decay of its daughters. The principle lines of interest are: 239 keV from ^{212}Pb and 583 keV and 2,614 keV, both from ^{208}Tl. Fig. 6.12 shows the spectrum of energy deposited in the LS from each source obtained from simulations. Data from a ^{22}Na source was also collected, but is not explicitly used in the main analysis.

The disk sources were placed in the tungsten collimator used for LUX γ-ray cali-

brations. The collimator had a 1.75 cm-diameter aperture during these calibrations. To deploy the source, the Screener was hoisted up to the water tank top, the collimator was placed on the Screener's top lid (aperture facing the LS volume), and the assembly was lowered back into the tank. The collected pulse area spectra from ^{137}Cs and ^{228}Th are shown below in Fig. 6.19. Simulations of these sources include the collimator geometry.

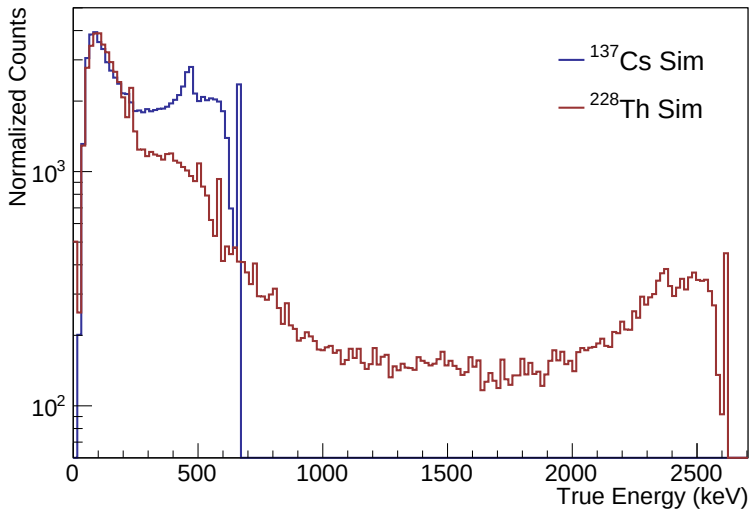

Figure 6.12: Distributions of true energy deposited in the LS from ^{137}Cs and ^{228}Th simulations showing the principle γ's absorbed and the distribution of Compton scatter events.

Thoron Source

The detector response to energy deposits from α's, β's, and γ's was calibrated using the thoron source described in Sec. 5.3.4. Of particular interest for tuning the detector response model are the α peaks provided by this calibration. A merged peak from ^{220}Rn and ^{216}Po is present while the gas is flowing. Data collected after the flow has stopped provides peaks from ^{212}Bi and ^{212}Po, the former through its direct α-decay (branching

ratio 36 %) and the latter by identifying the prompt ^{212}Po α's following the β-decay of ^{212}Bi (branching ratio 64 %).

In Fig. 6.13a raw pulse area spectra at different times during the Run 2 thoron calibration are shown in comparison to that of the low-background data. Peaks from ^{212}Bi and ^{212}Po α's are visible above a continuum of activity caused by β-decays of ^{212}Pb, ^{212}Bi, and ^{208}Tl. Fig. 6.13b shows the rate of ^{212}Bi-^{212}Po coincidences as a function of time since the nitrogen bubbling was stopped. The data clearly show the build-up of atoms in this part of the decay chain followed by decay according to the ^{212}Pb half-life of 10.6 h. This demonstrates that the later part of the chain comes in equilibrium with the ^{212}Pb population.

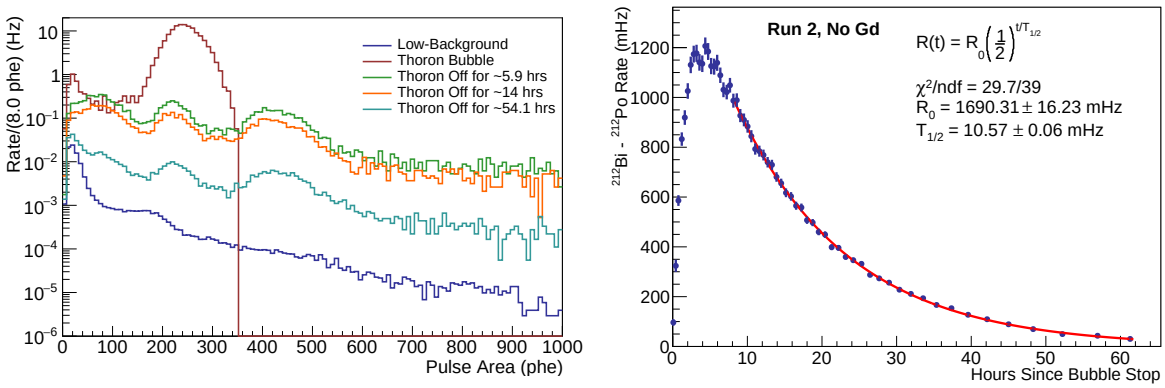

Figure 6.13: (a) Pulse area spectra collected during different periods of the Run 2 thoron calibration. For reference, the spectrum of low-background data is also shown. (b) Rate of ^{212}Bi-^{212}Po coincidences as a function of time since bubbling was stopped in the Run 2 thoron calibration. The 10.6 h half-life of ^{212}Pb is well constructed.

As described above, two thoron calibrations were performed in Run 1: the first after initial deployment of the detector and discovery of the PMT chamber leak and the second

prior to its removal. In Run 2, a single thoron calibration was performed prior to detector removal.

6.3 Detector Response Model

A detailed model of the detector geometry is implemented in the GEANT4-based BACCARAT framework used for LZ simulations. Visualizations of the detector geometry in the simulation are shown in Fig. 6.14. The detector simulation models the deposition of energy in the detector materials and the generation, propagation, and detection of optical photons born in the LS.

6.3.1 Optical Model

The optical model includes the wavelength-dependent emission and absorption properties of the LS discussed in Sec. 4.3.2. The acrylic absorption length and the indices of refraction for GdLS and acrylic are also included [88].

The model also includes the re-emission probability of the GdLS shown in Fig. 6.15. This is the probability that an absorbed photon of a given energy is re-emitted according to the bis-MSB spectrum in Fig. 4.11. We found that agreement between ^{228}Th γ calibration data and the simulation could only be obtained by including this effect in the optical response of the GdLS. The 2.6 MeV γ from this source produces Compton electrons above the 180 keV Cherenkov threshold in GdLS. With the addition of the re-emission process in the model, the far-UV Cherenkov photons that are more heavily

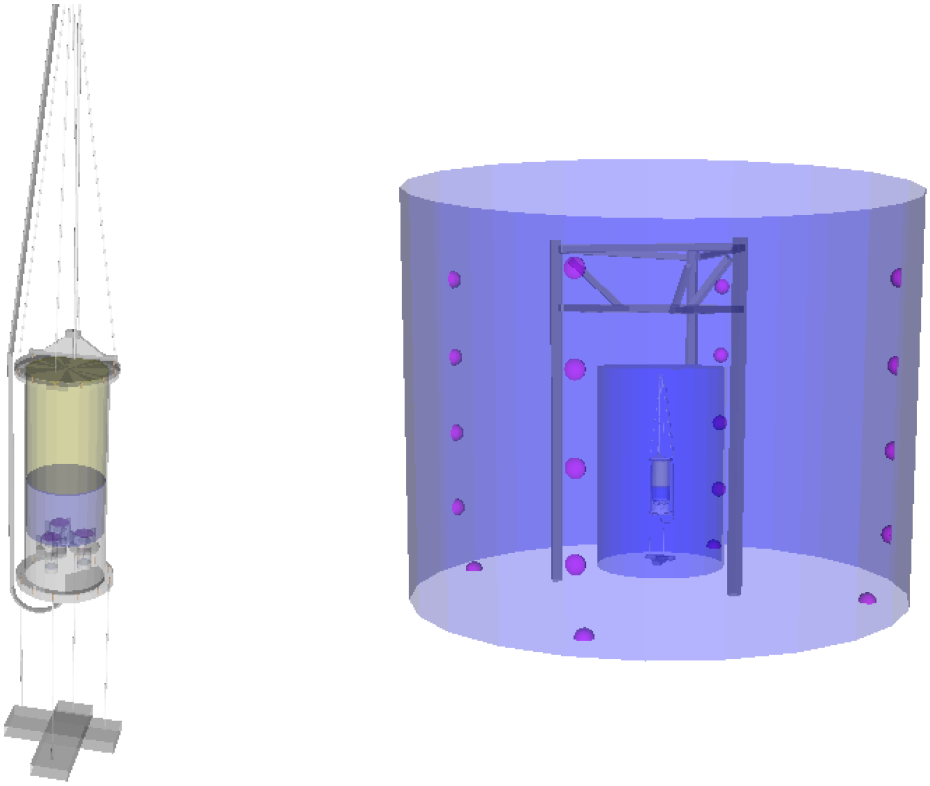

Figure 6.14: Visualizations of the detector geometry in the simulation. *Left:* Detailed view. *Right:* Showing detector placed in the water tank with the LUX detector stand and LUX water PMTs present.

absorbed in GdLS can be re-emitted at longer wavelengths and detected more efficiently.

The Tyvek surrounding the detector vessel is assumed to have the diffuse reflectivity dependence shown in Fig. 6.16. The shape of this dependence was measured in Ref. [65], while the overall scale was determined using the tests described in Sec. 5.3.3. The maximum reflectivity in the model is 98.1 %. The reflectivity and the LS light yield parameters are somewhat degenerate in the task of modeling the total number of photons collected by the PMTs. An overestimate of the true Tyvek reflectivity will result in a corresponding underestimate of the scintillator light yield, but the total number of collected quanta will largely remain the same.

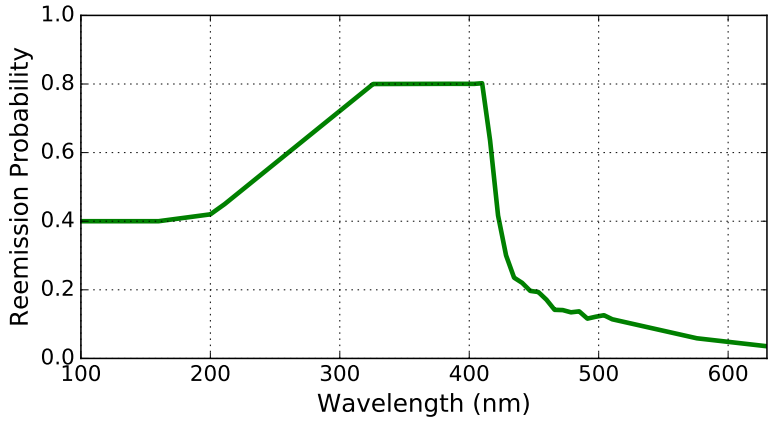

Figure 6.15: GdLS re-emission probability implemented in the optical model.

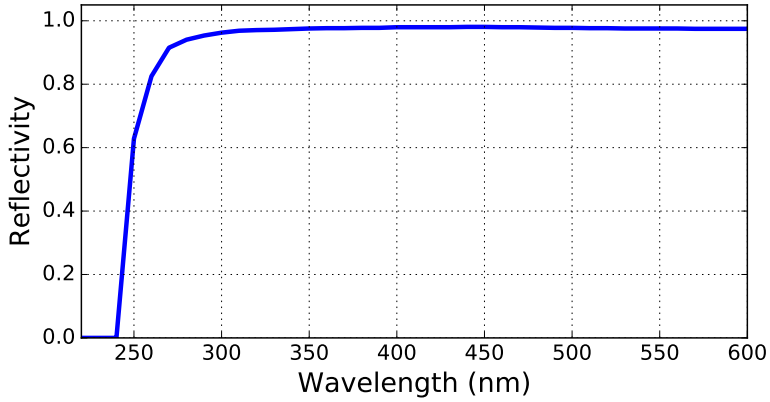

Figure 6.16: Wavelength dependence of the 1085D Tyvek reflectivity used in the detector optical model.

The creation of photoelectrons in the PMT photocathodes is implemented using the wavelength-depedent quantum efficiency shown in Fig. 6.17. During processing of simulated events, the number of collected photoelectrons in each tube is smeared according to the measured single photoelectron resolution, $(\sigma/\mu)_{\text{sphe}}$. The resolutions measured for the "Low HV" bias voltages are 42 %, 44 %, and 38 %.

The generation of optical photons from energy deposits in the LS is implemented using the model in Eq. 4.1. The parameters Y, kB, and C are determined by tuning the

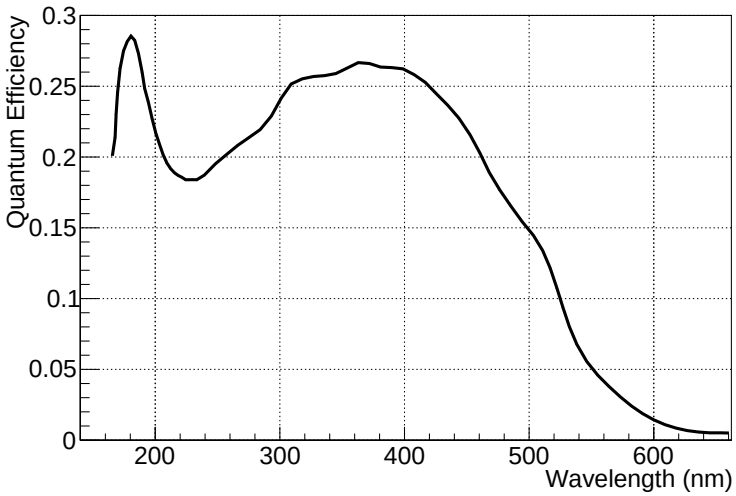

Figure 6.17: Wavelength dependence of the R11410-20 PMT quantum efficiency assumed in the detector response model.

simulation to the calibration data collected in each run.

6.3.2 Calibration of Simulation Response

To calibrate the simulated detector response to energy deposits from electrons, different values of Y and kB are simulated and compared with ^{137}Cs and ^{228}Th γ calibration data until good agreement via a χ^2 fit is obtained. The parameter C is set to zero for electron energy deposits. The kB parameter accounts for non-linearity in the scintillator response.

To determine the parameter errors, the grid of χ^2 values is then fit with a functional form resembling a 2D simple harmonic oscillator with spring constants k_x and k_y, minimum value of h_0 located at (x_0, y_0), and rotated by an angle ϕ in the plane:

$$
\begin{aligned}
f(x,y) &= \frac{1}{2}k_x x'^2 + \frac{1}{2}k_y y'^2 + h_0 \ , \\
x' &= (x - x_0)\cos\phi - (y - y_0)\sin\phi \\
y' &= (x - x_0)\sin\phi + (y - y_0)\cos\phi .
\end{aligned}
\tag{6.3}
$$

The best (kB, Y) pair for describing the data is taken as the values of (x_0, y_0) found by the fit. The 1σ errors (68.3% confidence interval) are found by drawing the contour of constant χ^2 defined by $\chi^2 = h_0 + 2.3$ (for a single parameter fit, a $\Delta\chi^2$ of 1 would be used for the same confidence interval). The result of this procedure is shown for both runs in Fig. 6.18 and the pulse area spectra for the best-fit parameters are shown with data in Fig. 6.19. Comparison of true energy deposits in the LS in Fig. 6.12 to spectra in Fig. 6.19 shows that the peaks in data are formed by the merging of Compton edges and photopeaks.

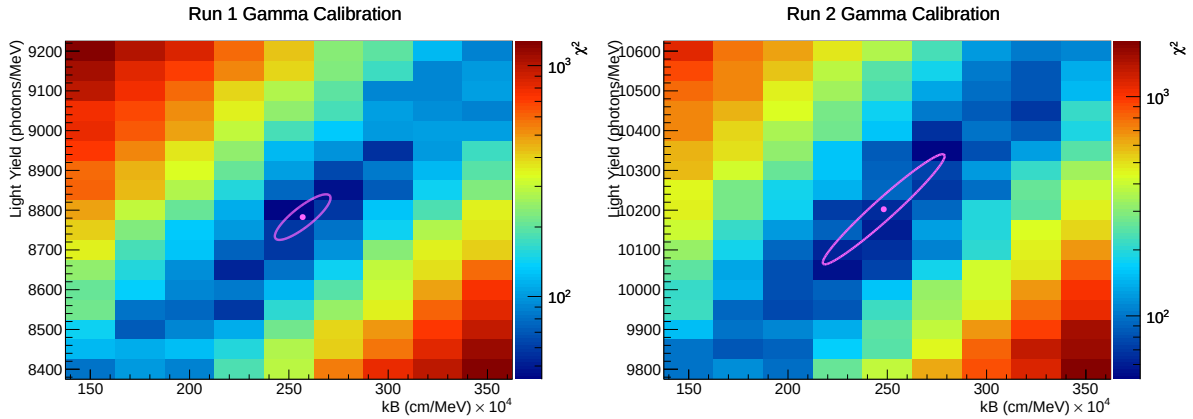

Figure 6.18: The χ^2 grid for Run 1 (left) and Run 2 (right) gamma calibration data. Shown also are the error ellipses found by computing $\Delta\chi^2 = 2.3$ for a confidence interval of 68.3%.

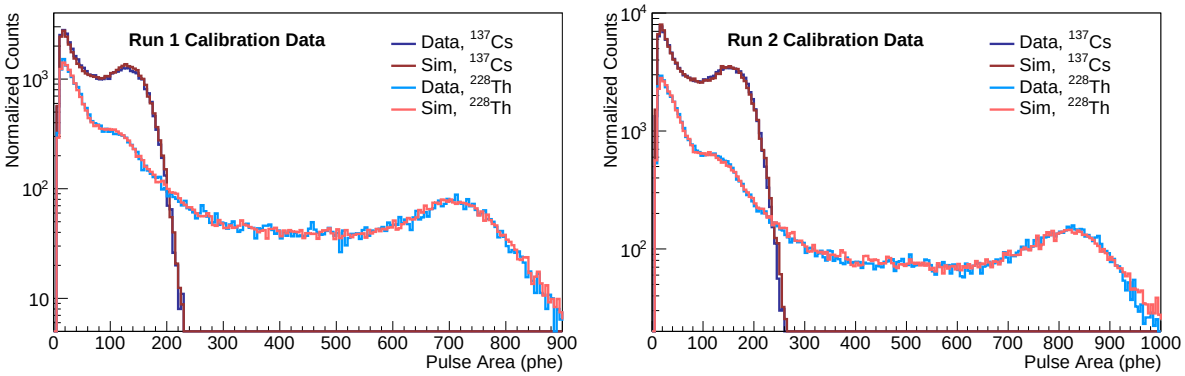

Figure 6.19: Pulse area spectra collected during calibrations with the ^{137}Cs and ^{228}Th sources. Overlaid are the simulated spectra obtained using the best fit Y and kB parameters.

The photoelectron yield in phe/MeV in each run is determined by simulating energy deposits from electrons uniformly throughout the LS volume. The resulting distributions are skew Gaussian, a consequence of variation in light collection along the LS chamber vertical axis. The size of this variation is ≈20 % across the full height. Simulations of uniform 1 MeV electrons in the LS give corresponding photoelectron yields of 321 ± 6 phe/MeV in Run 1 and 380 ± 12 phe/MeV in Run 2 using the mean values of the resulting skew Gaussian distributions. The error bars are obtained by varying Y and kB within their uncertainties and repeating the uniform electron simulations. These factors form the "approximate energy" scale used throughout this work; the non-linearity of the scintillator response with energy making it approximate. For the α fit results shown in Sec. 6.5.3, an "approximate quenched energy" scale is shown, which reports α energies in their electron-equivalent energy.

The detector response to α events is similarly determined by simulating a set of α energies for different values of kB and C. The mean number of collected phe in the

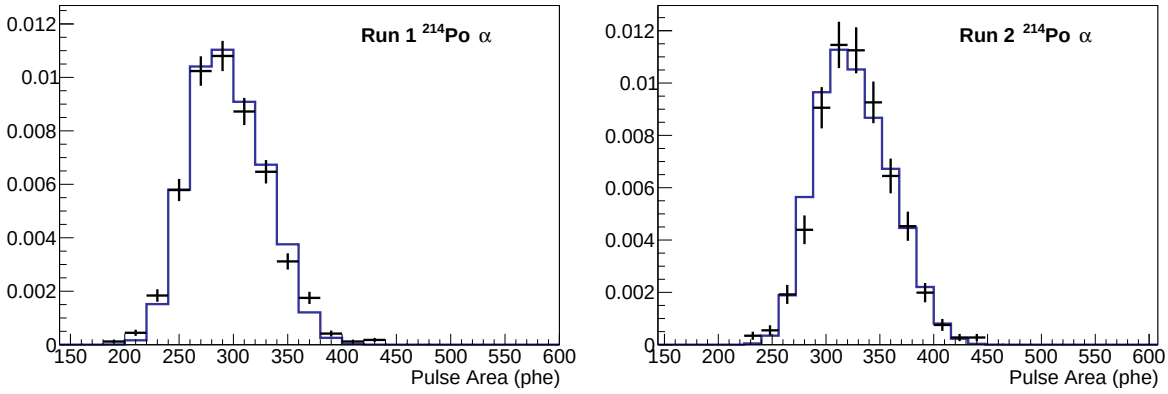

Figure 6.20: Pulse area spectra of ^{214}Po α-decays in both runs obtained from BiPo coincidence cuts. The simulated spectra obtained using the best fit kB and C parameters are shown in blue. Both spectra have unit normalization.

simulation is compared to that from each peak in data with a χ^2. The parameter errors are then determined following the same procedure as that for the γ parameters.

In addition to the α peaks provided by the thoron calibrations described above, three other α's can be used here. Early data from both runs provide an α peak from dissolved ^{222}Rn. All background data is analyzed for β-α coincidences from ^{214}Bi-^{214}Po ("BiPo") decays (see Section 6.5.2), allowing the construction of an α peak from ^{214}Po. This peak in data is shown in Fig. 6.20 along with the simulated response using the best fit kB and C parameters. A merged, low energy peak from ^{152}Gd/^{147}Sm decays is present in Run 1 data around ≈30 phe where GdLS was used (Fig. 6.27). Fig. 6.21 shows the peak position of each of the α's used in each run's fit, along with the best-fit peak position from the simulation.

Comparisons of the same α peak distributions during different thoron calibration periods show that the phe yield had changed during the calibration. It is likely that

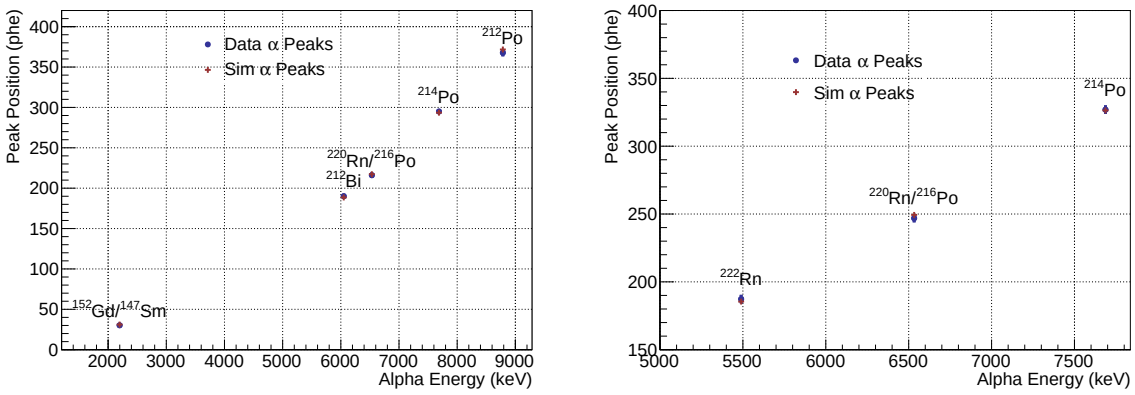

Figure 6.21: Peak position of the α's used from data (blue) in each run's fit for the detector response model. Shown in red are the best-fit positions from the model.

oxygen dissolved in the LS during the filling process was stripped by the active bubbling of nitrogen gas during the calibration. As a result, not all the available α peaks are used for determining the kB and C parameters. In Run 1, the α peaks from ^{152}Gd/^{147}Sm, ^{220}Rn/^{216}Po, ^{212}Bi, ^{214}Po, and ^{212}Po are used, while in Run 2 the peaks from ^{222}Rn, ^{220}Rn/^{216}Po, and ^{214}Po are used. Between calibrations, the phe yield is monitored using the position of the ^{214}Po peak and found to be stable to within 12 % in Run 1 and 6 % in Run 2; this is shown in Fig. 6.22.

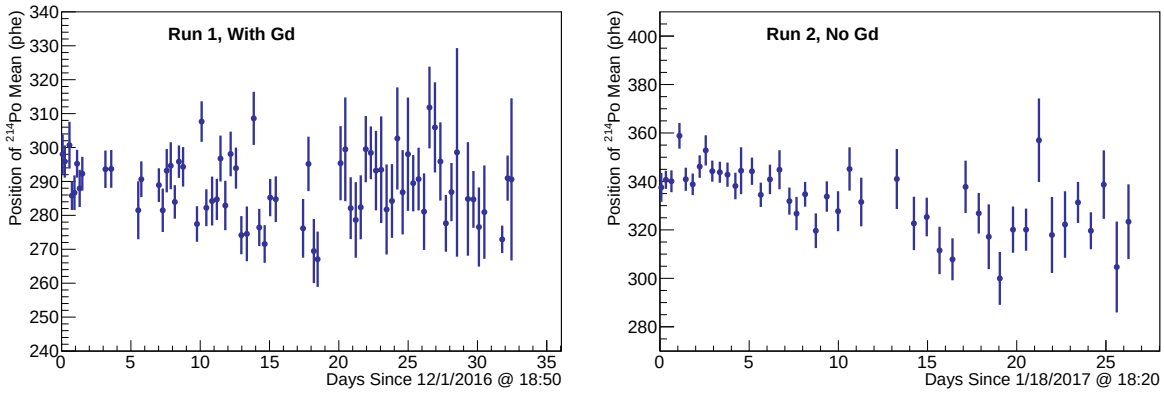

Figure 6.22: Position of the ^{214}Po α peak as a function of time since start of each run.

Table 6.2: Scintillator parameters deduced from tuning the GEANT4 detector simulation to γ and α calibration data. Also shown are the associated χ^2/ndf values for each of the fits.

Parameter	**Run 1**	**Run 2**
LS Light Yield, Y (photons MeV^{-1})	8783 ± 57	10202 ± 138
kB γ's (cm MeV^{-1})	0.0299 ± 0.0016	0.0288 ± 0.0036
kB α's (cm MeV^{-1})	0.00512 ± 0.00041	0.00744 ± 0.00070
C α's (cm^2 MeV^{-2})	$(2.43 \pm 0.43) \times 10^{-6}$	$(0.68 \pm 0.54) \times 10^{-6}$
γ Fit χ^2_{min}/ndf	55.7/46	56.7/46
α Fit χ^2_{min}/ndf	3.3/3	1.5/1

Tab. 6.2 summarizes the best fit simulation parameters used in each run. The lower light yield observed in Run 1 is thought to be from exposure of the LS to air during the filling process. This is also believed to be the cause of the higher ^{222}Rn rate at the beginning of that run.

The parameters kB and C describing α quenching in the LS are different for the two runs. The difference arises from the inclusion of the low energy ^{152}Gd/^{147}Sm α peak in the fit for Run 1. The values found here are generally consistent with those found in [118] where it is shown that a range of kB and C values can result in similar overall quenching. The differing values are therefore not a concern, as our focus is on the response to α's of energy 4 MeV to 9 MeV. This range contains α-decays from the uranium and thorium decay chains.

6.3.3 Pulse Shape Discrimination

The timing profile of emitted photons in the LS is dependent on the particle type. Energy deposits from particles such as α's that produce large amounts of ionization along their track produce photons with a characteristically slower time profile compared to

electrons [119]. This allows for PSD between α and γ/β events.

We use a simple parameter, the ratio of the pulse height to area as the discrimination variable. For a fixed pulse area, the characteristically slower pulses from α's have a smaller height than those from electrons, providing separation between pulses from these particle types. In Fig. 6.23, pulses from the external ^{228}Th source (magenta) are shown with data from the flow-through ^{220}Rn source (cyan and blue) in the height-to-area ratio versus area plane. The separation between α events and electron events is clear. As demonstrated in [119], better separation is possible when oxygen is removed from the LS, e.g. by thoroughly bubbling with nitrogen gas.

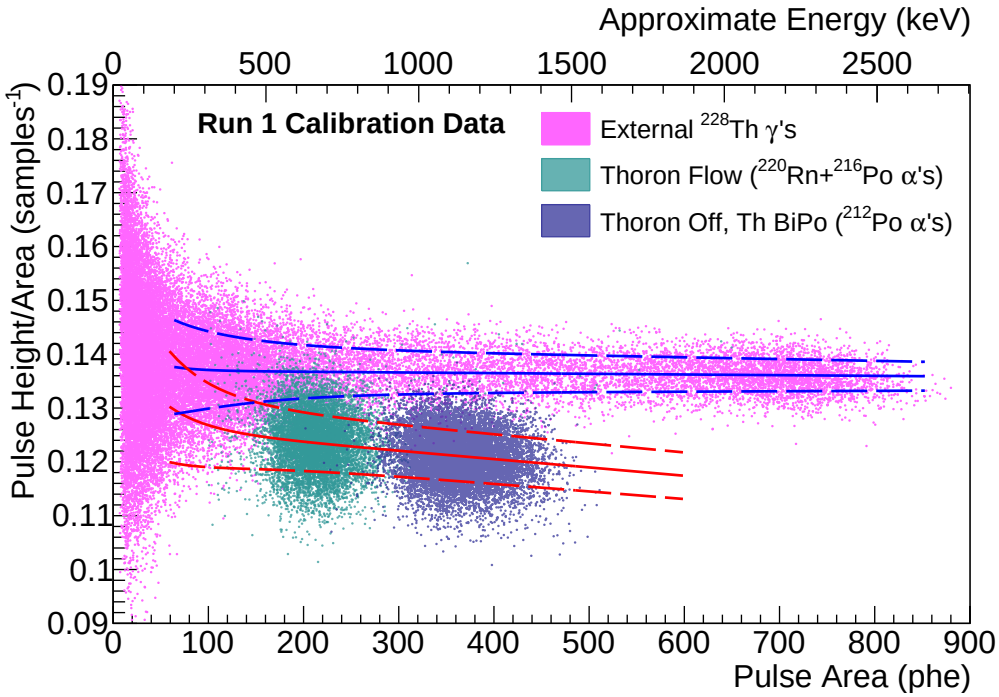

Figure 6.23: Calibration data with α's (cyan and blue) and γ's (magenta) shown in PSD space. Overlaid are the fit γ (blue) and α (red) band means (solid) and $\pm 1\sigma$ (dashed) curves.

The γ and α calibration data in each run are profiled by fitting a Gaussian function

to the height-to-area ratio distributions found in slices of pulse area. The means and variances obtained from the fit in each slice are subsequently fit to a linear plus exponential model, thus defining γ/β and α bands within the PSD space. The bands are shown also in Fig. 6.23.

Selections of α and γ/β events are made using cuts on the PSD parameter. For α events we take the PSD parameter to be 3σ below the calibrated γ/β band mean. For γ and β events we define a cut on the PSD parameter which takes the linear plus exponential form used to describe the band shape. The cut is at least 2σ above the calibrated α band mean at all energies.

The cut efficiencies in Run 1 are shown in Fig. 6.24. The efficiencies for both cuts are calculated both directly from thoron and γ source calibration data and using the parameterization of the bands. In the region where calibration data is available, good agreement is found between the band parameterization and the data, justifying the use of the band model in regions where there is no calibration data.

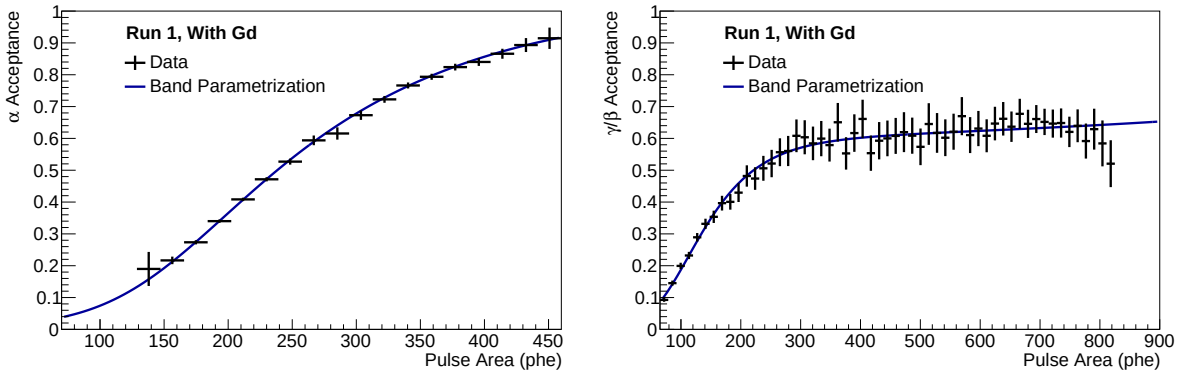

(a) (b)

Figure 6.24: (a) Acceptance of α events and (b) γ/β events as a function of pulse area computed using the Gaussian band parameterization of calibration data (blue) plotted with that computed using the data itself (black). Note that these are not fits.

6.4 Z-Scan Data

As discussed in Sec. 4.5, it was discovered that the rate from γ's in the Davis Cavern environment will contribute substantially to the singles rate in the OD. Initial estimates predicted a rate of nearly 100 Hz above a 200 keV threshold from this γ flux alone. This motivated a series of measurements undertaken with the Screener whereby data was collected with the detector located at different vertical positions within the water tank, collectively known as "z-scan data". The this data was then used to cross check the assumptions made in the simulations of the Davis Cavern background, namely the activity of the cavern rock assumed.

After low-background data was collected in each run, the Screener was moved to three different vertical positions within the water tank. Of primary interest to the OD the data taken with the detector very close to the top of the water tank as this is where the rate is expected to be the highest. At the bottom of the tank, the inverted steel pyramid

provides additional shielding making Screener measurements there less sensitive. In Run 1, one of the points probed was lower than the optimal position by 18 cm, the position of the titanium ballast preventing the use of a lower position. In this position the rate was observed to increase, providing evidence that the position used for taking low-background data was in fact very close to the optimal (lowest rate from external γ's) position.

The z-scan data taken at the conclusion of Run 2 is more informative as a higher vertical position in the water tank was probed. This point roughly corresponds to the height of the top of the OD acrylic tanks, roughly 130 cm below the water surface, where the external γ rate is expected to be highest in the OD. The Screener was placed with its top located 98 cm below the water surface so that the LS chamber would be approximately centered about this point. Fig. 6.25 shows this and the other points probed with the Screener on a scale cut-away model of LZ as well as the spectrum of pulse area collected in each position. The effects of an increased γ flux are obvious, with the spectra becoming progressively washed out due to the increased rate of Compton-scattered γ's in the LS.

The simulations of the Davis Cavern γ's described in Sec. 4.5 were repeated using the Screener geometry shown in Fig. 6.14. Both the measured and predicted count rate in the Screener above a 200 keV threshold as a function of vertical height in the water tank are shown in Fig. 6.26a. The key takeaway is that when the original cavern wall activity estimates are assumed, the count rate at the highest position is over predicted relative to what is measured. The conclusion is that the effective normalizations for these simulations are too large and therefore over predict the rate in the OD as well.

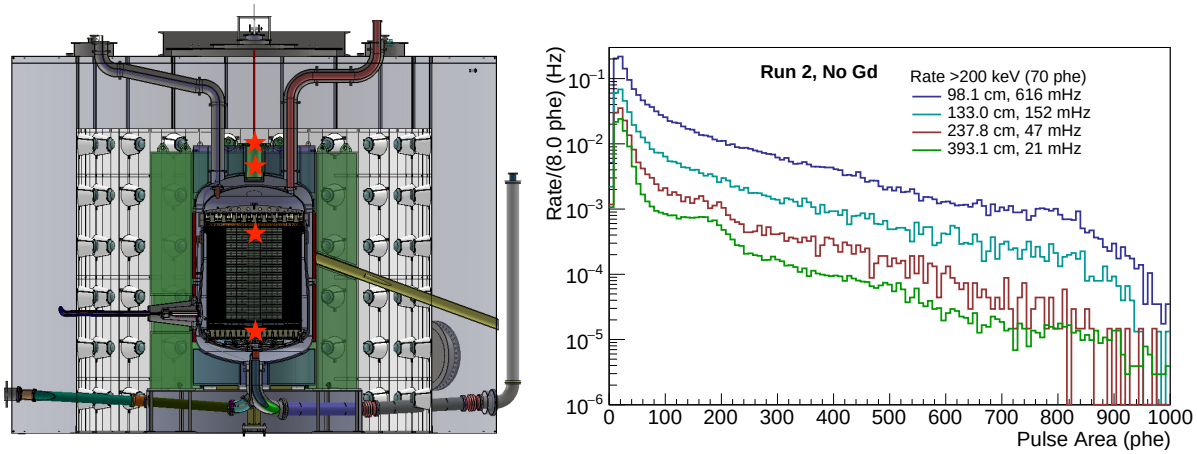

(a) (b)

Figure 6.25: (a) Cutaway CAD model of LZ showing the location of the center of the Screener LS chamber at each position in the water tank. (b) Collected pulse area spectra at each position in the water tank. The legend gives the height of water above the top of the detector in each position as well as the integrated rate >200 keV (≈70 phe).

In Fig 6.26b the cavern activity normalizations measured in a dedicated campaign are used to predict the Screener rate resulting in good agreement between the simulation and data.

In both Fig. 6.26a and Fig. 6.26b, the total count rate in the Screener is shown along with a curve representing the count rate due to sources external to the Screener. The latter is formed by subtracting from the total rate the rate measured in the optimal position, as the externals have negligible contribution in this position. During collection of z-scan data, the opening of the water tank port resulted in a measurable increase in the dissolved oxygen in the water. It is therefore assumed that the amount of dissolved radon increased as well. The large error bar on the second data point results from subtracting an estimated rate from dissolved radon which carries a large uncertainty.

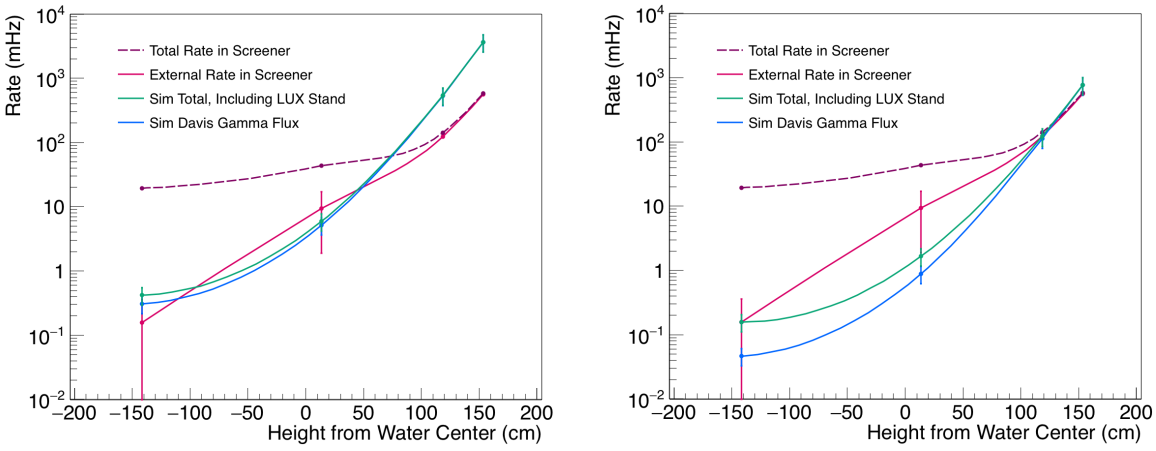

Figure 6.26: Rate above 200 keV in the Screener predicted by (a) old cavern rock normalizations and (b) new normalizations measured in a dedicated campaign. Plots by S. Shaw.

6.5 Measurement of Backgrounds in the LS

The plateaued rate at the end of each run arises from sources of radioactivity in the detector construction materials, the water tank/cavern environment, and radioimpurities in the scintillator. In this section I describe measurements of the LS radioimpurities using the low-background Screener data.

The inclusive low-background data counting rates above 200 keV in the GdLS and LS runs are (78.6 ± 0.4) mHz and (20.0 ± 0.1) mHz, respectively. The collected pulse area distributions for each run are shown in Fig. 6.27 and the distributions in PSD space are shown in Fig. 6.28. The livetime durations are 5.97 d for Run 1 and 11.83 d for Run 2.

The low-background data are divided into two primary regions:

1. Low pulse area region, $\lesssim$250 keV. The dominant source of rate in this region results from the β-decay of ^{14}C. In Run 1, a peak results from the α-decays of ^{152}Gd and

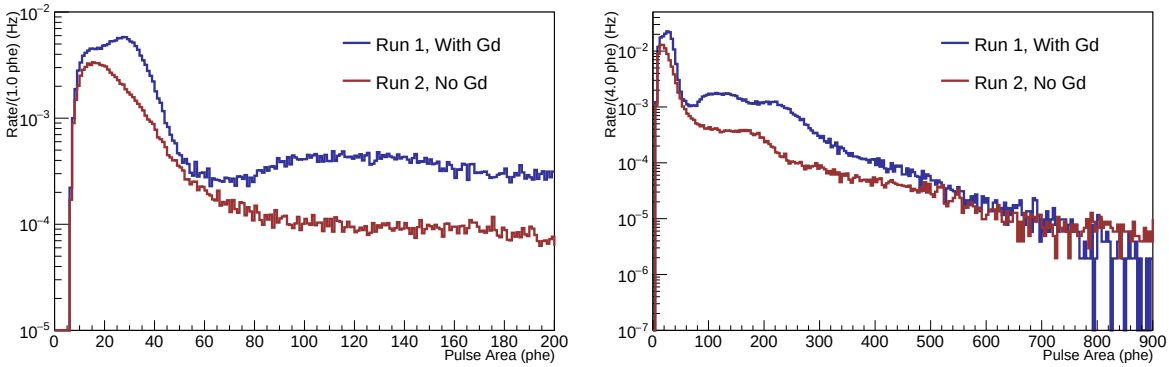

Figure 6.27: Run 1 and Run 2 low-background spectra shown in the low pulse area region (left) and over the full range of collected phe (right). The low energy peak at ≈30 phe from ^{152}Gd/^{147}Sm decays is visible in the Run 1 data on the left. Note that Run 1 and Run 2 do not share the same energy scale (phe/MeV).

^{147}Sm that are quenched into this region.

2. High pulse area region, $\gtrsim$250 keV. Pulses in this region result from γ backgrounds external to the LS and from the decays of the internal radioimpurities dissolved in the LS. PSD is used in this region to select α and γ/β events.

Specifically, the high pulse area region is defined by pulse areas >65 phe, corresponding to >222 keV, in Run 1 and >100 phe, corresponding to >281 keV, in Run 2. The inclusive count rates measured with these thresholds are (75.9 ± 0.4) mHz and (16.0 ± 0.1) mHz, respectively.

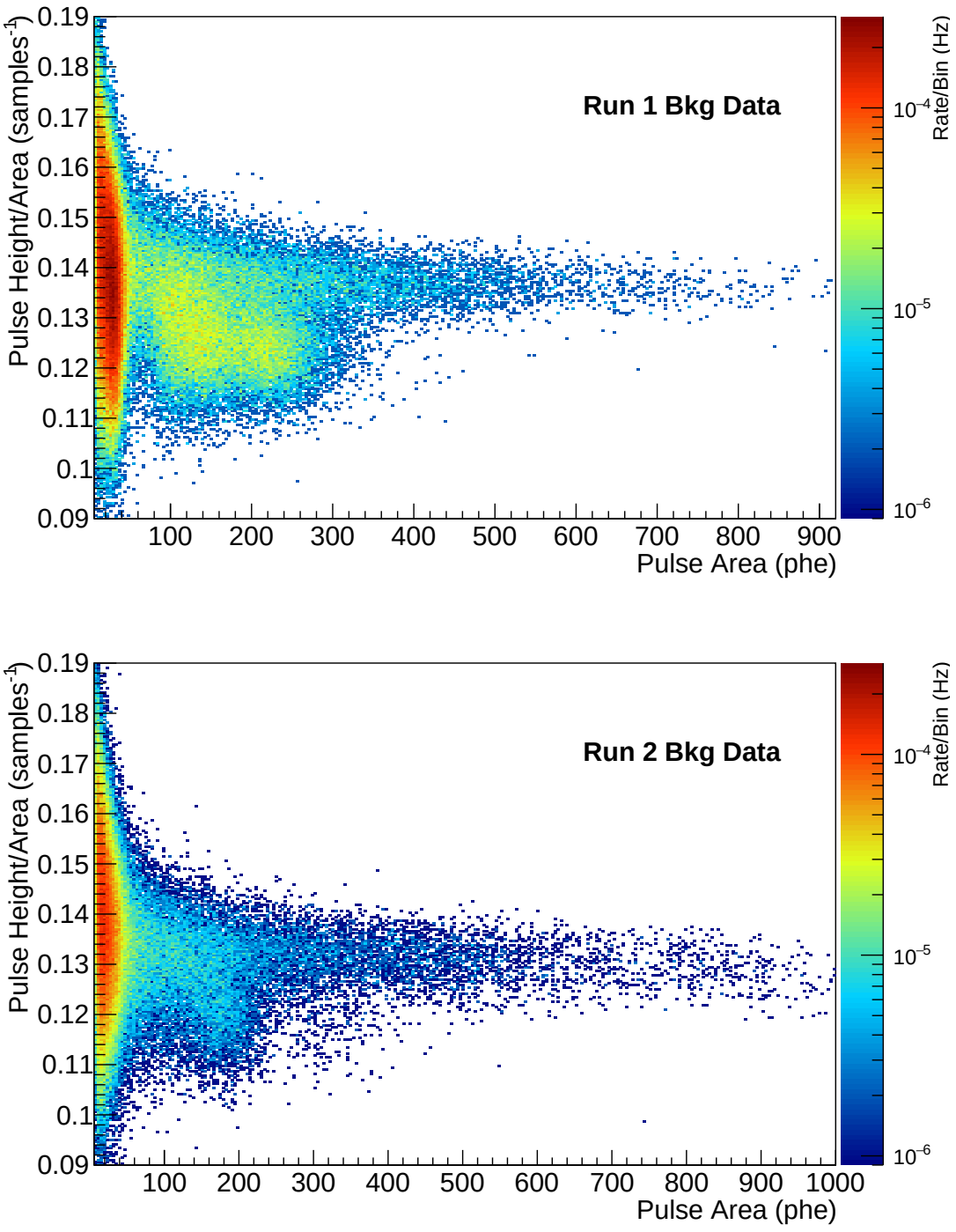

Figure 6.28: Run 1 and Run 2 low-background data shown in PSD space. The higher rate from α decays in Run 1 is noticeable. Note that Run 1 and Run 2 do not share the same energy scale (phe/MeV).

6.5.1 Measurement of ^{14}C Concentration

A measurement of the ultra-low $^{14}C/^{12}C$ ratio in pseudocumene-based LS was performed by the Borexino collaboration and found to be at the 10^{-18} level [69]. Here we follow nearly the same procedure to determine the ^{14}C concentration in our LS by fitting the low pulse area region of Run 2 with the ^{14}C β-decay ($Q = 156$ keV) shape.

The distribution of electron energies resulting from β-decay follows the form

$$N(W)\mathrm{d}W = pW(W_0 - W)^2 F(Z, W)C(W)\mathrm{d}W \tag{6.4}$$

where p, W, and W_0 are the electron momentum, energy, and endpoint energy in units of the electron mass, respectively. The Fermi function, $F(Z, W)$, corrects the kinematic shape by accounting for Coulomb interactions between the daughter nucleus and the electron. The distribution is further altered by a shape factor $C(W)$, which we take to have the form:

$$C(W) = 1 + aW. \tag{6.5}$$

As in [69], the tabulated values of the Fermi function in [120] were parameterized and used here.

The data in the low pulse area region is fit using the following convolution model:

$$R(W) = N_{\mathrm{C}} \int N(W')G(W', W)\,\mathrm{d}W' + N_{\mathrm{bkg}}B(W) \tag{6.6}$$

Here, $G(W', W)$ is a detector resolution function, which smears the true β-decay shape, $N(W')$. The ^{14}C and background shapes are weighted by their corresponding number of events, N_{C} and N_{bkg}, respectively.

The detector resolution function, $G(W', W)$, is observed in data to be non-Gaussian. This is best seen in the distributions of various α peaks, which are instead well-described by a skew-normal distribution with location, width, and skewness parameters ξ, ω, and α, respectively:

$$f(x) = \frac{1}{\sqrt{2\pi}\xi} e^{\frac{(x-\xi)^2}{2\omega^2}} \operatorname{erfc}\left[\frac{-\alpha(x-\xi)}{\sqrt{2}\omega}\right] \tag{6.7}$$

This description of $G(W', W)$ is accurately predicted by the simulation as a result of variations in light collection efficiency with position. The associated mean and variance of the skew-normal distribution are given by

$$\begin{aligned} \mu &= \xi + \omega\delta\sqrt{\frac{2}{\pi}}, \\ \sigma^2 &= \omega^2\left(1 - \frac{2}{\pi}\delta^2\right), \end{aligned} \tag{6.8}$$

with

$$\delta = \frac{\alpha}{\sqrt{1+\alpha^2}}.$$

Simulations of uniform energy deposits within the detector volume show that the detector resolution is well modeled by

$$\frac{\sigma}{\mu} = \sqrt{k_1^2 + \frac{k_2^2}{\mu}}. \tag{6.9}$$

At higher energies where γ calibration data is available, the first term dominates the resolution behavior. For fitting the low pulse area region, we fix k_1 to have the value of 0.087 predicted by the Monte Carlo and allow k_2 to float in the fit.

Extrapolation of the background simulations from Section 6.5.4 into the low pulse area region indicate that the background shape underlying the ^{14}C spectrum is well described by a decaying exponential plus a linear term. The integral of this shape then determines the number of background events, N_{bkg}, which is fixed during the fit.

The fit is performed between 20 and 80 phe. The following parameters are allowed to float freely:

- The number of ^{14}C events, N_{C}
- The scale factor that converts energy deposited in the LS to the observed number of phe, Q/E (phe/MeV)
- The constant k_2 in the detector resolution model, Eq. (6.9)
- The parameter a in the β-decay shape factor, $C(W)$.

From the fit number of ^{14}C decays, the concentration $^{14}\text{C}/^{12}\text{C}$ is calculated as

$$f(^{14}\text{C}/^{12}\text{C}) = \frac{A\,\tau\,M_{\text{LAB}}}{17.1\,m_{\text{LS}}\,N_A} \tag{6.10}$$

where A is the fit ^{14}C activity and τ is the ^{14}C mean lifetime (8,266.6 y). M_{LAB} is the molar mass of LAB (233.9 g/mol) and m_{LS} is the mass of LS in the detector during the run. The average number of carbon atoms in LAB is 17.1 and N_A is Avogadro's number. Eq. (6.10) returns the ratio $^{14}\text{C}/^{12}\text{C}$ as an atom fraction, not a mass fraction[1].

A good fit is obtained to the Run 2 data and shown in Fig. 6.29. A summary of the best fit values for the various parameters is given in Tab. 6.3. The $^{14}\text{C}/^{12}\text{C}$ value

[1] Both conventions are used in the literature, often without clear definition of units.

is given with a statistical error bar from the fit and a systematic error resulting from the uncertainty on the LS mass in the detector. The statistical uncertainty is larger than expected from pure event counting because of correlations between the number of ^{14}C decays, the energy scale, and energy resolution parameters. Precise knowledge of these parameters in the low-energy region from dedicated calibrations would improve the sensitivity of detectors similar to the Screener.

Our results are consistent with the $^{14}C/^{12}C$ ratio of $(3.3 \pm 0.5) \times 10^{-17}$ measured in LAB-based LS in Ref. [121], though our error is approximately a factor of 8× smaller. The level of contamination we measured here satisfies the requirements of the LZ OD. The expected ^{14}C rate above 100 keV in the OD is (7.0 ± 0.2) Hz.

Table 6.3: Results of fitting data in the low pulse area region from 20-80 phe with the ^{14}C + background model in Run 2.

Run 2: Livetime = 11.83 d; LS Mass = (23.2 ± 0.1) kg; Fit χ^2/ndf = 128.6/117

Parameter	**Fit Result**
Shape factor, a (MeV^{-1})	-0.34 ± 0.12
Resolution Parameter, k_2 (phe$^{1/2}$)	1.57 ± 0.07
Energy scale (phe MeV^{-1})	309 ± 4
^{14}C Activity (mBq)	110.7 ± 2.4
Concentration $^{14}C/^{12}C$ (10^{-17})	2.83 ± 0.06(stat.) ± 0.01(sys.)

Low-Energy Fit in Run 1

The same procedure as the above is also applied to the low pulse area data in Run 1. This fit must include a population to model the 2.2 MeV α from ^{152}Gd which is quenched into this region. The GdLS is loaded with Gd at 0.1% by mass and this number is known with an uncertainty of 5%. The expected rate of ^{152}Gd α decays is therefore (38 ± 2) mHz.

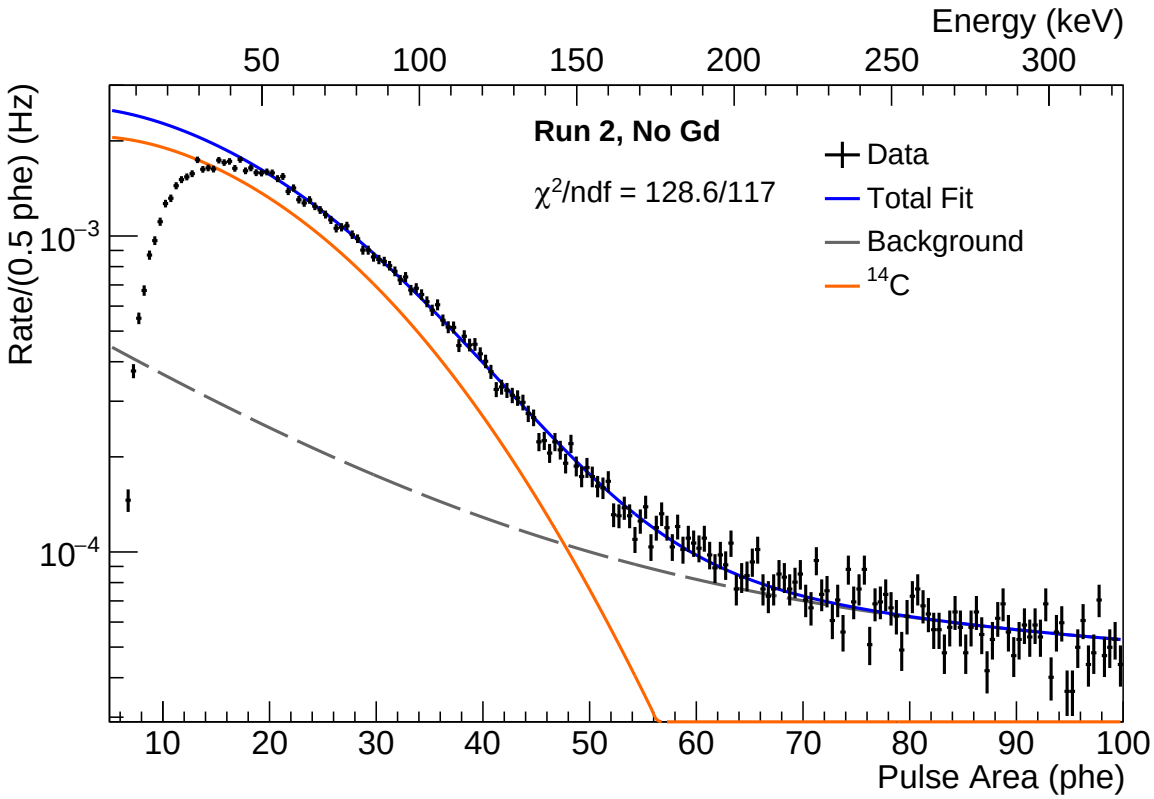

Figure 6.29: Run 2 low pulse area data shown with the best fit to the background plus ^{14}C β model. Shown at the top of the plot is the energy axis derived from the best-fit energy scale factor.

The observed rate in data is about 60 mHz, however, suggesting that there may be an additional GdLS impurity with a low-energy α decay in this region. This is motivated by the detection of other rare earth isotopes in the GdLS such as ^{176}Lu and ^{227}Ac (see below). A search for candidate low-energy α-emitting isotopes among the rare earth elements yields ^{147}Sm as a plausible explanation for the excess rate. ^{147}Sm exists with natural abundance of 14.9% and emits a 2.3 MeV α with a half-life of 1.06×10^{11} y. If the number of Sm and Lu atoms were the same (using the HPGe screening results of Sec. 4.5.3), we would expect a ^{147}Sm rate of ≈13 mHz which is within the right order of magnitude to explain the excess rate observed.

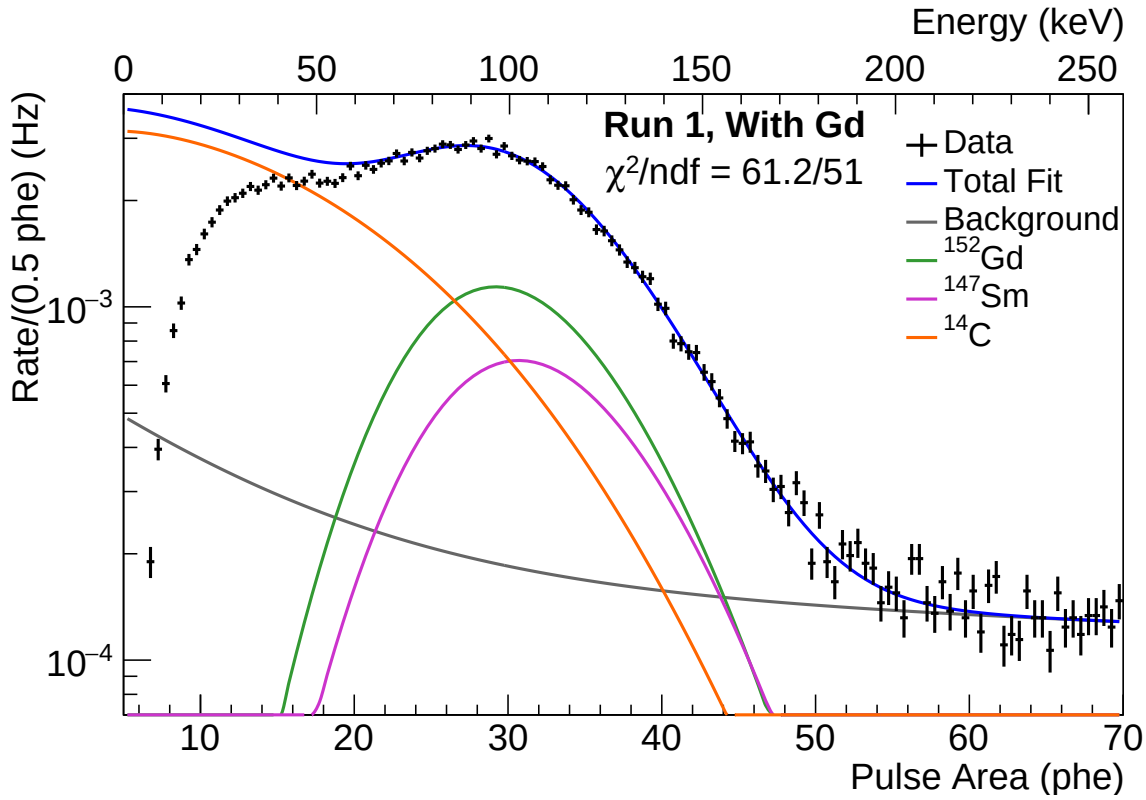

Figure 6.30: Run 1 low pulse area data shown with the best fit model which includes: background, ^{14}C, ^{152}Gd, and ^{147}Sm. Shown at the top of the plot is the energy axis derived from the best-fit energy scale factor.

The result of including ^{147}Sm in the low energy fit in Run 1 is shown in Fig. 6.30. The fit is performed between 22 and 50 phe and includes an additional parameter that quantifies the amount of quenching for the two α populations (the effective energy scale for α's then being the product of the energy scale factor and the quenching factor). The ^{14}C shape factor is held constant to the value found in the Run 2 fit. A good fit is obtained resulting in a ^{147}Sm specific activity of (1.02 ± 0.05) mBq/kg. This results in an OD rate of (13.0 ± 0.6) Hz above 100 keV. The other best-fit parameters are summarized in Tab. 6.4.

Table 6.4: Results of fitting data in the low pulse area region from 22-50 phe with a model comprised of: ^{14}C, background, ^{152}Gd, and ^{147}Sm in Run 1.

Run 1: Livetime = 5.97 d; LS Mass = (23.7 ± 0.1) kg; Fit χ^2/ndf = 61.2/51

Parameter	**Fit Result**
Shape factor, a (MeV^{-1})	fixed: -0.34
Resolution Parameter, k_2 (phe$^{1/2}$)	1.10 ± 0.02
Energy scale (phe MeV^{-1})	270 ± 7
α Quench Factor	0.051 ± 0.001
^{152}Gd Activity (mBq)	37.8 ± 0.9
^{147}Sm Activity (mBq)	24.1 ± 1.2
^{14}C Activity (mBq)	145.6 ± 6.7
Concentration ^{14}C/^{12}C (10^{-17})	3.64 ± 0.17(stat.) ± 0.02(sys.)

6.5.2 β-α and α-α Coincidence Rates

As mentioned in the introduction, the $^{238}U_m$, $^{235}U_l$, and $^{232}Th_l$ subchains are commonly measured by directly counting β-α or α-α coincidences. Each of these subchains contains a short-lived polonium isotope which allows a coincidence tag with the previous decay in the series. The relevant polonium half-lives in these three subchains are 164 µs (^{214}Po), 1.78 ms (^{215}Po), and 299 ns (^{212}Po), respectively.

Pulse pairs consistent with the expected α and β energies are counted in two coincidence windows within the larger 81.9 µs event window: 5 µs to 76 µs for the ^{238}U and ^{235}U chains and 0.4 µs to 4 µs for the ^{232}Th chain. The deadtime following each event prevents the use of larger windows for ^{214}Po and ^{215}Po decay. The PSD value of the first pulse in a coincident pair distinguishes the β-α events from the ^{238}U chain and the α-α events from the ^{235}U chain. The accidental coincidence background is largest when selecting β-α events in the ^{238}U chain and is calculated to be 0.08 events, making this measurement essentially background-free. Requiring that the second pulse (α pulse) be consistent with the expected quenched alpha energy removes background from PMT afterpulses, as they

have much smaller pulse areas [122].

The efficiency for selecting events with pulse pairs within each timing window is calculated analytically using the half-life of the polonium decay. The efficiency of cuts on pulse area (and therefore deposited energy) is assessed through simulation. The total efficiencies for the ^{238}U, ^{235}U, and ^{232}Th chain selections in Run 1 (Run 2) are 21.7 % (21.9 %), 2.7 % (2.7 %), and 32.1 % (32.6 %), respectively. The largest source of inefficiency results from the choice of coincidence windows, a limitation imposed by the maximum event length of the DAQ.

Table 6.5: Concentrations of various subchains calculated from the measured coincidence rates in each run.

Subchain	**Run 1 (mBq/kg)**	**Run 2 (mBq/kg)**
$^{238}U_m$	0.019 ± 0.003	0.023 ± 0.002
$^{235}U_l$	0.18 ± 0.02	< 0.0037 (90% CL)
$^{232}Th_l$	0.0071 ± 0.0019	0.00082 ± 0.00074

The subchain activities measured by coincidence counting in both runs are summarized in Tab. 6.5. The larger activities in the GdLS are consistent with the expectation that impurities enter through the Gd-loading process. In particular, no events consistent with the $^{235}U_l$ subchain sequence are observed in the unloaded LS data.

6.5.3 Fit to α Events

All of the α decays in the ^{238}U, ^{235}U, and ^{232}Th chains contribute to the event rate in the Screener and are distinguished from other sources by using the PSD selection discussed in Sec. 6.3.3. Fits to the pulse area spectra of selected α events are performed to measure the isotope activities throughout these chains.

Probability density functions (PDFs) in pulse area for the primary α-emitting isotopes in the ^{238}U, ^{235}U, and ^{232}Th chains are created by simulating 50k decays of each uniformly in the LS volume. The distributions of collected phe are then weighted by the measured phe-dependent acceptance (Fig. 6.24a) to obtain the expected shapes for each isotope.

Isotopes from the same subchains are summed to reduce the overall number of fit parameters. This results in six isotope populations: $^{238}U_e$, $^{238}U_m$, ^{210}Po, $^{235}U_l$, ^{232}Th, and $^{232}Th_l$. The $^{235}U_l$ PDF is not used in the Run 2 fit as no signature for this chain was found in Sec. 6.5.2. The coincidence rates measured in Sec. 6.5.2 constrain their associated subchain PDF normalizations during the fit. The remaining populations float freely.

The leakage of γ/β events into the α-selected data is negligible. In Run 1 the expected leakage is 26 events, while a total of 5823 events are accepted by the cut. In Run 2, the expected leakage is 9 events with 911 events passing the selection.

The large stopping power of α's restricts their origin to the LS itself or the inside acrylic surface of the LS chamber. In the latter case, radon daughter plate-out results in ^{210}Po α's depositing their energy in the LS with minimal energy loss in the acrylic due to their $\sim$100 nm implantation depth. This is short compared to the typical range of these α's in acrylic which is $\approx$30 µm.

An upper limit on the ^{210}Po surface activity is known from counting a $\sim$year old sample of acrylic from the manufacturer of the Screener vessel. The sample had no protective coating during its exposure time. An XIA UltraLo-1800 α counter [123] measured

a ^{210}Po surface activity of $(3.0 \pm 0.7)\,\mathrm{mBq/m^2}$ on this sample. The inside surface area of the Screener LS chamber is $0.52\,\mathrm{m^2}$, while only half the ^{210}Po α's interact in the LS. This gives the conservative upper limit of $(0.8 \pm 0.2)\,\mathrm{mHz}$ in the Screener. Given that the Screener is constructed of virgin acrylic and was kept in a nitrogen atmosphere whenever possible, the true surface activity is likely much smaller and so is ignored here.

6.5.4 Fit to γ/β Events

Complementary fits are performed to spectra of γ/β events selected using the cut described in Sec. 6.3.3. Subchain equilibrium suggests that activity measured through α-decays should have a concomitant activity through β-decays. The populations included in these fits are summarized here.

Event distributions resulting from sources of radioactivity external to the LS are obtained by simulation of decays in the detector construction materials. The expected number of counts from external ^{238}U, ^{232}Th, and ^{40}K are then obtained by normalizing to the detector material radioassay results from HPGe counting. The contribution from ^{222}Rn decays in the surrounding water is also included. The rate from ^{60}Co in the detector materials was found to be negligible.

In the ^{238}U, ^{235}U, and ^{232}Th chains, there are six, four, and five primary isotopes that decay by β emission, respectively. Of these, ^{234}Th, ^{210}Pb, ^{227}Ac, ^{231}Th, and ^{228}Ra are excluded as their β-decay endpoints fall below the range of the fit. As was done in the α fits, isotopes belonging to the $^{238}\mathrm{U_m}$, $^{235}\mathrm{U_l}$, and $^{232}\mathrm{Th_l}$ subchains are summed and

Table 6.6: Predicted rates from detector materials in each run above the specified threshold used in each fit. The rates given here have *not* had efficiencies applied. With a few exceptions, the errors mostly result from a 10 % systematic uncertainy associated with HPGe counting results of various components.

Component	Run 1, >65 phe (222 keV) (mHz)				Run 2, >100 phe (281 keV) (mHz)			
	^{238}U	Water ^{222}Rn	^{232}Th	^{40}K	^{238}U	Water ^{222}Rn	^{232}Th	^{40}K
Acrylic	0.0073 ± 0.0007	-	0.0026 ± 0.0003	0.0020 ± 0.0002	0.0061 ± 0.0006	-	0.0023 ± 0.0002	0.0018 ± 0.0002
LS Fill Tubing	0.048 ± 0.005	-	0.029 ± 0.002	0.0040 ± 0.0004	0.038 ± 0.004	-	0.024 ± 0.002	0.0035 ± 0.0004
Cables	3.02 ± 0.69	-	2.30 ± 0.40	0.45 ± 0.18	2.53 ± 0.58	-	1.96 ± 0.34	0.41 ± 0.16
PMT Bases	0.014 ± 0.001	-	0.0066 ± 0.0005	0.0013 ± 0.0001	0.011 ± 0.001	-	0.0054 ± 0.0004	0.0012 ± 0.0001
PMTs	1.12 ± 0.11	-	0.083 ± 0.006	0.0590 ± 0.0059	0.53 ± 0.05	-	0.050 ± 0.004	0.017 ± 0.002
Ropes	$(8.98 \pm 0.89) \times 10^{-5}$	-	$(1.81 \pm 0.18) \times 10^{-5}$	0.043 ± 0.004	$(7.72 \pm 0.77) \times 10^{-5}$	-	$(1.57 \pm 0.16) \times 10^{-5}$	0.0380 ± 0.0038
Tyvek	0.19 ± 0.02	-	0.45 ± 0.03	2.07 ± 0.21	0.16 ± 0.01	-	0.39 ± 0.03	1.92 ± 0.19
Isotope Totals	4.40 ± 0.82	1.44 ± 0.69	2.88 ± 0.44	2.63 ± 0.40	3.27 ± 0.65	1.16 ± 0.56	2.43 ± 0.37	2.39 ± 0.36
Run Totals	11.34 ± 1.23				9.25 ± 1.00			

constrained by the coincidence rates measured in Sec. 6.5.2. The isotopes that remain are allowed to float free, namely: ^{234}Pa, ^{210}Bi, ^{228}Ac.

The cosmic ray flux of protons and neutrons on the Earth's surface leads to the production of the isotope ^{7}Be through reactions on ^{12}C in the LS. The resulting electron capture decay of ^{7}Be can enter as a source of background through its emission of a 478 keV γ-ray 10.4 % of the time. The 53 d half-life of ^{7}Be means that the surface production rate and decay rate were very likely in equilibrium for both the loaded and unloaded LS used here. The expected rate of 478 keV γ-rays from ^{7}Be in the pseudocumene-based LS used by Borexino was estimated in [124]. By scaling those results and accounting for time spent underground (about 48 d and 29 d in Run 1 and 2, respectively), we might expect $\approx$1 mBq of γ-emitting ^{7}Be decays in the low-background data from each run. An independent estimate performed using the ACTIVIA software package [125] predicts a rate about a factor of 3$\times$ higher (demonstrating the large uncertainty associated with the activation rates). A PDF for ^{7}Be decay is included in the fits for both runs.

Another possible contaminant is ^{85}Kr. Present at the level of $\sim$1 Bq/m^3 in atmospheric air, ^{85}Kr decays primarily by emission of a 252 keV β with a half-life of 10.7 y. In

0.434 % of these decays, the daughter nucleus is left in a meta-stable state with half-life 1.01 µs. The deexcitation of this state results in the emission of a 514 keV γ that can be tagged in coincidence with the β. A set of selection cuts similar to those in Sec. 6.5.2 were devised to search for these coincidences in each run with total cut efficiencies of 13.6 % and 11.7 %. Two events pass these cuts in Run 1, while a single event passes in Run 2. The expected backgrounds from accidental coincidences are 0.035 and 0.003 events. The resulting concentrations are (0.27 ± 0.20) mBq/kg and (0.08 ± 0.08) mBq/kg, respectively. These are consistent with estimates of the air exposure during filling, which make use of the initial rates of ^{222}Rn in each run. ^{85}Kr populations in each fit are constrained with these normalizations and errors. In the much larger OD, preventing ^{85}Kr contamination during LS filling will be crucial.

In summary, the following populations are included with constraint terms in the fit: external U, Th, and K, water ^{222}Rn decays, $^{238}\mathrm{U}_{\mathrm{m}}$, $^{235}\mathrm{U}_{\mathrm{l}}$ (Run 1 only), $^{232}\mathrm{Th}_{\mathrm{l}}$, ^{176}Lu (Run 1 only), and ^{85}Kr. The following populations are included and allowed to float freely: ^{234}Pa, ^{210}Bi, ^{228}Ac, ^{7}Be, and ^{40}K.

6.5.5 Fit Results

Our strategy is to regard the α fits as the most robust technique for measuring the scintillator impurities. This comes about as a result of two observations: first, the shapes resulting from α events are more distinct than those from γ/β events, which tend to be relatively featureless and can overlap significantly. Second, the γ/β fits suffer from

having the external activity of the detector components as a background and contain a larger number of fit parameters.

The results from all fits are summarized in Tab. 6.8, where isotopes are grouped according to their decay chain. Where subchain results are given, the specified activity represents the activity of each isotope within the subchain. In general, we find consistency between the α fits and the γ/β fits within the various subchains where equilibrium is expected. Activity is measured in the early parts of both the ^{238}U and ^{232}Th chains different than that measured by β-α coincidences, demonstrating that secular equilibrium is broken. The elevated activity of the GdLS with respect to the unloaded LS sample is obvious. The inclusive Screener rates above 200 keV reconstructed from Tab. 6.8 are (89.5 ± 7.3) mHz in Run 1 and (25.1 ± 3.0) mHz in Run 2, which are generally consistent (within 1.7σ) with those measured in data.

The α fits are shown in Fig. 6.31. In the unloaded LS of Run 2, the prominent feature is from out-of-equilibrium ^{210}Po decay. In the GdLS, the α rate is mostly comprised of decays from the $^{235}\mathrm{U}_{\mathrm{l}}$ subchain, resulting in a smaller error on its concentration than that obtained from α-α coincidences.

The γ/β fits are shown in Fig. 6.32 and provide a useful cross-check for the α results. In the Run 2 γ/β fit the best-fit values for the external uranium, external potassium, and water ^{222}Rn activities are in general agreement with their predicted values as shown in Tab. 6.7. The amount of external thorium found by the fit is roughly a factor of two lower than predicted, but well constrained by the highest pulse area data. As the

external conditions in each run were the same, the best-fit value found in Run 2 is used to rescale the external thorium constraint for the GdLS fit in Run 1.

Table 6.7: Predictions and fit results for the rates from detector material backgrounds in each run's γ/β fit. The asterisk denotes that the predicted external ^{232}Th rate in Run 1 was scaled by the ratio of predicted to fit result found in Run 2.

Run 1, Efficiency Applied, >65 phe (222 keV) (mHz)				
	^{238}U	**Water ^{222}Rn**	**^{232}Th**	**^{40}K**
Predicted	1.21 ± 0.23	0.52 ± 0.25	0.52 ± 0.08*	1.23 ± 0.19
Fit Result	1.19 ± 0.19	0.55 ± 0.25	0.47 ± 0.07	0.97 ± 0.22
Run 2, Efficiency Applied, >100 phe (281 keV) (mHz)				
	^{238}U	**Water ^{222}Rn**	**^{232}Th**	**^{40}K**
Predicted	0.89 ± 0.18	0.37 ± 0.18	0.76 ± 0.12	0.82 ± 0.12
Fit Result	0.95 ± 0.21	0.41 ± 0.17	0.36 ± 0.07	0.63 ± 0.11

Table 6.8: Measured radioimpurity concentrations in both loaded and unloaded LS runs grouped by isotope type. Reported errors are statistical only and, where none are given, the one-sided upper limit at 90% CL is reported. A 0.4% systematic error resulting from the uncertainty on the LS mass in the detector also applies.

Isotope		**Gd-Loaded LS Activity (mBq/kg)**	**Unloaded LS Activity (mBq/kg)**	**Method**
^{238}U Chain	^{238}U,^{234}U	0.23 ± 0.02	-	α Fit
	^{238}U,^{234}U,^{230}Th	-	0.0055 ± 0.0052	α Fit
	^{234}Pa	0.33 ± 0.04	< 0.065	γ/β Fit
	^{238}U$_m$ Subchain	0.019 ± 0.003	0.023 ± 0.002	BiPo
	^{210}Bi	0.40 ± 0.26	0.30 ± 0.10	γ/β Fit
	^{210}Po	0.16 ± 0.02	0.099 ± 0.009	α Fit
^{235}U Chain	^{235}U$_l$ Subchain	0.185 ± 0.006	-	α Fit
^{232}Th Chain	^{232}Th	0.16 ± 0.04	0.059 ± 0.013	α Fit
	^{228}Ac	< 0.20	< 0.018	γ/β Fit
	^{232}Th$_l$ Subchain	0.0071 ± 0.0019	0.00082 ± 0.00074	BiPo
Other	^{40}K	< 0.34	< 0.14	γ/β Fit
	^{7}Be	< 2.69	1.67 ± 0.51	γ/β Fit
	^{85}Kr	< 0.31	0.069 ± 0.067	γ/β Fit
	^{176}Lu	0.25 ± 0.07	-	γ/β Fit

Our hypotheses regarding the locations of decay chain equilibrium breakage are motivated by the purification methods used to prepare the LS and GdLS discussed in Sec. 4.3. Both the water extraction and distillation techniques have demonstrated efficient removal

of heavy elements, in particular, lead and radium [126; 127]. In comparison, the Gd compound's purification effectively removes thorium, but is not effective at removing radium or actinium [71]. Our hypotheses are therefore the following: in the unloaded LS sample of Run 2 we expect that equilibrium is broken at the long-lived radium isotopes ^{226}Ra (α emitter, ^{238}U chain) and ^{228}Ra (soft β emitter, ^{232}Th chain). In the GdLS, we expect that efficient thorium removal leads to breaks at the long-lived thorium isotopes ^{230}Th (α emitter, ^{238}U chain) and ^{228}Th (α emitter, ^{232}Th chain).

The most sensitive test for finding the location of equilibrium breakage is in the α fits for each run. The α emitters ^{238}U through ^{226}Ra in the ^{238}U chain are successively removed from the BiPo-constrained $^{238}U_m$ population and allowed to float freely, both independently from one another and as a summed $^{238}U_e$ population. The fit χ^2/ndf from each iteration is recorded in Tab. 6.9. Improvement in the Run 1 fit is observed with the removal of isotopes up to ^{230}Th, after which the improvement is very small. A similar improvement is observed in Run 2, however, the case where no early ^{238}U chain isotopes are excluded from the $^{238}U_m$ population yields an acceptable χ^2 at 90 % CL. This is reflected in Tab. 6.8 where the concentration of ^{238}U +^{234}U is consistent with the measured BiPo coincidence rate.

Table 6.9: χ^2 values obtained when various ^{238}U early chain isotopes are allowed to float free, independent from the BiPo-constrained, $^{238}U_m$ PDF ending with ^{214}Po. Also given are the χ^2 values when those early chain isotopes are summed into a single, early chain PDF.

Early ^{238}U Chain Isotopes	**Run 1 χ^2/ndf**		**Run 2 χ^2/ndf**	
	Free	**Summed**	**Free**	**Summed**
None	147.4/70		63.2/51	
^{238}U	95.9/69	95.9/69	58.4/50	58.4/50
^{238}U, ^{234}U	68.1/68	69.6/69	50.4/49	50.4/50
^{238}U, ^{234}U, ^{230}Th	68.0/67	69.1/69	49.5/48	49.5/50
^{238}U, ^{234}U, ^{230}Th, ^{226}Ra	68.0/66	68.9/69	49.1/47	49.4/50

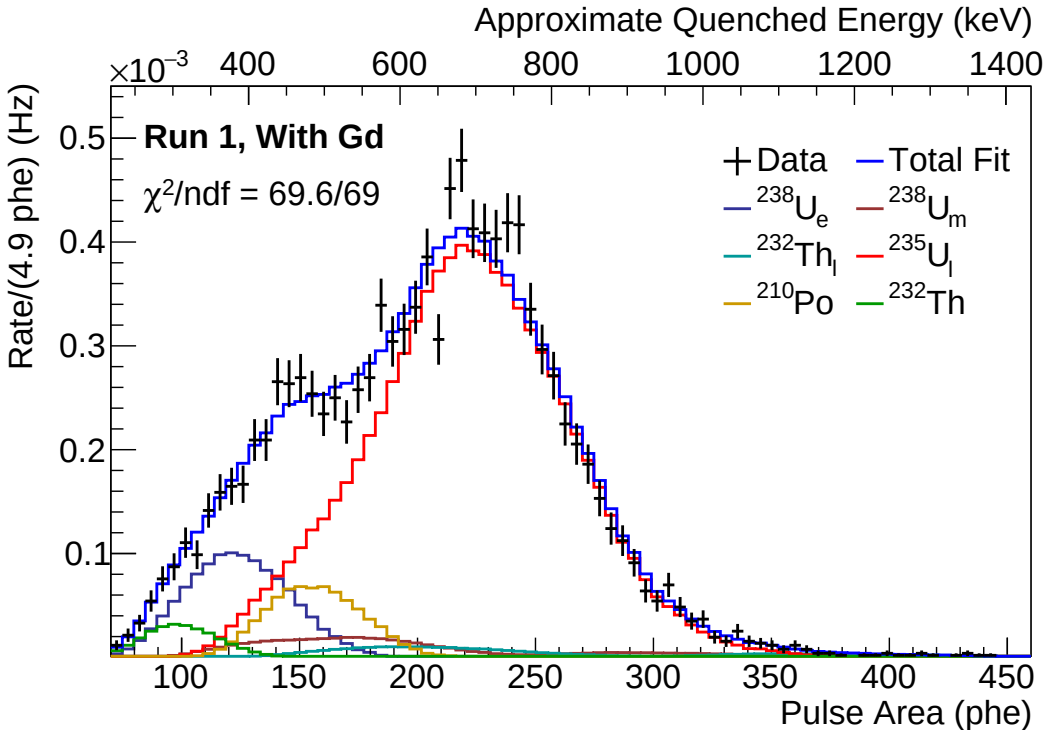

(a)

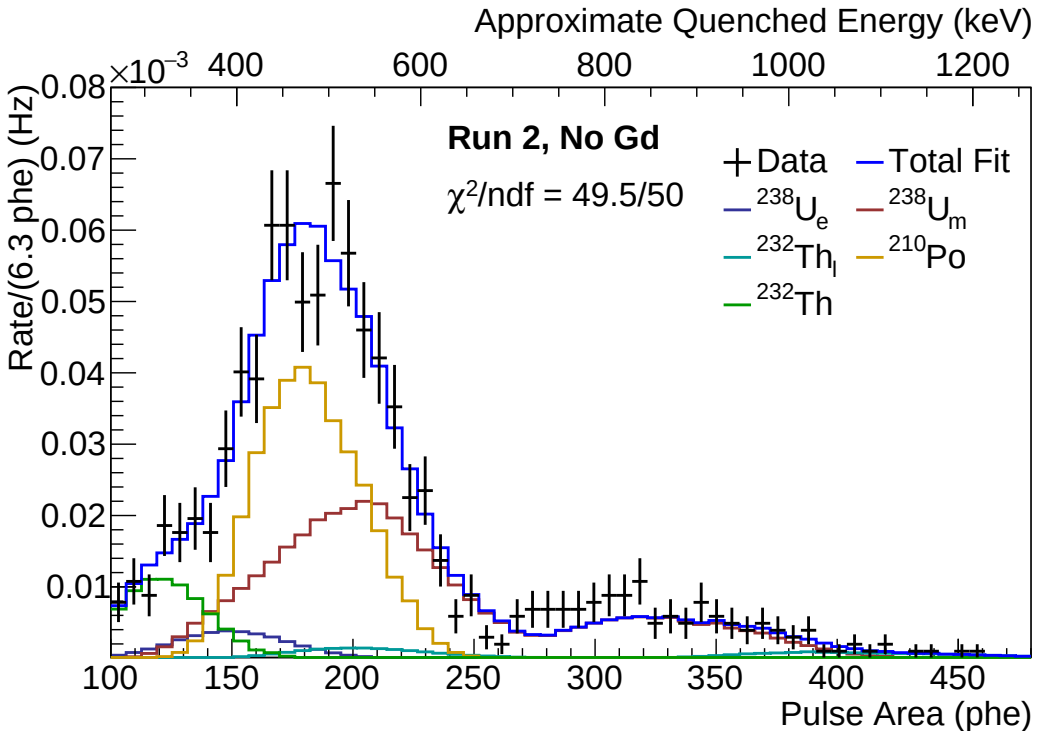

(b)

Figure 6.31: Best-fit to selection of α events in (a) the GdLS sample and (b) the unloaded LS sample.

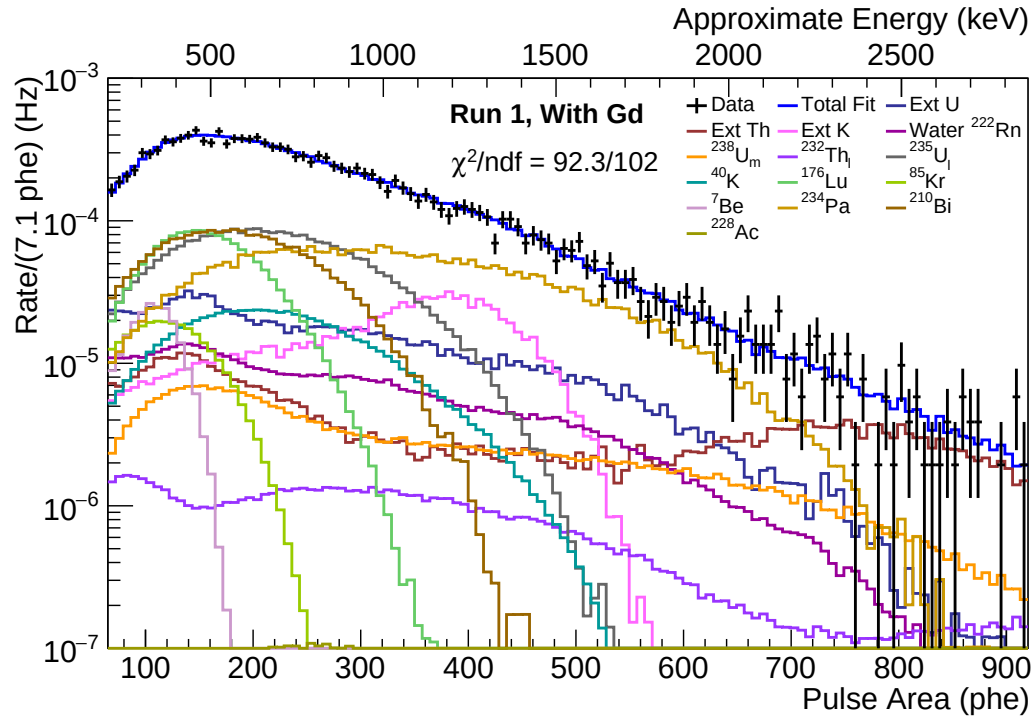

(a)

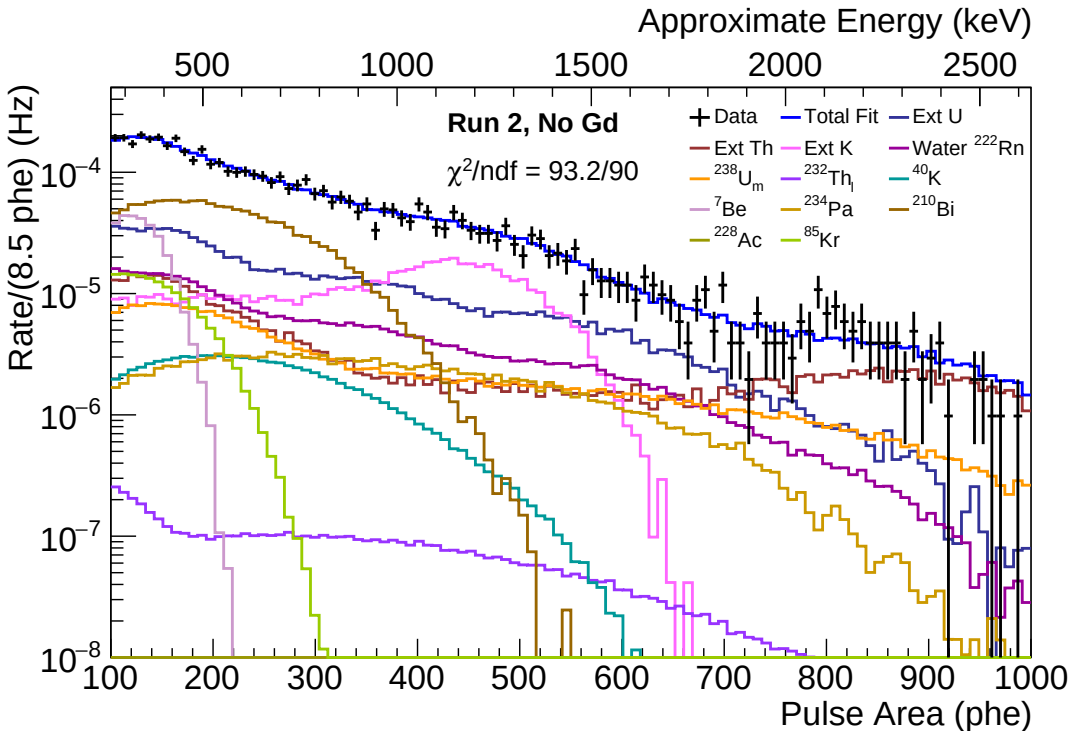

(b)

Figure 6.32: Best-fit to selection of γ/β events in (a) the GdLS sample and (b) the unloaded LS sample.

6.5.6 Inclusive Fits and Results

The inclusive Screener count rates implied by the radioimpurity concentrations of the previous section are within 1.7σ of that observed in data. An additional, inclusive fit was performed in each run to observe how the above results change under the constraint of equal rates, with no selection on pulse shape imposed. During the fit, all isotope populations begin with the concentrations measured in Tab. 6.8 and are constrained by those errors as well. In the $^{238}\mathrm{U}_{\mathrm{m}}$, $^{235}\mathrm{U}_{\mathrm{l}}$, and $^{232}\mathrm{Th}_{\mathrm{l}}$ subchains, the α and β emitting isotopes are summed into single populations for each. Furthermore, to reduce the number of fit parameters, the $^{238}\mathrm{U}_{\mathrm{m}}$ and $^{232}\mathrm{Th}_{\mathrm{l}}$ populations are fixed, as their rates are subdominant and well measured, for example, by counting pulse pairs in Sec. 6.5.2. The $^{235}\mathrm{U}_{\mathrm{l}}$ population is allowed to float as the combined rate from its α activity forms a very prominent feature in the pulse area spectrum of Run 1.

The inclusive fit results are given in Tab. 6.10 where the results of the previous section are also repeated for comparison. The fits and their residuals are shown in Fig. 6.33 and Fig. 6.34. Generally, we find a uniform reduction in concentration across all the isotope populations. We note, however, the 1.8σ discrepancy between results for ^{176}Lu in Run 1. Two attempts were made to rectify these results. First, the ^{176}Lu rate was fixed, which resulted in a change of $\Delta\chi^2 = 9.0$. Second, the constraint on ^{210}Bi was removed, allowing it to float free. In this iteration the best fit ^{176}Lu and ^{210}Bi rates were the same as that reported here.

Table 6.10: Radioimpurity concentrations measured in the α & β/γ fits and using the inclusive fit in both loaded and unloaded LS runs grouped by isotope type. Reported errors are statistical only and, where none are given, the one-sided upper limit at 90% CL is reported. A 0.4% systematic error resulting from the uncertainty on the LS mass in the detector also applies.

Isotope		**Gd-Loaded LS Activity (mBq/kg)**		**Unloaded LS Activity (mBq/kg)**	
		α & γ/β Fit	**Inclusive Fit**	**α & γ/β Fit**	**Inclusive Fit**
^{238}U Chain	^{238}U,^{234}U	0.23 ± 0.02	0.20 ± 0.01	-	-
	^{238}U,^{234}U,^{230}Th	-	-	0.0055 ± 0.0052	< 1.3
	^{234}Pa	0.33 ± 0.04	0.31 ± 0.02	< 0.065	0.021 ± 0.007
	^{238}U$_{\mathrm{m}}$ Subchain	0.019 ± 0.003		0.023 ± 0.002	
	^{210}Bi	0.40 ± 0.26	0.39 ± 0.12	0.30 ± 0.10	0.19 ± 0.01
	^{210}Po	0.16 ± 0.02	0.11 ± 0.02	0.099 ± 0.009	0.08 ± 0.01
^{235}U Chain	^{235}U$_{\mathrm{l}}$ Subchain	0.185 ± 0.006	0.19 ± 0.02	-	-
^{232}Th Chain	^{232}Th	0.16 ± 0.04	0.10 ± 0.02	0.059 ± 0.013	0.037 ± 0.008
	^{228}Ac	< 0.20	< 0.08	< 0.018	< 0.010
	^{232}Th$_{\mathrm{l}}$ Subchain	0.0071 ± 0.0019		0.00082 ± 0.00074	
Other	^{40}K	< 0.34	0.20 ± 0.08	< 0.14	0.015 ± 0.008
	^{7}Be	< 2.69	< 2.93	1.67 ± 0.51	1.16 ± 0.59
	^{85}Kr	< 0.31	< 0.29	0.069 ± 0.067	< 0.02
	^{176}Lu	0.25 ± 0.07	0.08 ± 0.06	-	-

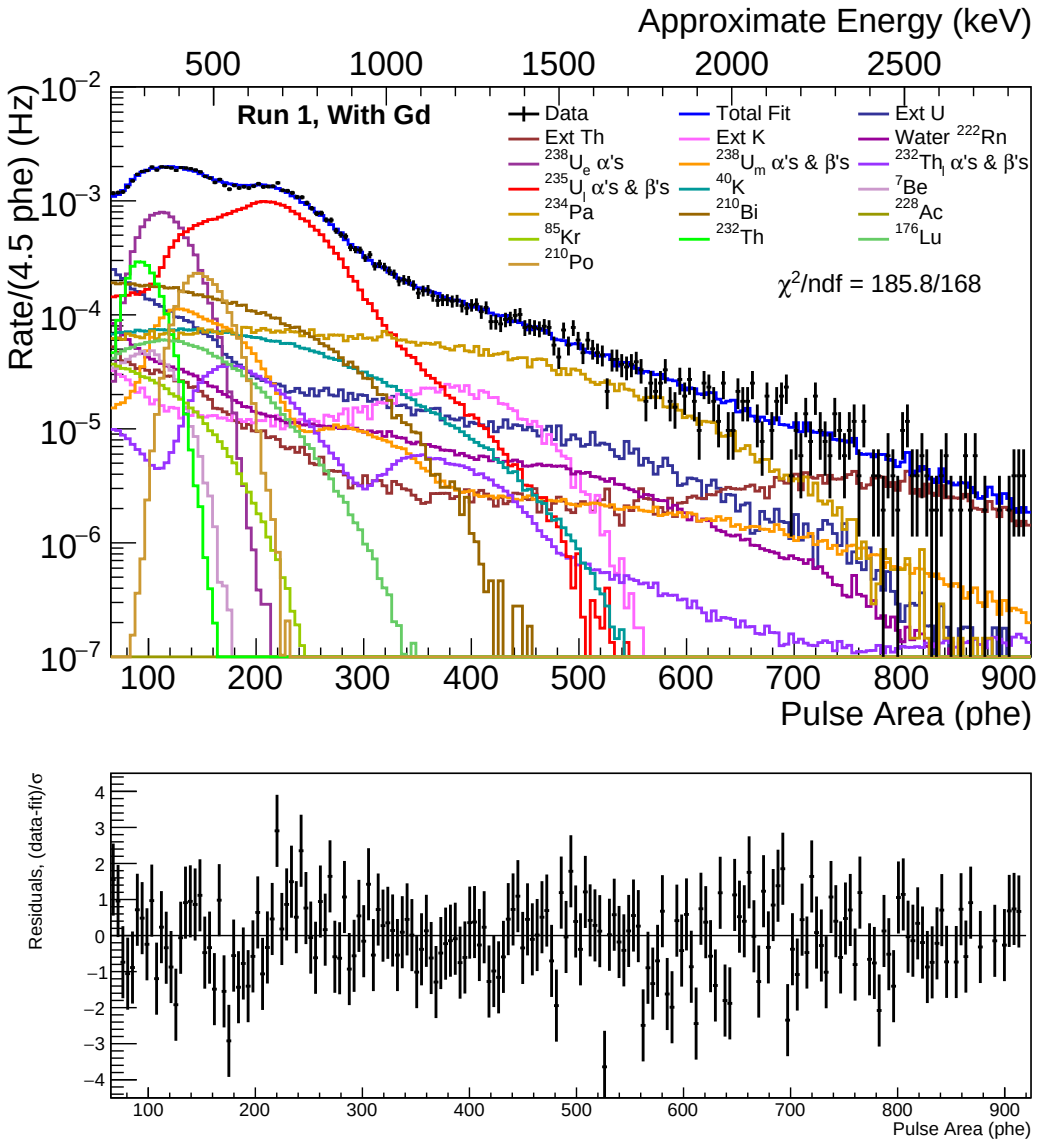

Figure 6.33: Inclusive fit to Run 1 data and fit residuals.

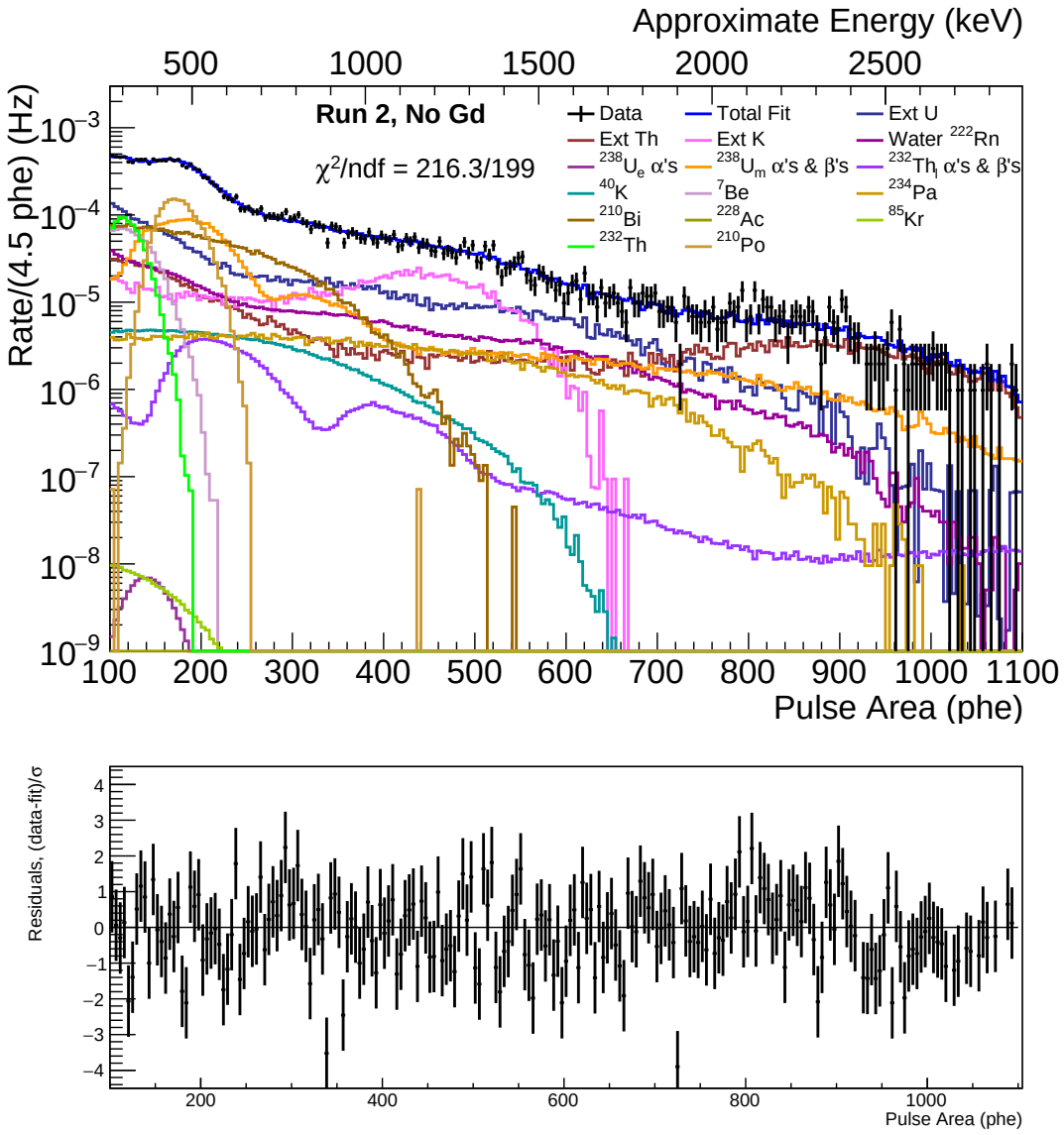

Figure 6.34: Inclusive fit to Run 2 data and fit residuals.

6.5.7 Rates in the OD

In Tab. 6.11 we use the Screener results from Tab. 6.8 to predict the contributions to the singles rate in the 17.3 tonnes of LS in the LZ OD. Rates are reported separately for α and β/γ decays and also given assuming no energy threshold and a 100 keV threshold. The contribution from ^{7}Be is not included as its half-life is small compared to the planned length of the experiment [32]. Similar results for the total α and β/γ rates in the OD derived from the inclusive fits given Tab. 6.10 are consistent within the errors given here.

Table 6.11: Predictions for the singles rate in 17.3 tonnes of LS in the OD calculated from the values in Tab. 6.8. Rates are given in the case of no energy threshold and a 100 keV threshold for both the unloaded and Gd-loaded LS.

Source	**Decay Type**	**Gd-Loaded LS Rate (Hz)**		**Unloaded LS Rate (Hz)**	
		No Threshold	**>100 keV**	**No Threshold**	**>100 keV**
^{238}U Chain	α	12.4 ± 0.6	12.4 ± 0.6	3.6 ± 0.2	3.6 ± 0.2
	β/γ	22.5 ± 6.4	11.9 ± 4.0	11.4 ± 2.5	5.4 ± 1.5
	All	34.8 ± 6.4	24.3 ± 4.0	15.0 ± 2.5	9.0 ± 1.5
^{235}U Chain	α	19.2 ± 0.3	19.2 ± 0.3	0	0
	β/γ	9.6 ± 0.2	5.8 ± 0.1	0	0
	All	28.8 ± 0.3	25.0 ± 0.3	0	0
^{232}Th Chain	α	3.4 ± 0.7	3.4 ± 0.7	1.1 ± 0.2	1.1 ± 0.2
	β/γ	0.2 ± 3.9	0.2 ± 2.7	0.0 ± 0.3	0.0 ± 0.2
	All	3.6 ± 4.0	3.6 ± 2.8	1.1 ± 0.4	1.1 ± 0.3
^{40}K	β/γ	1.7 ± 3.1	1.6 ± 2.9	0.3 ± 1.7	0.3 ± 1.6
^{85}Kr	β/γ	1.9 ± 2.8	1.5 ± 2.2	1.2 ± 1.2	0.9 ± 0.9
^{176}Lu	β/γ	4.3 ± 1.2	4.3 ± 1.2	0	0
^{14}C	β	82.5 ± 1.7	7.0 ± 0.2	82.5 ± 1.7	7.0 ± 0.2
^{152}Gd	α	27.9 ± 1.4	17.0 ± 0.9	0	0
^{147}Sm	α	17.6 ± 0.9	13.0 ± 0.6	0	0
Total	α	80.4 ± 1.9	65.0 ± 1.4	4.7 ± 0.3	4.7 ± 0.3
Total	β/γ	122.8 ± 8.8	32.5 ± 6.1	95.4 ± 3.7	13.7 ± 2.4
Total	All	203.2 ± 9.0	97.5 ± 6.3	100.1 ± 3.7	18.3 ± 2.4

In the OD, neutrons which moderate and subsequently capture in the GdLS can be tagged by the unique combination of a prompt, quenched proton recoil signal followed by a delayed electron recoil signal from the cascade of n-capture γ's. In the cases were the proton recoil signal is below threshold or non-existent, internal β/γ decays can mimic

the delayed n-capture signature. Internal α-decays, however, can be identified as being α-like by their pulse shape and so contribute less to the overall false veto probability. Use of a 200 keV threshold in the OD additionally reduces the rate from radioimpurities to (56.8 ± 5.5) Hz primarily by excluding pulses from ^{14}C, ^{152}Gd, and ^{147}Sm.

The overall cleanliness of the OD will be higher than that achieved in runs with the Screener. In particular, we expect the rate from ^{210}Pb daughters to be reduced through minimized exposure of OD components with radon-laden air. This includes not only the acrylic tanks themselves but also the inside surfaces of the LS filling system. Further improved filling techniques will also minimize the concentration of ^{85}Kr and ^{222}Rn in the final GdLS.

Bibliography

[1] V. C. Rubin and W. K. Ford, Jr., "Rotation of the Andromeda Nebula from a Spectroscopic Survey of Emission Regions," Astrophys. J. **159**, 379 (1970).

[2] V. C. Rubin, W. K. Ford, Jr., and N. Thonnard, "Rotational properties of 21 SC galaxies with a large range of luminosities and radii, from NGC 4605 /R = 4kpc/ to UGC 2885 /R = 122 kpc/," Astrophys. J. **238**, 471–487 (1980).

[3] K. G. Begeman, A. H. Broeils, and R. H. Sanders, "Extended rotation curves of spiral galaxies: Dark haloes and modified dynamics," Mon. Not. Roy. Astron. Soc. **249**, 523 (1991).

[4] P. A. R. Ade *et al.* (Planck), "Planck 2015 results. XIII. Cosmological parameters," Astron. Astrophys. **594**, A13 (2016), arXiv:1502.01589 [astro-ph] .

[5] G. Jungman, M. Kamionkowski, and K. Griest, "Supersymmetric dark matter," Phys. Rept. **267**, 195–373 (1996), arXiv:hep-ph/9506380 [hep-ph] .

[6] J. L. Feng, "Dark Matter Candidates from Particle Physics and Methods of Detection," Ann. Rev. Astron. Astrophys. **48**, 495–545 (2010), arXiv:1003.0904 [astro-ph.CO] .

[7] C. McCabe, "The Astrophysical Uncertainties Of Dark Matter Direct Detection Experiments," Phys. Rev. **D82**, 023530 (2010), arXiv:1005.0579 [hep-ph] .

[8] J. D. Lewin and P. F. Smith, "Review of mathematics, numerical factors, and corrections for dark matter experiments based on elastic nuclear recoil," Astropart. Phys. **6**, 87–112 (1996).

[9] C. McCabe, "The Earth's velocity for direct detection experiments," JCAP **1402**, 027 (2014), arXiv:1312.1355 [astro-ph.CO] .

[10] C. Savage, K. Freese, and P. Gondolo, "Annual Modulation of Dark Matter in the Presence of Streams," Phys. Rev. **D74**, 043531 (2006), arXiv:astro-ph/0607121 [astro-ph] .

[11] R. Bernabei *et al.*, "First model independent results from DAMA/LIBRA-phase2," (2018), arXiv:1805.10486 [hep-ex] .

[12] G. Adhikari *et al.*, "Initial Performance of the COSINE-100 Experiment," Eur. Phys. J. **C78**, 107 (2018), arXiv:1710.05299 [physics.ins-det] .

[13] F. Froborg (SABRE), "SABRE: WIMP modulation detection in the northern and southern hemisphere," *Proceedings, 14th International Conference on Topics in Astroparticle and Underground Physics (TAUP 2015): Torino, Italy, September 7-11, 2015*, J. Phys. Conf. Ser. **718**, 042021 (2016), arXiv:1601.05307 [physics.ins-det] .

[14] E. Segre, *Nuclei and Particles* (W. A. Benjamin, Inc, 1964).

[15] D. S. Akerib *et al.* (LUX), "Limits on spin-dependent WIMP-nucleon cross section obtained from the complete LUX exposure," Phys. Rev. Lett. **118**, 251302 (2017), arXiv:1705.03380 [astro-ph.CO] .

[16] R. H. Helm, "Inelastic and Elastic Scattering of 187-Mev Electrons from Selected Even-Even Nuclei," Phys. Rev. **104**, 1466–1475 (1956).

[17] C. Nehrkorn, *Testing the WIMP hypothesis with the LUX dark matter detector*, Ph.D. thesis, University of California, Santa Barbara (2017).

[18] G. Busoni *et al.*, "Recommendations on presenting LHC searches for missing transverse energy signals using simplified s-channel models of dark matter," (2016), arXiv:1603.04156 [hep-ex] .

[19] A. L. Fitzpatrick, W. Haxton, E. Katz, N. Lubbers, and Y. Xu, "The effective field theory of dark matter direct detection," J. Cosmol. Astropart. Phys. **2013**, 004 (2013), arXiv:1203.3542 [hep-ph] .

[20] E. Aprile *et al.* (XENON), "Dark Matter Search Results from a One Tonne×Year Exposure of XENON1T," Phys. Rev. Lett. **121**, 111302 (2018), arXiv:1805.12562 [astro-ph.CO] .

[21] V. Chepel and H. Araújo, "Liquid noble gas detectors for low energy particle physics," J. Instrum. **8**, R04001 (2013), arXiv:1207.2292 [physics.ins-det] .

[22] E. Conti *et al.* (EXO-200), "Correlated fluctuations between luminescence and ionization in liquid xenon," Phys. Rev. **B68**, 054201 (2003), arXiv:hep-ex/0303008 [hep-ex] .

[23] C. E. Dahl, *The physics of background discrimination in liquid xenon, and first results from Xenon10 in the hunt for WIMP dark matter*, Ph.D. thesis, Princeton U. (2009).

[24] J. Lindhard, V. Nielsen, M. Scharff, and P. Thomsen, "Integral equations governing radiation effects," Kgl. Danske Videnskab., Selskab. Mat. Fys. Medd. **33** (1963).

[25] M. Szydagis, N. Barry, K. Kazkaz, J. Mock, D. Stolp, M. Sweany, M. Tripathi, S. Uvarov, N. Walsh, and M. Woods (NEST), "NEST: A Comprehensive Model for Scintillation Yield in Liquid Xenon," J. Instrum. **6**, P10002 (2011), arXiv:1106.1613 [physics.ins-det] .

[26] D. S. Akerib *et al.* (LUX), "The Large Underground Xenon (LUX) Experiment," Nucl. Instrum. Meth. **A704**, 111–126 (2013), arXiv:1211.3788 [physics.ins-det] .

[27] D. S. Akerib *et al.* (LUX), "^{83m}Kr calibration of the 2013 LUX dark matter search," Phys. Rev. **D96**, 112009 (2017), arXiv:1708.02566 [physics.ins-det] .

[28] D. S. Akerib *et al.* (LUX), "Tritium calibration of the LUX dark matter experiment," Phys. Rev. **D93**, 072009 (2016), arXiv:1512.03133 [physics.ins-det] .

[29] D. S. Akerib *et al.* (LUX), "Calibration, event reconstruction, data analysis, and limit calculation for the LUX dark matter experiment," Phys. Rev. **D97**, 102008 (2018), arXiv:1712.05696 [physics.ins-det] .

[30] D. S. Akerib *et al.* (LUX), "Low-energy (0.7-74 keV) nuclear recoil calibration of the LUX dark matter experiment using D-D neutron scattering kinematics," (2016), arXiv:1608.05381 [physics.ins-det] .

[31] B. J. Mount *et al.*, "LUX-ZEPLIN (LZ) Technical Design Report," (2017), arXiv:1703.09144 [physics.ins-det] .

[32] D. S. Akerib *et al.* (LUX-ZEPLIN), "Projected WIMP Sensitivity of the LUX-ZEPLIN (LZ) Dark Matter Experiment," (2018), arXiv:1802.06039 [astro-ph.IM] .

[33] J. Heise, "The Sanford Underground Research Facility at Homestake," J. Phys. Conf. Ser. **606**, 012015 (2015), arXiv:1503.01112 [physics.ins-det] .

[34] D. S. Akerib *et al.* (LUX), "An Ultra-Low Background PMT for Liquid Xenon Detectors," Nucl. Instrum. Meth. **A703**, 1–6 (2013), arXiv:1205.2272 [physics.ins-det] .

[35] E. Aprile *et al.* (XENON1T), "Lowering the radioactivity of the photomultiplier tubes for the XENON1T dark matter experiment," Eur. Phys. J. **C75**, 546 (2015), arXiv:1503.07698 [astro-ph.IM] .

[36] E. Aprile *et al.* (XENON), "Results from a Calibration of XENON100 Using a Source of Dissolved Radon-220," Phys. Rev. **D95**, 072008 (2017), arXiv:1611.03585 [physics.ins-det] .

[37] J. I. Collar, "Applications of an $^{88}Y/Be$ photo-neutron calibration source to Dark Matter and Neutrino Experiments," Phys. Rev. Lett. **110**, 211101 (2013), arXiv:1303.2686 [physics.ins-det] .

[38] S. Shaw, *Dark Matter Searches with the LUX and LZ Dark Matter Experiments*, Ph.D. thesis, University College London (2016).

[39] D. S. Akerib *et al.* (LUX), "Chromatographic separation of radioactive noble gases from xenon," Astropart. Phys. **97**, 80–87 (2018), arXiv:1605.03844 [physics.ins-det] .

[40] C. A. O'Hare, "Dark matter astrophysical uncertainties and the neutrino floor," Phys. Rev. **D94**, 063527 (2016), arXiv:1604.03858 [astro-ph.CO] .

[41] D. Akimov *et al.* (COHERENT), "Observation of Coherent Elastic Neutrino-Nucleus Scattering," Science **357**, 1123–1126 (2017), arXiv:1708.01294 [nucl-ex] .

[42] D. Z. Freedman, "Coherent neutrino nucleus scattering as a probe of the weak neutral current," Phys. Rev. **D9**, 1389–1392 (1974).

[43] M. Redshaw, E. Wingfield, J. McDaniel, and E. G. Myers, "Mass and double-beta-decay Q value of Xe-136," Phys. Rev. Lett. **98**, 053003 (2007).

[44] S. Agostinelli *et al.* (GEANT4), "GEANT4: A Simulation toolkit," Nucl. Instrum. Meth. **A506**, 250–303 (2003).

[45] G. Cowan, K. Cranmer, E. Gross, and O. Vitells, "Asymptotic formulae for likelihood-based tests of new physics," Eur. Phys. J. **C71**, 1554 (2011), [Erratum: Eur. Phys. J.C73,2501(2013)], arXiv:1007.1727 [physics.data-an] .

[46] G. Cowan, K. Cranmer, E. Gross, and O. Vitells, "Power-Constrained Limits," (2011), arXiv:1105.3166 [physics.data-an] .

[47] D. S. Akerib *et al.* (LUX), "Results from a search for dark matter in the complete LUX exposure," Phys. Rev. Lett. **118**, 021303 (2017), arXiv:1608.07648 [astro-ph.CO] .

[48] E. Aprile *et al.* (XENON), "First Dark Matter Search Results from the XENON1T Experiment," Phys. Rev. Lett. **119**, 181301 (2017), arXiv:1705.06655 [astro-ph.CO] .

[49] X. Cui *et al.* (PandaX-II), "Dark Matter Results From 54-Ton-Day Exposure of PandaX-II Experiment," Phys. Rev. Lett. **119**, 181302 (2017), arXiv:1708.06917 [astro-ph.CO] .

[50] J. Billard, L. Strigari, and E. Figueroa-Feliciano, "Implication of neutrino backgrounds on the reach of next generation dark matter direct detection experiments," Phys. Rev. **D89**, 023524 (2014), arXiv:1307.5458 [hep-ph] .

[51] F. Ruppin, J. Billard, E. Figueroa-Feliciano, and L. Strigari, "Complementarity of dark matter detectors in light of the neutrino background," Phys. Rev. **D90**, 083510 (2014), arXiv:1408.3581 [hep-ph] .

[52] E. Bagnaschi *et al.*, "Likelihood Analysis of the pMSSM11 in Light of LHC 13-TeV Data," Eur. Phys. J. **C78**, 256 (2018), arXiv:1710.11091 [hep-ph] .

[53] E. Aprile *et al.* (XENON100), "XENON100 Dark Matter Results from a Combination of 477 Live Days," Phys. Rev. **D94**, 122001 (2016), arXiv:1609.06154 [astro-ph.CO] .

[54] C. Fu *et al.* (PandaX-II), "Spin-Dependent Weakly-Interacting-Massive-ParticleNucleon Cross Section Limits from First Data of PandaX-II Experiment," Phys. Rev. Lett. **118**, 071301 (2017), arXiv:1611.06553 [hep-ex] .

[55] C. Amole *et al.* (PICO), "Dark Matter Search Results from the PICO-60 C_3F_8 Bubble Chamber," Phys. Rev. Lett. **118**, 251301 (2017), arXiv:1702.07666 [astro-ph.CO] .

[56] M. Aaboud *et al.* (ATLAS), "Search for dark matter at $\sqrt{s} = 13$ TeV in final states containing an energetic photon and large missing transverse momentum with the ATLAS detector," Eur. Phys. J. **C77**, 393 (2017), arXiv:1704.03848 [hep-ex] .

[57] A. M. Sirunyan *et al.* (CMS), "Search for dark matter produced with an energetic jet or a hadronically decaying W or Z boson at $\sqrt{s} = 13$ TeV," JHEP **07**, 014 (2017), arXiv:1703.01651 [hep-ex] .

[58] K. Choi *et al.* (Super-Kamiokande), "Search for neutrinos from annihilation of captured low-mass dark matter particles in the Sun by Super-Kamiokande," Phys. Rev. Lett. **114**, 141301 (2015), arXiv:1503.04858 [hep-ex] .

[59] M. G. Aartsen *et al.* (IceCube), "Search for annihilating dark matter in the Sun with 3 years of IceCube data," Eur. Phys. J. **C77**, 146 (2017), arXiv:1612.05949 [astro-ph.HE] .

[60] P. Athron *et al.* (GAMBIT), "A global fit of the MSSM with GAMBIT," Eur. Phys. J. **C77**, 879 (2017), arXiv:1705.07917 [hep-ph] .

[61] "Reynolds Polymer Technology, Inc." (2018), 607 Hollingsworth Street, Grand Junction, CO 81505.

[62] "DowDupont Inc." (2018), 974 Centre Road, Wilmington, DE 19805 USA.

[63] "Material Concepts," (2018), 11620 Caroline Road, Philadelphia, PA 19154-2116.

[64] M. Janecek and W. W. Moses, "Optical reflectance measurements for commonly used reflectors," IEEE Trans. Nucl. Sci. **55**, 2432–2437 (2008).

[65] M. Janecek, "Reflectivity spectra for commonly used reflectors," IEEE Trans. Nucl. Sci. **59**, 490–497 (2012).

[66] Z.-Y. Yu *et al.*, "Study of a prototype water Cherenkov detector for the Daya Bay neutrino experiment," Nucl. Instrum. Meth. **A682**, 26–30 (2012).

[67] National Fire Protection Association, Technical Correlating Committee on Flammable and Combustible Liquids, *NFPA 30: Flammable and Combustible Liquids Code* (National Fire Protection Association, 2018).

[68] "CEPSA Química Bécancour, Inc." (2018), 5250 Bécancour Boulevard, Bécancour (Québec) G9H 3X3 Canada.

[69] G. Alimonti *et al.* (Borexino), "Measurement of the ^{14}C abundance in a low-background liquid scintillator," Phys. Lett. **B422**, 349–358 (1998).

[70] Y. Ding, J. Liu, Z. Wang, Z. Zhang, P. Zhou, and Y. Zhao, "A new gadolinium-loaded liquid scintillator for reactor neutrino detection," Nucl. Instrum. Meth. **A584**, 238–243 (2008).

[71] M. Yeh, J. B. Cumming, S. Hans, and R. L. Hahn, "Purification of lanthanides for large neutrino detectors: Thorium removal from gadolinium chloride," Nucl. Instrum. Meth. **A618**, 124–130 (2010).

[72] M. Furst and H. Kallmann, "Energy transfer by means of collision in liquid organic solutions under high energy and ultraviolet excitations," Phys. Rev. **94**, 503–507 (1954).

[73] H.-L. Xiao, J.-S. Deng, and N.-Y. Wang, "Oxygen quenching in a lab based liquid scintillator and the nitrogen bubbling model," Chin. Phys. C **34**, 571–574 (2010).

[74] H. Kallmann and M. Furst, "Fluorescence of solutions bombarded with high energy radiation (energy transport in liquids) part ii," Phys. Rev. **81**, 853–864 (1951).

[75] W. Beriguete *et al.*, "Production of a gadolinium-loaded liquid scintillator for the Daya Bay reactor neutrino experiment," Nucl. Instrum. Meth. **A763**, 82–88 (2014), arXiv:1402.6694 [physics.ins-det] .

[76] G. T. Wright, "Absolute Quantum Efficiency of Photofluorescence of Anthracene Crystals," Proc. of the Phys. Soc. B **68**, 241–248 (1955).

[77] G. T. Wright, "Absolute Scintillation Efficiency of Anthracene Crystals," Proc. of the Phys. Soc. B **68**, 929–937 (1955).

[78] C. N. Chou, "The nature of the saturation effect of fluorescent scintillators," Phys. Rev. **87**, 904–905 (1952).

[79] J. B. Birks, "Scintillations from Organic Crystals: Specific Fluorescence and Relative Response to Different Radiations," Proc. of the Phys. Soc. A **64**, 874–877 (1951).

[80] C. J. Taylor, W. K. Jentschke, M. E. Remley, F. S. Eby, and P. G. Kruger, "Response of some scintillation crystals to charged particles," Phys. Rev. **84**, 1034–1043 (1951).

[81] B. von Krosigk *et al.*, "Measurement of α-particle quenching in LAB based scintillator in independent small-scale experiments," Eur. Phys. J. **C76**, 109 (2016), arXiv:1510.00458 [physics.ins-det] .

[82] B. von Krosigk, L. Neumann, R. Nolte, S. Rottger, and K. Zuber, "Measurement of the proton light response of various LAB based scintillators and its implication for supernova neutrino detection via neutrino-proton scattering," Eur. Phys. J. **C73**, 2390 (2013), arXiv:1301.6403 [astro-ph.IM] .

[83] F. P. An *et al.* (Daya Bay), "Measurement of electron antineutrino oscillation based on 1230 days of operation of the Daya Bay experiment," Phys. Rev. **D95**, 072006 (2017), arXiv:1610.04802 [hep-ex] .

[84] M. Wang, G. Audi, A. Wapstra, F. Kondev, M. MacCormick, X. Xu, and B. Pfeiffer, "The ame2012 atomic mass evaluation," Chin. Phys. **C36**, 1603 (2012).

[85] "National Nuclear Data Center, ENDF/B-VII.1," `http://www.nndc.bnl.gov/sigma/index.jsp` (2011).

[86] M. Mastromarco *et al.* (n_{TOF}), "Cross section measurements of ^{155,157}Gd (n,γ) induced by thermal and epithermal neutrons," (2018), arXiv:1805.04149 [nucl-ex] .

[87] S. Mughabghab, ed., *Atlas of Neutron Resonances, Resonance Parameters and Thermal Cross Sections, Z=1-100, Fifth Edition* (Elsevier Science, Radarweg 29, PO Box 2111, 1000 AE Amsterdam, The Netherlands, 2006).

[88] B. R. Littlejohn, *Observation of Antineutrino Disappearance at the Daya Bay Experiment*, Ph.D. thesis, Wisconsin U., Madison (2012).

[89] F. P. An *et al.* (Daya Bay), "The Detector System of The Daya Bay Reactor Neutrino Experiment," Nucl. Instrum. Meth. **A811**, 133–161 (2016), arXiv:1508.03943 [physics.ins-det] .

[90] J. K. Ahn *et al.* (RENO), "RENO: An Experiment for Neutrino Oscillation Parameter θ_{13} Using Reactor Neutrinos at Yonggwang," (2010), arXiv:1003.1391 [hep-ex] .

[91] F. Bečvář, "Simulation of γ cascades in complex nuclei with emphasis on assessment of uncertainties of cascade-related quantities," Nucl. Instrum. Meth. **A417**, 434–449 (1998).

[92] D. Woodward, *Simulations of cosmic muons and background radiations for muon tomography and underground experiments*, Ph.D. thesis, University of Sheffield (2018).

[93] D. S. Akerib *et al.*, (2018), Manuscript in preparation.

[94] D. S. Akerib *et al.* (LZ), "Measurement of the gamma ray background in the davis cavern at the sanford underground research facility," (2018), Manuscript in preparation.

[95] M. Agostini *et al.* (Borexino), "First Simultaneous Precision Spectroscopy of *pp*, ^{7}Be, and *pep* Solar Neutrinos with Borexino Phase-II," (2017), arXiv:1707.09279 [hep-ex] .

[96] A. Gando *et al.* (KamLAND), "^{7}Be Solar Neutrino Measurement with KamLAND," Phys. Rev. **C92**, 055808 (2015), arXiv:1405.6190 [hep-ex] .

[97] A. G. Piepke, S. W. Moser, and V. M. Novikov, "Development of a Gd loaded liquid scintillator for electron anti-neutrino spectroscopy," Nucl. Instrum. Meth. **A432**, 392–398 (1999), arXiv:nucl-ex/9904002 [nucl-ex] .

[98] F. Boehm *et al.*, "Final results from the Palo Verde neutrino oscillation experiment," Phys. Rev. **D64**, 112001 (2001), arXiv:hep-ex/0107009 [hep-ex] .

[99] J. H. Choi *et al.* (RENO), "Observation of Energy and Baseline Dependent Reactor Antineutrino Disappearance in the RENO Experiment," Phys. Rev. Lett. **116**, 211801 (2016), arXiv:1511.05849 [hep-ex] .

[100] Y. Abe *et al.* (Double Chooz), "Improved measurements of the neutrino mixing angle θ_{13} with the Double Chooz detector," JHEP **10**, 086 (2014), [Erratum: JHEP02,074(2015)], arXiv:1406.7763 [hep-ex] .

[101] P. Fernández (Super-Kamiokande), "Status of GADZOOKS!: Neutron Tagging in Super-Kamiokande," *Proceedings, 37th International Conference on High Energy Physics (ICHEP 2014): Valencia, Spain, July 2-9, 2014*, Nucl. Part. Phys. Proc. **273-275**, 353–360 (2016).

[102] J. P. Pérez, *Radioactive Contamination in Neutrino Experimental Physics: the Cases of NEXT and Super-Kamiokande Experiments*, Ph.D. thesis, Universidad Autonoma de Madrid (2017).

[103] E. K. Hyde, I. Perlman, and G. T. Seaborg, *The Nuclear Properties of the Heavy Elements Volume II: Detailed Radioactivity Properties* (Prentice-Hall, Inc., Englewood Cliffs, NJ, USA, 1964).

[104] R. S. Boiko, "Chemical purification of lanthanides for low-background experiments," Int. J. Mod. Phys. **A32**, 1743005 (2017).

[105] P. Agnes *et al.* (DarkSide), "The veto system of the DarkSide-50 experiment," JINST **11**, P03016 (2016), arXiv:1512.07896 [physics.ins-det] .

[106] M. E. Monzani, *Characterization and calibration of the BOREXINO detector for Solar and Supernova Neutrinos*, Ph.D. thesis, Diderot U., Paris (2005).

[107] G. J. Keefer, *First obeservation of ^{7}Be solar neutrinos with KamLAND*, Ph.D. thesis, University of Alabama (2016).

[108] J. Bieringer, C. Schlosser, H. Sartorius, and S. Schmid, "Trace analysis of aerosol bound particulates and noble gases at the bfs in germany," Applied Radiation and Isotopes **67**, 672 – 677 (2009), 5th International Conference on Radionuclide Metrology - Low-Level Radioactivity Measurement Techniques ICRM-LLRMT'08.

[109] F. Cejnar, L. Wilhelmov, and P. Vrzala, "Noble gas solubility measurement in liquid scintillator solvents," The International Journal of Applied Radiation and Isotopes **28**, 281 – 284 (1977).

[110] D. C. Malling, S. Fiorucci, M. Pangilinan, J. J. Chapman, C. H. Faham, J. R. Verbus, and R. J. Gaitskell, "Dark Matter Search Backgrounds from Primordial Radionuclide Chain Disequilibrium," (2013), (unpublished), arXiv:1305.5183 [astro-ph] .

[111] B. J. Mount *et al.*, "Black Hills State University Underground Campus," Appl. Radiat. Isot. **126**, 130–133 (2017).

[112] "International Polymer Solutions," (2018), 5 Studebaker, Irvine, CA 92618, USA.

[113] J. Beringer *et al.* (Particle Data Group), "Review of Particle Physics (RPP)," Phys. Rev. **D86**, 010001 (2012).

[114] "Eckert & Ziegler Isotope Products, Inc." (2018), 24937 Avenue Tibbitts, Valencia, CA 91355 USA.

[115] J. Heise, "The sanford underground research facility," in *15th International Conference on Topics in Astroparticle and Underground Physics (TAUP 2017) Sudbury, Ontario, Canada, July 24-28, 2017* (2017) arXiv:1710.11584 [physics.ins-det] .

[116] D. S. Akerib *et al.* (LZ), "Identification of Radiopure Titanium for the LZ Dark Matter Experiment and Future Rare Event Searches," Astropart. Phys. **96**, 1–10 (2017), arXiv:1702.02646 [physics.ins-det] .

[117] D. Yu. Akimov, A. I. Bolozdynya, Yu. V. Efremenko, V. A. Kaplin, A. V. Khromov, Yu. A. Melikyan, and V. V. Sosnovtsev, "Observation of light emission from Hamamatsu R11410-20 photomultiplier tubes," Nucl. Instrum. Meth. **A794**, 1–2 (2015), arXiv:1504.07651 [physics.ins-det] .

[118] B. von Krosigk, *Measurement of proton and α particle quenching in LAB based scintillators and determination of spectral sensitivities to supernova neutrinos in the SNO+ detector*, Ph.D. thesis, Technische Universität Dresden (2015).

[119] H. M. O'Keeffe, E. O'Sullivan, and M. C. Chen, "Scintillation decay time and pulse shape discrimination in oxygenated and deoxygenated solutions of linear alkylbenzene for the SNO+ experiment," Nucl. Instrum. Meth. **A640**, 119–122 (2011), arXiv:1102.0797 [physics.ins-det] .

[120] H. Behrens and J. Janecke, *Numerical Tables for Beta Decay*, Vol. 4 (Springer-Verlag, Berlin, 1969) in Landolt-Brnstein - Group I Elementary Particles, Nuclei and Atoms.

[121] I. R. Barabanov *et al.*, "Measurement of the ^{14}C content in liquid scintillators by means of a small-volume detector in the low-background chamber of the baksan neutrino observatory," Physics of Atomic Nuclei **80**, 1146–1152 (2017), [Yad. Fiz. 80,no. 6, 665 (2017)].

[122] L. Baudis, A. Behrens, A. Ferella, A. Kish, T. Marrodan Undagoitia, D. Mayani, and M. Schumann, "Performance of the Hamamatsu R11410 Photomultiplier Tube in cryogenic Xenon Environments," JINST **8**, P04026 (2013), arXiv:1303.0226 [astro-ph.IM] .

[123] "XIA LLC," (2018), 31057 Genstar Rd, Hayward, CA 94544.

[124] R. B. Vogelaar, J. Benziger, F. P. Calaprice, and N. Darnton, "Removal of cosmogenic ^{7}Be from scintillators," Nucl. Instrum. Meth. **372**, 59 – 62 (1996).

[125] J. J. Back and Y. A. Ramachers, "ACTIVIA: Calculation of Isotope Production Cross-sections and Yields," Nucl. Instrum. Meth. **A586**, 286–294 (2008), (ACTIVIA), arXiv:0709.3472 [nucl-ex] .

[126] R. Ford, M. Chen, O. Chkvorets, D. Hallman, and E. Vazquez-Jauregui, "SNO+ scintillator purification and assay," *Proceedings, 3rd Topical Workshop on Low radioactivity techniques (LRT 2010): Sudbury, Canada, August 28-29, 2010*, AIP Conf. Proc. **1338**, 183–194 (2011).

[127] G. Keefer *et al.* (KamLAND), "Laboratory studies on the removal of radon-born lead from KamLANDs organic liquid scintillator," Nucl. Instrum. Meth. **A769**, 79–87 (2015), arXiv:1312.0977 [physics.ins-det] .